

TUNING OF METAL ION SELECTIVITY BY VARYING NUMBER OF COORDINATING ATOMS
IN QUINOLINE-DERIVED FLUORESCENT SENSORS



A Dissertation Submitted in Partial Fulfillment of the Requirements
for the Degree of Doctor of Philosophy in Chemistry

Department of Chemistry

FACULTY OF SCIENCE

Chulalongkorn University

Academic Year 2020

Copyright of Chulalongkorn University

การปรับความเลือกจำเพาะไอออนโลหะด้วยการปรับเปลี่ยนจำนวนอะตอมโคออร์ดิเนตในฟลูออเรส
เซนต์เซ็นเซอร์จากควิโนลีน



วิทยานิพนธ์นี้เป็นส่วนหนึ่งของการศึกษาตามหลักสูตรปริญญาวิทยาศาสตรดุษฎีบัณฑิต
สาขาวิชาเคมี ภาควิชาเคมี
คณะวิทยาศาสตร์ จุฬาลงกรณ์มหาวิทยาลัย
ปีการศึกษา 2563
ลิขสิทธิ์ของจุฬาลงกรณ์มหาวิทยาลัย

Thesis Title	TUNING OF METAL ION SELECTIVITY BY VARYING NUMBER OF COORDINATING ATOMS IN QUINOLINE- DERIVED FLUORESCENT SENSORS
By	Mr. Jutawat Hojitsiriyant
Field of Study	Chemistry
Thesis Advisor	Professor MONGKOL SUKWATTANASINITT, Ph.D.
Thesis Co Advisor	Professor VITHAYA RUANGPORNVISUTI, Ph.D.

Accepted by the FACULTY OF SCIENCE, Chulalongkorn University in Partial
Fulfillment of the Requirement for the Doctor of Philosophy

..... Dean of the FACULTY OF SCIENCE
(Professor POLKIT SANGVANICH, Ph.D.)

DISSERTATION COMMITTEE

..... Chairman
(Professor VUDHICHAJ PARASUK, Ph.D.)

..... Thesis Advisor
(Professor MONGKOL SUKWATTANASINITT, Ph.D.)

..... Thesis Co-Advisor
(Professor VITHAYA RUANGPORNVISUTI, Ph.D.)

..... Examiner
(Professor PAITON RASHATASAKHON, Ph.D.)

..... Examiner
(Professor THAWATCHAI TUNTULANI, Ph.D.)

..... External Examiner
(Assistant Professor Nakorn Niamnont, Ph.D.)

จุฬาวัดน์ หอจิตศิริยานนท์ : การปรับความเลือกจำเพาะไอออนโลหะด้วยการปรับเปลี่ยนจำนวนอะตอมโคออร์ดิเนตในฟลูออเรสเซนต์เซ็นเซอร์จากควิโนลีน. (TUNING OF METAL ION SELECTIVITY BY VARYING NUMBER OF COORDINATING ATOMS IN QUINOLINE-DERIVED FLUORESCENT SENSORS) อ.ที่ปรึกษาหลัก : ศ. ดร.มงคล สุขวัฒนาสินธุ์, อ.ที่ปรึกษาร่วม : ศ. ดร.วิทยา เรืองพรวิสุทธิ์

ไอออนแคดเมียมและไอออนสังกะสีเป็นไอออนโลหะในหมู่ 12 ซึ่งมีความเป็นพิษที่แตกต่างกันแต่มีความสามารถในการจับกับลิแกนด์ส่วนใหญ่ที่ใกล้เคียงกัน โดยในงานศึกษานี้ ได้ออกแบบและสังเคราะห์กลุ่มของอนุพันธ์ควิโนลีนเพื่อเป็นฟลูออเรสเซนต์เซ็นเซอร์แบบเพิ่มสัญญาณที่จำเพาะกับไอออนแคดเมียม โดยโครงสร้างของสารนั้นจะถูกออกแบบออกเป็นระบบเพื่อศึกษาผลกระทบของอะมิโนโปรตอน จำนวนไนโตรเจนอะตอมโคออร์ดิเนต หมู่ควิโนลีน-พีโคลีนและหมู่แทนที่ ต่อความสามารถในการตรวจวัดไอออนโลหะ การศึกษาทำการหาค่าคงที่การเกิดสารประกอบเชิงซ้อนของลิแกนด์ในตัวกลางที่เป็นน้ำด้วยวิธีการไทเทรตแบบการดูดกลืนแสง จากผลการทดลองพบว่าลิแกนด์ชนิดเฮกซะเดนเตดและเตตระเดนเตดแบบไม่มีอะมิโนโปรตอนให้ค่าคงที่การเกิดสารประกอบเชิงซ้อนกับไอออนแคดเมียมและสังกะสีสูงตามลำดับ โดยลิแกนด์ L6 ซึ่งเป็นเฮกซะเดนเตดลิแกนด์แบบไม่มีอะมิโนโปรตอน ที่ประกอบด้วยควิโนลีน 2 หมู่และพีโคลีน 2 หมู่ มีความไวต่อการจับไอออนแคดเมียมสูงที่สุดโดยให้ค่าการเรืองแสงสัมพัทธ์ที่ 480 นาโนเมตรถึง 118 เท่าและให้ความจำเพาะเจาะจงกับแคดเมียมสูงที่สุด โดยให้ค่าอัตราส่วนค่าคงที่การเกิดสารประกอบเชิงซ้อนของไอออนแคดเมียมต่อไอออนสังกะสีที่ 32 เท่า สาร L5 ซึ่งเป็นเตตระเดนเตดลิแกนด์แบบไม่มีอะมิโนโปรตอน ที่ประกอบด้วยควิโนลีน 1 หมู่ และพีโคลีน 2 หมู่ให้ค่าคงที่การเกิดสารประกอบเชิงซ้อนกับไอออนสังกะสีสูงสุด การเพิ่มจำนวนหมู่ควิโนลีนส่งผลให้ความสามารถในการจับไอออนโลหะและการเรืองแสงสัมพัทธ์ต่ำลง และพบการดับสัญญาณการเรืองแสงแทนในสาร L12 และ L13 ซึ่งมีหมู่ควิโนลีนอยู่ 3 และ 4 หมู่ตามลำดับ การใส่หมู่แทนที่ที่มีคุณสมบัติดึงอิเล็กตรอนส่งผลให้ค่าการเรืองแสงสัมพัทธ์สูงขึ้นแต่ให้ค่าคงที่การเกิดสารประกอบเชิงซ้อนต่ำลง ดังนั้นสาร L6 จึงถูกเลือกเพื่อนำไปเพิ่มประสิทธิภาพเพื่อเป็นตัวตรวจวัดเชิงแสงสำหรับไอออนแคดเมียม พบว่าการใช้สาร L6 คู่กับ ไตรฟิโคลิลเอมีน(เตตระเดนเตดลิแกนด์ที่มีโครงสร้างคล้าย L4 แต่ไม่ให้สัญญาณเรืองแสง) จะช่วยเพิ่มความจำเพาะในการตรวจวัดไอออนแคดเมียมอย่างมีนัยสำคัญ โดยสามารถตรวจวัดไอออนแคดเมียมได้ที่มีความเข้มข้นต่ำสุดได้ถึง 69 นาโนโมลาร์ และตรวจสอบความเข้มข้นของไอออนแคดเมียมในเซลล์ได้ตั้งแต่ 0.1 ถึง 10 ไมโครโมลาร์

สาขาวิชา เคมี
ปีการศึกษา 2563

ลายมือชื่อนิสิต
ลายมือชื่อ อ.ที่ปรึกษาหลัก
ลายมือชื่อ อ.ที่ปรึกษาร่วม

5671930223 : MAJOR CHEMISTRY

KEYWORD: Fluorescence sensors, Cadmium detection, Zinc detection, Metal ion sensors,
Metal complex, Quinoline derivatives

Jutawat Hojitsiriyant : TUNING OF METAL ION SELECTIVITY BY VARYING NUMBER OF
COORDINATING ATOMS IN QUINOLINE-DERIVED FLUORESCENT SENSORS. Advisor: Prof.
MONGKOL SUKWATTANASINITT, Ph.D. Co-advisor: Prof. VITHAYA RUANGPORNVISUTI,
Ph.D.

Both Cd^{2+} and Zn^{2+} are metal ions in group 12 elements with very different toxicities but similar binding properties to most organic and biological ligands. In this work, a series of quinoline derivatives were synthesized and studied with an aim for Cd^{2+} selective turn-on fluorescent sensors. The structures of the compounds were designed to systematically evaluate the effects of amino protons, number of N-coordinating atoms, quinoline/picoline moieties and substituents on the sensing properties. The association constants of all synthesized ligands were studied by UV-vis absorption titration in aqueous solution. The results revealed that the ligands having 6- and 4- donor atoms and absent of amino proton gave higher association constants for Cd^{2+} and Zn^{2+} , respectively. L6, a ligand with 2 quinolines/2 picolines and 6 N atoms without amino proton, exhibited the highest Cd^{2+} sensitivity providing 118-fold of fluorescence enhancement (I/I_0) at 480 nm and highest $\text{Cd}^{2+}/\text{Zn}^{2+}$ selectivity giving the $\text{Cd}^{2+}/\text{Zn}^{2+}$ association constant ratio of 32. L5, a tetradentate ligand containing 1 quinoline/2 picolines without amino protons showed highest association constant for Zn^{2+} . The greater number of the quinoline units led to lower binding affinity and lower I/I_0 . Fluorescence quenching was even observed for ligands having solely 3 and 4 quinoline units (L12 and L13). Electron withdrawing substituents gave higher I/I_0 but lower association constants. L6 was thus selected for further optimization as Cd^{2+} fluorescent sensor. The selectivity of Cd^{2+} detection by L6 was significantly improved by an addition of tripicolylamine (TPA), a non-fluorescent tetradentate ligand, that provided the limit of detection Cd^{2+} of 69 nM. In the fluorescence cell imaging, L6 could monitor Cd^{2+} in the concentration range of 0.1–10 μM .

Field of Study: Chemistry

Student's Signature

Academic Year: 2020

Advisor's Signature

Co-advisor's Signature

ACKNOWLEDGEMENTS

First of all, I would like to express my deepest appreciation to my advisor, Professor Dr. Mongkol Sukwattanasinitt for giving me a great opportunities, valuable advice, relentless support, unparalleled knowledge, and encouragement throughout of this research. I would also like to extend my deepest gratitude to my co-advisor, Professor Dr. Vithaya Ruangpornvisuti for generous advice, invaluable guidance, and suggestion.

I would like to gratefully acknowledge the committees, Professor Dr. Vudhichai Parasuk, Professor Dr. Paitoon Rashatasakon, Professor Dr. Thawatchai Tuntulani and Assistant Professor Dr. Nakorn Niamnont for their kindness, valuable suggestion, and recommendations.

My sincere thanks also go to Professor Dr. Paitoon Rashatasakhon, Professor Dr. Sumrit Wacharasindhu, Professor Dr. Tanapat Palaga, Assistant Professor Dr. Anawat Ajavakom, and Dr. Sakulsuk Unarunotai for their attention and suggestion during our research group meeting.

I am also grateful to Assistant professor Dr. Kittipong Chainok and Ms. Chatphorn Theppitak for giving me suggestion and considerable helps in X-ray Crystallography.

Special thanks to Ms. Pawittra Chaibuth for giving me her ligands to study in this research and many significant supports. My appreciation is also given to Dr Kanokthorn Boonkitpatarakul, Dr Nattawut Yotapan, Dr Warothorn Paisuwan, Jadetapong Klahan, Chakrit Yimsukanan, Atchareeporn Smata, Apiwat Promchat, Yuthana Sanpradit, Phoom Sangsuwan, Trin Saetan, Suthikorn Jantra and every member in MAPS group for their help and suggestion during my graduate research.

I would like to thank (1) Thailand Research Fund (MRG5980037 and RTA6180007); (2) Thailand National Nanotechnology Center (NANOTEC), NSTDA, Ministry of Science and Technology, Thailand, through its program of Research Network NANOTEC (RNN) for the financial support of this work. I must also thank to Science Achievement Scholarship of Thailand (SAST) for great opportunity and scholarships.

Finally, I would like to express my thankfulness to my parents and my special one who always stand by my side during both of my pleasant and hard time.

Jutawat Hojitsiriyonont

TABLE OF CONTENTS

	Page
.....	iii
ABSTRACT (THAI).....	iii
.....	iv
ABSTRACT (ENGLISH).....	iv
ACKNOWLEDGEMENTS.....	v
TABLE OF CONTENTS.....	vi
LIST OF TABLES.....	1
LIST OF FIGURES.....	2
LIST OF ABBREVIATION.....	16
CHAPTER 1 INTRODUCTION.....	18
1.1 Fluorescence.....	18
1.2 Fluorescence chemosensor.....	19
1.3 Fluorescent sensing mechanism.....	20
1.3.1 Photo-induced electron transfer (PET).....	20
1.3.1 Intramolecular charge transfer (ICT).....	21
1.4 Cadmium.....	22
1.5 Cadmium sensor.....	23
1.6 Objective.....	32
CHAPTER 2 EXPERIMENT.....	35
2.1 Chemicals and materials.....	35
2.2 Analytical instruments.....	35

2.3 Synthesis procedure	36
2.3.1 Synthesis of L1.....	36
2.3.2 Synthesis of L2.....	36
2.3.3 Synthesis of L3.....	37
2.3.4 Synthesis of L4.....	37
2.3.5 Synthesis of L5.....	38
2.3.6 Synthesis of L6.....	38
2.3.7 Synthesis of L7.....	39
2.3.8 Synthesis of L8.....	39
Preparation of QNNO.....	39
Preparation of L8.....	40
2.3.9 Synthesis of L9.....	40
Preparation of 3QN.....	40
Preparation of L9.....	41
2.3.10 Synthesis of L10–L13.....	42
Preparation of 8-Bromoquinoline.....	42
2.3.10.1 Synthesis of L10.....	42
2.3.10.2 Synthesis of L11	43
2.3.10.3 Synthesis of L12.....	43
2.3.10.1 Synthesis of L13.....	44
2.4 Photophysical property study	44
2.4.1 Absorption	44
2.4.2 Fluorescence.....	45
2.5 Fluorescent sensing study.....	45

2.5.1 Selectivity.....	45
2.5.2 Fluorescence titration.....	46
2.5.3 Masking reagent.....	46
2.5.4 Limit of detection (LOD).....	46
2.5.5 Cell culture and fluorescent imaging.....	47
2.6 Ligand and metal ion binding study	48
2.6.1 Job's plot.....	48
2.6.2 Association constant (K_a).....	48
2.6.3 X-ray crystallography.....	49
CHAPTER 3 RESULTS AND DISCUSSION.....	51
3.1 Synthesis.....	51
3.1.1 Synthesis of L1 and L5	51
3.1.2 Synthesis of L2 and L6	53
3.1.3 Synthesis of L3, L4 and L7.....	55
3.1.4 Synthesis of L8.....	58
3.1.6 Synthesis of L9.....	60
3.1.7 Synthesis of L10	62
3.1.8 Synthesis of L11–L13	63
3.1.9 Synthesis of L14–L17	66
3.2 Photophysical properties.....	68
3.2.1 Photophysical properties of L1–L6.....	68
3.2.2 Photophysical properties of L7–L9.....	70
3.2.3 Photophysical properties of L10–L13.....	72
3.2.4 Photophysical properties of L14–L17.....	73

3.3 Fluorescence sensing properties.....	75
3.3.1 Fluorescence sensing properties of L1–L6.....	76
3.3.2 Fluorescence sensing properties of L7–L9.....	78
3.3.3 Fluorescence sensing properties of L10–L13.....	81
3.3.4 Fluorescence sensing properties of L14–L17.....	83
3.4 Association constants.....	85
3.4.1 Association constant of L1–L9.....	87
3.4.2 Association constant of L10–L13.....	89
3.4.3 Association constant of L14–L17.....	90
3.5 Condition optimization for Cd ²⁺ detection.....	91
3.5.1 Effects of pH.....	91
3.5.2 Selectivity and interference study.....	92
3.5.3 Masking agent study.....	93
3.5.4 Limit of detection.....	96
3.5.5 Detection of Cd ²⁺ in living cells.....	97
3.6 Structures of Cd ²⁺ Complexes.....	98
3.6.1 X-ray crystallography.....	98
3.6.2 ¹ H NMR titration.....	100
CHAPTER 4 CONCLUSION.....	103
APPENDIX.....	104
REFERENCES.....	168
VITA.....	175

LIST OF TABLES

Table 1.1 Summarization of some fluorescent for Cd ²⁺ and Zn ²⁺ detection.	30
Table 1.2 Summarization of some fluorescent for Cd ²⁺ and Zn ²⁺ detection. (continued).....	30
Table 1.3 Summarization of some fluorescent for Cd ²⁺ and Zn ²⁺ detection (continued).....	32
Table 3.1 Association constant (K _a) of L1–L9 with Cd ²⁺ and Zn ²⁺ in aqueous solution	88
Table 3.2 Association constant (K _a) of L10–L12 with Cd ²⁺ and Zn ²⁺ in aqueous solution.....	90
Table 3.3 Association constant (K _a) of L14–L17 with Cd ²⁺ and Zn ²⁺ in aqueous solution.....	91

LIST OF FIGURES

Figure 1.1 Jablonski diagram.	19
Figure 1.2 Simplified diagram for PET process.	21
Figure 1.3 Simplified diagram for ICT process.	22
Figure 1.4 Molecular structure of R1 and Fluorescence titration spectra with Cd^{2+} and Zn^{2+}	24
Figure 1.5 (a) Molecular structure of R2–R4 and fluorescence enhancement ratio (F/F_0) of (b) R2 , (c) R3 and (d) R4 , in the presence of various metal ions (grey bar) and in the co-presence of Zn^{2+} and another metal ion tested for interference (black bar).	24
Figure 1.6 (a) Molecular structure of R5 and (b) fluorescence spectra of R5 in the presence of various metal ions.	25
Figure 1.7 Molecular structure and fluorescence spectrum of (a) R6 and (b) R7 in the presence of metal ions.	25
Figure 1.8 Proposed structure of (a) R7·Cd and (b) R7·Zn	26
Figure 1.9 Molecular structure of R8 and chelation enhanced fluorescence effect.	26
Figure 1.10 Molecular structures of (a) R9 , and X-ray crystal structure of (b) R9·Zn and (c) R9·Cd complexes.	27
Figure 1.11 (a) Molecular structure of R10 and (b) fluorescence enhancement ratio (I/I_0) of R10 in the presence of various metal ions (white bar) and in the co-presence of Cd^{2+} and another metal ion tested for interference (black bar).	27
Figure 1.12 (a) Molecular structure of R11O , R11S and R11N (b) fluorescence enhancement ratio (I/I_0) of R11O (red bar), R11S (blue bar) and R11N (green bar) in the presence of various metal ions.	28
Figure 1.13.	28
Figure 1.14 X-ray crystal structure of (a) R11O·Cd and (b) R11O·Zn	28

Figure 1.15 The proposed binding mode of R12 with Cd^{2+} and Zn^{2+}	29
Figure 1.16 Target molecules L1–L6	33
Figure 1.17 Target molecules L7–L9	33
Figure 1.18 Target molecules L10–L13	34
Figure 1.19 Target molecules L14–L17	34
Figure 3.1 Synthesis of L1 and L5	52
Figure 3.2 ^1H NMR spectra of 8-aminoquinoline, L1 , and L5 in CDCl_3	53
Figure 3.3 Synthesis of L2 and L6	54
Figure 3.4 ^1H NMR spectra of 8-hydroxyquinoline, L2 and L6 in $(\text{CD}_3)_2\text{SO}$	55
Figure 3.5 Synthesis of L3 and L4	56
Figure 3.6 ^1H NMR spectra of L3 in CD_3CN , and L4 in $(\text{CD}_3)_2\text{CO}$	57
Figure 3.7 Synthesis of L7 and ^1H NMR spectrum of L7 in CD_3CN	58
Figure 3.8 Synthesis of L8	59
Figure 3.9 ^1H NMR spectra of QNNQ and L8 in $(\text{CD}_3)_2\text{CO}$	60
Figure 3.10 Synthesis of L9	61
Figure 3.11 ^1H NMR spectra of 3QN in $(\text{CD}_3)_2\text{CO}$, and L9 in $(\text{CD}_3)_2\text{SO}$	62
Figure 3.12 Synthesis of L10 and ^1H NMR spectrum of L10 in $(\text{CD}_3)_2\text{SO}$	63
Figure 3.13 Synthesis of 8-bromoquinoline and L11–L13	64
Figure 3.14 ^1H NMR spectra of 8-bromoquinoline in CDCl_3 ; and L11 , L12 and L12 in $(\text{CD}_3)_2\text{SO}$	65
Figure 3.15 Synthesis of L14–L17	66
Figure 3.16 ^1H NMR of L14–L17 in $(\text{CD}_3)_2\text{SO}$	67
Figure 3.17 (a) Molecular structures of L1–L6 with their key photophysical properties and (b) absorption (solid line) and emission (dash line) spectra excited at 300 nm. All	

ligands were in aqueous solution with $[L] = 30 \mu\text{M}$ for absorption and $[L] = 10 \mu\text{M}$ for emission.....	69
Figure 3.18 (a) Molecular structures of L7–L9 with their key photophysical properties and (b) absorption (solid line) and emission (dash line) spectra excited at 300 nm. All ligands were in aqueous solution with $[L] = 30 \mu\text{M}$ for absorption and $[L] = 10 \mu\text{M}$ for emission.....	71
Figure 3.19 (a) Molecular structures of L10–L13 with their key photophysical properties and (b) absorption (solid line) and emission (dash line) spectra excited at 300 nm. All ligands were in aqueous solution with $[L] = 30 \mu\text{M}$ for absorption and $[L] = 10 \mu\text{M}$ for emission.....	72
Figure 3.20 (a) Molecular structures of L14–L17 with their key photophysical properties and (b) absorption (solid line) and emission (dash line) spectra excited at 300 nm. All ligands were in aqueous solution with $[L] = 30 \mu\text{M}$ for absorption and $[L] = 10 \mu\text{M}$ for emission.....	74
Figure 3.21 Chemical structure of L1–L6	76
Figure 3.22 Fluorescence spectra of L1–L6 ($10 \mu\text{M}$) tested with various metal ions ($10 \mu\text{M}$) in Tris HCl buffer solution pH 7.	77
Figure 3.23 Relative intensity of L1–L6 ($10 \mu\text{M}$) in the presence of various metal ion ($10 \mu\text{M}$).....	78
Figure 3.24 Chemical structure of L7–L9	78
Figure 3.25 Fluorescence spectra of L7–L9 ($10 \mu\text{M}$) tested with various metal ions ($10 \mu\text{M}$) in Tris HCl buffer solution pH 7.	80
Figure 3.26. Relative intensity of L7–L9 ($10 \mu\text{M}$) in the presence of various metal ion ($10 \mu\text{M}$).....	80
Figure 3.27 Chemical structure of L10–L13	81
Figure 3.28 Fluorescence spectra of L10–L13 ($10 \mu\text{M}$) tested with various metal ions ($10 \mu\text{M}$) in Tris HCl buffer solution pH 7.	82

Figure 3.29 Relative intensity of L10–L13 (10 μM) in the presence of various metal ion (10 μM).....	82
Figure 3.30 Chemical structure of L14–L17	83
Figure 3.31 Fluorescence spectra of L14–L17 (10 μM) tested with various metal ions (10 μM) in Tris HCl buffer solution pH 7.	84
Figure 3.32 Relative intensity of L14–L17 (10 μM) in the presence of various metal ion (10 μM).....	84
Figure 3.33 a) UV titration between L1 and Cd^{2+} (inset) summary table of the results of the curve fitting, b) scatter plots between absorbance and amount of Cd^{2+} at 253, 300 and 350 nm, the lines show non-linear curve fitting of the absorbance values at all three wavelengths used for determination of K_a value. c) the residual plots of the corresponding fitting.	86
Figure 3.34 Chemical structure of L1–L9	87
Figure 3.35 Chemical structure of L10–L13	89
Figure 3.36 Chemical structure of L14–L17	90
Figure 3.37 pH-dependence of emission intensity at 480 nm of 10 μM L6 and L6 in the absence, presence of 10 μM Cd^{2+} , or Zn^{2+} in NaOH/HCl-pH-adjusted Tris HCl buffer solution.....	92
Figure 3.38. (a) Photograph of L6 (10 μM) in the present of metal ions (10 μM) in a buffer solution (20 mM Tris HCl, pH = 7.4). (b) Fluorescence responses (I/I_0) at 480 nm of L6 (10 μM) to metal ions in a buffer solution (20 mM Tris HCl, pH = 7.4 at $\lambda_{\text{ex}} = 300$ nm. Red bar represents response to each metal ion. Gray bar represents response to Cd^{2+} in the presence of another competitive metal ion. All $[M] = 10 \mu\text{M}$	93
Figure 3.39. Fluorescence intensity at 480 nm of L6 solutions in the absence and presence of Cd^{2+} and Zn^{2+} ions ($[\text{L6}] = 10 \mu\text{M}$, $[M] = 10 \mu\text{M}$) tested with various masking agents (10 μM) in a buffer solution (20 mM Tris HCl, pH = 7.4).	94

Figure 3.40. Fluorescence intensity at 480 nm of L6 , L6+Cd , L6+Zn and L6+Cd+Zn solution ($[L6] = 10 \mu\text{M}$, $[M] = 10 \mu\text{M}$) in the presence of various concentration of TPA (5–200 μM) in a buffer solution (20 mM Tris HCl, pH = 7.4).	95
Figure 3.41. Fluorescence responses (I/I_0) at 480 nm of L6 (10 μM) to metal ions in a buffer solution (20 mM Tris HCl, pH = 7.4 at $\lambda_{\text{ex}} = 300 \text{ nm}$ in the presence of TPA (200 μM). Red bars represent responses to each metal ion. Gray bars represent responses to Cd^{2+} in the presence of each competitive metal ion. $[M] = 10 \mu\text{M}$	96
Figure 3.42. a) Fluorescence titration between 10 μM L6 and Cd^{2+} in the presence of 20 equiv. TPA in Tris HCl buffered solution pH 7. b) Plot between emission intensity at 480 nm and concentration of Cd^{2+} . (inset) Fluorescent titration calibration line at low concentration for determination of LOD.	97
Figure 3.43. Fluorescence images of 1 μM L6 and Cd^{2+} in HeLa cells. (a) bright-field transmission images (b) merged images (c) fluorescence image. (d) Average brightness $((R+G+B)/3)$ of cells corresponding to the fluorescent images. (scalebar = 25 μM and image contrast and brightness were all adjusted equally).....	98
Figure 3.44 The coordination environment of Cd(II) ion and the ligand L in (a) L1·Cd , (b) L5·Cd , and (c) L6·Cd . The ellipsoids drawn at the 30% probability level and all hydrogen atoms are omitted for clarity.....	99
Figure 3.45. The coordination environment of Cd(II) ion and the ligand L1 . The ellipsoids drawn at the 30% probability level and all hydrogen atoms are omitted for clarity.....	100
Figure 3.46. ^1H NMR titration spectrum of L6·Zn in $(\text{CD}_3)_2\text{SO}$	101
Figure 3.47 ^1H NMR titration spectrum of L6·Cd in $(\text{CD}_3)_2\text{SO}$	102
Figure A 1 ^1H NMR of L1 in CDCl_3	104
Figure A 2 ^{13}C NMR of L1 in CD_3CN	104
Figure A 3 HRMS of L1.....	105

Figure A 4 ^1H NMR of L2 in $(\text{CD}_3)_2\text{SO}$	105
Figure A 5 HRMS of L2	106
Figure A 6 ^1H NMR of L3 in CD_3CN	106
Figure A 7 ^{13}C NMR of L3 in CD_3CN	107
Figure A 8 HRMS of L3	107
Figure A 9 ^1H NMR of L4 in $(\text{CD}_3)_2\text{CO}$	108
Figure A 10 ^{13}C NMR of L4 in $(\text{CD}_3)_2\text{CO}$	108
Figure A 11 HRMS of L4	109
Figure A 12 ^1H NMR of L5 in CD_3Cl	109
Figure A 13 ^{13}C NMR of L5 in $(\text{CD}_3)_2\text{SO}$	110
Figure A 14 HRMS of L5	110
Figure A 15 ^1H NMR of L6 in $(\text{CD}_3)_2\text{SO}$	111
Figure A 16 ^{13}C NMR of L6 in $(\text{CD}_3)_2\text{SO}$	111
Figure A 17 HRMS of L6	112
Figure A 18 ^1H NMR of L7 in CD_3CN	112
Figure A 19 ^{13}C NMR of L7 in CD_3CN	113
Figure A 20 HRMS of L7	113
Figure A 21 ^1H NMR of QNNQ in $(\text{CD}_3)_2\text{CO}$	114
Figure A 22 ^{13}C NMR of QNNQ in $(\text{CD}_3)_2\text{CO}$	114
Figure A 23 HRMS of QNNQ.....	115
Figure A 24 ^1H NMR of L8 in $(\text{CD}_3)_2\text{CO}$	115
Figure A 25 ^1H NMR of 3QN in $(\text{CD}_3)_2\text{CO}$	116
Figure A 26 ^{13}C NMR of 3QN in $(\text{CD}_3)_2\text{CO}$	116
Figure A 27 HRMS of 3QN.	117

Figure A 28 ^1H NMR of L9 in $(\text{CD}_3)_2\text{SO}$	117
Figure A 29 ^{13}C NMR of L9 in $(\text{CD}_3)_2\text{SO}$	118
Figure A 30 HRMS of L9	118
Figure A 31 ^1H NMR of L10 in $(\text{CD}_3)_2\text{SO}$	119
Figure A 32 ^{13}C NMR of L10 in $(\text{CD}_3)_2\text{SO}$	119
Figure A 33 HRMS of L10	120
Figure A 34 ^1H NMR of 8-bromoquinoline in CD_3Cl	120
Figure A 35 ^1H NMR of L11 in $(\text{CD}_3)_2\text{SO}$	121
Figure A 36 ^{13}C NMR of L11 in $(\text{CD}_3)_2\text{SO}$	121
Figure A 37 HRMS of L11	122
Figure A 38 ^1H NMR of L12 in $(\text{CD}_3)_2\text{SO}$	122
Figure A 39 ^{13}C NMR of L12 in $(\text{CD}_3)_2\text{SO}$	123
Figure A 40 HRMS of L12	123
Figure A 41 ^1H NMR of L13 in $(\text{CD}_3)_2\text{SO}$	124
Figure A 42 ^{13}C NMR of L13 in $(\text{CD}_3)_2\text{SO}$	124
Figure A 43 HRMS of L13	125
Figure A 44 ^1H NMR of L14 in $(\text{CD}_3)_2\text{SO}$	125
Figure A 45 ^{13}C NMR of L14 in $(\text{CD}_3)_2\text{SO}$	126
Figure A 46 ^1H NMR of L15 in $(\text{CD}_3)_2\text{SO}$	126
Figure A 47 ^{13}C NMR of L15 in $(\text{CD}_3)_2\text{SO}$	127
Figure A 48 ^1H NMR of L16 in $(\text{CD}_3)_2\text{SO}$	127
Figure A 49 ^{13}C NMR of L16 in $(\text{CD}_3)_2\text{SO}$	128
Figure A 50 ^1H NMR of L17 in $(\text{CD}_3)_2\text{SO}$	128
Figure A 51 ^{13}C NMR of L17 in $(\text{CD}_3)_2\text{SO}$	129

Figure A 52 absorbance of L1–L6 (30 μM) in the presence of Cd^{2+} or Zn^{2+} (30 μM) in aqueous solution.....	130
Figure A 53 absorbance of L7–L9 (30 μM) in the presence of Cd^{2+} or Zn^{2+} (30 μM) in aqueous solution.....	130
Figure A 54 absorbance of L10–L13 (30 μM) in the presence of Cd^{2+} or Zn^{2+} (30 μM) in aqueous solution.	131
Figure A 55 absorbance of L14–L17 (30 μM) in the presence of Cd^{2+} or Zn^{2+} (30 μM) in aqueous solution.	131
Figure A 56 Job's plots of L1 with Cd^{2+} (left) and Zn^{2+} (right).....	132
Figure A 57 Job's plots of L2 with Cd^{2+} (left) and Zn^{2+} (right).....	132
Figure A 58 Job's plots of L3 with Cd^{2+} (left) and Zn^{2+} (right).....	132
Figure A 59 Job's plots of L4 with Cd^{2+} (left) and Zn^{2+} (right).....	133
Figure A 60 plots of L5 with Cd^{2+} (left) and Zn^{2+} (right).....	133
Figure A 61 Job's plots of L6 with Cd^{2+} (left) and Zn^{2+} (right).....	133
Figure A 62 a) UV titration between L1 and Cd^{2+} (inset) summary table of the results of the curve fitting, b) scatter plots between absorbance and amount of Cd^{2+} at 253, 300 and 350 nm, the lines show non-linear curve fitting of the absorbance values at all three wavelengths used for determination of K_a value. c) the residual plots of the corresponding fitting.	134
Figure A 63 a) UV titration between L1 and Zn^{2+} (inset) summary table of the results of the curve fitting, b) scatter plots between absorbance and amount of Zn^{2+} at 253, 300 and 350 nm, the lines show non-linear curve fitting of the absorbance values at all three wavelengths used for determination of K_a value. c) residual plots of the corresponding fitting.	135
Figure A 64 a) UV titration between L2 and Cd^{2+} (inset) summary table of the results of the curve fitting, b) scatter plots between absorbance and amount of Cd^{2+} at 254, 300 and 370 nm, the lines show non-linear curve fitting of the absorbance values at	

all three wavelengths used for determination of K_a value. c) the residual plots of the corresponding fitting.	136
Figure A 65 UV titration between L2 and Zn^{2+} (inset) summary table of the results of the curve fitting, b) scatter plots between absorbance and amount of Zn^{2+} at 254, 300 and 370 nm, the lines show non-linear curve fitting of the absorbance values at all three wavelengths used for determination of K_a value. c) residual plots of the corresponding fitting.	137
Figure A 66 a) UV titration between L3 and Cd^{2+} (inset) summary table of the results of the curve fitting, b) scatter plots between absorbance and amount of Cd^{2+} at 350 nm, the line shows non-linear curve fitting of the absorbance values used for determination of K_a value. c) residual plots of the corresponding fitting.....	138
Figure A 67 a) UV titration between L3 and Zn^{2+} (inset) summary table of the results of the curve fitting, b) scatter plots between absorbance and amount of Zn^{2+} at 250 300 and 300 nm, the lines show non-linear curve fitting of the absorbance values at all three wavelengths used for determination of K_a value. c) residual plots of the corresponding fitting.	139
Figure A 68 UV titration between L4 and Cd^{2+} (inset) summary table of the results of the curve fitting, b) scatter plots between absorbance and amount of Cd^{2+} at 300 nm, the line shows non-linear curve fitting of the absorbance values used for determination of K_a value. c) residual plots of the corresponding fitting.....	140
Figure A 69 UV titration between L4 and Zn^{2+} (inset) summary table of the results of the curve fitting, b) scatter plots between absorbance and amount of Zn^{2+} at 350 nm, the line shows non-linear curve fitting of the absorbance values used for determination of K_a value. c) residual plots of the corresponding fitting.....	141
Figure A 70 a) UV titration between L5 and Cd^{2+} (inset) summary table of the results of the curve fitting, b) scatter plots between absorbance and amount of Cd^{2+} at 254, 300 and 350 nm, the lines show non-linear curve fitting of the absorbance values at all three wavelengths used for determination of K_a value. c) residual plots of the corresponding fitting.	142

Figure A 71 a) UV titration between L5 and Zn^{2+} (inset) summary table of the results of the curve fitting, b) scatter plots between absorbance and amount of Zn^{2+} at 253, 300 and 350 nm, the lines show non-linear curve fitting of the absorbance values at all three wavelengths used for determination of K_a value. c) residual plots of the corresponding fitting.	143
Figure A 72 a) UV titration between L6 and Cd^{2+} (inset) summary table of the results of the curve fitting, b) scatter plots between absorbance and amount of Cd^{2+} at 255, 300 and 350 nm, the lines show non-linear curve fitting of the absorbance values at all three wavelengths used for determination of K_a value. c) residual plots of the corresponding fitting.	144
Figure A 73 a) UV titration between L5 and Zn^{2+} (inset) summary table of the results of the curve fitting, b) scatter plots between absorbance and amount of Zn^{2+} at 253, 300 and 350 nm, the lines show non-linear curve fitting of the absorbance values at all three wavelengths used for determination of K_a value. c) residual plots of the corresponding fitting.	145
Figure A 74 a) UV titration between L7 and Cd^{2+} (inset) summary table of the results of the curve fitting, b) scatter plots between absorbance and amount of Cd^{2+} at 300 and 350 nm, the lines show non-linear curve fitting of the absorbance values at both wavelengths used for determination of K_a value. c) residual plots of the corresponding fitting.	146
Figure A 75 a) UV titration between L7 and Zn^{2+} (inset) summary table of the results of the curve fitting, b) scatter plots between absorbance and amount of Zn^{2+} at 336 nm, the line shows non-linear curve fitting of the absorbance values used for determination of K_a value. c) residual plots of the corresponding fitting.....	147
Figure A 76 a) UV titration between L8 and Cd^{2+} (inset) summary table of the results of the curve fitting, b) scatter plots between absorbance and amount of Cd^{2+} at 254, 300 and 350 nm, the lines show non-linear curve fitting of the absorbance values at all three wavelengths used for determination of K_a value. c) residual plots of the corresponding fitting.	148

Figure A 77 a) UV titration between **L8** and Zn^{2+} (inset) summary table of the results of the curve fitting, b) scatter plots between absorbance and amount of Zn^{2+} at 336 nm, the line shows non-linear curve fitting of the absorbance values used for determination of K_a value. c) residual plots of the corresponding fitting..... 149

Figure A 78 a) UV titration between **L9** and Cd^{2+} (inset) summary table of the results of the curve fitting, b) scatter plots between absorbance and amount of Cd^{2+} at 300 and 350 nm, the lines show non-linear curve fitting of the absorbance values at both wavelengths used for determination of K_a value. c) residual plots of the corresponding fitting. 150

Figure A 79 a) UV titration between **L9** and Zn^{2+} (inset) summary table of the results of the curve fitting, b) scatter plots between absorbance and amount of Zn^{2+} at 300 nm, the line shows non-linear curve fitting of the absorbance values used for determination of K_a value. c) residual plots of the corresponding fitting..... 151

Figure A 80 a) UV titration between **L10** and Cd^{2+} (inset) summary table of the results of the curve fitting, b) scatter plots between absorbance and amount of Cd^{2+} at 420 nm, the lines show non-linear curve fitting of the absorbance values used for determination of K_a value. c) residual plots of the corresponding fitting..... 152

Figure A 81 a) UV titration between **L10** and Zn^{2+} (inset) summary table of the results of the curve fitting, b) scatter plots between absorbance and amount of Zn^{2+} at 420 nm, the line shows non-linear curve fitting of the absorbance values used for determination of K_a value. c) residual plots of the corresponding fitting..... 153

Figure A 82 a) UV titration between **L11** and Cd^{2+} (inset) summary table of the results of the curve fitting, b) scatter plots between absorbance and amount of Cd^{2+} at 300 and 370 nm, the lines show non-linear curve fitting of the absorbance values at both wavelengths used for determination of K_a value. c) residual plots of the corresponding fitting. 154

Figure A 83 a) UV titration between **L11** and Zn^{2+} (inset) summary table of the results of the curve fitting, b) scatter plots between absorbance and amount of Zn^{2+} at 253, 300 and 350 nm, the lines show non-linear curve fitting of the absorbance values at

all three wavelengths used for determination of K_a value. c) residual plots of the corresponding fitting.	155
Figure A 84 a) UV titration between L12 and Cd^{2+} (inset) summary table of the results of the curve fitting, b) scatter plots between absorbance and amount of Cd^{2+} at 320 nm, the line shows non-linear curve fitting of the absorbance values used for determination of K_a value. c) residual plots of the corresponding fitting.....	156
Figure A 85 a) UV titration between L12 and Zn^{2+} (inset) summary table of the results of the curve fitting, b) scatter plots between absorbance and amount of Zn^{2+} at 320 nm, the line shows non-linear curve fitting of the absorbance values used for determination of K_a value. c) residual plots of the corresponding fitting.....	157
Figure A 86 a) UV titration between L13 and Cd^{2+} (inset) summary table of the results of the curve fitting, b) scatter plots between absorbance and amount of Cd^{2+} at 320 nm, the line shows non-linear curve fitting of the absorbance values used for determination of K_a value. c) residual plots of the corresponding fitting.....	158
Figure A 87 a) UV titration between L13 and Zn^{2+} (inset) summary table of the results of the curve fitting, b) scatter plots between absorbance and amount of Zn^{2+} at 320 nm, the line shows non-linear curve fitting of the absorbance values used for determination of K_a value. c) residual plots of the corresponding fitting.....	159
Figure A 88 a) UV titration between L14 and Cd^{2+} (inset) summary table of the results of the curve fitting, b) scatter plots between absorbance and amount of Cd^{2+} at 260, 310 and 360 nm, the lines show non-linear curve fitting of the absorbance values at all three wavelengths used for determination of K_a value. c) residual plots of the corresponding fitting.	160
Figure A 89 a) UV titration between L14 and Zn^{2+} (inset) summary table of the results of the curve fitting, b) scatter plots between absorbance and amount of Zn^{2+} at 259, 310 and 360 nm, the lines show non-linear curve fitting of the absorbance values at all three wavelengths used for determination of K_a value. c) residual plots of the corresponding fitting.	161

Figure A 90 a) UV titration between **L15** and Cd^{2+} (inset) summary table of the results of the curve fitting, b) scatter plots between absorbance and amount of Cd^{2+} at 260, 310 and 360 nm, the lines show non-linear curve fitting of the absorbance values at all three wavelengths used for determination of K_a value. c) residual plots of the corresponding fitting. 162

Figure A 91 a) UV titration between **L15** and Zn^{2+} (inset) summary table of the results of the curve fitting, b) scatter plots between absorbance and amount of Zn^{2+} at 250 and 350 nm, the lines show non-linear curve fitting of the absorbance values at both wavelengths used for determination of K_a value. c) residual plots of the corresponding fitting. 163

Figure A 92 a) UV titration between **L16** and Cd^{2+} (inset) summary table of the results of the curve fitting, b) scatter plots between absorbance and amount of Cd^{2+} at 260, 310 and 360 nm, the lines show non-linear curve fitting of the absorbance values at all three wavelengths used for determination of K_a value. c) residual plots of the corresponding fitting. 164

Figure A 93 a) UV titration between **L16** and Zn^{2+} (inset) summary table of the results of the curve fitting, b) scatter plots between absorbance and amount of Zn^{2+} at 260, 310 and 360 nm, the lines show non-linear curve fitting of the absorbance values at all three wavelengths used for determination of K_a value. c) residual plots of the corresponding fitting. 165

Figure A 94 a) UV titration between **L17** and Cd^{2+} (inset) summary table of the results of the curve fitting, b) scatter plots between absorbance and amount of Cd^{2+} at 340 nm, the line shows non-linear curve fitting of the absorbance values used for determination of K_a value. c) residual plots of the corresponding fitting. 166

Figure A 95 a) UV titration between **L17** and Zn^{2+} (inset) summary table of the results of the curve fitting, b) scatter plots between absorbance and amount of Zn^{2+} at 340 nm, the line shows non-linear curve fitting of the absorbance values used for determination of K_a value. c) residual plots of the corresponding fitting. 167



จุฬาลงกรณ์มหาวิทยาลัย
CHULALONGKORN UNIVERSITY

LIST OF ABBREVIATION

λ	wavelength,
λ_{em}	maximum emission wavelength
$\lambda_{max}, \lambda_{abs}$	maximum absorption wavelength
λ_{ex}	excitation wavelength
s.	second(s)
h	hour(s)
d	day(s)
Å	angstrom(s)
nm	nanometer(s)
cm	centimeter(s)
nM	nanomolar(s)
μ M	micromolar(s)
mM	millimolar(s)
M	molar(s)
μ L	microliter(s)
mL	milliliter(s)
L	liter(s)
mg	milligram(s)
g	gram(s)
Hz	hertz(s)
MHz	megahertz(s)
ppm	part(s) per million
Ω	ohm(s)
K	Kelvin
$^{\circ}$ C	degree Celsius
rt	room temperature
UV	ultraviolet light
Vis	visible light
ϵ	molar absorption coefficient

ϕ	quantum yield
HRMS	high resolution mass spectrometry
m/z	mass to charge ratio
NMR	nuclear magnetic resonance
δ	chemical shift (NMR)
J	coupling constant (NMR)
s	singlet (NMR)
d	doublet (NMR)
t	triplet (NMR)
q	quartet (NMR)
m	multiplet (NMR)
dd	doublet of doublet (NMR)
td	triplet of doublet (NMR)
K_a	association constant
e.g.	for example
I/I_0	relative emission intensity
DMSO	dimethyl sulfoxide
DMF	dimethyl formamide

CHAPTER 1

INTRODUCTION

1.1 Fluorescence

Fluorescence is the electromagnetic wave, usually belong to the ultraviolet, visible, and near-infrared regions, emitted by a substance that has absorbed light or other forms of energy. The fluorescence process may be simplified as illustrated by a Jablonski diagram as shown in Figure 1.1 [1, 2]. The S_0 and S_n lines refer to the electronic ground and excited states of a molecule, respectively. A molecule can absorb a photon and is excited from its electronic ground state to one of the electronic excited states e.g., S_2 or S_1 . According to the Franck-Condon principle, the absorption process takes place so rapidly ($\approx 10^{-15}$ s) that the molecule does not have enough time to change its geometry. The geometry of the molecule adjusts considerably slower ($\approx 10^{-14}$ – 10^{-11} s) to the lowest vibrational state of S_1 via internal conversion (IC) and vibrational relaxation (VR). The internal conversion and vibrational relaxation are the nonradioactive decay that the relaxation from a higher electronic state to a lower electronic state does not emit photon. The fluorescence process occurs when the molecule in this S_1 state releases the energy in form of light to return to the ground state that takes place in 10^{-9} – 10^{-6} s time scale. The excited molecule may also return to the ground state via external conversion (EC) by a collision or interaction with another molecule (e.g., polar solvent). The singlet excited state S_1 may also undergo intersystem crossing (ISC) to triplet state T_1 which usually live longer than singlet state resulting in quenching by quencher (e.g., oxygen) or radiative relaxation to ground state by phosphorescence. Although the intersystem crossing is in principle forbidden, the presence of heavy atoms (e.g., Br and Hg) in the molecule increases the probability of intersystem crossing promoted by large spin-orbit coupling [3]. The fluorescence is usually emitted at longer wavelength than its absorption due to the energy loss by vibrational relaxation and geometrical relaxation. The different in wavelength between maximum absorption and maximum emission is called stroke shift (stroke shift = $\lambda_{em} - \lambda_{abs}$). since the maximum absorption and maximum emission depend on the geometry, flexible molecules, or molecules

with high difference in geometry between ground state and excited state have large stroke shift. In contrast, the stroke shift of rigid molecules is small.

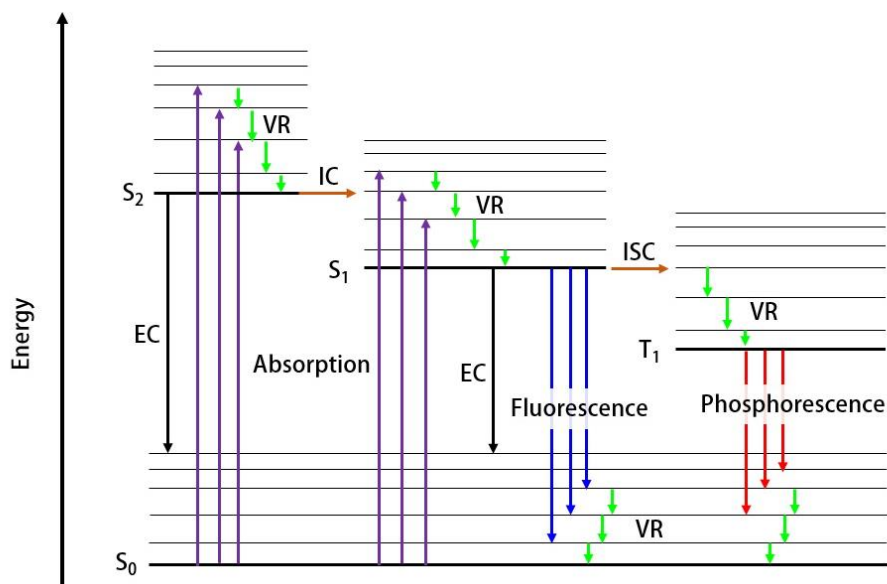


Figure 1.1 Jablonski diagram.

1.2 Fluorescence chemosensor

Chemosensor is a sensory compound which containing two main parts which are recognition unit (receptor) and signaling unit. The chemosensor is used for producing detectable signals when it interacts with an analyte. Fluorescence chemosensor is a chemosensor having fluorophore as a signaling unit to emit fluorescent signal [4]. Nowadays, fluorescence chemosensor plays an important role in detection of chemical and biological substances because of their many advantages over other methods[5-10]. It not only gives a high sensitivity and naked-eye detection but also allow us to detect analytes in the sample that hard to directly detect such as biological samples. There are three types of fluorescence signaling. i) turn-on mode, fluorescence sensors give an enhanced fluorescence signal upon interaction with an analyte. in contrast , ii) turn-off mode, the fluorescence signal of sensor is quenched upon interaction with an analyte. iii) ratiometric mode, the fluorescence signal of sensor is shifted to another wavelength upon binding with an analyte.

1.3 Fluorescent sensing mechanism

Fluorescent sensing mechanism refers to any process that change the fluorescence properties of the sensor upon binding with an analyte which include photo-induced electron transfer (PET) [11-15], intramolecular charge transfer (ICT) [16-21], excited-state intramolecular proton transfer (ESIPT) [16, 20, 22], Förster resonance energy transfer (FRET) [23-25], aggregation-induced emission enhancement (AIEE)/aggregation caused quenching (ACQ) [26-29], excimer/exciple [30-32], and isomerization [33]. The sensing compounds in this thesis were designed based on PET and ICT.

1.3.1 Photo-induced electron transfer (PET).

PET process occurs when a receptor or an analyte has either its highest occupied molecular orbital (HOMO) or the lowest unoccupied molecular orbital (LUMO) level between HOMO and LUMO of the fluorophore. i) Acceptor fluorophore, the excited fluorophore with half-filled HOMO accepts the electron from HOMO of the receptor. The excited electron in LUMO of fluorophore is then transferred to the HOMO of the receptor (Figure 1.2 left), ii) Donor fluorophore, the excited electron in LUMO of the fluorophore is transferred to the LUMO of the receptor followed by the transfer of the electron back to the LUMO of the fluorophore (Figure 1.2 right). the electron transfer process is non-radiative process with result in quenching of the fluorescence. So, turn-on and turn-off mode fluorescent sensor can be design based on promoting or inhibiting of the PET process.

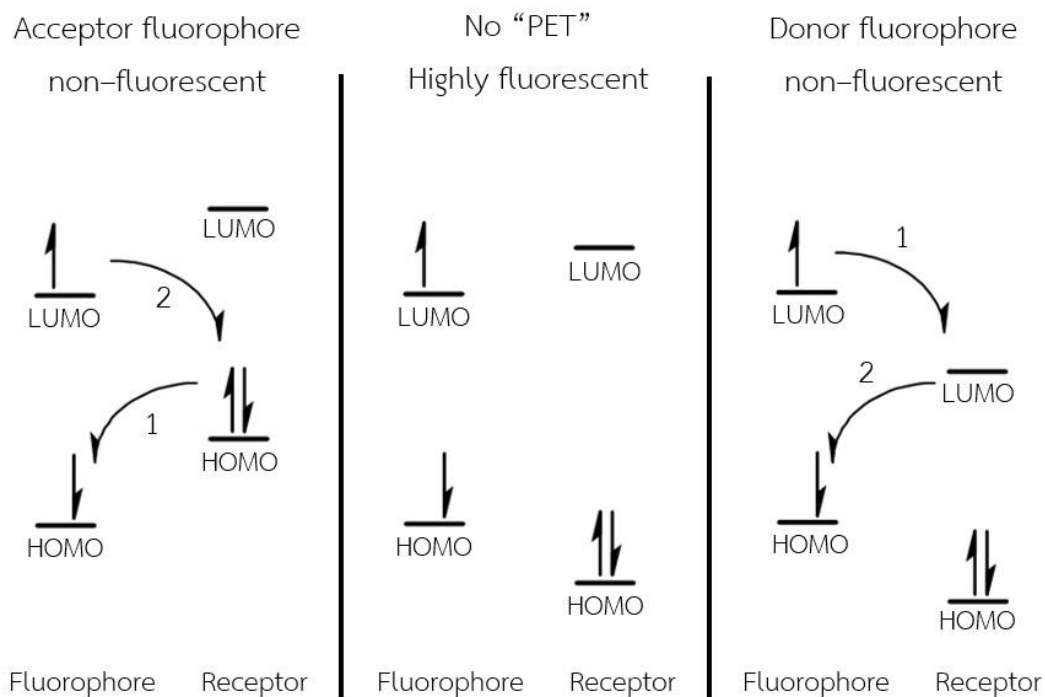


Figure 1.2 Simplified diagram for PET process.

1.3.1 Intramolecular charge transfer (ICT)

The ICT process can be simply illustrated by Figure 1.3. The locally excited state (LE) is in the locally most stable excited state of S_1 . When the fluorophore has an electron donating group (e.g., $-NR_2$, $-OR$) conjugated to an electron withdrawing group (e.g., $>C=O$, $-CN$), the different in dipole moment between S_1 and S_0 will be very high. Consequently, the relaxation process produces a new lower energy excited state called intramolecular charge transfer (ICT) state having significantly different geometry from the LE state. The smaller energy gap between S_0 and S_1 not only results in the red-shifted fluorescence but also promote the intramolecular conversion process caused decreasing in fluorescent intensity. So, the fluorescent sensor can be designed based on the degree of the ICT to be turn-off, turn-on, and ratiometric mode.

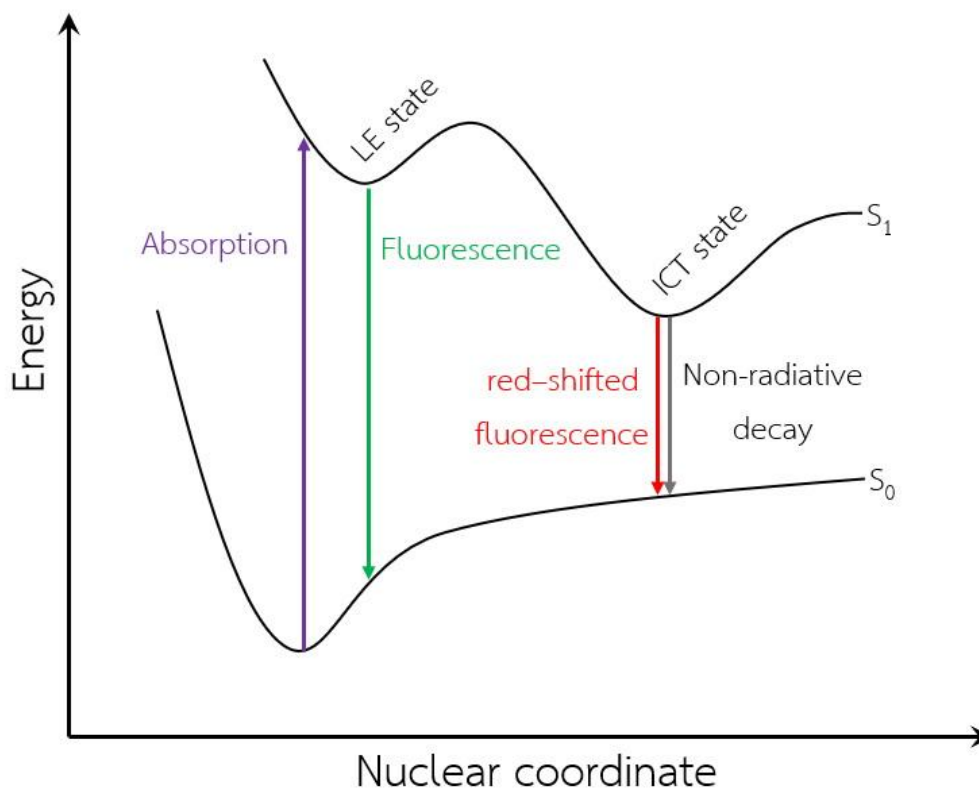


Figure 1.3 Simplified diagram for ICT process.

1.4 Cadmium

Cadmium (Cd) is a transition metal in the earth's crust. It is usually found with Zinc (Zn) in form of sulfide, sulfate, oxide, and chloride compounds. Cadmium was mainly produced by obtaining the byproduct from Zn refining. For a long time, Cadmium was used as pigments, Ni-Cd batteries, steel corrosion-resistant, plastic stabilizer, and neutron absorber. Nowadays, although people try to use less cadmium by replacing it with another element because of high toxicity, the global production of cadmium has been slightly increasing for the last ten years (2010–2020) [34]. The cadmium exposure is commonly by directly contact in industrial or agricultural workplaces or via a food chain [35]. Once the cadmium was taken, it will be absorbed by kidneys and accumulated there throughout the lifetime because of the long biological half-life of cadmium in kidney (9–38 years) [36], high level of accumulation of cadmium causes many diseases and symptoms such as respiratory disease, cardiovascular disease, renal failure, bone disorders, Itai-Itai, osteoporosis,

and cancer [37-39]. Therefore, the world health organization (WHO) sets the limit of cadmium ion concentration in drinking water to be 0.003 mg/L or 44 nM [40]. Until now, there are various techniques for cadmium ion detections available such as inductively couple plasma mass spectrometry (ICP-MS), atomic absorption spectrometry (ICP-AAS), atomic emission spectrometry (ICP-AES). However, these methods are not easily applied for real-time monitoring of environment and biological systems. In comparison, using the fluorescence chemosensor offer advantages over the other methods: high sensitivity and selectivity, short detection time, and cost-effective ness. Nevertheless, cadmium and zinc are in the same group of the periodic table, so they have many properties in common such as the common oxidation state of their ions. Consequently, the chemosensor that is likely to bind with Cd^{2+} also tend to bind with Zn^{2+} [41-44]. Therefore, knowing structure parameters affecting $\text{Cd}^{2+}/\text{Zn}^{2+}$ binding ability is very important for design of fluorescence chemosensor for either Cd^{2+} or Zn^{2+} detection.

1.5 Cadmium sensor

In 2007, Lu et al. reported a sensor **R1** containing dipicolylamine (DPA) group as a receptor. In ethanol-water solution (1:9), **R1** responded to Cd^{2+} and Zn^{2+} (Figure 1.4) [45]. In the presence of Cd^{2+} , the emission maximum of **R1** was slightly enhanced and blue-shifted from 531 nm to 487 nm because the Cd^{2+} chelation reduced electron donating ability of amino groups to the carbonyl groups and, consequently, prevent ICT. In contrast, the existence of Zn^{2+} induced the deprotonation of **R1** resulting in more ICT process. The emission maximum is slightly quenched and red-shifted to 558 nm. Although association constant of **R1**•**Cd** complex is higher than Zn^{2+} complex, the detection of Cd^{2+} was disturbed by Zn^{2+} .

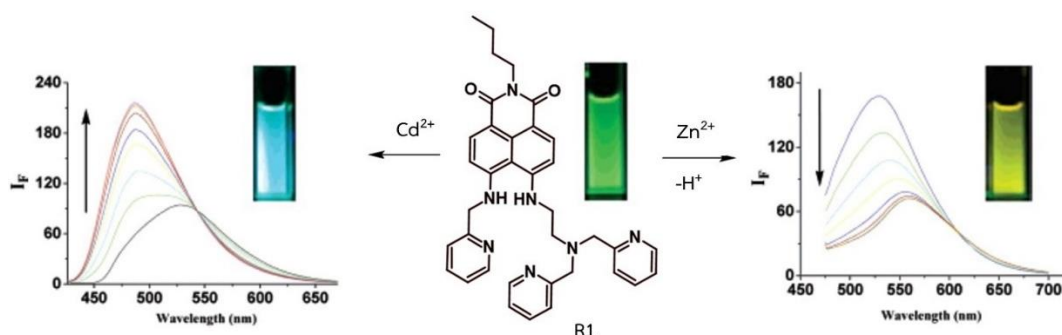


Figure 1.4 Molecular structure of **R1** and Fluorescence titration spectra with Cd^{2+} and Zn^{2+}

Other DPA containing sensors **R2–R4** were reported by Xue et al. for Zn^{2+} detection. These sensors were substituted at 8-hydroxy position by three different groups (benzyl, 2-picolyl, and methyl carboxylic acid) [46]. The Zn^{2+} binding affinities ($\log K_a$) of **R2–R4** are 8.86, 12.07, and 15.35, respectively. The result showed that the substitution at 8-position play a significant role in Zn^{2+} binding. However, the Zn^{2+} sensors developed in this work give low fluorescent enhancement (≈ 4 –12 folds) due to the high quantum yield of the free sensors ($\phi = 2.9$ –9.0%). Moreover, the detections were interfered by many transition metal ions especially Cd^{2+} . According to the fluorescent intensity of the $\text{Cd}^{2+} + \text{Zn}^{2+}$ solution that approach to the intensity of Cd^{2+} solution, it can imply that the binding affinities of these ligand toward Cd^{2+} are higher than those for Zn^{2+} (Figure 1.5).

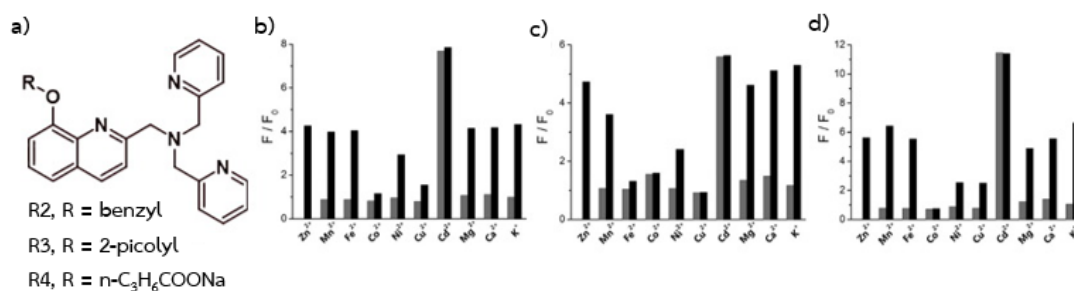


Figure 1.5 (a) Molecular structure of **R2–R4** and fluorescence enhancement ratio (F/F_0) of (b) **R2**, (c) **R3** and (d) **R4**, in the presence of various metal ions (grey bar) and in the co-presence of Zn^{2+} and another metal ion tested for interference (black bar).

In 2008, Tang et al. reported a turn-on sensor **R5**, based on 8-hydroxyquinoline, for selective detection of Cd^{2+} (Figure 1.6) [47]. The high selectivity is caused by the rigidity of **R5**, according to specific ionic radius and geometry of complex. The binding ratio between **R5** and Cd^{2+} is 1:2 resulting in low fluorescence enhancement (≈ 3.5 -fold) and high limit of detection of $9 \mu\text{M}$ of Cd^{2+} .

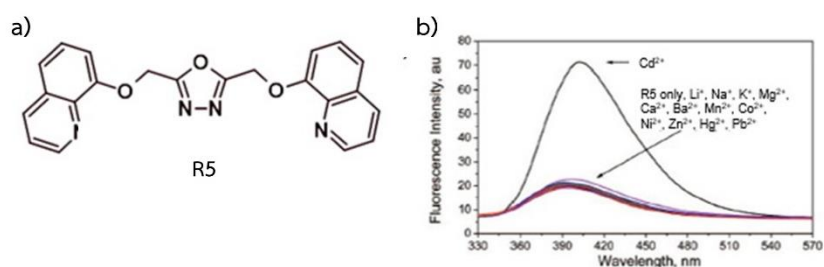


Figure 1.6 (a) Molecular structure of **R5** and (b) fluorescence spectra of **R5** in the presence of various metal ions.

In 2009, Xue et al. published two DPA-substituted quinolone sensors **R6** and **R7** [48, 49]. Both sensors showed fluorescent changes upon addition of Cd^{2+} and Zn^{2+} (Figure 1.7). For penta-dentate ligand **R6**, both of Cd^{2+} and Zn^{2+} equally enhance the emission at 420 and 460 nm, respectively. On the other hand, the emission of hexadentate ligand **R7** was significantly enhanced at 422 nm upon the addition of Cd^{2+} . In the presence of Zn^{2+} , the deprotonation occurred at amide proton, resulting in large red-shift and small enhancement. According to the ^1H NMR results, the **R7** was proposed to act as hexadentate and pentadentate ligand in complexing with Cd^{2+} and Zn^{2+} , respectively (Figure 1.8).

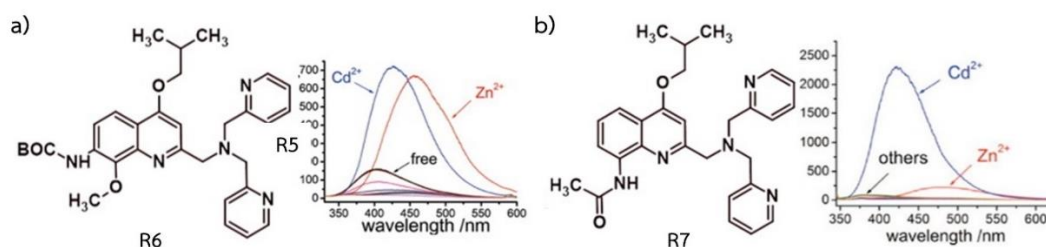


Figure 1.7 Molecular structure and fluorescence spectrum of (a) **R6** and (b) **R7** in the presence of metal ions.

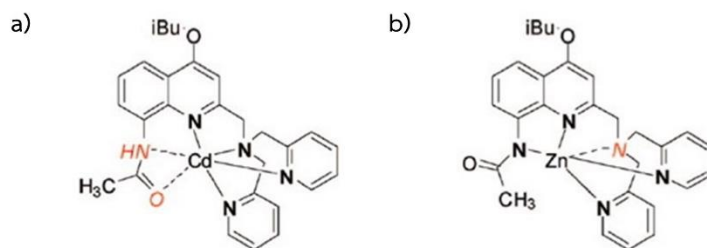


Figure 1.8 Proposed structure of (a) **R7·Cd** and (b) **R7·Zn**.

In 2011, a highly planar polypyridyl ligand **R8** was synthesized by Zhao et al. [50]. It showed excellent selectivity because the cavity size in the planar conformation perfectly matches the size of Cd^{2+} (Figure 1.9). In dichloromethane-acetonitrile (1:9), Cd^{2+} enhances an emission at 465 nm due to the increase of π -conjugation and molecular rigidity. In contrast, Zn^{2+} bound with only three pyridyl rings to form a non-planar complex and, consequently change the color from colorless to dark brown without fluorescence signal observed.

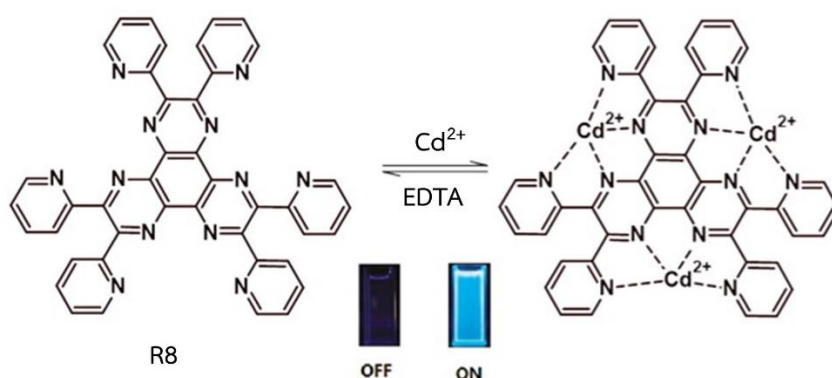


Figure 1.9 Molecular structure of **R8** and chelation enhanced fluorescence effect.

In 2012, Zhou et al. reported fluorescent sensor **R9** containing hydroxy, and amino, quinoline for distinguishing Cd^{2+} and Zn^{2+} ions [51]. In ethanol solution, Cd^{2+} turned on the fluorescence of **R9** at 410 nm based on PET inhibition mechanism. On the other hand, **R9** provided a ratiometric detection for Zn^{2+} due to the ICT enhancement mechanism. Zn^{2+} bound with both amino-, and hydroxyquinoline moieties with coordination number of 5 while Cd^{2+} bound with **R9** at only hydroxyquinoline part with coordination number of 6 (Figure 1.10). Moreover, Zn^{2+} complexation also resulted in a deprotonation of the amide N-H group of the ligand.

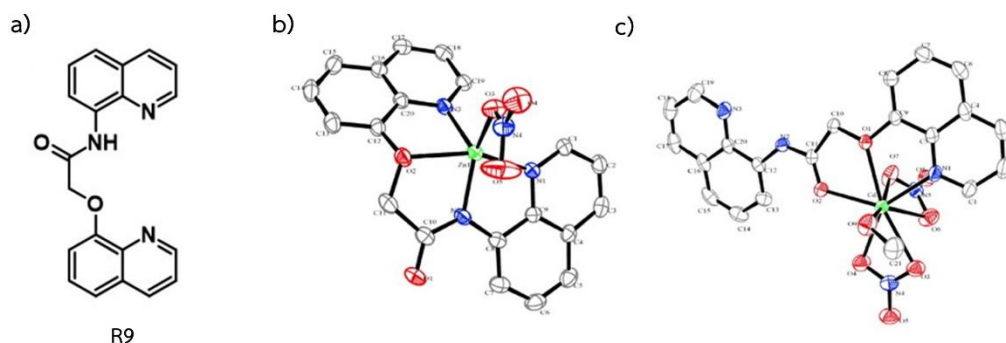


Figure 1.10 Molecular structures of (a) **R9**, and X-ray crystal structure of (b) **R9·Zn** and (c) **R9·Cd** complexes.

In 2016, Liu et al. synthesized a DPA sensor **R10** for Cd^{2+} detection in DMSO [52]. Upon binding with Cd^{2+} , **R10** underwent amide tautomerization resulting in a fluorescence enhancement at 555 nm. This sensor showed excellent selectivity toward Cd^{2+} but several transition metal ions such as Co^{2+} , Ni^{2+} , Cu^{2+} and Zn^{2+} can significantly interfere the fluorescence signal (Figure 1.11).

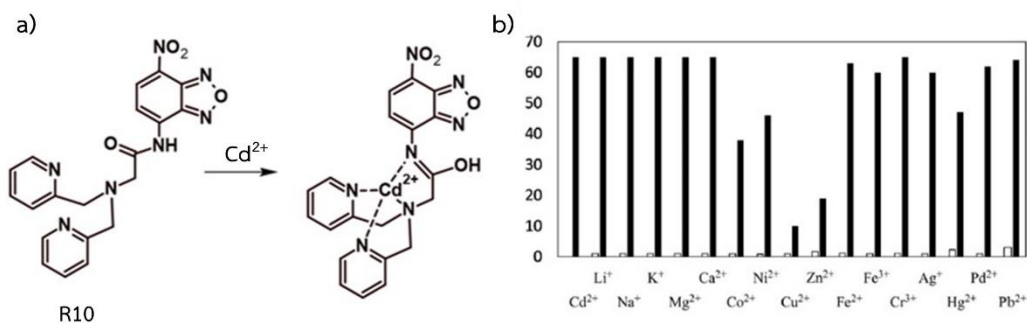


Figure 1.11 (a) Molecular structure of **R10** and (b) fluorescence enhancement ratio (I/I_0) of **R10** in the presence of various metal ions (white bar) and in the co-presence of Cd^{2+} and another metal ion tested for interference (black bar).

In 2017, Mikata et al, synthesis a series of quinoline-based turn-on fluorescent sensors (**R11O**, **R11S** and **R11N**) containing different coordinating atom (O, S, NH) [53]. The result showed that all sensors selectively enhanced the fluorescent at 418–428 nm toward Cd^{2+} with high sensitivity ($I/I_0 \approx 20$ –40 times) (Figure 1.12). the study found that **R11N** gave highest association constant for Cd^{2+} . The X-ray crystallography of **R11O·Cd** and **R11O·Zn** revealed the difference in binding mode between Cd^{2+} and

Zn^{2+} (Figure 1.13). It showed that Cd^{2+} bound with **R11O** with coordination number of 6 while Zn^{2+} bound with **R11O** with coordination number of 4.

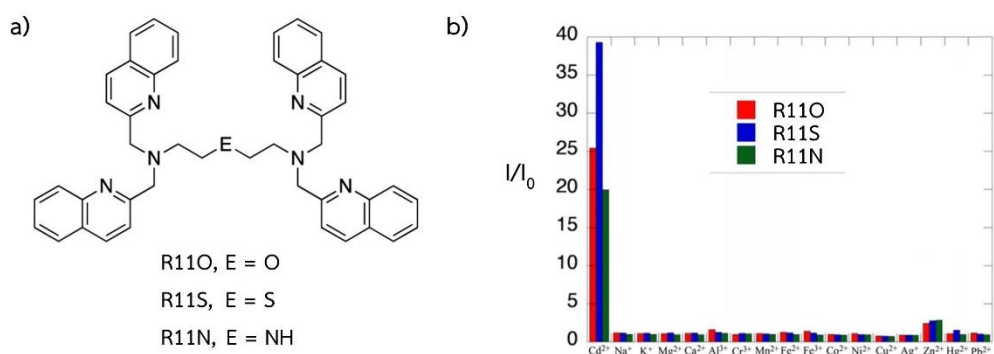


Figure 1.12 (a) Molecular structure of **R11O**, **R11S** and **R11N** (b) fluorescence enhancement ratio (I/I_0) of **R11O** (red bar), **R11S** (blue bar) and **R11N** (green bar) in the presence of various metal ions.

Figure 1.13

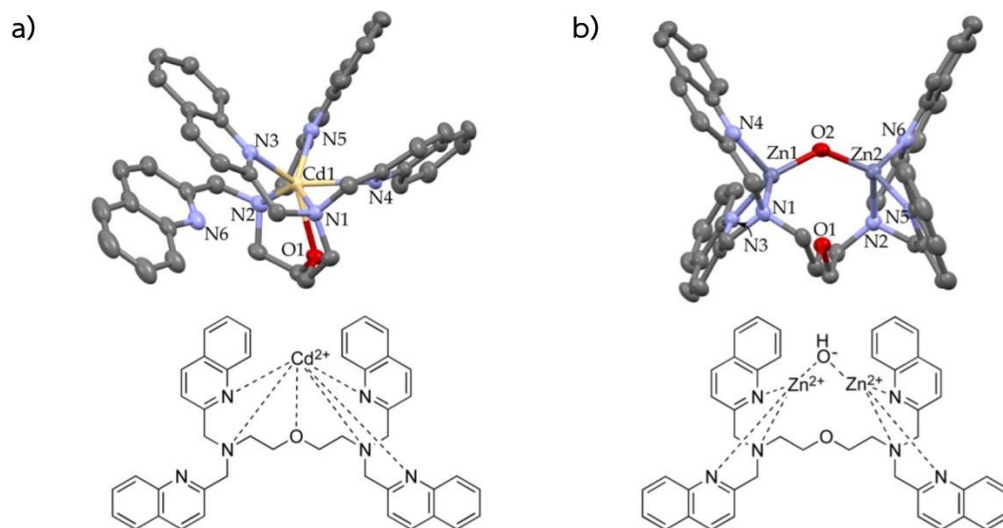


Figure 1.14 X-ray crystal structure of (a) **R11O**-Cd and (b) **R11O**-Zn

In 2019, Song and Zhang reported a quinoline-based fluorescent sensor (**R12**) for discriminative detection of Cd^{2+} and Zn^{2+} [54]. The sensor has an amide functional group as a receptor which can undergo tautomerization between amide and imidic forms. In water-rich medium, **R12** preferred binding with Zn^{2+} with an increment of

fluorescence emission at 498 nm ($I/I_0=16$) (Figure 1.14). While in acetonitrile-rich medium, R12 underwent tautomerization to imidic form and preferred binding with Cd^{2+} with an increment of fluorescence emission at 500 nm ($I/I_0=4$).

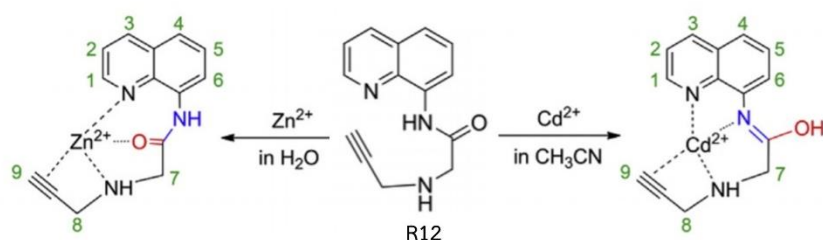


Figure 1.15 The proposed binding mode of **R12** with Cd^{2+} and Zn^{2+} .

The structure and their important sensing properties of the Cd^{2+} fluorescent sensors described above are summarized in table 1.1. According to the literature reports, quinoline derivatives are interesting ligands for metal cation binding that can provide turn-on and ratiometric fluorescence signals. The selectivity depends on the substituents especially on C2 and C8 position of quinoline. The ligands with highly charged receptor (e.g., amide, phenol) bind with Zn^{2+} stronger than Cd^{2+} . DPA is a selective receptor for Zn^{2+} and Cd^{2+} but it is not effective enough to distinguish between Cd^{2+} and Zn^{2+} . Moreover, the medium also has an effect in binding preference. In high polar medium, the ligands would rather bind with Zn^{2+} than Cd^{2+} and, vice versa. Ligands containing acidic protons seems to promote Zn^{2+} binding. However, increasing the number of coordinating atoms of the ligands seems to improve the selectivity toward Cd^{2+} , the bigger cation. There are a few reports concerning DPA modified quinoline at C2 [46, 48, 49] but there have not been reports about DPA modified quinolines at C8 which will be the subject for this proposed research. The numbers of 2-picolyl and 8-aminoquinoline moieties will be varied in order to systematically compare their effects on sensitivity and selectivity in detection of Cd^{2+} and Zn^{2+} .

Table 1.1 Summarization of some fluorescent for Cd²⁺ and Zn²⁺ detection.

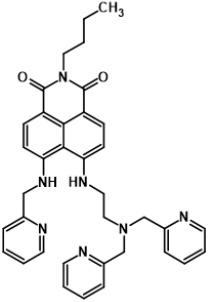
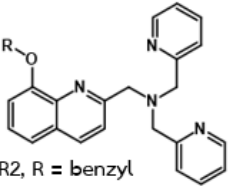
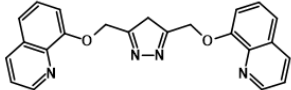
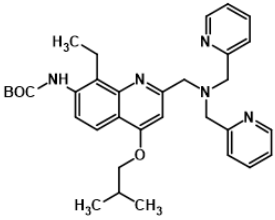
Ligand	λ_{em} (nm)	medium	I/I ₀ (I ₀ /I)	Log(K _a)	LOD	ref
	Cd²⁺: 500 Zn²⁺: 498	ethanol/H ₂ O 1:9 ethanol/H ₂ O 1:9	3 (2)	5.76 5.22	100 nM	[45]
 R2, R = benzyl R3, R = 2-picolyl R4, R = n-C ₃ H ₆ COONa	Zn²⁺: R2 455 R3 430 R4 438	water water water	4 6 12	8.86 12.07 15.35		[46]
	Cd²⁺: 397	methanol/H ₂ O 1:9	3.5	5.2	9 μM	[47]
	Cd²⁺: 405	CH ₃ CN/H ₂ O 1:1	12		238 μM	[48]

Table 1.2 Summarization of some fluorescent for Cd²⁺ and Zn²⁺ detection.

(continued)

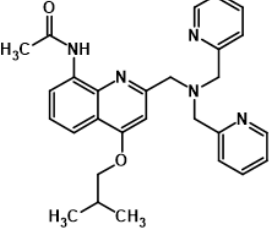
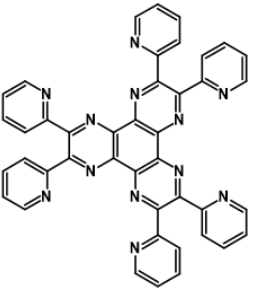
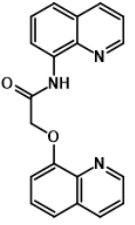
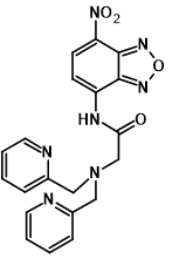
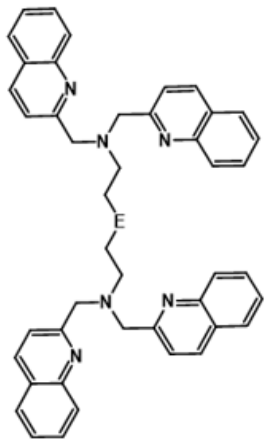
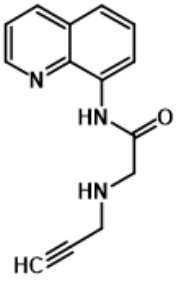
Ligand	λ_{em} (nm)	medium	I/I ₀	Log(K _a)	LOD	ref
	Cd²⁺: 422	DMSO/water 1:4	40	12.6		[49]
	Cd²⁺: 456	CH ₂ Cl ₂ /CH ₃ CN 1:9	16	4.57, 4.07, 3.61		[50]
	Cd²⁺: 410 Zn²⁺: 486	ethanol ethanol	14 3	5.99 4.26		[51]
	Cd²⁺: 567	water	65		10 nM	[52]

Table 1.3 Summarization of some fluorescent for Cd²⁺ and Zn²⁺ detection
(continued)

Ligand	λ_{em} (nm)	medium	I/I ₀	Log(K _a)	LOD	ref
 <p>R11O, E = O R11S, E = S R11N, E = NH</p>	Cd²⁺: R11O 428	DMF/water 1:1	25	6.38	22 nM	[53]
	R11S 418					
	R11N 420					
	Cd²⁺: 500	CH ₃ CN/water 7:3	4	4.57		[54]
	Zn²⁺: 498					

1.6 Objective

The objectives of this work are to synthesize evaluate a series of picolyl conjugated 8-aminoquinoline derivatives having different numbers of nitrogen coordinating atoms with and without amino proton (N-H) as turn-on fluorescent sensors for Cd²⁺ (Figure 1.12–1.14). The variety of the N-coordinating atoms and the

presence of amino proton(s) are incorporated to investigate the effects on $\text{Cd}^{2+}/\text{Zn}^{2+}$ selectivity, and their fluorescent properties. The sensing study is aimed to optimize the sensing applications in aqueous media, naked eye detection, and fluorescence imaging.

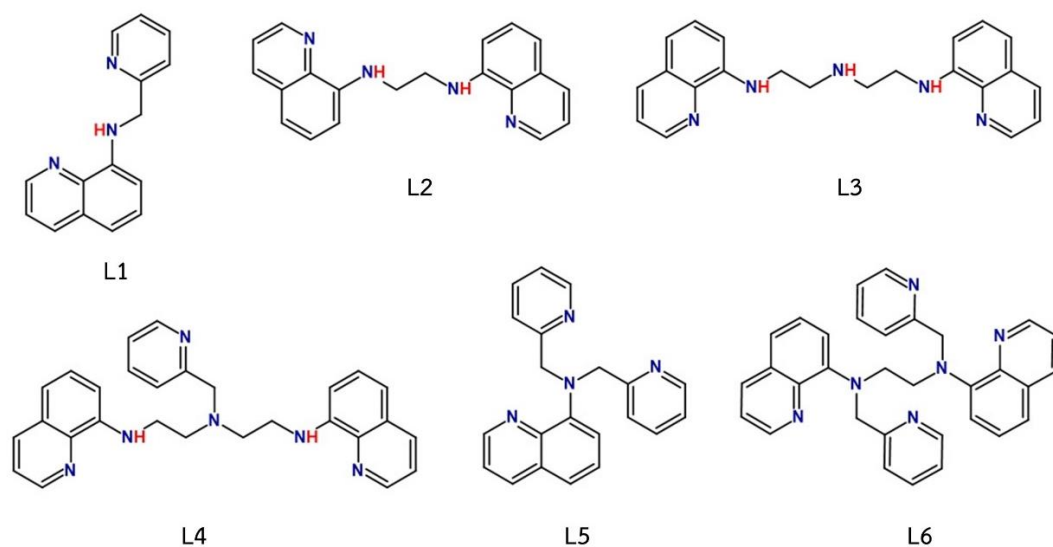


Figure 1.16 Target molecules L1-L6.

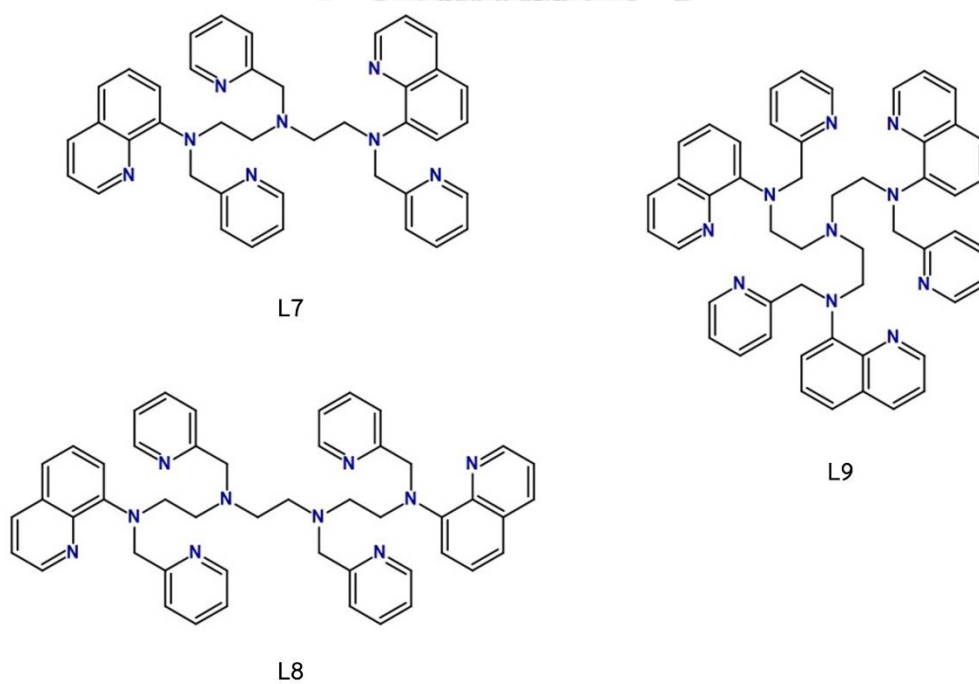
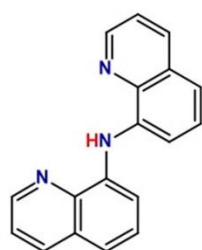
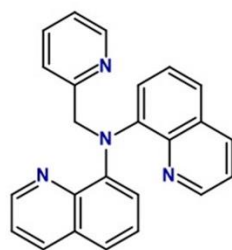


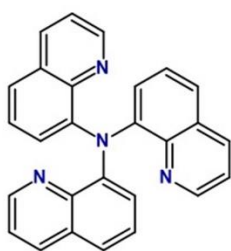
Figure 1.17 Target molecules L7-L9.



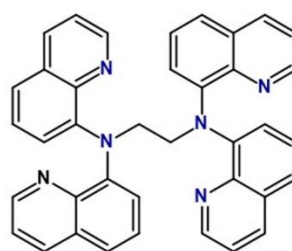
L10



L11

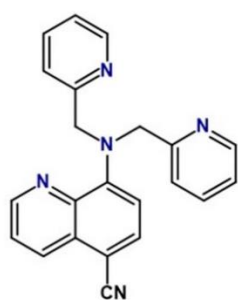


L12

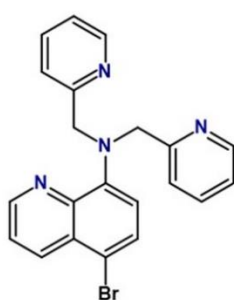


L13

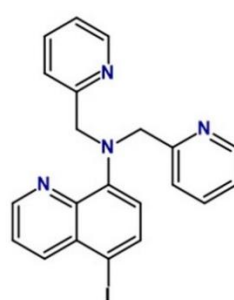
Figure 1.18 Target molecules L10–L13.



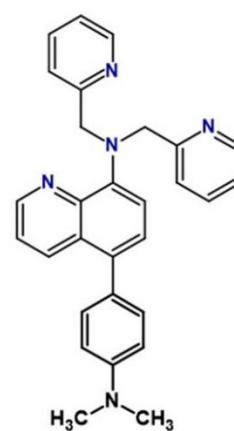
L14



L15



L16



L17

Figure 1.19 Target molecules L14–L17

CHAPTER 2

EXPERIMENT

2.1 Chemicals and materials

8-Hydroxyquinoline, diethylenetriamine, triethylenetetramine, 2-bromoaniline, anhydrous sodium sulfate, potassium iodide, potassium carbonate and sulfuric acid were purchased from Merck (Germany). 8-Aminoquinoline and 2-(chloromethyl)pyridine were purchased from TCI (Japan). Ethylenediamine, tris(2-aminoethyl)amine, glycerol, copper(I) iodide and sodium metabisulfite were purchased from Sigma-Aldrich. All other reagents were non-selectively purchased from TCI, Merck, or Sigma-Aldrich. The solvents used for reactions were reagent grade and used without further purification. The solvents used for extraction and chromatography were commercial grade and distilled before using. Thin layer chromatography (TLC) was performed on Merck aluminium oxide 60 F254 neutral or Merck silica gel 60 F254 TLC plates. Column chromatography was performed on aluminium oxide 90 active neutral (70–230 mesh) and silica gel 60 (70–230 mesh). All aqueous experiments utilized deionized Milli-Q water (18.2 M Ω -cm at 25 °C) prepared via Merck MilliQ-water system.

2.2 Analytical instruments

^1H NMR and ^{13}C NMR were acquired from a sample solution in CDCl_3 , CD_3CN , CD_3OD , $(\text{CD}_3)_2\text{SO}$ and $(\text{CD}_3)_2\text{CO}$ on Bruker AVANCE (400 MHz for ^1H NMR, 100 MHz for ^{13}C NMR) or JEOL (500 MHz for ^1H NMR, 125 MHz for ^{13}C NMR) NMR spectrometers. High resolution mass spectra were recorded on an electrospray ionization mass spectrometer (MicroTOF, Bruker Daltonics). UV-visible absorption and emission spectra were obtained on an Agilent 8453 UV-visible Spectroscopy System and Agilent Cary Eclipse Fluorescence Spectrophotometer, respectively, in a quartz cell with 1 cm path length at 25 °C. X-ray diffraction data were collected using a Bruker D8 QUEST CMOS PHOTON II and operating at $T = 298(2)$ K.

2.3 Synthesis procedure

2.3.1 Synthesis of L1

In a round-bottomed flask, 2-(chloromethyl)pyridine hydrochloride (492 mg, 3.00 mmol), potassium carbonate (2.100 g, 15.19 mmol), potassium iodide (50 mg, 0.30 mmol) and 8-aminoquinoline (432 mg, 3.00 mmol) were dissolved in acetonitrile (30 mL) and refluxed for 3 hours. After allowed to cool to room temperature, the reaction mixture was dried by rotary evaporator. The crude product was added to the saturated sodium carbonate solution (20 mL) and then extracted with dichloromethane (3×15 mL). The organic extracts were combined and dried over sodium sulfate and purified by column chromatography (silica gel, gradient of 0–1% methanol in dichloromethane) to provide the desired product as a yellowish oil (397.1 mg, 1.69 mmol). Yield: 56% ; ^1H NMR (400 MHz, CDCl_3) δ 8.74 (dd, $J = 4.0, 1.4$ Hz, 1H), 8.60 (d, $J = 4.1$ Hz, 1H), 8.01 (d, $J = 8.3$ Hz, 1H), 7.53 (ddd, $J = 7.6, 5.7, 1.8$ Hz, 1H), 7.40 – 7.24 (m, 3H), 7.17 – 7.08 (m, 1H), 7.04 (d, $J = 8.0$ Hz, 2H), 6.59 (d, $J = 7.6$ Hz, 1H), 4.68 (d, $J = 5.9$ Hz, 2H). ^{13}C NMR (101 MHz, CD_3CN) δ 149.99 (s), 148.11 (s), 145.39 (s), 139.09 (s), 137.52 (s), 136.81 (s), 129.57 (s), 128.62 (s), 123.03 (s), 122.56 (s), 122.35 (s), 118.18 (s), 114.92 (s), 105.93 (s), 49.08 (s). HRMS; m/z calculated for $[\text{L1}+\text{Na}]^+$: $[\text{C}_{15}\text{H}_{13}\text{N}_3\text{Na}]^+$ is 258.10072; found 258.1017.

2.3.2 Synthesis of L2

In a sealed tube, 8-hydroxyquinoline (3.000 g, 20.7 mmol), ethylenediamine (0.75 mL, 11.2 mmol) and sodium metabisulfite (3.954 g, 20.7 mmol) were dissolved in water (35 mL) and stirred at 115 °C for 7 days. After allowed to cool to room temperature, the reaction mixture was made to strong base ($\text{pH} > 12$) by sodium hydroxide. The filtered solid collected by filtration was added to the saturated sodium carbonate solution (20 mL) and extracted with dichloromethane (3×15 mL). The organic extracts were combined and dried over sodium sulfate and purified by recrystallization in methanol to provide the desired product as a yellowish solid (1.724 g, 11.0 mmol). Yield: 53% ; ^1H NMR (400 MHz, DMSO) δ 8.72 (d, $J = 3.0$ Hz, 2H), 8.20 (d, $J = 7.8$ Hz, 2H), 7.49 (dd, $J = 8.2, 4.2$ Hz, 2H), 7.37 (t, $J = 7.9$ Hz, 2H), 7.06 (d, J

= 8.0 Hz, 2H), 6.81 (t, J = 11.0 Hz, 4H), 3.63 (s, J = 2.2 Hz, 4H). HRMS; m/z calculated for $[\mathbf{L2}+\text{Na}]^+$: $[\text{C}_{20}\text{H}_{18}\text{N}_4\text{Na}]^+$ is 337.14292; found 337.1429.

2.3.3 Synthesis of L3

In a sealed tube, 8-hydroxyquinoline (3.000 g, 20.7 mmol), diethylenetriamine (1.20 ml, 11.4 mmol) and sodium metabisulfite (3.954 g, 20.7 mmol) were dissolved in water (35 mL) and stirred at 115 °C for 9 days. After allowed to cool to room temperature, the reaction mixture was made to strong base ($\text{pH}>12$) by sodium hydroxide and extracted with dichloromethane (3×20mL). The organic extracts were combined and dried over sodium sulfate and purified column chromatography (alumina, dichloromethane) to provide the desired product as a yellowish solid (1.484 g 4.15 mmol). Yield 40%; ^1H NMR (400 MHz, CD_3CN) δ 8.75 – 8.50 (m, 1H), 8.11 (d, J = 8.3 Hz, 1H), 7.40 (dd, J = 8.3, 4.2 Hz, 1H), 7.34 (t, J = 7.9 Hz, 1H), 7.04 (d, J = 8.1 Hz, 1H), 6.69 (d, J = 7.6 Hz, 1H), 6.48 (s, 1H), 3.38 (q, J = 5.8 Hz, 2H), 3.00 (t, J = 6.0 Hz, 2H). ^{13}C NMR (101 MHz, CD_3CN) δ 147.97 (s), 146.12 (s), 139.11 (s), 136.83 (s), 129.68 (s), 128.85 (s), 122.55 (s), 114.44 (s), 105.44 (s), 49.11 (s), 43.84 (s). HRMS; m/z calculated for $[\mathbf{L3}+\text{Na}]^+$: $[\text{C}_{22}\text{H}_{23}\text{N}_5\text{Na}]^+$ is 380.18512; found 380.1855.

2.3.4 Synthesis of L4

In a round-bottomed flask, 2-(chloromethyl)pyridine hydrochloride (222.1 mg, 1.35 mmol), potassium carbonate (850.6 mg, 6.15 mmol), potassium iodide (22.5 mg 0.14 mmol) and **L3** (440 mg, 1.23 mmol) were dissolved in acetonitrile (20 mL) and refluxed for 3 hours. After allowed to cool to room temperature, the reaction mixture was dried by rotary evaporator. The crude product was added to the saturated sodium carbonate solution (20 mL) and then extracted with dichloromethane (3×15 mL). The organic extracts were combined and dried over sodium sulfate and purified by column chromatography (alumina, dichloromethane) to provide the desired product as a yellowish oil (462.0 mg, 1.03 mmol). Yield: 84% ; ^1H NMR (400 MHz, Acetone) δ 8.66 (d, 2H), 8.44 (d, J = 4.5 Hz, 1H), 8.10 (dd, J = 8.2, 1.1 Hz, 2H), 7.80 (d, J = 7.8 Hz, 1H), 7.48 (td, J = 7.7, 1.0 Hz, 1H), 7.39 (dd, J = 8.3, 4.2 Hz, 2H), 7.26 (t, J = 7.9 Hz, 2H), 7.11 – 7.05 (m, 1H), 7.00 (d, J = 8.1 Hz, 2H), 6.82 (d, J = 14.0 Hz, 2H), 6.58 (d, J = 7.6 Hz, 2H), 3.94 (s, 2H), 3.45 (q, J = 5.9 Hz, 4H), 2.98 (t, J =

6.2 Hz, 4H). ^{13}C NMR (101 MHz, Acetone) δ 160.90 (s), 149.49 (s), 147.61 (s), 145.99 (s), 139.30 (s), 136.96 (s), 136.49 (s), 129.64 (s), 128.63 (s), 124.08 (s), 122.65 (s), 122.26 (s), 114.04 (s), 105.15 (s), 61.55 (s), 54.07 (s), 41.92 (s). HRMS; m/z calculated for $[\text{L4}+\text{Na}]^+$: $[\text{C}_{28}\text{H}_{28}\text{N}_6\text{Na}]^+$ is 471.22731; found 471.2267.

2.3.5 Synthesis of L5

In a round-bottomed flask, 2-(chloromethyl) pyridine hydrochloride (1.968 g, 12.0 mmol), potassium carbonate (2.211 g, 16.0 mmol), potassium iodide (50 mg, 0.30 mmol) and 8-aminoquinoline (432 mg, 3.00 mmol) were dissolved in acetonitrile (40 mL) and stirred at room temperature for 4 days. The reaction mixture was dried by rotary evaporator. The crude product was added to the saturated sodium carbonate solution (20 mL) and then extracted with dichloromethane (3x15 mL). The organic extracts were combined and dried over sodium sulfate and purified by column chromatography (alumina, 1:1 ethyl acetate/dichloromethane) to provide the desired product as a yellowish solid (411 mg, 1.26 mmol). Yield: 42% ; ^1H NMR (400 MHz, CDCl_3) δ 8.83 (dd, $J = 4.1, 1.8$ Hz, 1H), 8.48 (d, $J = 5.0$ Hz, 2H), 8.05 (dd, $J = 8.3, 1.7$ Hz, 1H), 7.56 – 7.42 (m, 4H), 7.33 (dd, $J = 8.3, 4.1$ Hz, 1H), 7.28 (dd, $J = 7.3, 6.3$ Hz, 1H), 7.22 (t, $J = 7.8$ Hz, 1H), 7.05 (ddd, $J = 6.8, 5.0, 1.8$ Hz, 2H), 6.99 (dd, $J = 7.6, 1.1$ Hz, 1H), 4.92 (s, 4H). ^{13}C NMR (101 MHz, DMSO) δ 148.73 (s), 147.54 (s), 146.11 (s), 141.96 (s), 136.48 (d, $J = 13.5$ Hz), 129.46 (s), 126.41 (s), 121.94 (d, $J = 3.5$ Hz), 121.14 (s), 120.12 (s), 117.12 (s), 58.71 (s), 54.85 (s). HRMS; m/z calculated for $[\text{L7}+\text{Na}]^+$: $[\text{C}_{21}\text{H}_{18}\text{N}_4\text{Na}]^+$ is 349.14292; found 349.1427.

2.3.6 Synthesis of L6

In a round-bottomed flask, 2-(chloromethyl)pyridine hydrochloride (892.2 mg, 5.44 mmol), potassium carbonate (1.75 g, 12.692 mmol), potassium iodide (602.0 mg, 3.63 mmol) and L2 (570.0mg, 1.81mmol) were dissolved in acetonitrile (40 mL) and stirred at room temperature for 4 days. The reaction mixture was dried by rotary evaporator. The crude product was added to the saturated sodium carbonate solution (20 mL) and then extracted with dichloromethane (3x15 mL). The organic extracts were combined and dried over sodium sulfate and purified by column chromatography (alumina, dichloromethane) to provide the desired product as a

yellowish solid (608.4 mg, 1.22 mmol). Yield: 68% ; ^1H NMR (400 MHz, DMSO) δ 8.86 (s, 1H), 8.55 (d, $J = 4.9$ Hz, 1H), 8.50 (d, $J = 7.9$ Hz, 1H), 7.82 (t, $J = 7.9$ Hz, 1H), 7.73 – 7.62 (m, 1H), 7.51 (t, $J = 9.3$ Hz, 2H), 7.42 (t, $J = 7.9$ Hz, 1H), 7.36 – 7.28 (m, 1H), 7.24 (d, $J = 7.4$ Hz, 1H), 4.45 (s, 2H), 3.71 (s, $J = 17.0$ Hz, 2H). ^{13}C NMR (101 MHz, DMSO) δ 159.40 (s), 148.72 (s), 146.90 (s), 146.48 (s), 141.60 (s), 136.33 (d, $J = 3.6$ Hz), 129.42 (s), 126.45 (s), 121.84 (s), 121.60 (s), 120.96 (s), 119.06 (s), 115.52 (s), 58.44 (s), 51.55 (s). HRMS; m/z calculated for $[\text{L6}+\text{Na}]^+$: $[\text{C}_{32}\text{H}_{28}\text{N}_6\text{Na}]^+$ is 519.22731; found 519.2274.

2.3.7 Synthesis of L7

In a round-bottomed flask, 2-(chloromethyl)pyridine hydrochloride (667 mg, 4.06 mmol), potassium carbonate (1.123 g, 8.12 mmol), potassium iodide (23 mg 0.14 mmol) and **L3** (440 mg, 1.23 mmol) were dissolved in acetonitrile (25 mL) and stirred at room temperature for 4 days. The reaction mixture was dried by rotary evaporator. The crude product was added to the saturated sodium carbonate solution (20 mL) and then extracted with dichloromethane (3×15 mL). The organic extracts were combined and dried over sodium sulfate and purified by column chromatography (alumina, dichloromethane) to provide the desired product as a yellowish oil (108 mg, 0.17 mmol). Yield: 14% ; ^1H NMR (400 MHz, CD_3CN) δ 8.65 (s, 2H), 8.43 (d, $J = 4.4$ Hz, 2H), 8.32 (s, 1H), 8.11 (d, $J = 8.0$ Hz, 2H), 7.51 (t, $J = 7.1$ Hz, 2H), 7.41 (t, $J = 7.9$ Hz, 1H), 7.36 – 7.26 (m, 6H), 7.22 (t, $J = 7.8$ Hz, 2H), 7.15 – 7.03 (m, 4H), 6.92 (d, $J = 7.5$ Hz, 2H), 4.71 (s, 3H), 3.69 – 3.55 (m, 6H), 2.79 (t, $J = 7.0$ Hz, 4H). ^{13}C NMR (101 MHz, CD_3CN) δ 160.85 (s), 149.78 (s), 149.47 (s), 148.15 (s), 143.46 (s), 137.26 (s), 137.10 (s), 136.96 (s), 130.84 (s), 127.35 (s), 123.62 (s), 123.09 (s), 122.77 (s), 122.62 (s), 121.91 (s), 120.63 (s), 117.65 (s), 61.98 (s), 60.12 (s), 53.52 (s), 52.86 (s). HRMS; m/z calculated for $[\text{L7}+\text{H}]^+$: $[\text{C}_{40}\text{H}_{39}\text{N}_8]^+$ is 631.32977; found 631.34347.

2.3.8 Synthesis of L8

Preparation of QNNQ

In a sealed tube, 8-hydroxyquinoline (3.000 g, 20.7 mmol), triethylenetetramine (1.70 mL, 11.4 mmol) and sodium metabisulfite (3.954 g, 20.7 mmol) were dissolved in water (35 mL) and stirred at 115 °C for 9 days. After allowed to cool to room temperature, the reaction mixture was made to strong base (pH>12) by sodium

hydroxide and extracted with dichloromethane (3×20mL). The organic extracts were combined and dried over sodium sulfate and purified column chromatography (alumina, dichloromethane) to provide the desired product as a yellowish solid (1.684 g 4.2 mmol). Yield 40% ; ¹H NMR (400 MHz, Acetone) δ 8.70 (dd, *J* = 26.8, 4.1 Hz, 1H), 8.14 (t, *J* = 9.3 Hz, 1H), 7.45 (dd, *J* = 8.3, 4.1 Hz, 1H), 7.40 (dd, *J* = 8.3, 4.1 Hz, 1H), 7.36 (dd, *J* = 16.7, 8.3 Hz, 1H), 7.08 – 7.01 (m, 1H), 6.69 (dd, *J* = 10.8, 7.8 Hz, 1H), 6.65 (s, 1H), 3.38 (dt, *J* = 19.0, 5.6 Hz, 2H), 3.00 (t, *J* = 6.0 Hz, 1H), 2.97 (s, 1H), 2.92 (t, *J* = 6.2 Hz, 1H), 2.81 (s, 2H). ¹³C NMR (126 MHz, Actone) δ 146.84 (s), 145.29 (s), 138.39 (s), 135.74 (s), 128.83 (s), 127.90 (s), 121.51 (s), 113.21 (d, *J* = 2.6 Hz), 104.27 (d, *J* = 3.2 Hz), 79.70 – 76.32 (m), 48.53 – 48.09 (m), 41.59 (d, *J* = 8.3 Hz). . HRMS; *m/z* calculated for [QNNQ+H]⁺: [C₂₄H₂₉N₆]⁺ is 401.24537; found 401.25480.

Preparation of L8

In a round-bottomed flask, 2-(chloromethyl)pyridine hydrochloride (902 mg, 5.50 mmol), potassium carbonate (1.106 g, 8.0 mmol), potassium iodide (166 mg 1.0 mmol) and QNNQ (400.0 mg, 1.0 mmol) were dissolved in acetonitrile (25 mL) and stirred at room temperature for 4 days. The reaction mixture was dried by rotary evaporator. The crude product was added to the saturated sodium carbonate solution (20 mL) and then extracted with dichloromethane (3×15 mL). The organic extracts were combined and dried over sodium sulfate and purified by column chromatography (alumina, gradient of 0–1% methanol in dichloromethane) to provide the desired product as a yellowish oil (31 mg, 0.04 mmol). Yield: 14% ; ¹H NMR (400 MHz, Acetone) δ 8.73 (dd, *J* = 4.0, 1.7 Hz, 2H), 8.46 (d, *J* = 4.8 Hz, 2H), 8.38 (d, *J* = 4.1 Hz, 2H), 8.15 (dd, *J* = 8.2, 1.1 Hz, 2H), 7.54 (ddd, *J* = 14.7, 7.4, 1.4 Hz, 2H), 7.53 (ddd, *J* = 15.0, 7.6, 1.5 Hz, 2H), 7.46 (d, *J* = 7.9 Hz, 1H), 7.37 (dd, *J* = 8.3, 4.1 Hz, 1H), 7.30 (dd, *J* = 12.0, 4.6 Hz, 2H), 7.28 – 7.21 (m, 1H), 7.11 (dd, *J* = 12.5, 7.5 Hz, 2H), 6.99 (d, *J* = 6.4 Hz, 1H), 4.79 (s, 2H), 3.76 – 3.70 (m, 2H), 3.69 (s, 1H), 2.60 (s, 2H).

2.3.9 Synthesis of L9

Preparation of 3QN

In a sealed tube, 8-hydroxyquinoline (3.000 g, 20.7 mmol), tris(2-aminoethyl)amine (1.10 mL, 7.3 mmol) and sodium metabisulfite (3.928 g, 20.7

mmol) were dissolved in water (35 mL) and stirred at 115 °C for 9 days. After allowed to cool to room temperature, the reaction mixture was made to strong base (pH>12) by sodium hydroxide and extracted with dichloromethane (3×20mL). The organic extracts were combined and dried over sodium sulfate and purified column chromatography (alumina, dichloromethane) to provide the desired product as a yellowish solid (1.562 g, 2.96 mmol). Yield: 43% ; ¹H NMR (400 MHz, Acetone) δ 8.57 (d, *J* = 3.8 Hz, 2H), 8.11 (d, *J* = 8.2 Hz, 2H), 7.37 (dd, *J* = 8.2, 4.1 Hz, 2H), 7.24 (t, *J* = 7.9 Hz, 2H), 7.01 (d, *J* = 8.1 Hz, 2H), 6.80 (s, 2H), 6.57 (d, *J* = 7.6 Hz, 2H), 3.46 (q, *J* = 6.1 Hz, 4H), 3.06 (t, *J* = 6.3 Hz, 4H). ¹³C NMR (101 MHz, Acetone) δ 147.63 (s), 145.94 (s), 139.28 (s), 136.44 (s), 129.63 (s), 128.59 (s), 122.22 (s), 114.04 (s), 105.12 (s), 54.81 (s), 42.48 (d, *J* = 7.7 Hz). HRMS; *m/z* calculated for [**3QN**+Na]⁺: [C₃₃H₃₃N₇Na]⁺ is 550.26951; found 550.2706.

Preparation of L9

In a round-bottomed flask, 2-(chloromethyl)pyridine hydrochloride (508.5 mg, 3.08 mmol), potassium carbonate (635.8 mg, 4.62 mmol), potassium iodide (22.5 mg, 0.14 mmol) and **3QN** (280.0 mg, 0.70 mmol) were dissolved in acetonitrile (15 mL) and stirred at room temperature for 4 days. The reaction mixture was dried by rotary evaporator. The crude product was added to the saturated sodium carbonate solution (20 mL) and then extracted with dichloromethane (3×15 mL). The organic extracts were combined and dried over sodium sulfate and purified by column chromatography (alumina, gradient of 0-1% methanol in dichloromethane) to provide the desired product as a yellowish oil (40 mg, 0.052 mmol). Yield: 7% ; ¹H NMR (400 MHz, DMSO) δ 8.56 (dd, *J* = 4.0, 1.6 Hz, 2H), 8.43 (d, *J* = 4.2 Hz, 2H), 8.17 (dd, *J* = 8.3, 1.5 Hz, 1H), 7.57 (td, *J* = 7.7, 1.6 Hz, 1H), 7.33 (dd, *J* = 8.3, 4.1 Hz, 1H), 7.29 (d, *J* = 8.5 Hz, 1H), 7.27 (d, *J* = 8.3 Hz, 1H), 7.22 (t, *J* = 7.8 Hz, 1H), 7.15 (dd, *J* = 6.8, 5.4 Hz, 1H), 6.87 (d, *J* = 7.6 Hz, 1H), 4.67 (s, 2H), 3.57 – 3.50 (m, 2H), 2.79 – 2.72 (m, 2H). ¹³C NMR (101 MHz, DMSO) δ 159.38 (s), 148.63 (s), 146.89 (s), 146.60 (s), 141.68 (s), 136.22 (s), 129.39 (s), 126.32 (s), 121.78 (s), 121.59 (s), 120.83 (s), 119.12 (s), 115.84 (s), 58.52 (s), 52.77 (s), 52.10 (s). HRMS; *m/z* calculated for [**L9**+H]⁺: [C₅₁H₄₉N₁₀]⁺ is 801.41416; found 801.42062.

2.3.10 Synthesis of L10–L13

Preparation of 8-Bromoquinoline

The 8-Bromoquinoline can be prepared according to the literature [55]. In a round-bottomed flask, 2-Bromoaniline (1.000 g, 5.81 mmol), glycerol (1.71 mL, 23.4 mmol), ferrous sulfate heptahydrate (242 mg, 0.87 mmol) and iodine (15 mg, 0.06 mmol) were dissolved in sulfuric acid (5mL) and refluxed for 4 hours.

After allowed to cool to room temperature, the reaction mixture was neutralized with 10% sodium hydroxide solution and extracted with dichloromethane (3×20 mL). The organic extracts were combined and dried over sodium sulfate and purified by column chromatography (silica gel, 5% ethyl acetate in hexane) to provide the desired product as a yellowish oil (725 mg, 3.48 mmol). yield: 60%; ¹H NMR (400 MHz, CDCl₃) δ 8.85 (dd, *J* = 4.2, 1.5 Hz, 1H), 7.93 (dd, *J* = 8.3, 1.4 Hz, 1H), 7.83 (dt, *J* = 18.7, 9.3 Hz, 1H), 7.54 (t, *J* = 8.4 Hz, 1H), 7.29 – 7.21 (m, 1H), 7.17 (t, *J* = 7.8 Hz, 1H).

2.3.10.1 Synthesis of L10

8-hydroxyquinoline (500 mg, 3.44 mmol), 8-aminoquinoline (497 mg, 3.44 mmol) and sodium metabisulfite (655 mg, 3.44 mmol) were dissolved in water (10 mL) and stirred at 115 °C for 9 days. After allowed to cool to room temperature, the reaction mixture was made to strong base (pH>12) by sodium hydroxide and extracted with dichloromethane (3×20mL). The organic extracts were combined and dried over sodium sulfate and purified column chromatography (alumina, dichloromethane) to provide the desired product as a yellowish solid (249 mg, 0.92 mmol). Yield: 27%; ¹H NMR (400 MHz, DMSO) δ 10.74 (d, *J* = 9.2 Hz, 1H), 8.99 (d, *J* = 4.0 Hz, 2H), 8.40 (d, *J* = 8.2 Hz, 2H), 7.95 (d, *J* = 7.7 Hz, 2H), 7.65 (dd, *J* = 8.2, 4.1 Hz, 2H), 7.60 (t, *J* = 7.9 Hz, 2H), 7.48 (d, *J* = 8.1 Hz, 2H). ¹³CNMR (126 MHz, DMSO) δ 148.88 (s), 139.41 (s), 138.20 (s), 137.07 (s), 129.10 (s), 127.95 (s), 122.74 (s), 118.56 (s), 110.27 (s). HRMS; *m/z* calculated for [L10+H]⁺: [C₁₈H₁₄N₃]⁺ is 272.11877; found 272.12117.

2.3.10.2 Synthesis of L11

In a sealed tube, **L1** (300 mg, 1.28 mmol), 8-Bromoquinoline (265 mg, 1.28 mmol), potassium carbonate (352 mg 2.55 mmol), copper (I) iodide (49 mg, 0.25 mmol) and L-proline (59 mg, 0.51 mmol) were dissolved in DMSO (7 mL) and stirred at 160 °C for 3 days. After allowed to cool to room temperature, the reaction mixture was added to the water (40 mL) and then extracted with ethyl acetate for several times. The organic extracts were combined, washed with water (3×30 mL) and dried over sodium sulfate and purified by column chromatography (alumina, ethyl acetate) to provide the desired product as a yellowish solid (324 mg, 0.90 mmol). Yield: 70%; ¹H NMR (400 MHz, DMSO) δ 8.54 (d, *J* = 2.6 Hz, 2H), 8.46 (d, *J* = 4.4 Hz, 1H), 8.26 (d, *J* = 7.4 Hz, 2H), 7.94 (d, *J* = 7.9 Hz, 1H), 7.58 (t, *J* = 6.7 Hz, 1H), 7.53 (d, *J* = 7.9 Hz, 2H), 7.44 – 7.37 (m, 2H), 7.34 (t, *J* = 7.9 Hz, 2H), 7.21 (d, *J* = 7.4 Hz, 2H), 7.18 – 7.11 (m, 1H), 5.60 (s, 2H). ¹³C NMR (101 MHz, DMSO) δ 159.96 (s), 148.32 (s), 147.96 (s), 146.90 (s), 142.36 (s), 136.20 (s), 136.12 (s), 129.34 (s), 126.43 (s), 122.05 (s), 121.90 (s), 121.72 (s), 121.28 (s), 120.95 (s), 59.63 (s). HRMS; *m/z* calculated for [**L11**+H]⁺: [C₁₈H₁₄N₃]⁺ is 363.16097; found 363.16395.

2.3.10.3 Synthesis of L12

In a sealed tube, 8-Aminoquinoline (104 mg, 0.72 mmol), 8-Bromoquinoline (300 mg, 1.44 mmol), potassium carbonate (433 mg 3.13 mmol), copper(I) iodide (28 mg, 0.15 mmol) and L-proline (33 mg, 0.27 mmol) were dissolved in DMSO (5 mL) and stirred at 160 °C for 3 days. After allowed to cool to room temperature, the reaction mixture was added to the water (40 mL) and then extracted with ethyl acetate for several times. The organic extracts were combined, washed with water (3×30 mL) and dried over sodium sulfate and purified by column chromatography (alumina, ethyl acetate) to provide the desired product as a yellowish solid (120 mg, 0.30 mmol). Yield: 42%; ¹H NMR (400 MHz, DMSO) δ 8.38 (d, *J* = 2.7 Hz, 1H), 8.28 (d, *J* = 8.2 Hz, 1H), 7.62 (d, *J* = 8.0 Hz, 1H), 7.43 – 7.27 (m, 2H), 7.01 (d, *J* = 7.5 Hz, 1H). ¹³C NMR (101 MHz, DMSO) δ 148.16 (s), 147.71 (s), 142.71 (s), 135.93 (s), 129.29 (s), 126.48 (s), 124.25 (s), 122.74 (s), 120.85 (s). HRMS; *m/z* calculated for [**L12**+H]⁺: [C₁₈H₁₄N₃]⁺ is 399.16097; found 399.16802.

2.3.10.1 Synthesis of L13

In a sealed tube L2 (300 mg, 0.95 mmol), 8-Bromoquinoline (400 mg, 1.92 mmol), potassium carbonate (530 mg 3.83 mmol), copper (I) iodide (40 mg, 0.21 mmol) and L-proline (44 mg, 0.38 mmol) were dissolved in DMSO (5 mL) and stirred at 160 °C for 3 days. After allowed to cool to room temperature, the reaction mixture was added to the water (40 mL) and then extracted with ethyl acetate for several times. The organic extracts were combined, washed with water (3×30 mL) and dried over sodium sulfate and purified by column chromatography (alumina, ethyl acetate) to provide the desired product as a yellowish solid (54 mg, 0.10 mmol). Yield: 10%; ¹H NMR (400 MHz, DMSO) δ 8.47 (d, *J* = 2.6 Hz, 1H), 8.27 (d, *J* = 8.3 Hz, 1H), 7.50 (t, *J* = 21.2 Hz, 1H), 7.40 (dd, *J* = 8.2, 4.1 Hz, 1H), 7.35 (t, *J* = 7.8 Hz, 1H), 7.21 (d, *J* = 7.5 Hz, 1H), 4.70 (s, 1H). ¹³C NMR (101 MHz, DMSO) δ 147.75 (s), 147.00 (s), 142.31 (s), 136.17 (s), 129.42 (s), 126.48 (s), 121.58 (s), 121.21 (s), 120.91 (s), 52.10 (s). HRMS; *m/z* calculated for [L13+H]⁺: [C₁₈H₁₄N₃]⁺ is 569.24537; found 569.24630.

2.4 Photophysical property study

2.4.1 Absorption

The stock solution of L1–17 (5 mM) in DMSO were prepared. The absorption spectra of all ligands were recorded from 190 nm to 1100 nm at ambient temperature. Molar Absorption Coefficients (ϵ) of all fluorophores were estimated from UV absorption spectra of analytical samples in Milli-Q water at various concentration. The absorbance at absorption maximum wavelength (λ_{\max}) were plotted against the concentration (M). The line of best fit passing through the origin were created according to the data plot. The Molar Absorption Coefficients were obtained from the slopes of the line of best fit according to the following equation:

$$A = \epsilon bC$$

where *A* is the absorbance,

b is the cell path length (cm),

C is the concentration (M), and

ϵ is the Molar Absorption Coefficient (M⁻¹·cm⁻¹).

2.4.2 Fluorescence

The stock solutions of analytical samples were diluted to 10 μM in 0.1% DMSO/H₂O (v/v). The emission spectra of fluorophores were recorded from 350 nm to 650 nm at ambient temperature using an excitation wavelength at 300 nm to 350 nm. The fluorescence quantum yields of analytical samples were performed in 0.1% DMSO/H₂O (v/v). each sample used quinin sulfate ($\phi_{\text{st}} = 0.54$; $\lambda_{\text{max}} = 336$ nm) in 0.10 M H₂SO₄ [56]. The UV-Vis absorption spectra of the analytical samples and reference at varied concentrations were recorded. The maximum absorbance of all samples should never exceed 0.1. The fluorescence emission spectra of the same solutions using appropriate excitation wavelength (λ_{max}) of each compound. Graphs of integrated fluorescent emission intensities were plotted against the absorbance the respective excitation wavelengths. The line of best fit passing through the origin were created according to the data plot. The fluorescence quantum yields (ϕ_x) were calculated from the slopes (m) of the lines of best fit according to the following equation:

$$\phi_x = \phi_{\text{st}} \left(\frac{m_x}{m_{\text{st}}} \right) \left(\frac{\eta_x^2}{\eta_{\text{st}}^2} \right)$$

Where ϕ_x and ϕ_{st} are the fluorescence quantum yield of sample and standard reference, respectively,
 m_x and m_{st} are the slope of the line of best fit of sample and standard reference, respectively, and
 η_x and η_{st} are the refractive index of sample and standard reference, respectively.

2.5 Fluorescent sensing study

2.5.1 Selectivity

The stock solution of various metal ions (Li⁺, Na⁺, K⁺, Ca²⁺, Ba²⁺, Mg²⁺, Fe²⁺, Co²⁺, Ni²⁺, Cu²⁺, Zn²⁺, Cd²⁺, Ag⁺, Hg²⁺, Pb²⁺, Fe³⁺, Cr³⁺ and Al³⁺) were prepared at 1.0 mM in Milli-Q water from corresponding acetate, nitrate, or chlorate salts. The stock solution of sensing compound in DMSO (5 mM, 20 μL) and the stock solution of metal ions in water (10 mM, 1.0 μL) were diluted with 200 μL of 0.200 M Tris HCl buffer (pH = 7) in

a 1-mL quartz cuvette. The final volume was adjusted to 1.000 mL by adding Milli-Q water. The final concentration of each fluorophore is 10 μM in 0.2% DMSO/H₂O (v/v). the emission spectra of all sensors were recorded from 350 nm to 650 nm using an excitation wavelength at 300–350 nm.

2.5.2 Fluorescence titration

The stock solution of **L6** in DMSO (5 mM, 2 μL) was diluted with Milli-Q water (990 μL) in a 1-mL quartz cuvette. Designated volumes (1.0–10.0 μL) of the Cd²⁺ stock solution (1.0 mM) in Milli-Q water was added into the sensor solution. The final volumes were adjusted to 1.000 mL by adding Milli-Q water. The emission spectra of all solutions were recorded from 350 nm to 650 nm at ambient temperature using an excitation wavelength at 300 nm.

2.5.3 Masking reagent

The Stock solution of **L6** in DMSO (5 mM, 2 μL) and designated amount of various masking reagents (DPA, TPA, and EDTA) were diluted with 200 μL of 0.200 M Tris HCl buffer (pH = 7) in a 1-mL quartz cuvette. The stock solution of metal ion (Cd²⁺ or Zn²⁺) in Milli-Q water (5 mM, 2 μL) was added to the solution. The final volumes were adjusted to 1.000 mL by adding Milli-Q water. The emission spectra of all solutions were recorded from 350 nm to 650 nm at ambient temperature using an excitation wavelength at 300 nm.

2.5.4 Limit of detection (LOD)

In fluorescent sensing, limit of detection (LOD) is the lowest concentration of analyte in a sample that is required to produce a signal greater than three times the standard deviation of the blank sample. But the value is not necessarily quantitated as an exact value. The limit of detection is obtained by plotting of fluorescent intensity against concentration of Cd²⁺ (M) at low concentration. The line of best fit was created according to the data plot giving a slope (m) and y-intercept (c). The limit of detection was calculated from following equation:

$$\text{LOD} = \frac{I_0 + 3\text{SD} - c}{M}$$

Where LOD is the limit of detection (M),

I_0 is the fluorescent intensity of blank,

SD is the standard deviation of fluorescent intensity of the sensor,

m is the slope of the line of best fit, and

c is the y-intercept of the line of best fit.

2.5.5 Cell culture and fluorescent imaging

The HeLa cell line (JCRB No. JCRB9004) were purchased from JCRB cell bank and cultured in Eagle's Minimum Essential Medium (EMEM) supplemented with 10 % heat-inactivated FBS, 100 units/mL of penicillin, and 100 $\mu\text{g}/\text{mL}$ of streptomycin at 37 $^{\circ}\text{C}$ in a humidified atmosphere of 5% $\text{CO}_2/95$ % air. After cells were cultured in 8-well chambered slide for at least one day, the cells in 400 μL EMEM were treated with 4 μL of 100 μM **L6** in DMSO (final concentration: 1 μM **L6**, 1% DMSO in EMEM) and incubated for 30 min at 37 $^{\circ}\text{C}$. The treated cells were washed with 0.1 M PBS (3 \times 200 μL) to remove remaining **L6**. Then, EMEM was added, followed by 2 μL of 2, 20, 200 and 2000 μM $\text{Cd}(\text{NO}_3)_2$ solution (final concentration: 0.01, 0.1, 1.0 and 10 μM) and incubated for 30 min at 37 $^{\circ}\text{C}$ and then washed with 0.1 M PBS pH 7.4 (3 \times 200 μL) to remove the extracellular Cd^{2+} . The samples were treated with 4% paraformaldehyde solution for 10 min at 37 $^{\circ}\text{C}$. The solutions were slowly removed from the chambers. Then, the chamber's wall was removed. contrast agent (moviol) was carefully dropped on the slide (1–2 drops for each well). The slide was covered with cover slide. The fluorescence images of the cells were taken by Olympus FluoView FV1000 confocal microscope using the excitation wavelength at 350 nm and detection wavelength at 465 nm.

The images were converted into TIF file by Olympus FluoroView Ver.4.2 software. Then the brightness of images was uniformly adjusted by Adobe Photoshop and the gray scale was evaluated by ImageJ software. The brightness was obtained from all pixels within the size of circle centered at the nucleus center of each cell. The brightness values were averaged from the values in the range of 25–75 percentiles.

2.6 Ligand and metal ion binding study

2.6.1 Job's plot

Designated volume of sensing compound stock solution (5.0 mM, 0–6.0 μL) and Cd^{2+} or Zn^{2+} stock solution (1.0 mM, 0–30 μL) were diluted with Milli-Q water in 1-mL Quartz cuvette. The mole ratio between sensing compound and metal ion are 0:1, 1:3, 1:2, 1:1, 2:1 3:1, and 1:0. The final volumes were adjusted to 1.000 mL by adding Milli-Q water. The absorption spectra of the solution were recorded from 190 nm to 350 nm at ambient temperature. Graph of corrected absorbance at absorption maximum (λ_{max}) were plotted against mole fraction of the sensing compound and metal ion. The maximum or minimum of absorbance corresponds to the stoichiometric of the sensing compound and metal ion.

2.6.2 Association constant (K_a)

The association constant or binding constant was obtained by UV-vis absorption titration followed by curve-fitting. The stock solution of the sensing ligand in DMSO (5 mM, 6 μL) was diluted with Milli-Q water (994 μL) in a 1-mL quartz cuvette. Designated volumes (1.0–20 μL) of the $\text{Cd}^{2+}/\text{Zn}^{2+}$ stock solution (1.0–5.0 mM) was added to the solution until the absorbance reach saturation. The absorption spectra of the solution were recorded from 190 nm to 350 nm at ambient temperature. For curve fitting, the absorbance at 1–3 wavelengths were selected and plotted against concentration of Cd^{2+} or Zn^{2+} . The curve of best fit was created according to the data plot from following equation by Nelder-mead method with starting K_a value of 100:

$$A = \epsilon_L[L] + \epsilon_{LM}[LM]$$

Where the absorbance of free metal ion is negligible, and [L] and [LM] are the concentrations of the sensing ligand and its metal ion complex which obtained from following equations:

$$[L] = \frac{\left([L_0] - [M_0] - \frac{1}{K_a}\right) + \sqrt{\left([L_0] - [M_0] - \frac{1}{K_a}\right)^2 + 4 \frac{[L_0]}{K_a}}}{2}$$

$$[LM] = \frac{\left(\frac{1}{k_a} + [L_0] + [M_0]\right) - \sqrt{\left(\frac{1}{k_a} + [L_0] + [M_0]\right)^2 - 4[L_0][M_0]}}{2}$$

Where $[L_0]$ is the starting concentration of sensing compound (M),

$[M_0]$ is the starting concentration of sensing compound-metal ion complex (M),

k_a is the association constant,

ϵ_L is the molar absorptivity of the sensing compound,

ϵ_{LM} is the molar absorptivity of the complex of sensing compound and metal ion, and

A is the absorbance.

2.6.3 X-ray crystallography

A suitable good-quality single crystal of the complex (**L1·Cd**, **L5·Cd**, and **L6·Cd**) was mounted to the end of a hollow glass fibre. Data were measured using ω and ϕ scans and using Mo-K α radiation ($\lambda = 0.71073 \text{ \AA}$). The total number of runs and images was based on the strategy calculation from the program APEX3 and unit cell indexing was refined using SAINT [57]. Data reduction was performed using SAINT and SADABS were used for absorption correction [57]. The structure was solved with the ShelXT structure solution program using combined Patterson and dual-space recycling methods [58]. The structure was refined by least squares using ShelXL [59]. All non-hydrogen atoms were refined anisotropically. All hydrogen atoms of the organic ligands were generated geometrically. For **L1·Cd**, the N-H hydrogen atom was in a difference-Fourier map and refined freely. Positional disorder in the nitrate anion was restrained through the PART, RIGU, and ISOR commands, and the structure was refined as an inversion twin. Whole molecule disorder of the complex **L5·Cd** and the dianionic $[\text{Cd}(\text{NO}_3)_4]^{2-}$ species in **L6·Cd** was modeled via the PART, RIGU, and ISOR commands where necessary. Attempts to locate and model the highly disordered solvent molecules in these complexes were unsuccessful. Thus, the SQUEEZE subroutine of the PLATON software suite was applied to remove the scattering from the highly disordered solvent molecules, and solvent-free diffraction intensities were

produced [60]. Crystallographic data have been deposited with the Cambridge Crystallography Data Centre with deposition numbers CCDC no. 1979176 (**L1·Cd**), 1979177 (**L5·Cd**) and 1979178 (**L6·Cd**).



CHAPTER 3

RESULTS AND DISCUSSION

The results of the development of picolyl-quinoline conjugated ligands as fluorescent sensors for metal ions are discussed in order of the 6 followings key sections: synthesis, photophysical properties, fluorescence sensing properties, association constants, Cd²⁺ detection, structures of Cd²⁺ complexes.

3.1 Synthesis

The synthesis and structure characterization by ¹H NMR of all synthesized ligands (**L1**–**L17**) are presented and discussed in this section. The numeric characterization data such as ¹H NMR, ¹³C NMR and HRMS are presented in the experimental section and their spectra are provided in the appendices. The results are presented and discussed in subsection of successive groups of ligands based on their synthesis similarity and sequence.

3.1.1 Synthesis of **L1** and **L5**

L1 and **L5** were synthesized from 8-aminoquinoline as shown in Figure 3.1. The synthesis was achieved by refluxing 8-aminoquinoline with 1.0 equivalent of picolyl chloride in the presence of KI as a catalyst for 3 hours. The reaction gave **L1** as the major product and **L5** along with the unreacted starting 8-aminoquinoline. **L1** was isolated in 56% yield by column chromatography. For the synthesis of **L5**, the same reaction was applied using 4.0 equivalents of picolyl chloride and the reaction was performed at the room temperature for 4 days. This reaction condition afforded **L5** as the major product along with **L1** and the tripicolylammonium salt. The salt was eliminated by aqueous extraction and **L5** was isolated in 42% yield by column chromatography.

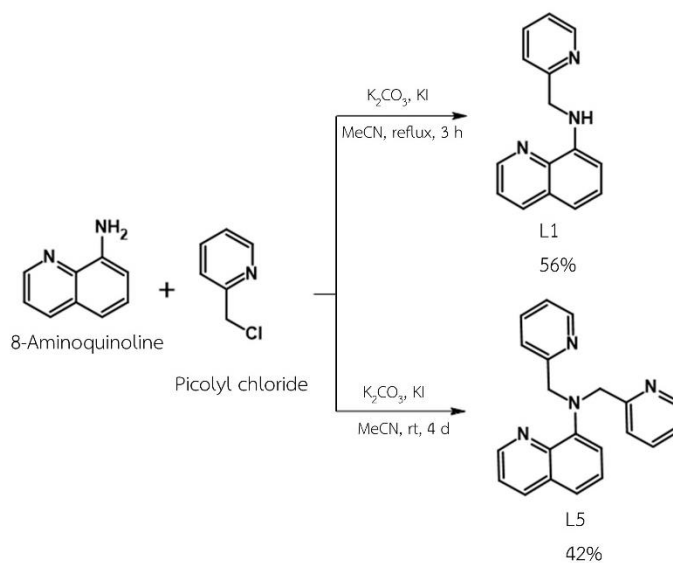


Figure 3.1 Synthesis of **L1** and **L5**.

The 1H NMR spectra of **L1** and **L5** in $CDCl_3$ are shown in Figure 3.2. The signals could be assigned to all the protons in the corresponding structures. The methylene proton (H_f) signals of **L1** and **L5** appeared at 4.68 ppm and 4.92 ppm, respectively. These peaks confirmed the successful picolylation to 8-aminoquinoline. The integration ratio of the signal of the methylene protons to the signal of the quinoline protons (e.g., H_a or H_c) were 2:1 and 4:1 corresponding to the mono- and dipicolylation in **L1** and **L5**, respectively. Moreover, the absence of N-H (H_g) proton signal in the spectrum of **L5** confirmed its tertiary amine structure.

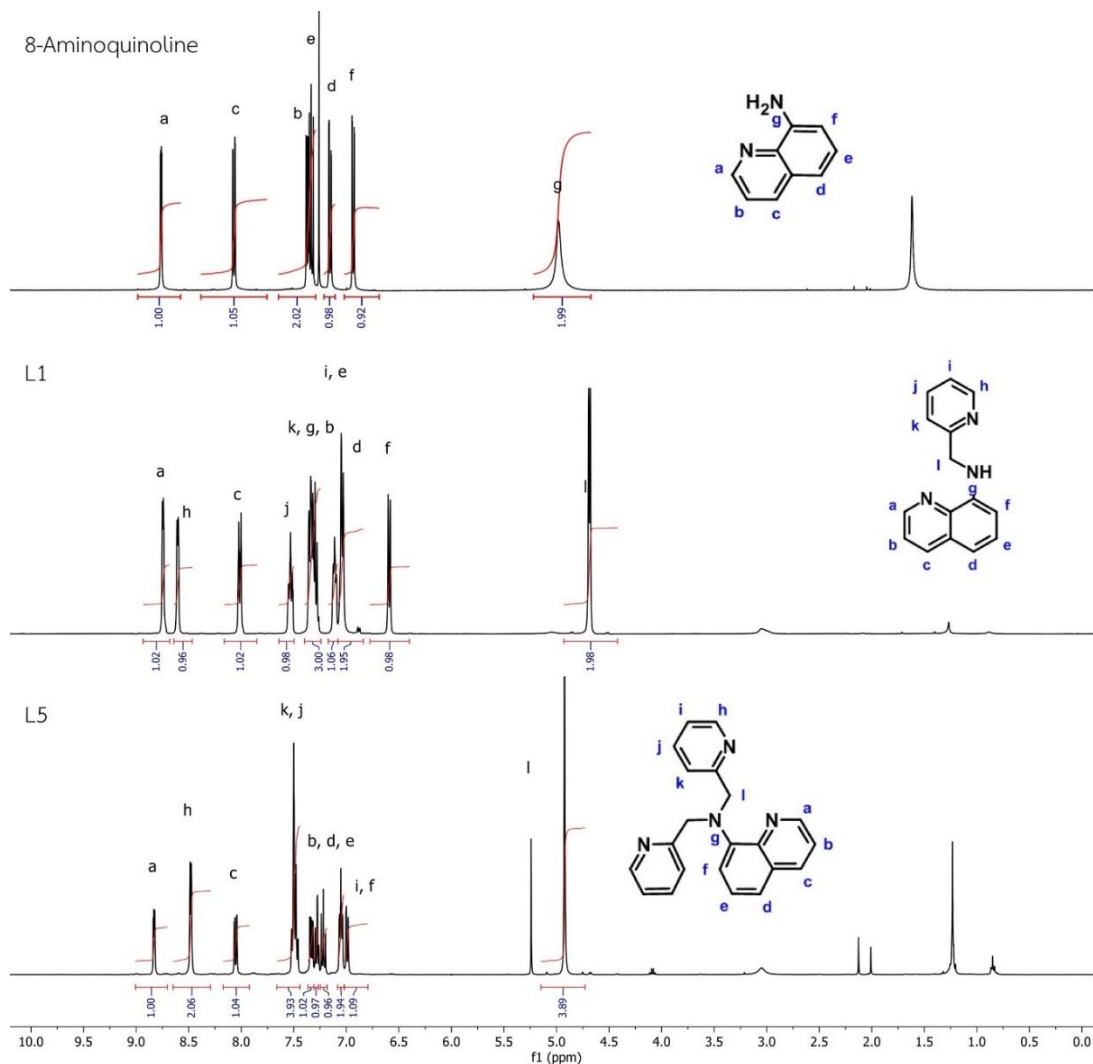


Figure 3.2 ^1H NMR spectra of 8-aminoquinoline, **L1**, and **L5** in CDCl_3 .

3.1.2 Synthesis of **L2** and **L6**

L2 was synthesized from a modified Bucherer reaction as shown in Figure 3.3. The synthesis was achieved by heating of 8-hydroxyquinoline and 0.54 equivalent of ethylenediamine in the presence of sodium metabisulfite at $115\text{ }^\circ\text{C}$ for 7 days in a sealed tube. The reaction gave **L2** along with the unreacted starting 8-hydroxyquinoline. An incomplete reaction come from the evaporation of the 8-hydroxyquinoline. **L2** was isolated in 53% by crystallization in methanol. For **L6**, the synthesis was achieved by stirring the **L2** with picolyl chloride in the presence of KI as a catalyst at room temperature for 4 days. The reaction gave **L6** in 68% yield after column chromatography.

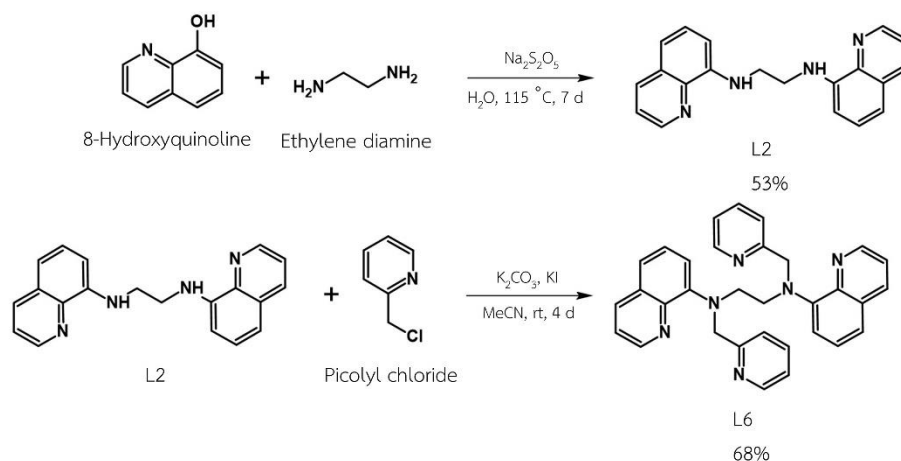


Figure 3.3 Synthesis of **L2** and **L6**.

The ^1H NMR spectra of **L2** and **L6** in $(\text{CD}_3)_2\text{SO}$ are shown in Figure 3.4. The signals could be assigned to all protons in the corresponding structures. For the spectrum of **L2**, the signals of quinoline protons ($\text{H}_{\text{a-f}}$) appeared at aromatic region (6.5–9.0 ppm). The integration ratio of the signal of the methylene protons (H_{h}) to the signal of the quinoline protons (e.g., H_{a} or H_{c}) were 2:1 confirming that 2 quinolyl group was successfully attached at each end of the ethylene diamine. For **L6**, the additional characteristic peak of the methylene protons (H_{m}) of the picolyl groups appeared as a singlet peak at 4.45 ppm. The integration ratio of the signal of these methylene protons (H_{m}) to the signal of the quinoline protons (e.g., H_{a} or H_{c}) was 2:1 confirming the presence of two picolyl groups in the structure.

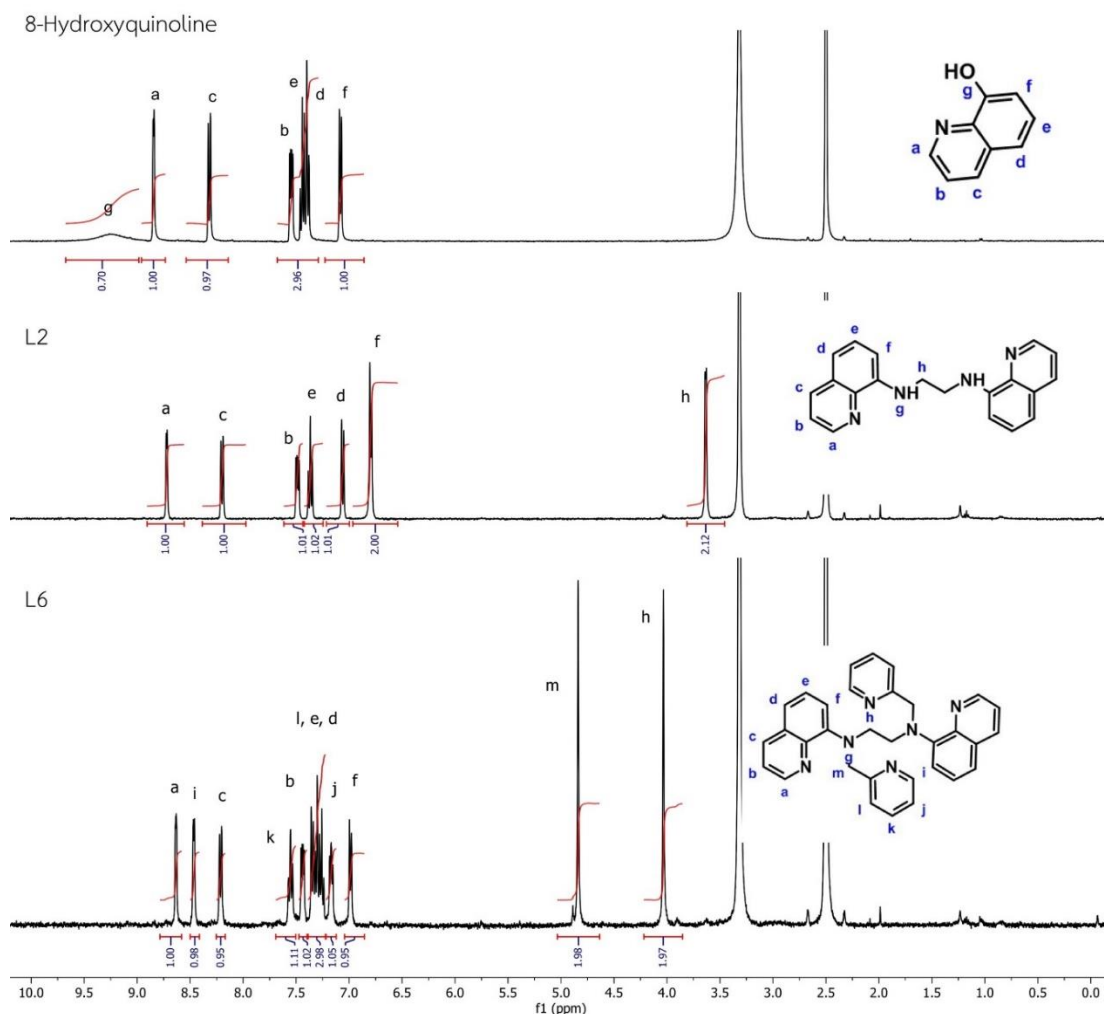


Figure 3.4 ^1H NMR spectra of 8-hydroxyquinoline, **L2** and **L6** in $(\text{CD}_3)_2\text{SO}$.

3.1.3 Synthesis of **L3**, **L4** and **L7**

L3 was synthesized from a modified Bucherer reaction as shown in Figure 3.5. The synthesis was achieved by heating 8-Hydroxyquinoline and diethylene triamine in the presence of sodium metabisulfite at $115\text{ }^\circ\text{C}$ for 9 days. The reaction gave **L3** as the major product with some unreacted starting 8-hydroxyquinoline. **L3** was isolated in 40% yield by column chromatography. For synthesis of **L4**, the synthesis was achieved by heating **L3** and picolyl chloride in the presence of KI at $80\text{ }^\circ\text{C}$ for 3 hours. **L4** was isolated in 84% yield by column chromatography. The high yield of **L4** suggests that **L3** is a reasonably good nucleophile.

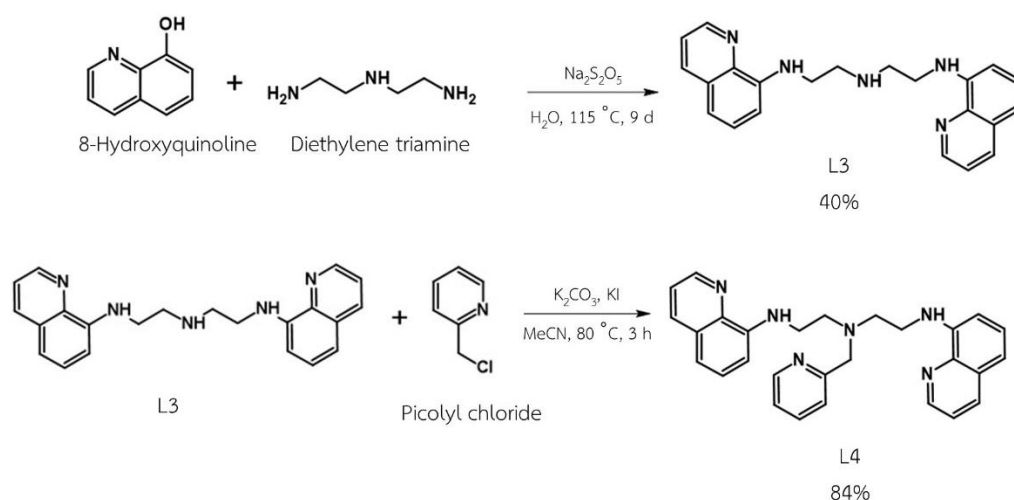


Figure 3.5 Synthesis of **L3** and **L4**.

The ^1H NMR spectra of **L3** and **L4** in $(\text{CD}_3)_2\text{SO}$ are shown in Figure 3.6. The signals could be assigned to all protons in the corresponding structures. For the spectrum of **L3**, the signals of quinoline protons ($\text{H}_{\text{a-g}}$) appeared at aromatic region (6.5–9.0 ppm). The integration ratio of the signal of the methylene protons (H_{h} or H_{i}) to the signal of the quinoline protons (e.g., H_{a} or H_{c}) were 2:1 confirming that 2 quinolyl group was successfully attached at each end of the ethylene diamine. For **L4**, the additional characteristic peak of the methylene protons (H_{n}) of the picolyl groups appeared as a singlet peak at 3.83 ppm. The integration ratio of the signal of the methylene protons (H_{n}) to the signal of the quinoline protons (e.g., H_{a} or H_{c}) was 1:1. Moreover the spectrum of **L4** showed only one set of quinoline protons confirming the symmetrical structure derived from the monopicolylation at the middle N atom of diethylenetriamine.

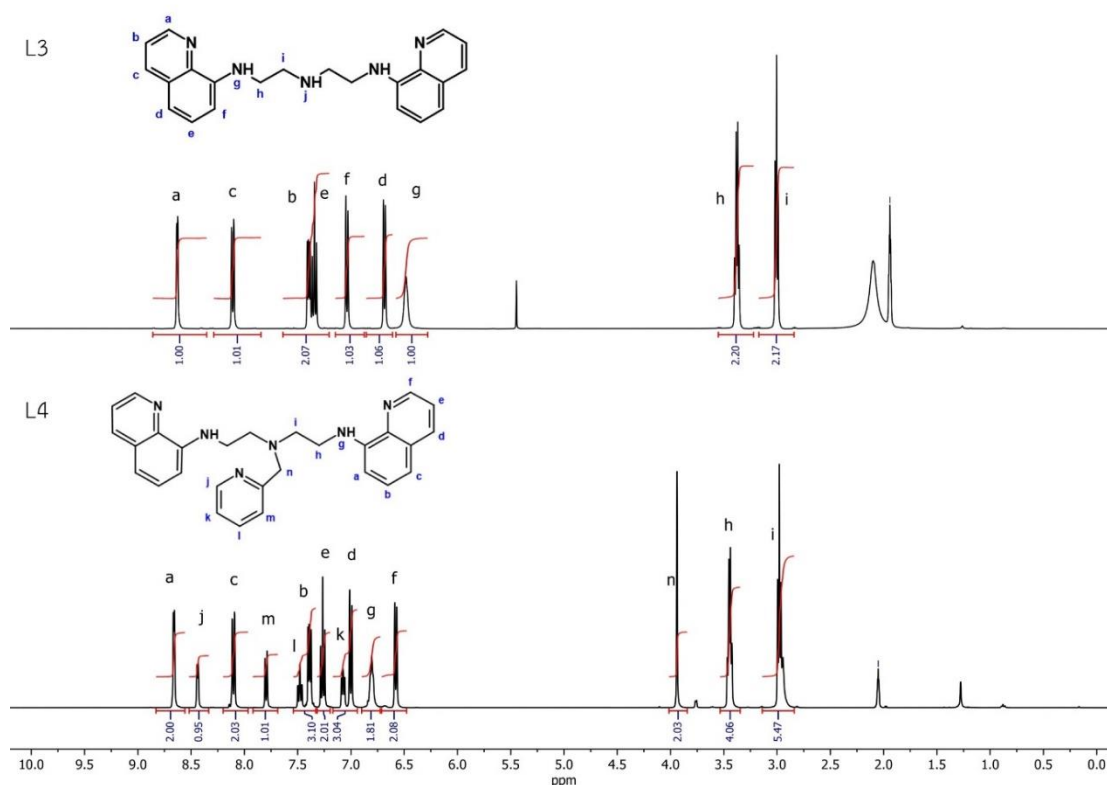


Figure 3.6 ^1H NMR spectra of **L3** in CD_3CN , and **L4** in $(\text{CD}_3)_2\text{CO}$.

L7 was synthesized from the same reaction used in the synthesis of **L4** but performed at room temperature using 4.0 equivalents of picolyl chloride (Figure 3.7). The reaction gave **L7** along with partial and over substituted products. **L7** was thus isolated in only 14% yield by column chromatography.

The ^1H NMR spectra of **L7** in CD_3CN , are shown in Figure 3.7. All signals could be assigned to all protons in the corresponding structure. In comparison with **L4**, the spectrum of **L7** showed one additional set of picolyl group in aromatic region (6.5–9.0 ppm). The integration ratio of the signal of the picolyl protons (H_p) to the signal of the quinoline protons (e.g., H_a or H_c) was 1:1 confirming the presence of two additional picolyl groups on the other 2 N atoms.

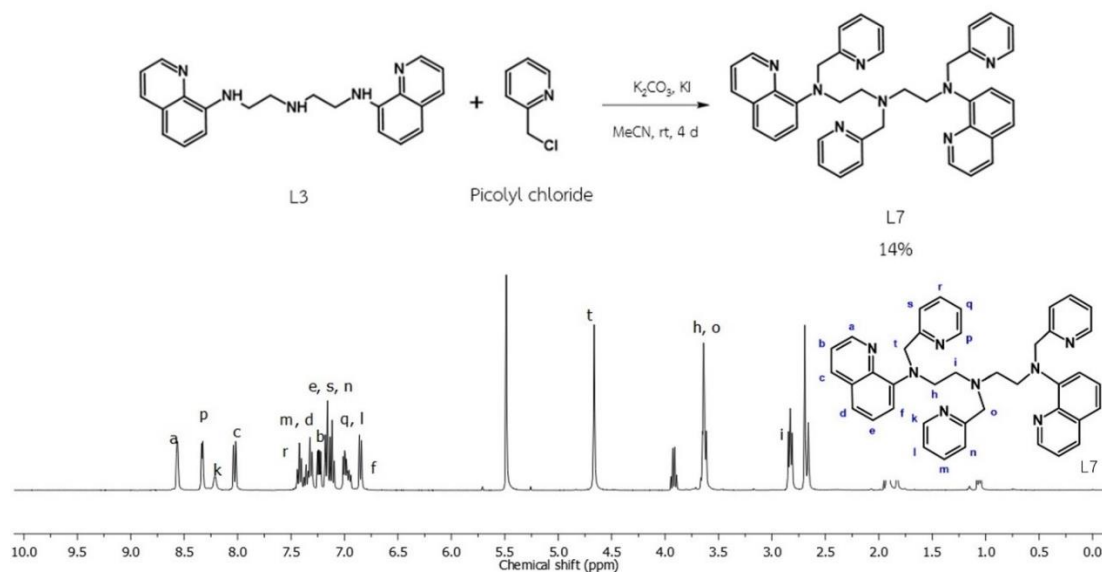


Figure 3.7 Synthesis of **L7** and 1H NMR spectrum of **L7** in CD_3CN .

3.1.4 Synthesis of **L8**

L8 was synthesized from **QNNQ** which was obtained from a modified Bucherer reaction between 8-hydroxyquinoline and triethylenetetramine as shown in Figure 3.8. The Bucherer reaction gave **QNNQ** along with the unreacted starting 8-hydroxyquinoline. **QNNQ** was isolated in 40% yield by column chromatography. The synthesis of **L8** was then achieved by stirring **QNNQ** with picolyl chloride in the presence of KI at room temperature for 4 days. The reaction gave **L8** along with partial substitution, over substitution and some elimination products. **L8** was thus isolated in only 14% yield by column chromatography.

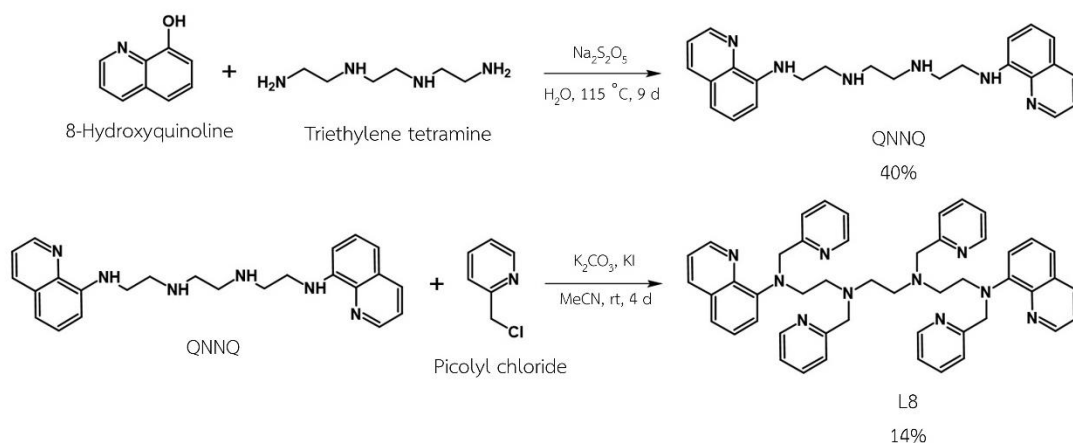


Figure 3.8 Synthesis of **L8**.

The ^1H NMR spectra of **QNNQ** and **L8** in $(\text{CD}_3)_2\text{CO}$ are shown in Figure 3.9. All signals could be assigned to all protons in the corresponding structures. For the spectrum of **QNNQ**, the signals of quinoline protons ($\text{H}_{\text{a-f}}$) appeared at aromatic region (6.5–9.0 ppm). The integration ratio of the signal of the methylene protons (H_{r}) to the signal of the quinoline protons (e.g., H_{a} or H_{c}) were 2:1 confirming that 2 quinolyl groups were successfully attached at both ends of the triethylenetetraamine. The characteristic ^1H NMR peaks of picolyl protons in **L8** appeared as 2 sets at 8.47 (H_{l}) and 8.37 ppm (H_{q}). The integration ratio of the signal of both picolyl protons (H_{l} and H_{q}) to the signal of the quinolyl protons (e.g., H_{a} or H_{c}) was 2:1 confirming the presence of 4 picolyl groups in the structure.

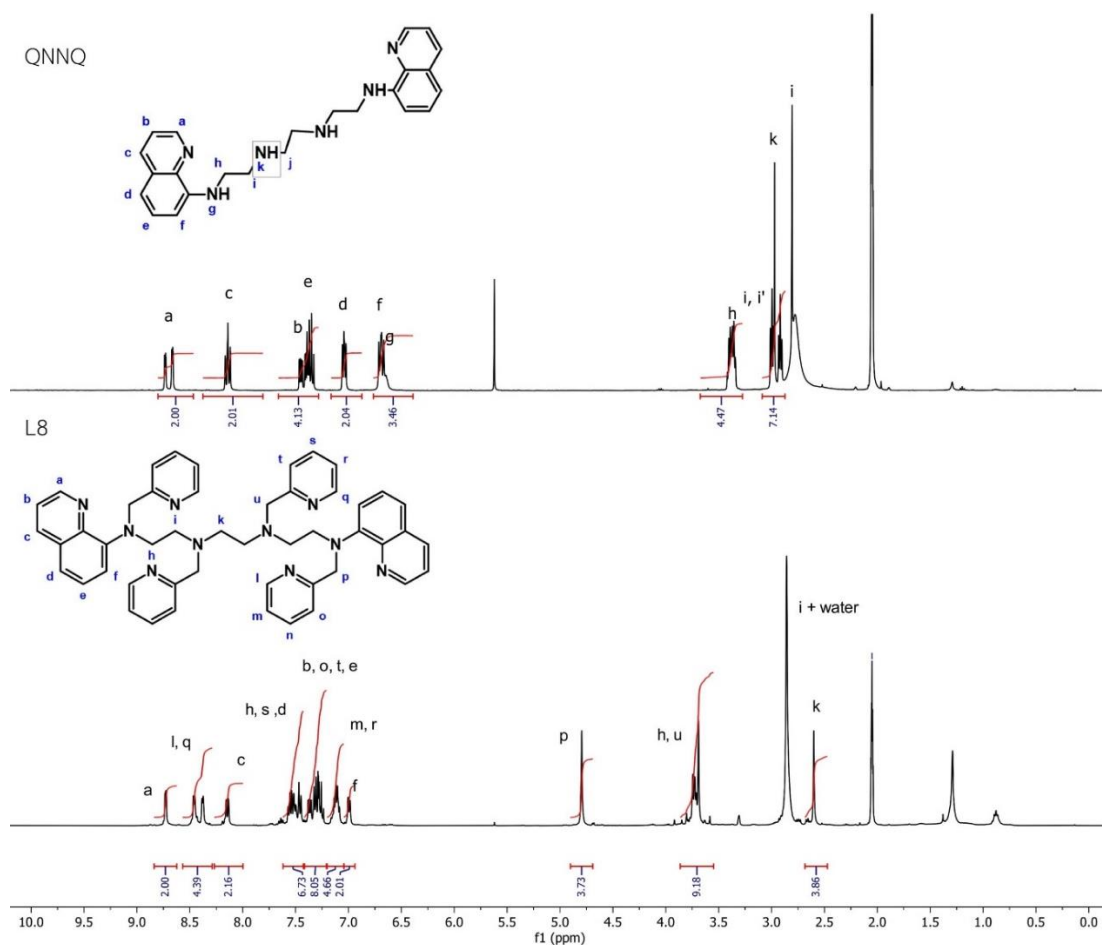


Figure 3.9 ^1H NMR spectra of **QNNQ** and **L8** in $(\text{CD}_3)_2\text{CO}$.

3.1.6 Synthesis of **L9**

L9 was synthesized from **3QN** which was obtained from a modified Bucherer reaction between 8-hydroxyquinoline, and tris(2-aminoethyl)amine as shown in Figure 3.10. The Bucherer reaction gave **3QN** along with the unreacted starting 8-hydroxyquinoline. **3QN** was isolated in 43% yield by crystallization in methanol. The synthesis of **L9** was then achieved by stirring **3QN** with picolyl chloride in the presence of KI at room temperature for 4 days. The reaction gave **L9** along with partial substitution, over substitution and some elimination products. **L9** was thus isolated in only 7% yield by column chromatography.

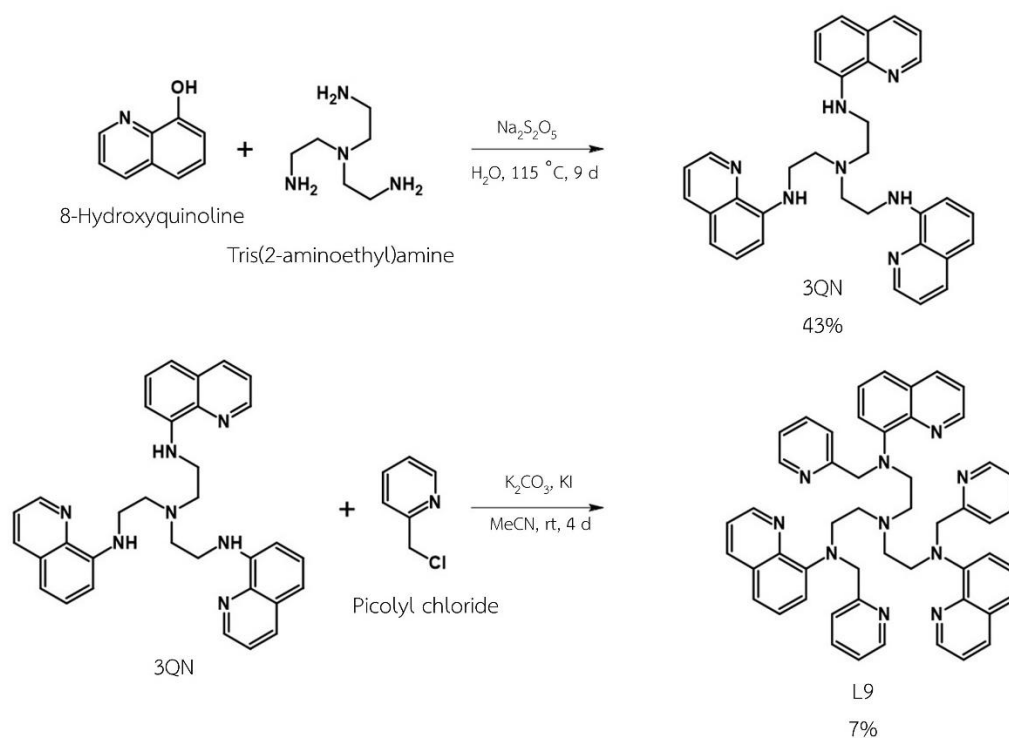


Figure 3.10 Synthesis of **L9**.

The ^1H NMR spectra of **3QN** in $(\text{CD}_3)_2\text{CO}$, and **L9** in $(\text{CD}_3)_2\text{SO}$ are shown in Figure 3.11. All signals could be assigned to all protons in the corresponding structures. For the spectrum of **3QN**, the signals of quinoline protons ($\text{H}_{\text{a-f}}$) appeared at aromatic region (6.5–9.0 ppm). The integration ratio of the signal of the methylene protons (H_{n}) to the signal of the quinolyl protons (e.g., H_{a} or H_{c}) were 2:1 confirming that 3 quinolyl groups were successfully attached at each end of the tris(2-aminoethyl)amine. For **L9**, the characteristic signals of picolyl protons appeared in 2 sets at 8.47 (H_{l}) and 8.37 ppm (H_{q}). The methylene protons (H_{n}) of the picolyl groups appeared as a singlet peak at 4.67 ppm with the 1:1 integration ratio of $\text{H}_{\text{n}}:\text{H}_{\text{a}}$ that confirmed the successful substitution of all three picolyl groups.

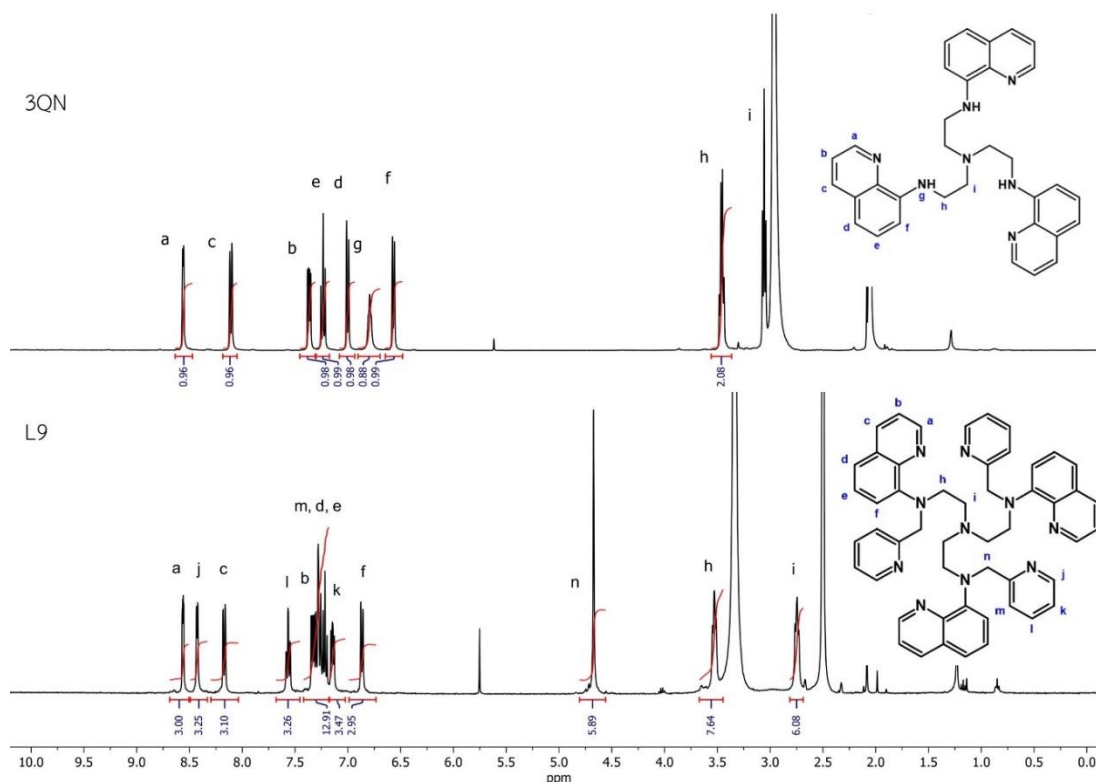


Figure 3.11 ¹H NMR spectra of **3QN** in (CD₃)₂CO, and **L9** in (CD₃)₂SO.

3.1.7 Synthesis of **L10**

L10 was synthesized from a modified Bucherer reaction as shown in Figure 3.12. The synthesis was achieved by heating 8-hydroxyquinoline and 1.0 equivalent of 8-aminoquinoline in the presence of sodium metabisulfite at 115 °C for 9 days in sealed tube. The reaction gave **L10** as a major product with some unreacted starting 8-Hydroxyquinoline and 8-Aminoquinoline. **L10** was isolated in 27% yield by crystallization in methanol.

The ¹H NMR spectrum of **L10** in (CD₃)₂SO are shown in Figure 3.12. The signals could be assigned to all protons in the corresponding structure. The signal of quinoline proton (H_{a-f}) appeared at aromatic region (7.0–9.0 ppm). The characteristic signal is the N-H (H_g) peak appeared in a very low field region at 11.75 ppm due to the intramolecular H-bond between N-H and N atom in the quinoline groups.

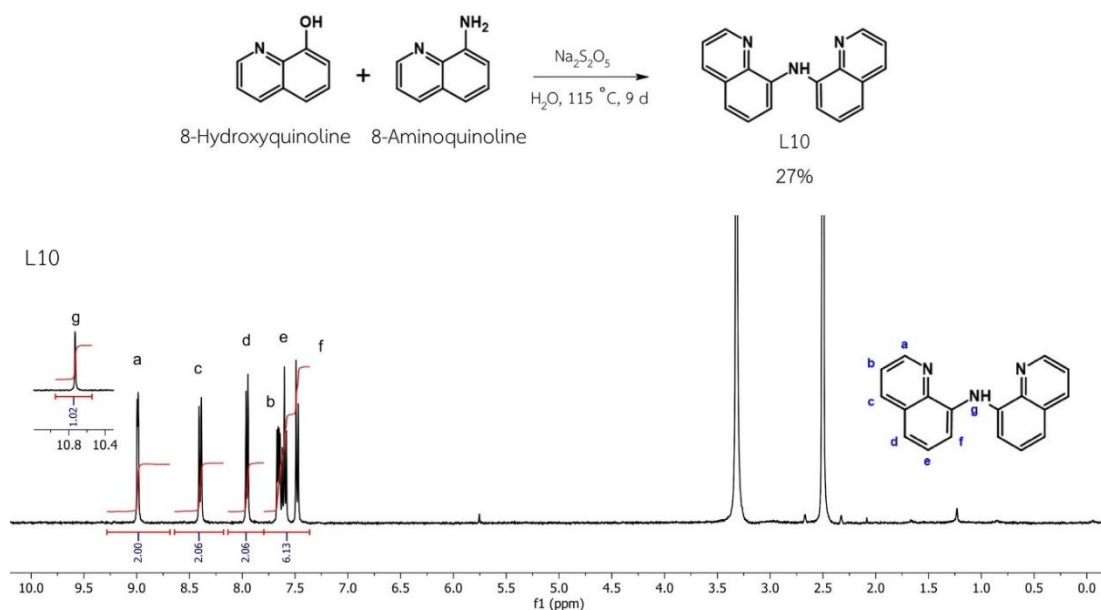


Figure 3.12 Synthesis of **L10** and ¹H NMR spectrum of **L10** in (CD₃)₂SO.

3.1.8 Synthesis of L11–L13

L11–L13 were synthesized from an Ullmann-type aryl-amination as shown in Figure 3.13. The syntheses were achieved by heating 8-bromoquinoline and corresponding amine in the presence of L-proline and CuI at 160 °C for 3 days. The reactions gave **L11–L13** as a major product in 71%, 42% and 10% yield after column chromatography. The 8-bromoquinoline precursor was synthesized from a condensation as shown in Figure 3.13. The synthesis was achieved by refluxing 2-bromoaniline and glycerol in concentrated sulfuric acid in the presence of ferrous sulfate and iodine. The reaction gave 8-bromoquinoline in 43% yield after column chromatography.

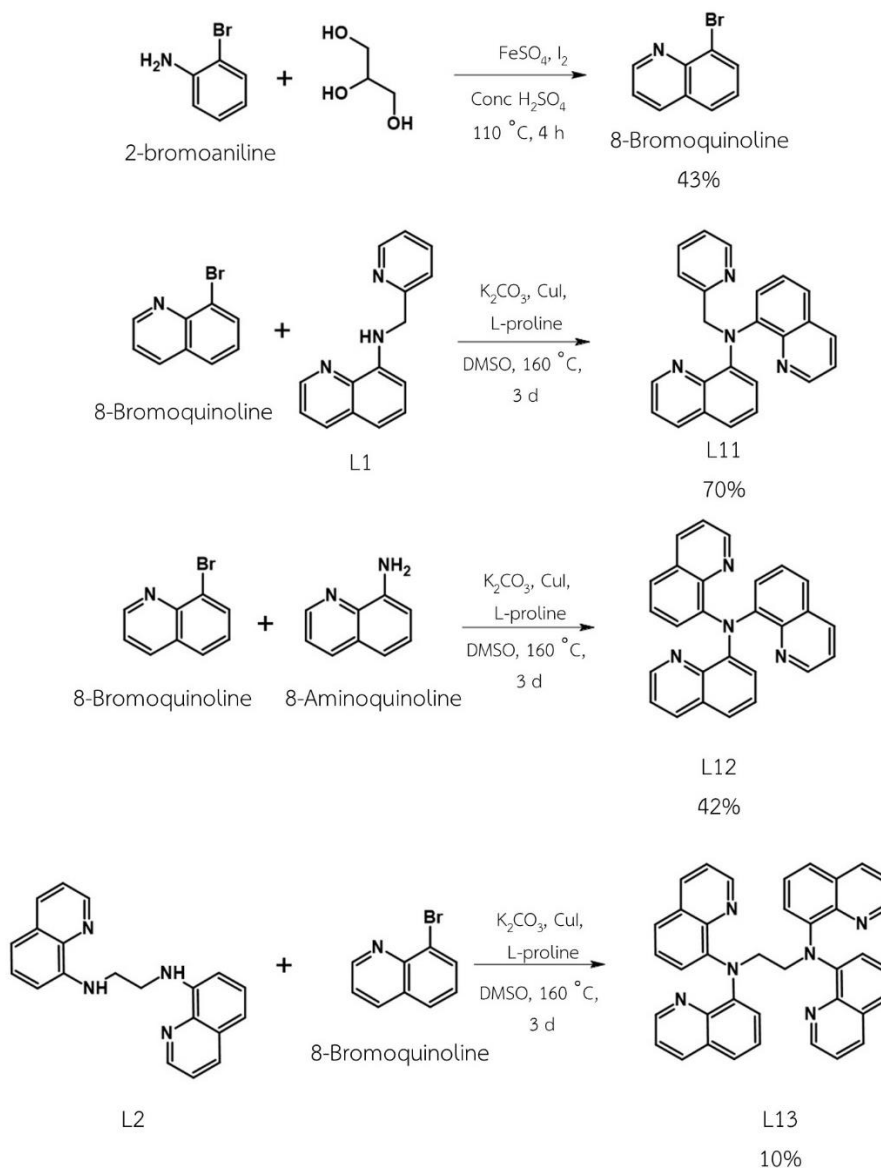


Figure 3.13 Synthesis of 8-bromoquinoline and **L11**–**L13**.

The ^1H NMR spectra of 8-bromoquinoline in CDCl_3 ; and **L11** and **L12** in $(\text{CD}_3)_2\text{SO}$ are shown in Figure 3.14. The signals could be assigned to all protons in the corresponding structures. For the spectrum of 8-bromoquinoline, the signal of quinoline proton (H_{a-f}) appeared at aromatic region (7.0–9.0 ppm) that confirmed the ring closure and aromatization of quinoline from 2-bromoaniline. For **L11**, the spectrum showed the integration ratio of quinolyl proton (e.g., H_a or H_c) to picolyl protons (e.g., H_h) of 2:1 assuring that the quinoline ring was successfully connected to

L1. For **L12**, the amino protons (H_g) disappeared indicating a formation of the tertiary amine. For **L13**, the integration ratio of the signal of the methylene protons (H_h) to the signal of the quinolyl protons (e.g., H_a or H_c) were 1:1 confirming that two quinolines were successfully incorporated into the ligand. Moreover, the disappearance of N-H peak (H_g) confirmed a formation of the tertiary amine.

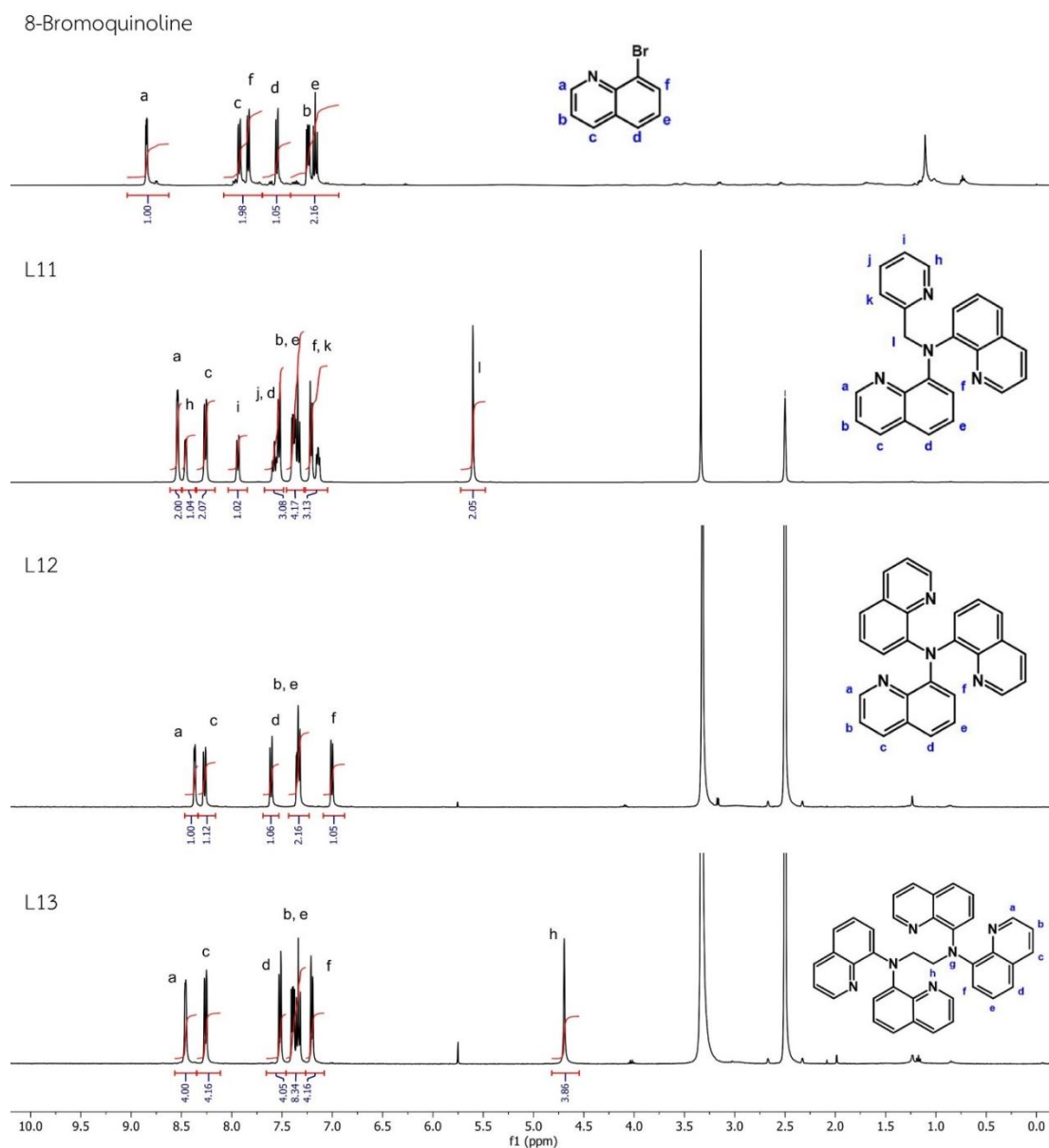


Figure 3.14 ^1H NMR spectra of 8-bromoquinoline in CDCl_3 ; and **L11**, **L12** and **L12** in $(\text{CD}_3)_2\text{SO}$.

3.1.9 Synthesis of L14–L17

L14–L17 were synthesized by Pawittra Chaibuth according to the Figure 3.15. The ^1H NMR spectra in Figure 3.16 confirm their structures and purities.

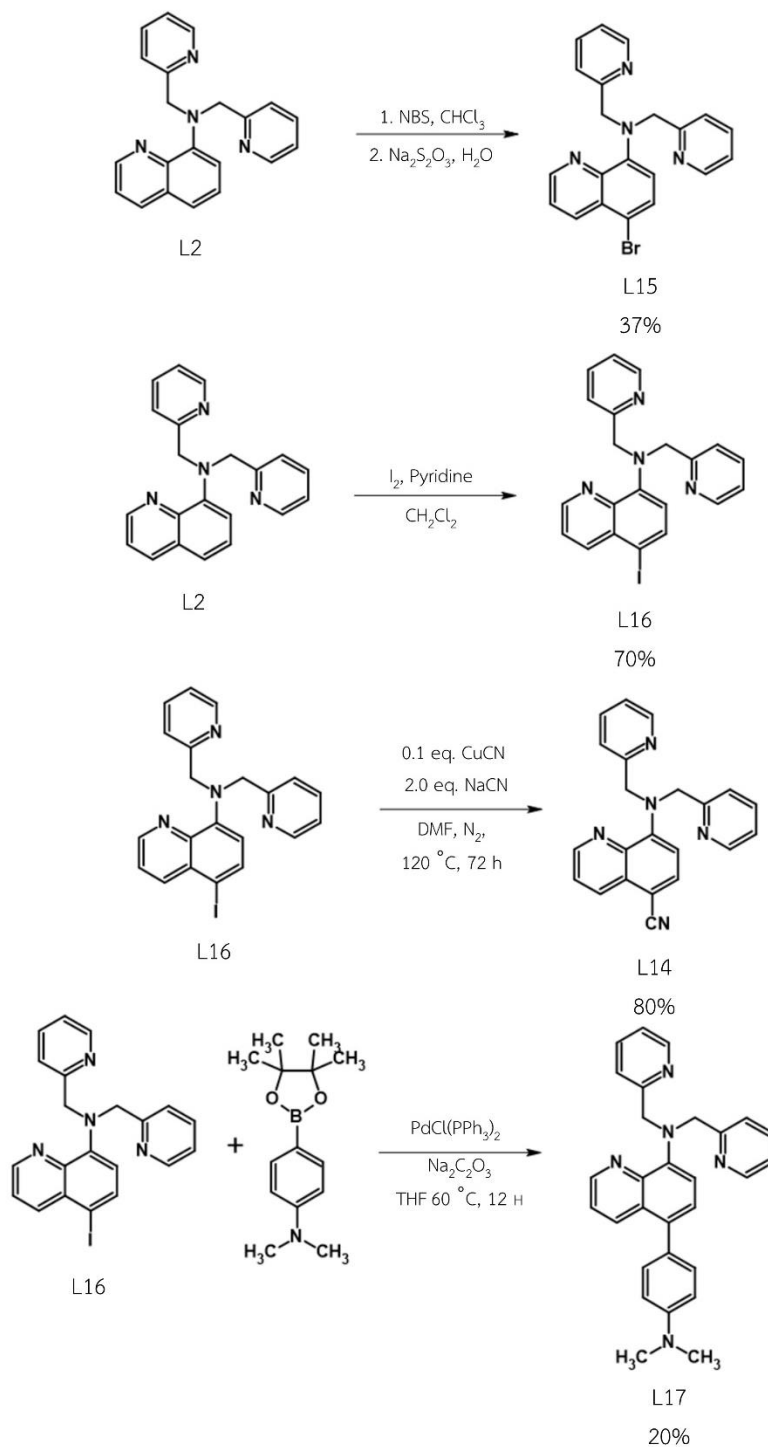
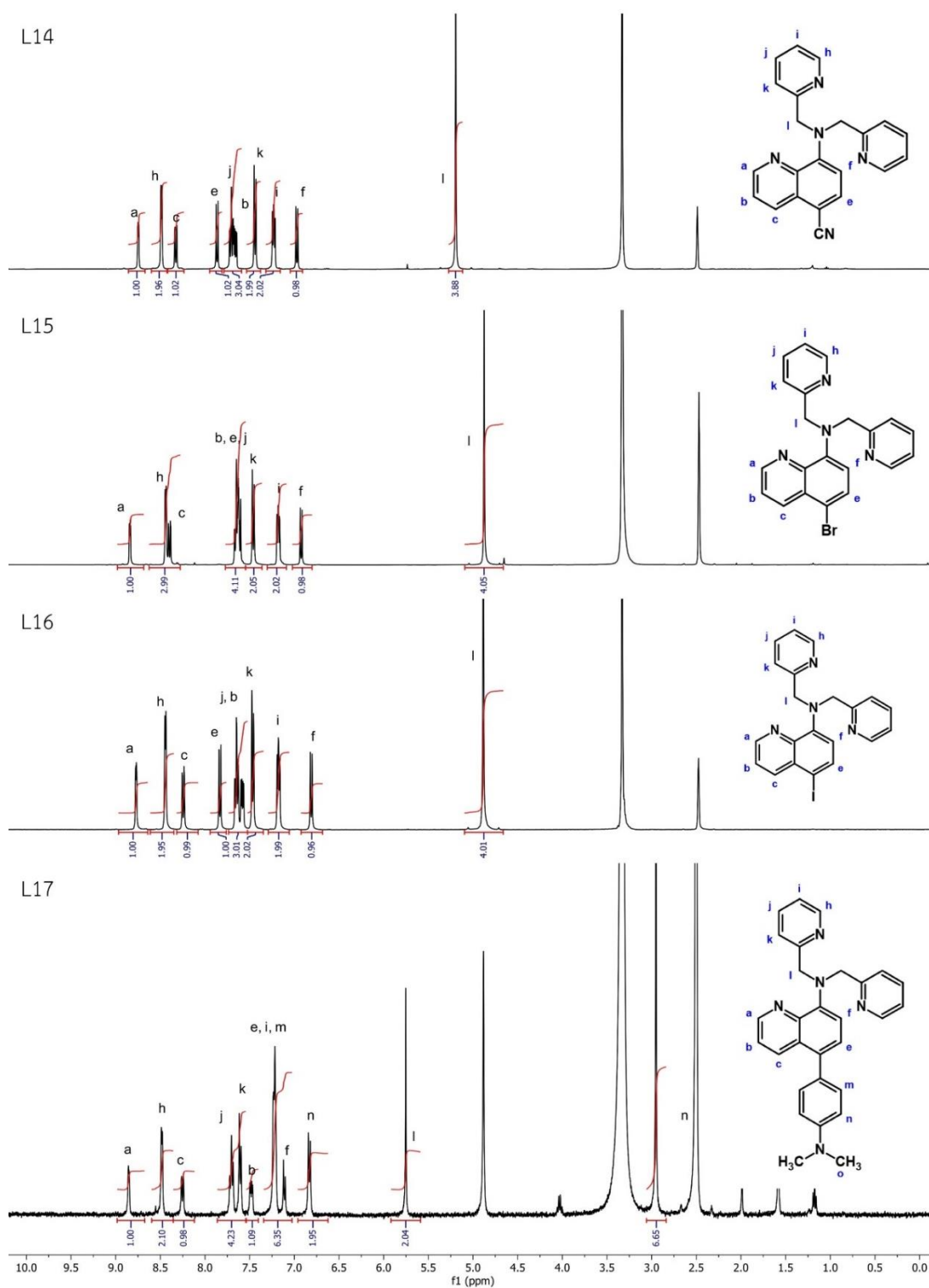


Figure 3.15 Synthesis of L14–L17.



3.2 Photophysical properties

The photophysical properties of all ligands including UV-vis absorptions, emissions and fluorescence quantum yields were studied in aqueous solutions of the ligands. The fluorescence quantum yields were studied by the relative method using quinin sulfate as the standard. The results are presented and discussed in the following successive order of **L1–L6**, **L7–L9**, **L10–L13** and **L14–L17**.

3.2.1 Photophysical properties of L1–L6

Figure 3.17 shows the molecular structures of **L1–L6** with their maximum absorption wavelengths (λ_{max}), maximum emission wavelengths (λ_{em}) and fluorescence quantum efficiencies (Φ) along with their absorption and emission spectra.



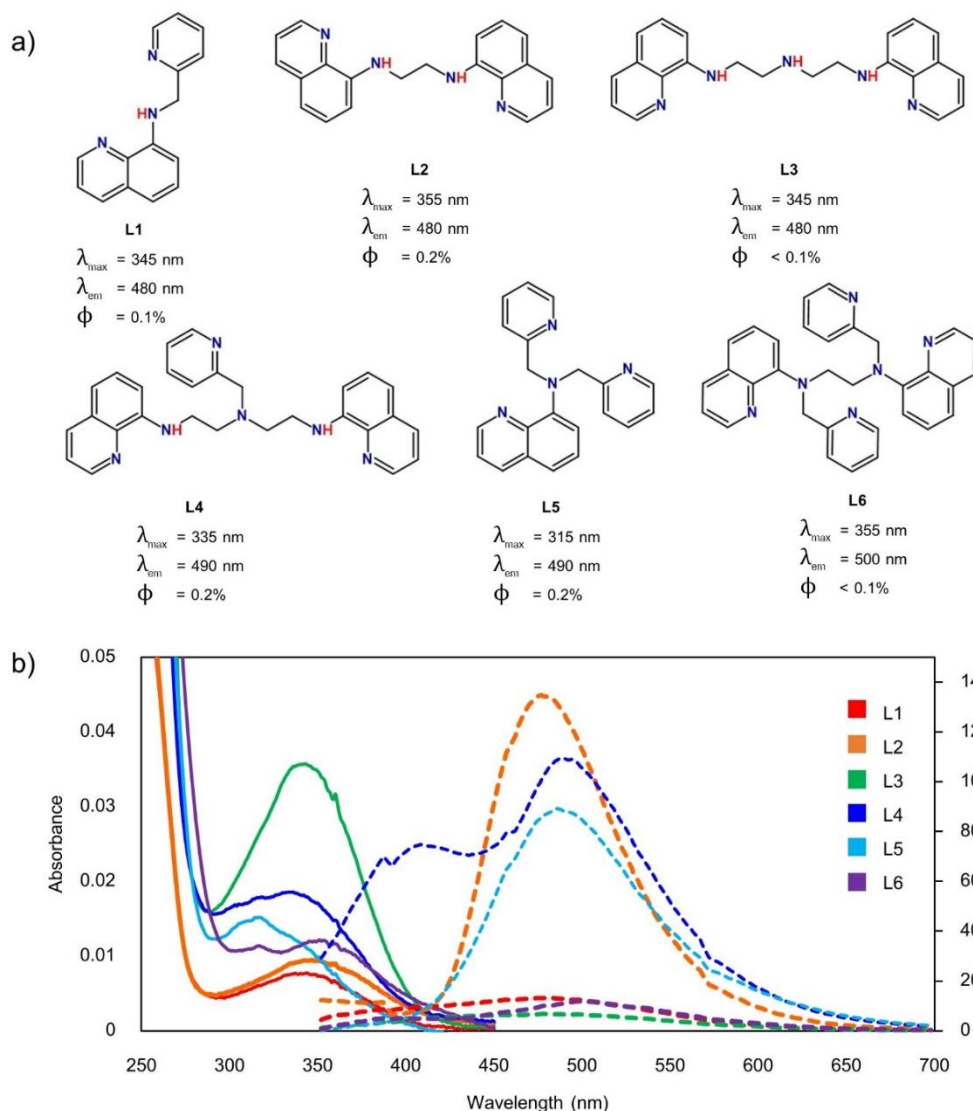


Figure 3.17 (a) Molecular structures of **L1–L6** with their key photophysical properties and (b) absorption (solid line) and emission (dash line) spectra excited at 300 nm. All ligands were in aqueous solution with $[L] = 30 \mu\text{M}$ for absorption and $[L] = 10 \mu\text{M}$ for emission.

In aqueous solution, each ligand showed two absorption bands with λ_{\max} around 250 nm and 315–350 nm (Figure 1b). The longer wavelength absorption corresponds to the $\pi\text{--}\pi^*$ transition of the amino quinoline moiety while the shorter wavelength one corresponds to the $\pi\text{--}\pi^*$ transition of both amino quinoline and picolyl moieties. Notably, **L5** has absorption of the amino quinoline at a slightly

shorter wavelength (315 nm) than the other ligands (350 nm). This may be due to a highly twisted conformation adopted by the bulkiness around the N atom limiting the electron delocalization from the lone pair electron on the amino N into the quinoline π -system. For **L6**, the absorption spectrum contains both bands at 315 and 350 nm which suggests the co-existence of the twisted and non-twisted conformations. The result may be due to that the ethylamino group in **L6** is less sterically crowded than the picolyl group in **L5**. For the emission spectra, most ligands showed a single emission peak around 480–500 nm, corresponding to the emission of quinoline rings, except **L4** which also had an additional peak at 400 nm which is likely to be the emission of the picolyl group. This result suggests that lower efficiency of the energy transfer from the picolyl groups to the quinoline ring due to the longer distance between picolyl and quinoline groups in **L4**. The fluorescence quantum efficiencies of all ligands were lower than 0.2% attributed to the nonradiative PET process from the nitrogen lone pair electrons to the quinoline rings and some geometrical relaxation.

3.2.2 Photophysical properties of L7–L9

Figure 3.18 shows the molecular structures of **L7–L9** with their maximum absorption wavelengths (λ_{max}), maximum emission wavelengths (λ_{em}) and fluorescence quantum efficiencies (ϕ) along with their absorption and emission spectra.

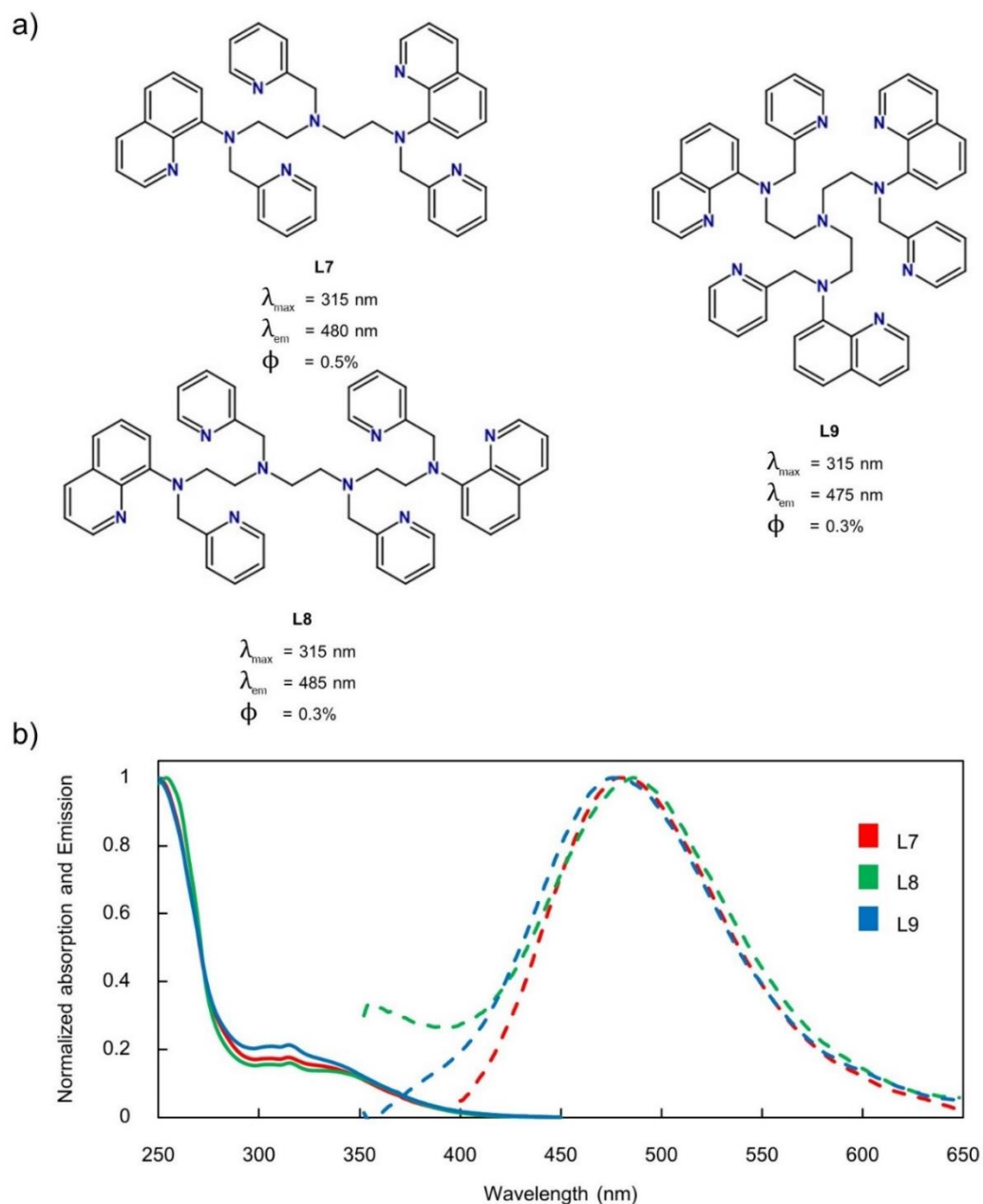


Figure 3.18 (a) Molecular structures of **L7–L9** with their key photophysical properties and (b) absorption (solid line) and emission (dash line) spectra excited at 300 nm. All ligands were in aqueous solution with $[L] = 30 \mu\text{M}$ for absorption and $[L] = 10 \mu\text{M}$ for emission.

Since the structures of **L7–L9** are homologous to **L6**, their λ_{max} , λ_{em} and ϕ are similar to those of **L6**. The compounds have broad absorption bands with two maxima at 315 and 350 nm. For the emission, **L7–L9** emitted the fluorescence with

the maximum intensity at 480 nm with low fluorescence quantum efficiency of 0.3–0.5% that signified the strong involvement of the PET and geometrical relaxation.

3.2.3 Photophysical properties of L10–L13

Figure 3.19 shows the molecular structures of **L10–L13** with their maximum absorption wavelengths (λ_{\max}), maximum emission wavelengths (λ_{em}) and fluorescence quantum efficiencies (ϕ) along with their absorption and emission spectra.

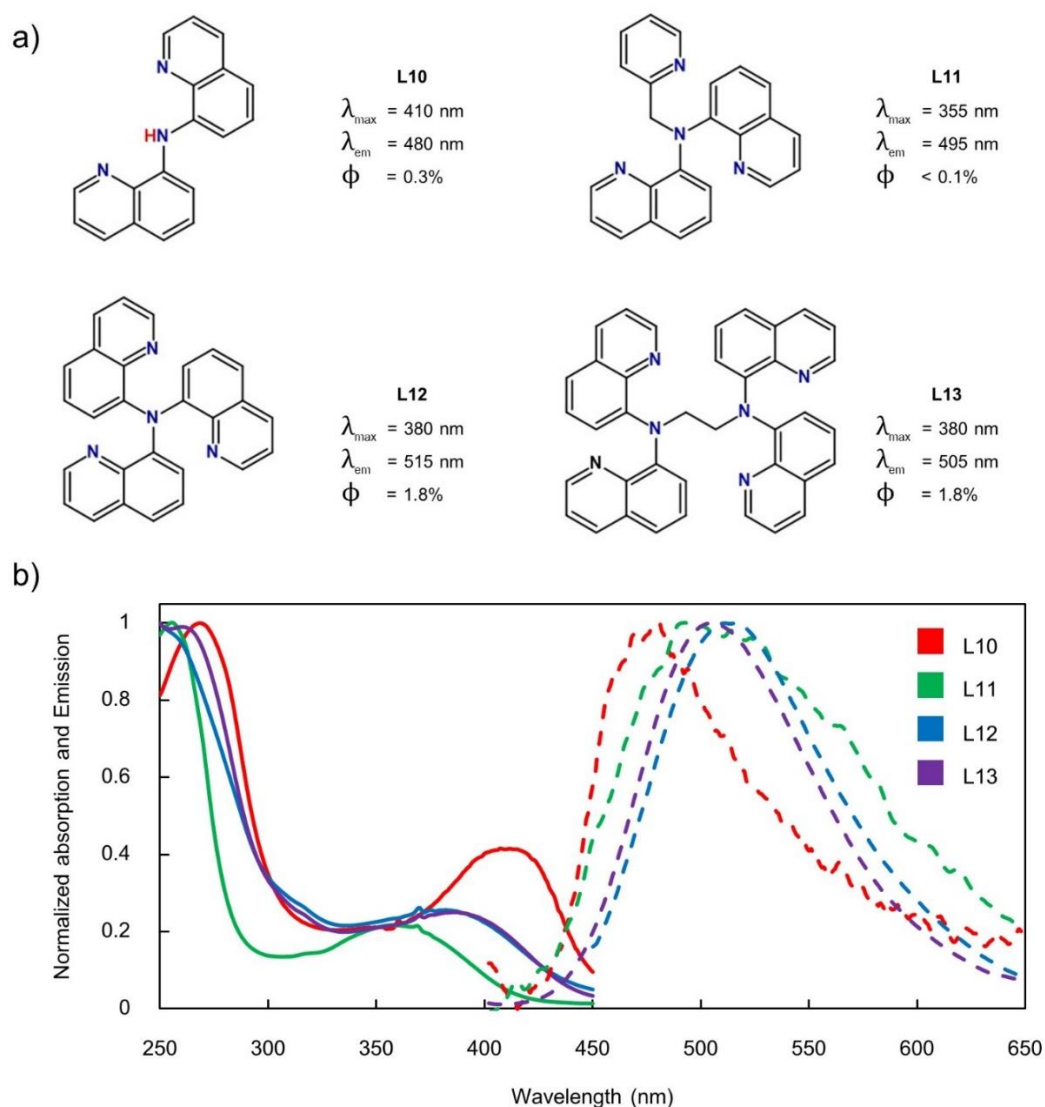


Figure 3.19 (a) Molecular structures of **L10–L13** with their key photophysical properties and (b) absorption (solid line) and emission (dash line) spectra excited at

300 nm. All ligands were in aqueous solution with $[L] = 30 \mu\text{M}$ for absorption and $[L] = 10 \mu\text{M}$ for emission.

The structure of **L10** is similar to **L1** of which picolyl group is replaced with the quinoline group. **L10** has an absorption band with λ_{max} at 420 nm corresponding to the $\pi\text{-}\pi^*$ transition of the quinoline group. A large red-shift (≈ 65 nm) in comparison with **L1** was due the extended π -conjugation of the two quinoline rings with the lone pair electrons of N. Compound **L11** and **L12** are tertiary amines similar to **L5**. They have absorption bands with λ_{max} at 355 nm and 380 nm, respectively. The shorter λ_{max} of **L11** and **L12** in comparison with **L10** suggest that their quinoline rings are less likely to be not in the same plane. The longer absorption wavelength of **L12** in comparison with **L11** is also due to the replacement of the picolyl group with the quinoline ring. **L13** showed absorption band relatively similar to **L12**. For the emission, the compounds showed the maximum fluorescence in the range of 480-515 nm belonging to the emission of quinoline group with low fluorescence quantum efficiency (0.3–1.8%) due to the PET and geometrical relaxation.

3.2.4 Photophysical properties of L14–L17

Figure 3.20 shows the molecular structures of **L14–L17** with their maximum absorption wavelengths (λ_{max}), maximum emission wavelengths (λ_{em}) and fluorescence quantum efficiencies (ϕ) along with their absorption and emission spectra.

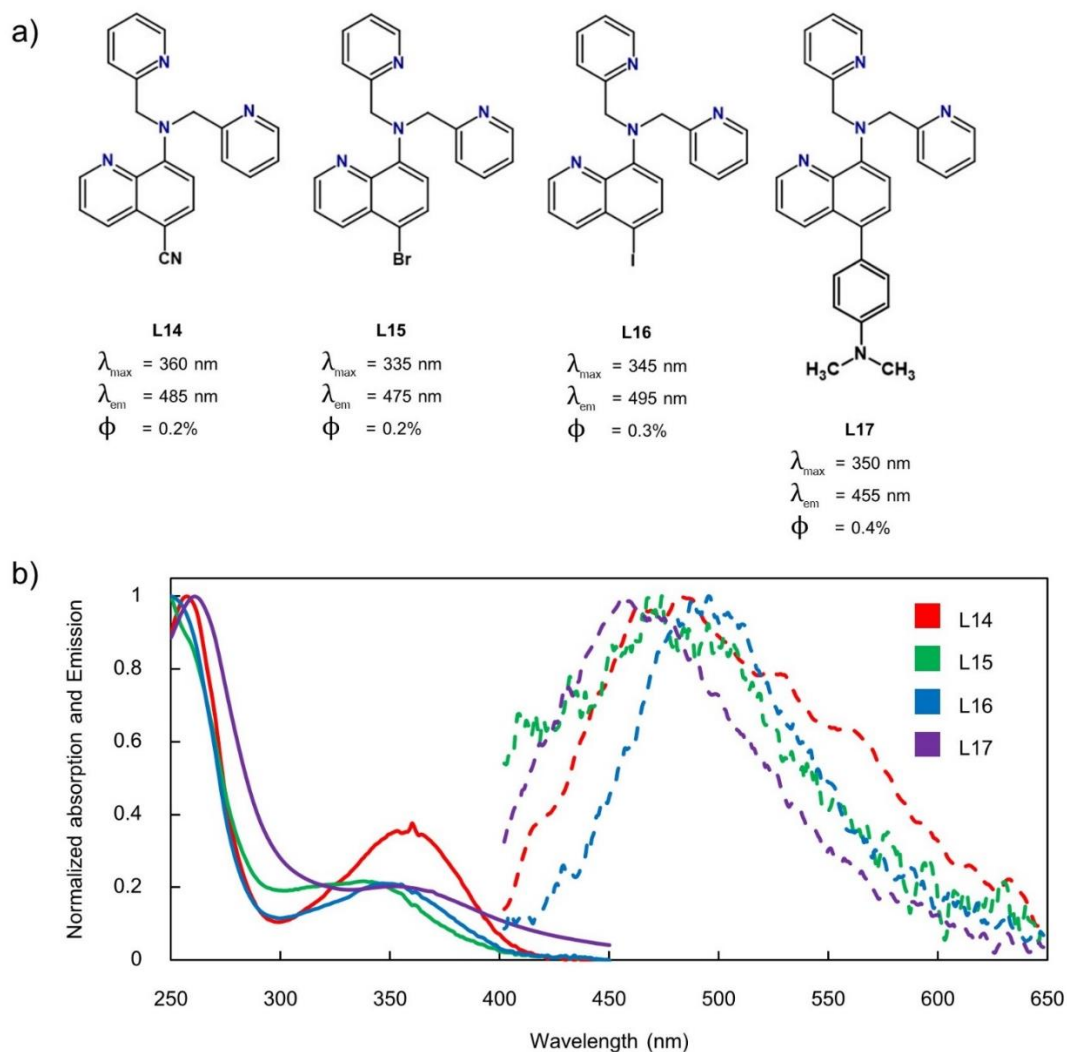


Figure 3.20 (a) Molecular structures of **L14–L17** with their key photophysical properties and (b) absorption (solid line) and emission (dash line) spectra excited at 300 nm. All ligands were in aqueous solution with $[L] = 30 \mu\text{M}$ for absorption and $[L] = 10 \mu\text{M}$ for emission.

Compound **L14–L17** are derivatives of **L5** with different substituents on the quinoline ring at C5. They have similar absorption bands with the λ_{max} in the range of 335–360 nm corresponding to the $\pi\text{--}\pi^*$ transition of the quinoline group. **L14** has the longest λ_{max} due to the push-pull effect between C5–C \equiv N and C8–NR₂ via the π -conjugated system of the quinoline ring. Interestingly, **L17** which has longer π -conjugated extension exhibits shorter λ_{max} than that of **L14** due to the non-planarity

of the biphenyl moiety. The broader absorption band of **L17** may be caused by the rotation of the dimethylaminophenyl group. For emission, all compounds gave similarly low fluorescence quantum efficiency (0.3–0.4%), due to the PET and geometrical relaxation, with broad emission band in the range of 400–700 nm.

3.3 Fluorescence sensing properties

The absorption spectra of all ligands (**L1–L17**) in the presence of Cd^{2+} or Zn^{2+} were recorded in aqueous solution. Upon the addition to aqueous solutions of the metal ions, a new absorption band at a shorter wavelength (300 nm) gradually increased at the expense of the original absorption band of the ligand with the increasing Cd^{2+} or Zn^{2+} added (Figure A53–A56). The blue-shift generally occurred when the donating lone pair electrons involving in the π -conjugation system of the fluorophore bind to a positively charged metal ion due to the greater stabilization of the HOMO than the LUMO. The fluorescence sensing and selectivity of all ligands were screened with various metal ions i.e., Li^+ , Na^+ , K^+ , Ca^{2+} , Ba^{2+} , Mg^{2+} , Fe^{2+} , Co^{2+} , Ni^{2+} , Cu^{2+} , Zn^{2+} , Cd^{2+} , Ag^+ , Hg^{2+} , Pb^{2+} , Fe^{3+} , Cr^{3+} and Al^{3+} in aqueous solution. The solutions were excited at their Cd-complex maximum absorption (around 300–390 nm). The results are presented and discussed in successive series of **L1–L6**, **L7–L9**, **L10–L13** and **L14–L17** as follows.

3.3.1 Fluorescence sensing properties of L1–L6

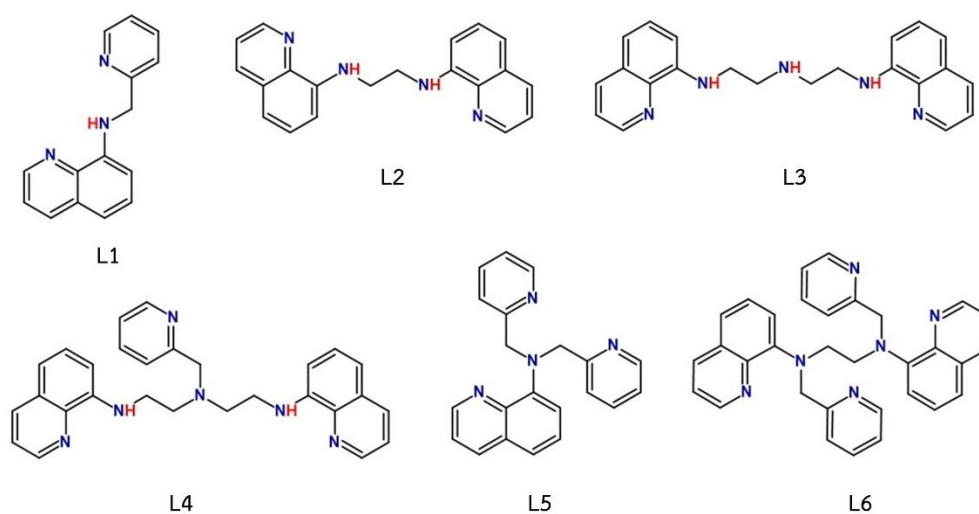


Figure 3.21 Chemical structure of L1–L6.

The emission spectra of L1–L6 in the absence and presence of various metal ions in Tris HCl buffer solution pH 7 are shown in Figure 3.22. The enhancement of the emission at 480–520 nm by either Zn^{2+} or Cd^{2+} confirmed the selective binding of the ligands with these two metal ions. The observed chelation enhancement fluorescence (CHEF) suggested that the complexation could reduce the nonradiative PET and geometrical relaxation processes. The complexes of Zn^{2+} of L1–L4 showed red-shifted emission with slight increases in the relative fluorescence enhancement (I/I_0) (Figure 3.23). The binding of Zn^{2+} to these ligands generally increases the amino proton acidity that in turn facilitates the deprotonation. The intermolecular excited state proton transfer (ESPT) between the amino proton of the complexes to the solvent (H_2O) can somewhat modulate the fluorescence enhancement and cause emission red shift in the Zn^{2+} complexes. On the other hand, red shift of the emission was observed for the complex of Cd^{2+} with L2–L4 but not with L1. These results suggest that the ESPT process in Cd complex requires the ligands with higher denticity.

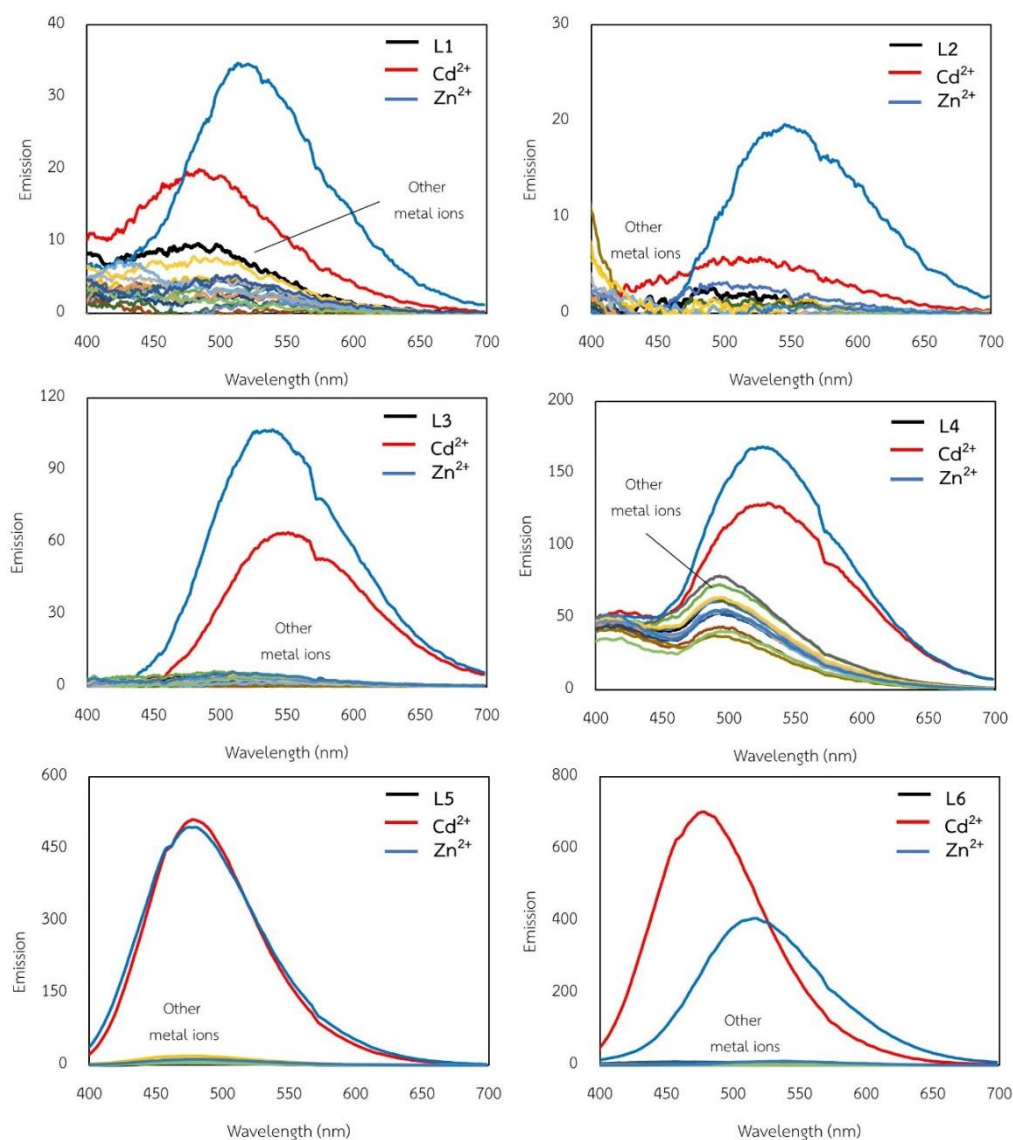


Figure 3.22 Fluorescence spectra of **L1–L6** (10 μM) tested with various metal ions (10 μM) in Tris HCl buffer solution pH 7.

L5 and **L6**, which have no amino proton, showed dramatically increase in I/I_0 over up to 125 times upon binding with Cd^{2+} and Zn^{2+} (Figure 3.23). The results confirmed that ESPT played a significant role in modulating the fluorescence enhancement of the complexes. Moreover, no red shift of the emission of Cd^{2+} and Zn^{2+} complexes was observed except for the **L6·Zn** complex. This complex gave an emission peak at 520 nm with lower fluorescence quantum efficiency. It is important to note that **L6** has 6 coordinating atoms with rather rigid and preorganized structure

for chelation. If all 6 coordinating atoms of **L6** bind with the rather small Zn^{2+} cation, there will be no room for Zn^{2+} to coordinate with counterions. Consequently, the complex will be positive charge that its excited state may undergo significant relaxation via ligand/counterion exchange.

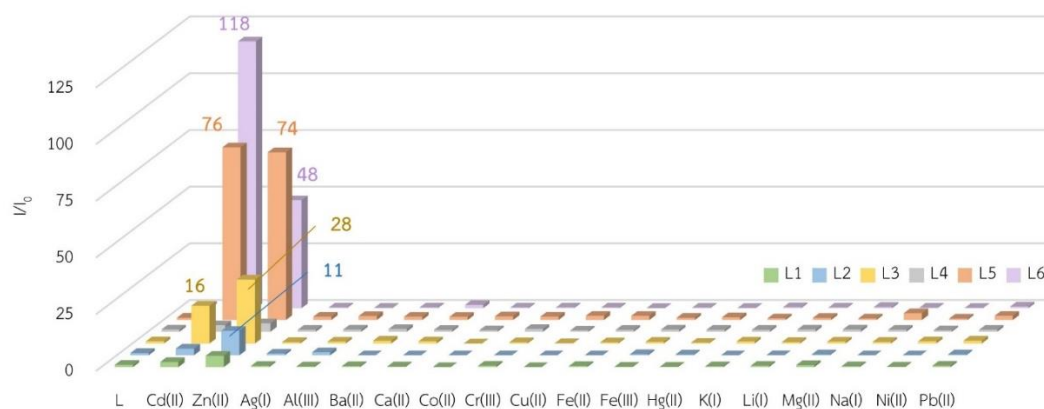


Figure 3.23 Relative intensity of **L1–L6** (10 μM) in the presence of various metal ion (10 μM).

3.3.2 Fluorescence sensing properties of L7–L9

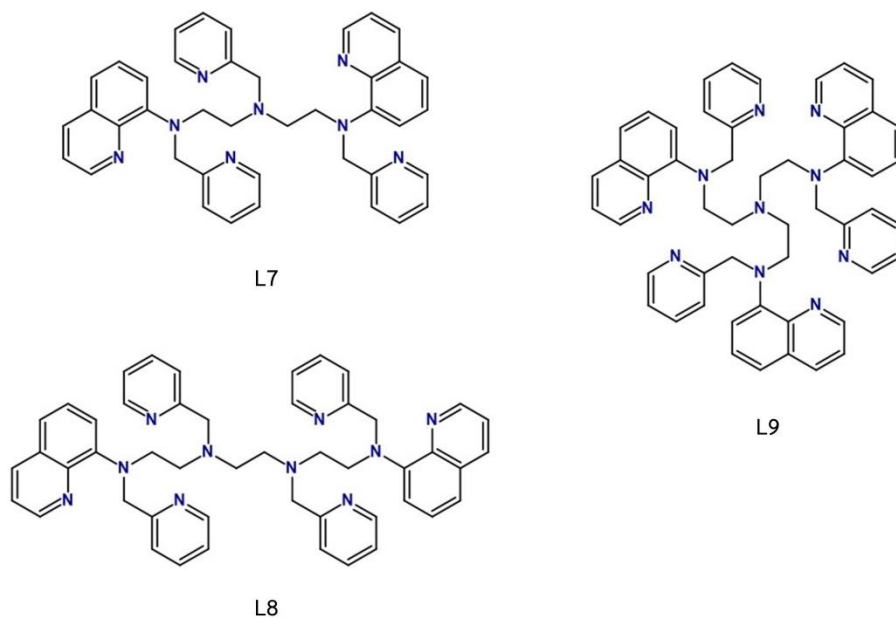


Figure 3.24 Chemical structure of **L7–L9**.

According to the results of **L1–L6**, it showed that the ligands without amino proton showed high relative fluorescence enhancement upon addition of Cd^{2+} and Zn^{2+} because of the absence of ESPT process. Moreover, the higher number of N-coordinating atoms show higher selectivity toward Cd^{2+} . Consequently, **L7–L9** having 8–10 N-coordinating atoms without amino proton were synthesized to study the fluorescence selectivity and sensitivity. The emission spectra of **L7–L9** in the absence and presence of various metal ions in Tris HCl buffer solution pH 7 are shown in Figure 3.25. In aqueous solution, all ligands (**L7–L9**) showed selective fluorescence enhancement at 480 nm upon addition of either Cd^{2+} or Zn^{2+} . Again, the enhancements are due to the restriction of PET and geometrical relaxation process. Addition of Cd^{2+} to the solution of **L7–L9** dramatically increase the fluorescence emission intensity up to 59 times, while Zn^{2+} gave lower I/I_0 (2–19 times) (Figure 3.26). However, the selectivity and sensitivity of **L7–L9** for Cd^{2+} detection are lower than those of **L6**. These results suggest that not all of the N coordinating atoms of **L7–L9** bind to a single Cd^{2+} cation due to steric hindrance of these large ligands and need of counterion binding for charge balance.

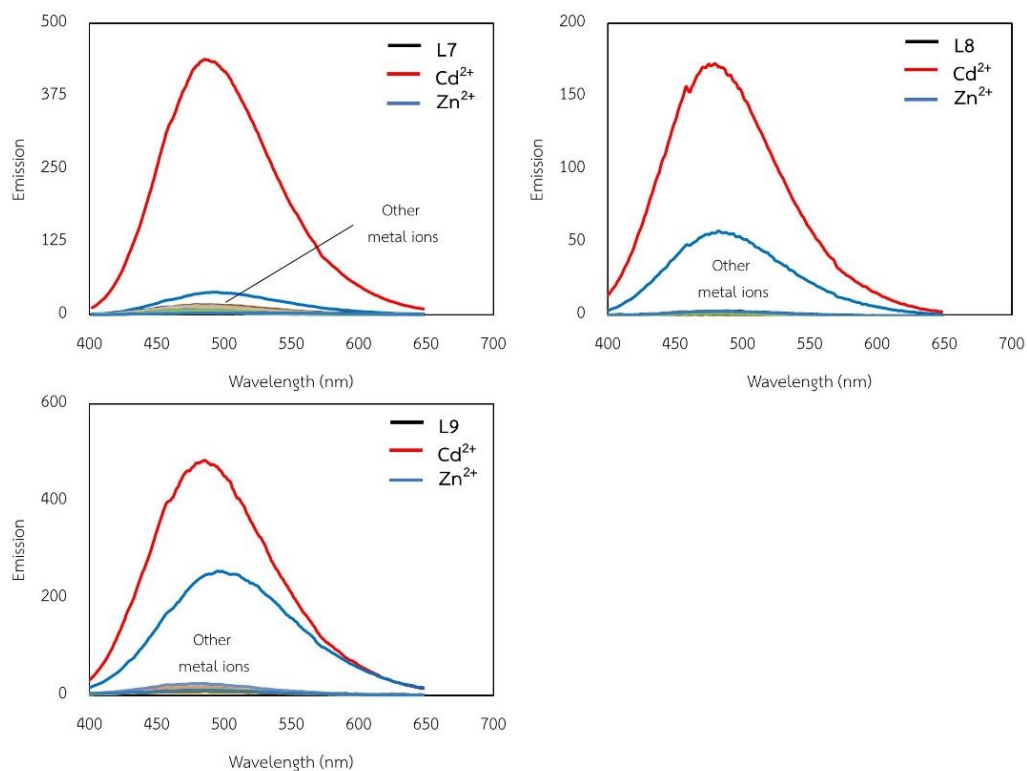


Figure 3.25 Fluorescence spectra of L7–L9 (10 μM) tested with various metal ions (10 μM) in Tris HCl buffer solution pH 7.

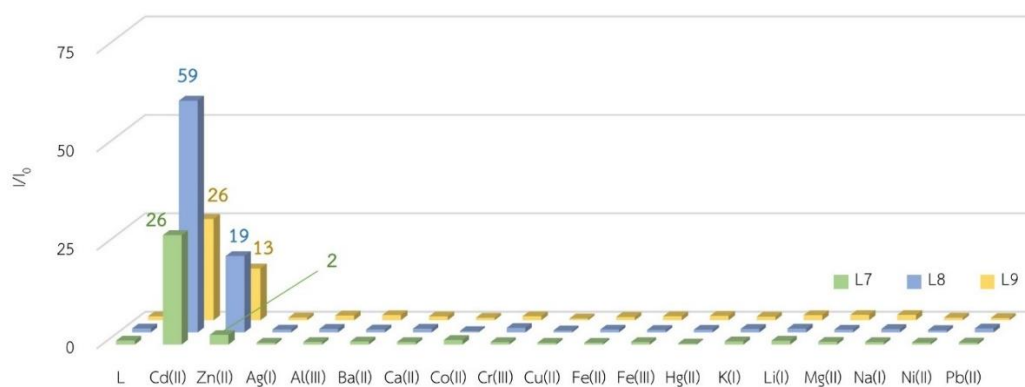


Figure 3.26. Relative intensity of L7–L9 (10 μM) in the presence of various metal ion (10 μM).

3.3.3 Fluorescence sensing properties of L10–L13

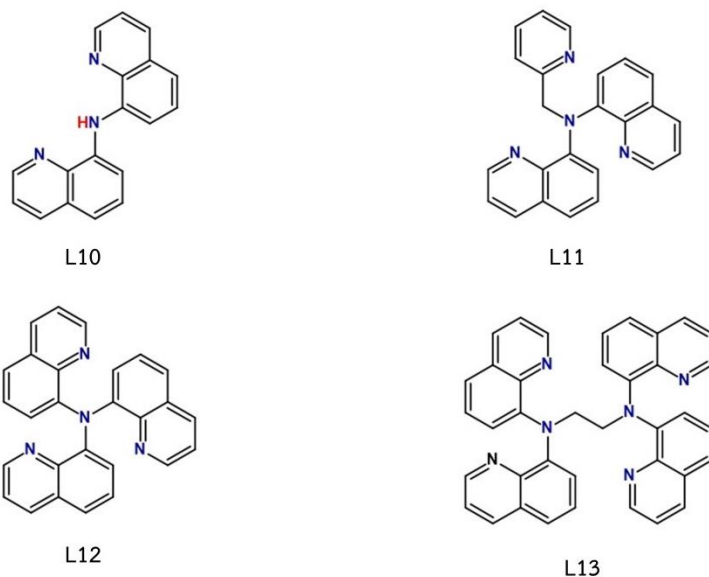


Figure 3.27 Chemical structure of L10–L13.

Ligands **L10–L13** are the results of replacing of picolyl groups in **L1**, **L5** and **L6** by quinoline groups to study the effect of quinoline groups on the fluorescence sensitivity and selectivity. The emission spectra of **L10–L13** in the absence and presence of various metal ions in Tris HCl buffer solution pH 7 are shown in Figure 3.28. Addition of Cd^{2+} or Zn^{2+} into **L10** solution increased the fluorescence emission intensity at 600 nm. In comparison with **L1**, the red-shift emission came from the high planarity of **L10** in the complex structures as a result of the deprotonation of the amino proton. This also caused higher I/I_0 than **L1** (Figure 3.29). Unfortunately, **L11** and **L12** did not show any improvement in the fluorescence enhancement ratio in comparison to their predecessor **L5**. Upon addition of Cd^{2+} or Zn^{2+} , **L11** showed lower I/I_0 than **L5** probably due to energy transfer between the neighboring quinoline groups in their octahedral complex structures. This effect is more pronounced for **L12**, which contains more quinoline groups, that even showed fluorescence quenching after binding with either Cd^{2+} or Zn^{2+} . The similar quenching result was also observed in the case of **L13**.

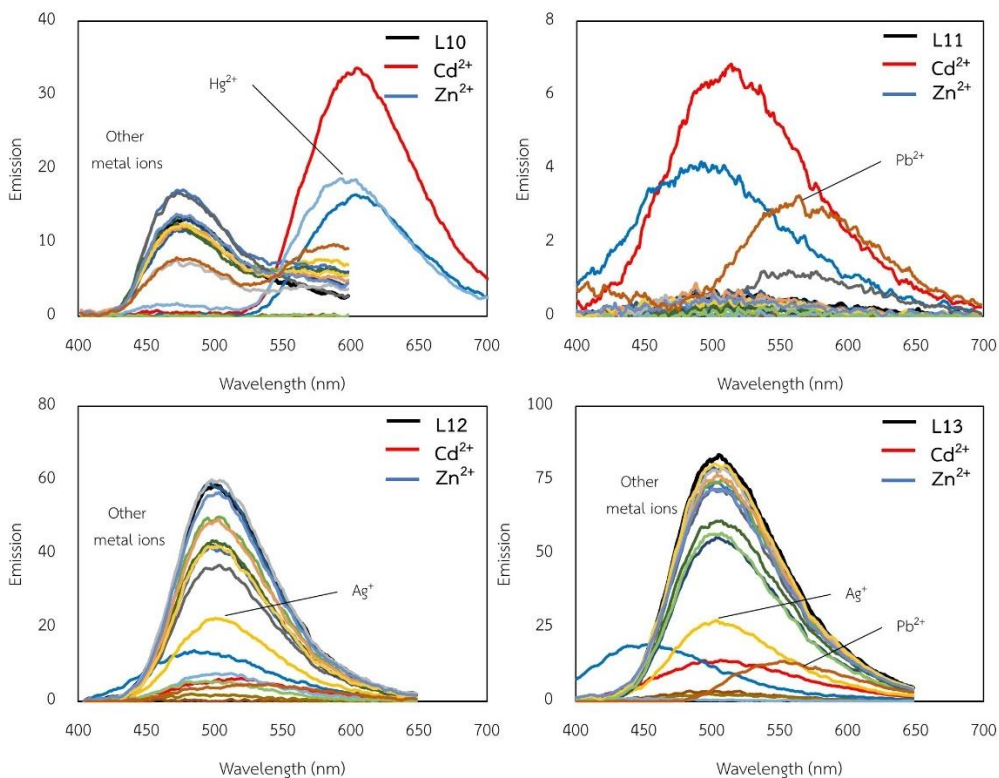


Figure 3.28 Fluorescence spectra of **L10–L13** (10 μM) tested with various metal ions (10 μM) in Tris HCl buffer solution pH 7.

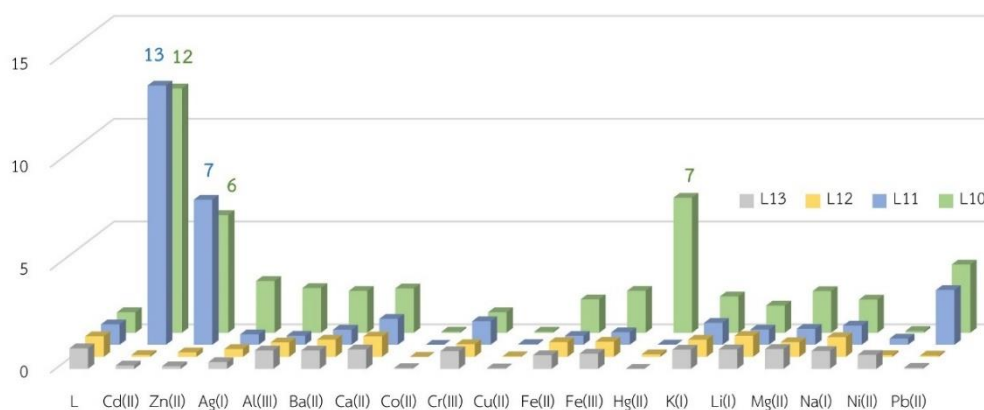


Figure 3.29 Relative intensity of **L10–L13** (10 μM) in the presence of various metal ion (10 μM).

3.3.4 Fluorescence sensing properties of L14–L17

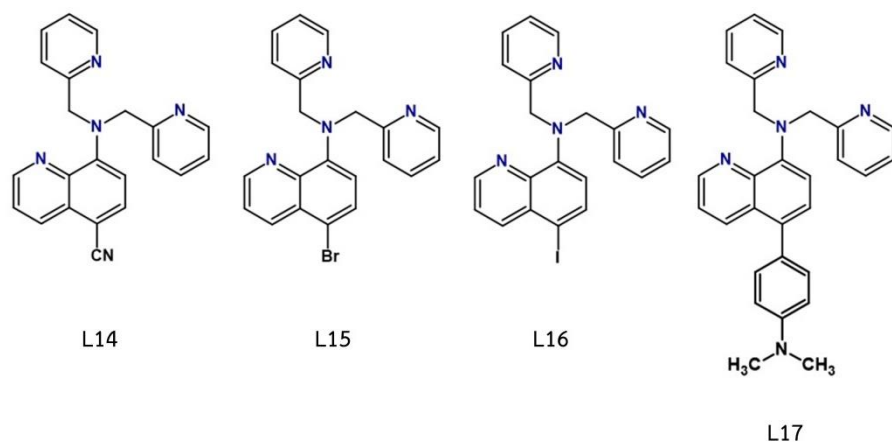


Figure 3.30 Chemical structure of **L14–L17**.

The effects of substituents on selectivity and sensitivity were also investigated by varying the substitution groups on the 5th position of the quinoline moiety in **L5**. The emission spectra of **L14–L17** in the absence and presence of various metal ions in Tris HCl buffer solution pH 7 are shown in Figure 3.31. In comparison with **L5**, ligand **L14** with nitrile group exhibited higher I/I_0 for Cd^{2+} possibly due to the reduction of electron push-pull effect upon the complexation (Figure 3.32). For **L15** and **L16** containing bromine and iodine substituent, respectively, the I/I_0 were significantly lower than **L5** due to the heavy atom effects. Moreover, **L17** containing an electron donating group (dimethylaminophenyl) showed very low I/I_0 because the ligand itself has a high initial emission. Besides, the Cd^{2+} complexation may promote the ICT relaxation of the excited **L17·Cd** complex.

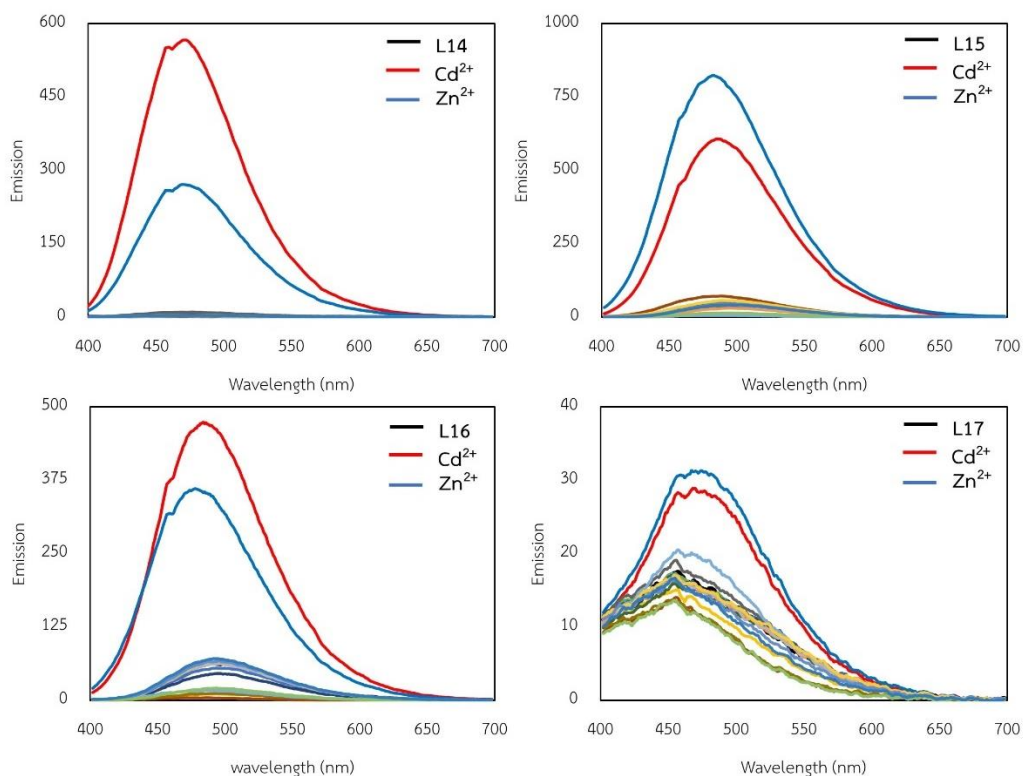


Figure 3.31 Fluorescence spectra of **L14–L17** (10 μM) tested with various metal ions (10 μM) in Tris HCl buffer solution pH 7.

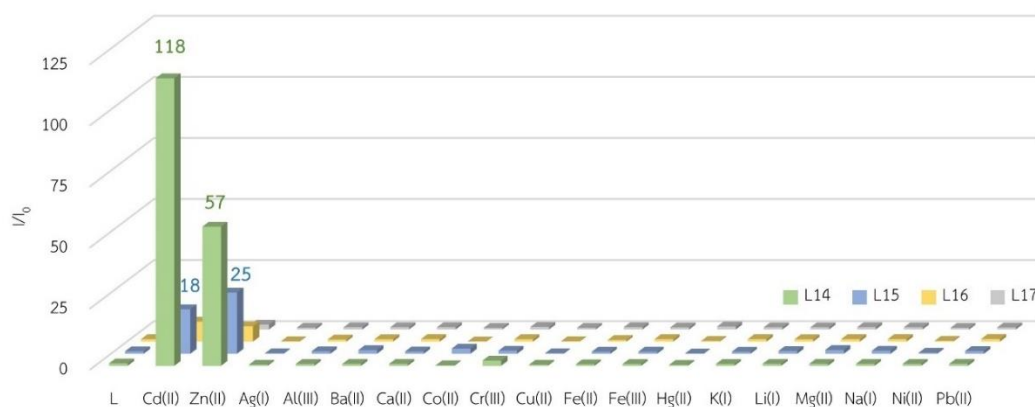


Figure 3.32 Relative intensity of **L14–L17** (10 μM) in the presence of various metal ion (10 μM).

3.4 Association constants

To gain insight understanding of sensitivity and selectivity of the ligands, the association constants (K_a) of all ligands (**L1–L17**) were determined by nonlinear curve fitting using the BindFit v0.5 program from the Open Access website supramolecular.org. The K_a values were determined by ligand-metal ion UV titration using the 1:1 complexation curve fitting model. For example, the absorption spectra obtained from the absorption titration of **L1** with Cd^{2+} are shown in Figure 3.33a. The curve fitting was performed by using the absorbance at three wavelengths i.e., 253, 300 and 350 nm in the presence of various concentration of Zn^{2+} (Figure 3.33b). the quality of the curve fitting for every selected wavelength was illustrated by residual plot in Figure 3.33b. The obtained association constant, and the error of fitting are summarized in the inset of Figure 3.33a. The details of the others are provided in appendices. The association constants are presented and discussed in successive series of **L1–L9**, **L10–L13** and **L14–L17** as follows.

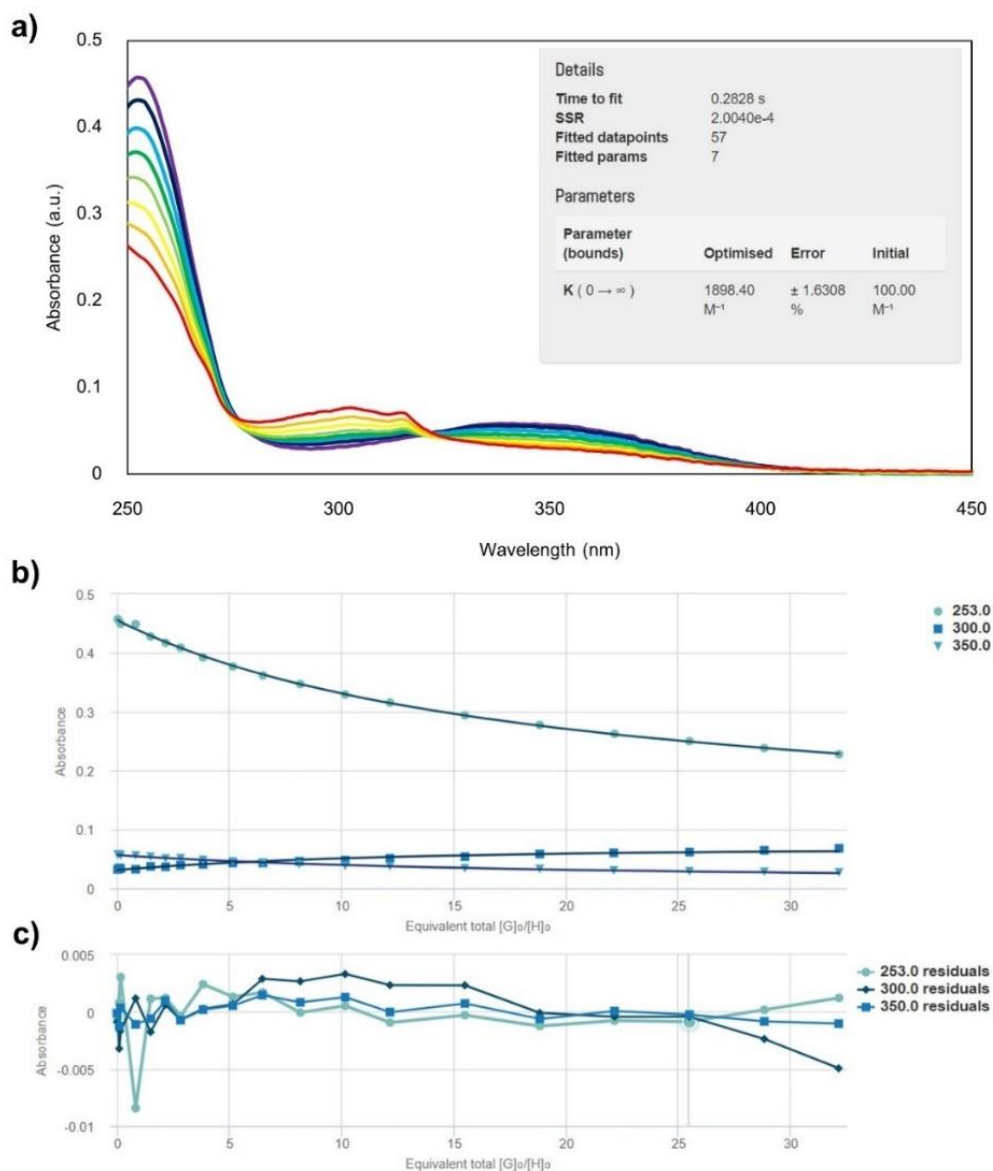


Figure 3.33 a) UV titration between **L1** and Cd^{2+} (inset) summary table of the results of the curve fitting, b) scatter plots between absorbance and amount of Cd^{2+} at 253, 300 and 350 nm, the lines show non-linear curve fitting of the absorbance values at all three wavelengths used for determination of K_a value. c) the residual plots of the corresponding fitting.

3.4.1 Association constant of L1–L9

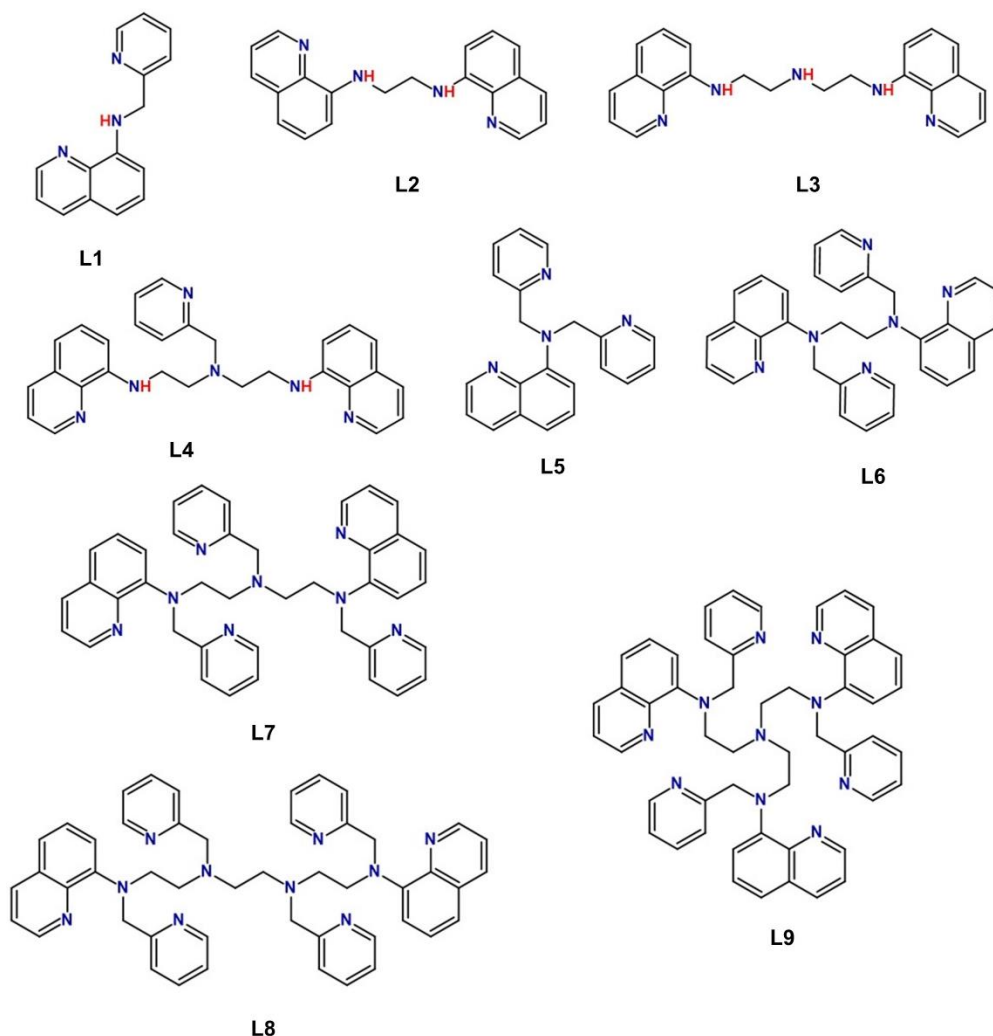


Figure 3.34 Chemical structure of L1–L9.

The association constants of L1–L9 presented in Table 3.1 showed that the amino protons and number of N atoms in the ligands significantly affected the binding ability of the ligands to Zn^{2+} and Cd^{2+} . The ligand L1–L4 which have amino proton (N-H) have higher K_a value for Zn^{2+} . While the ligand L5–L9 which have no amino proton have higher K_a values than those of the ligands having amino protons because the N atom of a tertiary amine generally has higher electron density than that of a secondary amine. This effect is more pronounced for the softer cation (Cd^{2+}) in comparison with the harder one (Zn^{2+}). Moreover, increasing the number N-coordinating atoms increased the K_a values for both Zn^{2+} and Cd^{2+} up to 4 and 6

atoms, **L5** and **L6**, respectively. Then the K_a values started decreasing with the increasing number of N-coordinating atoms. That is because of the preference coordination number (CN) of Cd^{2+} complex is 7–8. The crystal structures of **L6·Cd** shows that Cd^{2+} binds with **L6** with coordination number of 8, 6-coordinate from **L6** and 2-coordinate from a nitrate group, leaving the other nitrate group outside the complex. Even tetradentate ligand, **L5**, Cadmium ion binds with coordination number of 7, 4-coordinate from **L1** and 3-coordinate from two nitrate groups. Furthermore, the highest association constant for Zn^{2+} is **L5** which has four N-coordinating atoms because Zn^{2+} is likely to form a complex with coordination number of 5–6. The results confirmed that the binding strength directly contributed to higher fluorescence enhancement as well as the higher selectivity toward Cd^{2+} of the ligands without amino proton.

Table 3.1 Association constant (K_a) of **L1–L9** with Cd^{2+} and Zn^{2+} in aqueous solution

Compound	Number of		Log(K_a)	
	N	H	Cd^{2+}	Zn^{2+}
L1	3	1	3.28	4.76
L2	4	2	5.64 ^a	6.17 ^a
L3	5	3	4.76	4.98
L4	6	2	6.02	6.54
L5	4	-	7.51	8.16
L6	6	-	8.60	7.09
L7	8	-	6.77	5.09
L8	10	-	4.88	6.24
L9	10	-	6.17	5.27

^aExperiments were carried out in ethanol due to limited solubility of **L2** in water.

3.4.2 Association constant of L10–L13

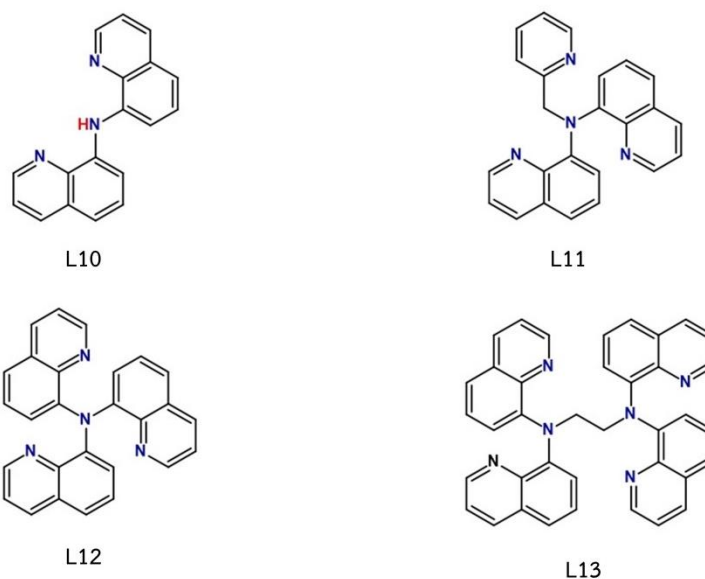


Figure 3.35 Chemical structure of L10–L13.

The association constants of **L10–L13** are presented in table 3.2. The results are consistent with the previous results that the ligand with 6 coordinating atoms (**L13**) gave the highest K_a values toward Cd^{2+} , and the ligand with 4 coordinating atoms (**L11**) gave the highest K_a values toward Zn^{2+} . Moreover, in comparison with their analogous structures (**L1**, **L5** and **L6**), The results generally showed that replacing the picolyl group with quinolyl group lowered the K_a values in both Cd^{2+} and Zn^{2+} because the complexes had higher angular strain caused by the more rigid ligands. However, **L10·Zn** complex showed significantly higher K_a than **L1·Zn** because of the deprotonation is easier to occur for maintaining the π -conjugation between two quinoline rings.

Table 3.2 Association constant (K_a) of **L10–L12** with Cd^{2+} and Zn^{2+} in aqueous solution

Compound	Number of		$\text{Log}(K_a)$	
	N	H	Cd^{2+}	Zn^{2+}
L10	3	1	3.31	6.41
L11	4	-	5.83	7.43
L12	4	-	6.03	5.65
L13	6	-	6.50	7.23

3.4.3 Association constant of **L14–L17**

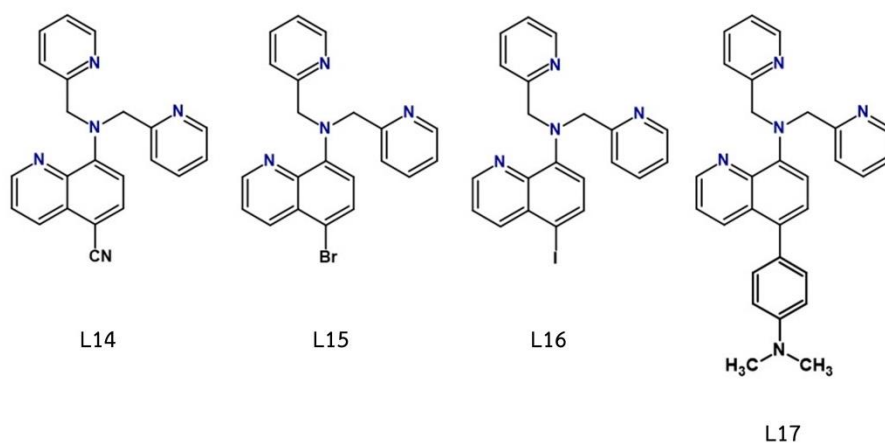


Figure 3.36 Chemical structure of **L14–L17**.

The association constants of **L14–L17** are presented in table 3.3. The results showed that the electron withdrawing group slightly decreased K_a values for both Cd^{2+} and Zn^{2+} for **L14–L16** because of less electron density on the amino group. Unfortunately, the K_a of **L17** could not be obtained because neither the titrations with Cd^{2+} nor Zn^{2+} gave significant change in the absorbance.

Table 3.3 Association constant (K_a) of **L14–L17** with Cd^{2+} and Zn^{2+} in aqueous solution

Compound	Number of		Log(K_a)	
	N	H	Cd ²⁺	Zn ²⁺
L14	4	-	6.77	7.96
L15	4	-	7.54	6.73
L16	4	-	8.14	7.77
L17	4	-	n/a	n/a

3.5 Condition optimization for Cd^{2+} detection

3.5.1 Effects of pH

To use **L6** as a fluorescent sensor for Cd^{2+} detection, the effects of pH on the Cd^{2+} detection of **L6** were studied by measurement of the emission intensity of **L6** solutions in the absence and presence of Cd^{2+} or Zn^{2+} . To our delight, the fluorescent sensing system based on **L6** showed very stable fluorescence responses within a pH range of 4.0–9.0 (Figure 3.37). The results indicated that the complexation between **L6** and Cd^{2+} is more favorable than the protonation of the N atoms in the ligand or the binding between the metal ions and hydroxide ion in this pH range.

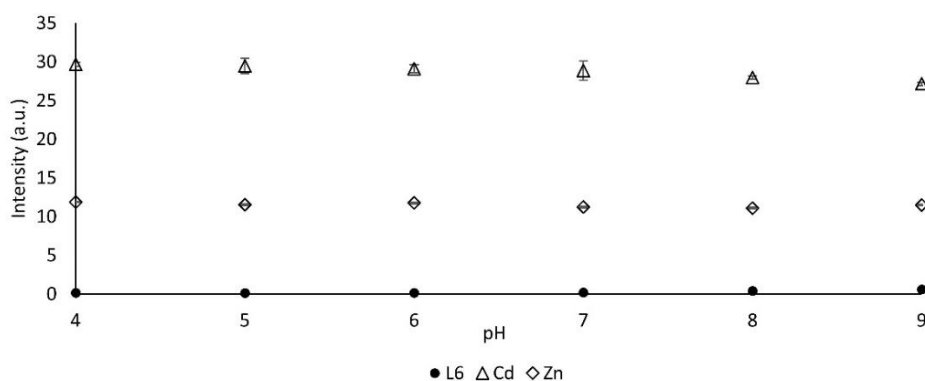


Figure 3.37 pH-dependence of emission intensity at 480 nm of 10 μM **L6** and **L6** in the absence, presence of 10 μM Cd^{2+} , or Zn^{2+} in NaOH/HCl-pH-adjusted Tris HCl buffer solution.

3.5.2 Selectivity and interference study

The fluorescence sensing selectivity of **L6** was studied against various common metal ions (Li^+ , Na^+ , K^+ , Ca^{2+} , Ba^{2+} , Mg^{2+} , Fe^{2+} , Co^{2+} , Ni^{2+} , Cu^{2+} , Zn^{2+} , Cd^{2+} , Ag^+ , Hg^{2+} , Pb^{2+} , Fe^{3+} , Cr^{3+} and Al^{3+}) at 1.0 equivalent (10 μM) in aqueous solution (0.2% DMSO in 0.20 M pH7 Tris HCl buffer solution). Only Cd^{2+} and Zn^{2+} induced the fluorescence enhancement of **L6** giving the enhancement ratio (I/I_0) at 480 nm of 120 and 50 times, respectively (Figure 3.38). While the other metal ions did not significantly affect the fluorescence of the ligand. To evaluate the possible interference from the other metal ions in Cd^{2+} detection, the fluorescence ratio at 480 nm of **L6·Cd** solution was also measured in the presence of another competitive ion. The alkali and alkaline earth metal ions did not interfere the detection of Cd^{2+} by **L6**. However, some transition metal ions such as Zn^{2+} , Fe^{2+} , Co^{2+} , Ni^{2+} , Cu^{2+} , Hg^{2+} and Pb^{2+} partially reduced the fluorescent intensity of **L6·Cd** presumably by the competitive binding of these metal to **L6**.

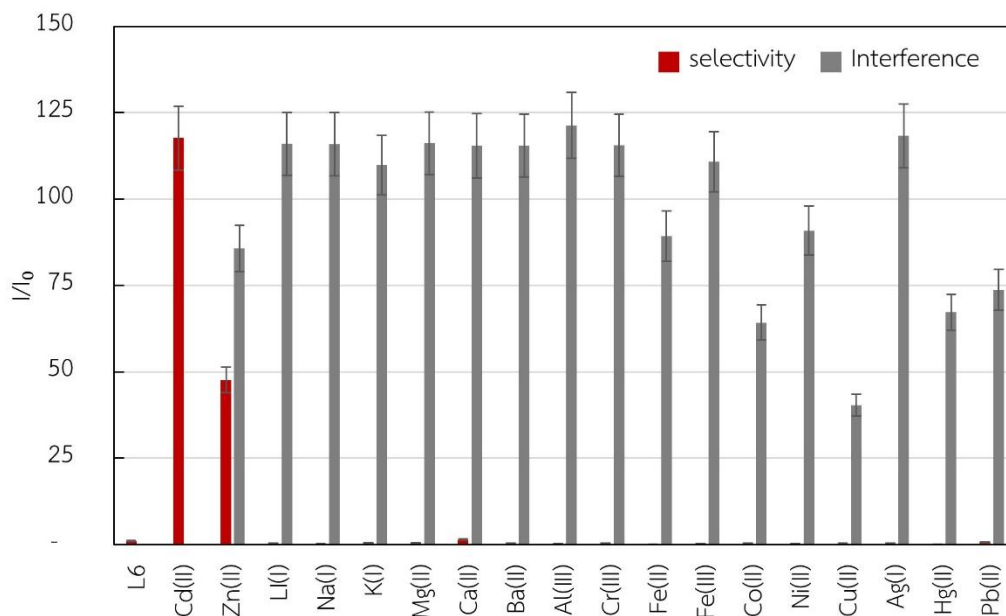


Figure 3.38. (a) Photograph of **L6** (10 μM) in the presence of metal ions (10 μM) in a buffer solution (20 mM Tris HCl, pH = 7.4). (b) Fluorescence responses (I/I_0) at 480 nm of **L6** (10 μM) to metal ions in a buffer solution (20 mM Tris HCl, pH = 7.4 at $\lambda_{\text{ex}} = 300$ nm). Red bar represents response to each metal ion. Gray bar represents response to Cd^{2+} in the presence of another competitive metal ion. All $[M] = 10 \mu\text{M}$.

3.5.3 Masking agent study

To reduce the interference of Zn^{2+} and other metal ions, three masking agents i.e., dipicolylamine (DPA), tripicolylamine (TPA), ethylenediamine tetraacetate (EDTA), were investigated. First, the masking agents were tested for the **L6** solutions containing Cd^{2+} and Zn^{2+} . The results showed that DPA did not show any significant effect on the fluorescence intensities of all solutions indicating that DPA, which has only 3 N-coordinating atoms, could not compete with binding ability of **L6** to both metal ions (Figure 3.39). In contrast, EDTA sharply reduced the fluorescence intensities of both **L6+Cd** and **L6+Zn** solutions due to the strong binding ability of EDTA which is a hexadentate ligand containing negatively charged carboxylate groups. It is important to note that the signal of **L6+Cd+Zn** solution was as high as **L6+Cd** solution due to a limited amount of EDTA used in the experiment. Both DPA and EDTA were thus not appropriate masking agents for the Cd^{2+} detection. TPA showed the best characters of masking agents for that it reduced the fluorescence

intensity of **L6+Zn** solution while minimally affected the fluorescence of **L6+Cd** solution. This resulted in improved signal from **L6+Cd+Zn** solution to the level closed to that of **L6+Cd** solution. Therefore, TPA is a masking agent of choice for Cd^{2+} detection with **L6**.

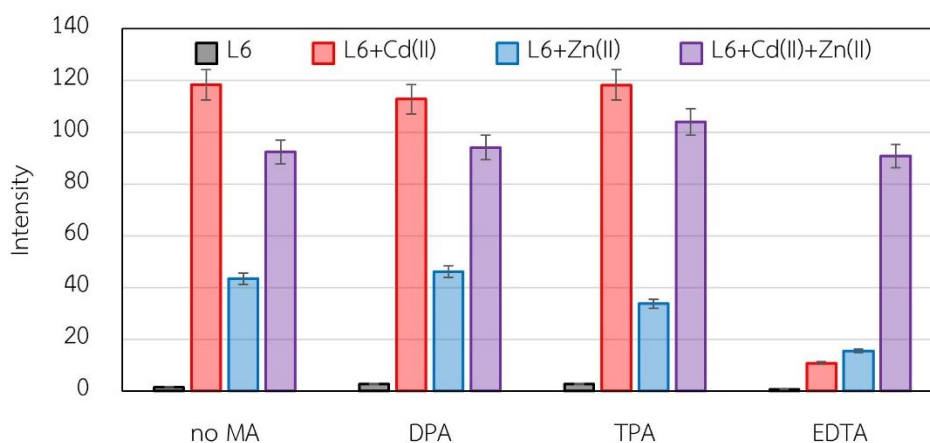


Figure 3.39. Fluorescence intensity at 480 nm of **L6** solutions in the absence and presence of Cd^{2+} and Zn^{2+} ions ($[\text{L6}] = 10 \mu\text{M}$, $[\text{M}] = 10 \mu\text{M}$) tested with various masking agents ($10 \mu\text{M}$) in a buffer solution (20 mM Tris HCl , $\text{pH} = 7.4$).

The optimum concentration of TPA masking agent was studied in the range of $5.0 \mu\text{M}$ to $200 \mu\text{M}$. The fluorescence intensity of **L6+Zn** solution decreased with the increasing concentration of TPA. At $200 \mu\text{M}$ of TPA the fluorescence intensity of **L6+Zn** solution became insignificant and the fluorescence intensity of **L6+Cd+Zn** solution was as high as that of **L6+Cd** solution (Figure 3.40). These results indicated that the optimum TPA concentration for masking the interference from Zn^{2+} was $200 \mu\text{M}$.

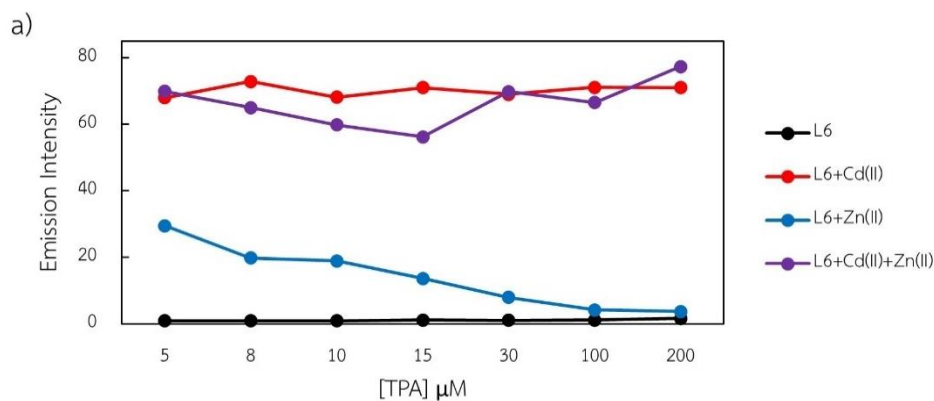


Figure 3.40. Fluorescence intensity at 480 nm of **L6**, **L6+Cd**, **L6+Zn** and **L6+Cd+Zn** solution ($[\text{L6}] = 10 \mu\text{M}$, $[\text{M}] = 10 \mu\text{M}$) in the presence of various concentration of TPA (5–200 μM) in a buffer solution (20 mM Tris HCl, pH = 7.4).

The fluorescence sensing selectivity and interference of **L6** (10 μM) were evaluated again in the presence of 200 μM of TPA masking agents. The result shows great improvement of selectivity and interference (Figure 3.41). Only Cd^{2+} showed fluorescence enhancement of **L6**; however, the fluorescent enhancement ratio (I/I_0) was lower from 118-time to 25-time due to the emission background of TPA. For competitive study, TPA reduced the interference not only from Zn^{2+} but also from the interfering metal ions (Fe^{2+} , Co^{2+} , Ni^{2+} , Cu^{2+} , Hg^{2+} and Pb^{2+}). In case of 4th row metal ions which are smaller than Cd^{2+} , they prefer binding with the lower coordination number ligand, TPA. Surprisingly, the interferences from 5th row metal ions (Hg^{2+} and Pb^{2+}) were also reduced. It is possible that two molecules of TPA cooperatively bind with the 5th row metal ions. These results suggested that **L6** shows the highest association constant for Cd^{2+} that all interfering metal ions can be masked by a single reagent.

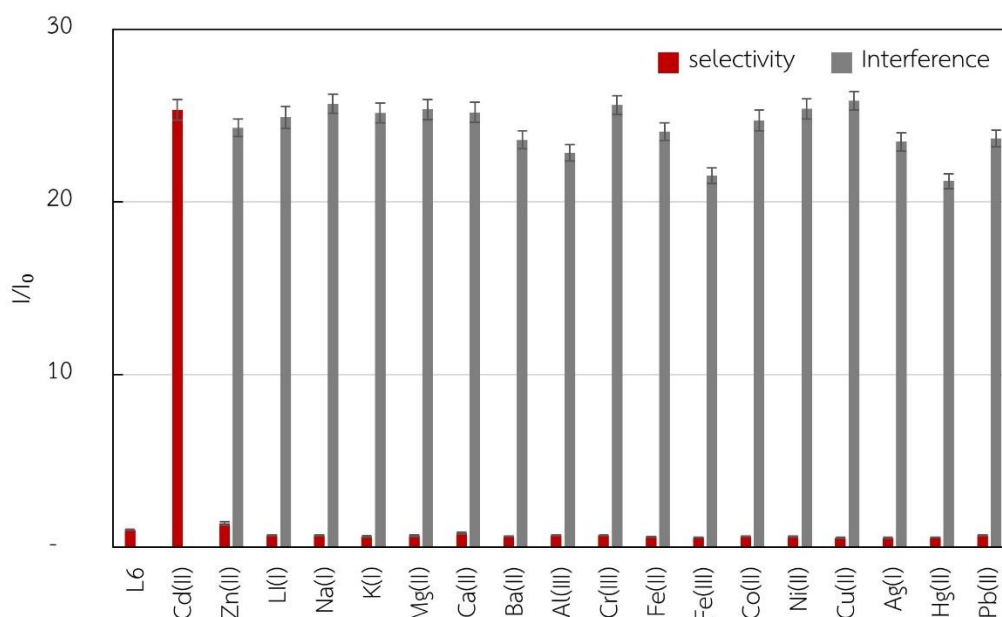


Figure 3.41. Fluorescence responses (I/I_0) at 480 nm of **L6** (10 μM) to metal ions in a buffer solution (20 mM Tris HCl, pH = 7.4 at $\lambda_{\text{ex}} = 300$ nm in the presence of TPA (200 μM). Red bars represent responses to each metal ion. Gray bars represent responses to Cd^{2+} in the presence of each competitive metal ion. $[M] = 10$ μM .

3.5.4 Limit of detection

To determine the detection limit of **L6**, the emission intensities at 480 nm at varied Cd^{2+} concentrations were measured in aqueous solutions pH 7. At low concentration, a good linear association was obtained in the range of 80–500 nM Cd^{2+} ($R^2=0.9983$) giving the detection limit of 69 nM which is still slightly higher than the regulations for cadmium allowed to be presence in drinking water (USEPA = 44 nM, WHO = 27 nM) (Figure 3.42).

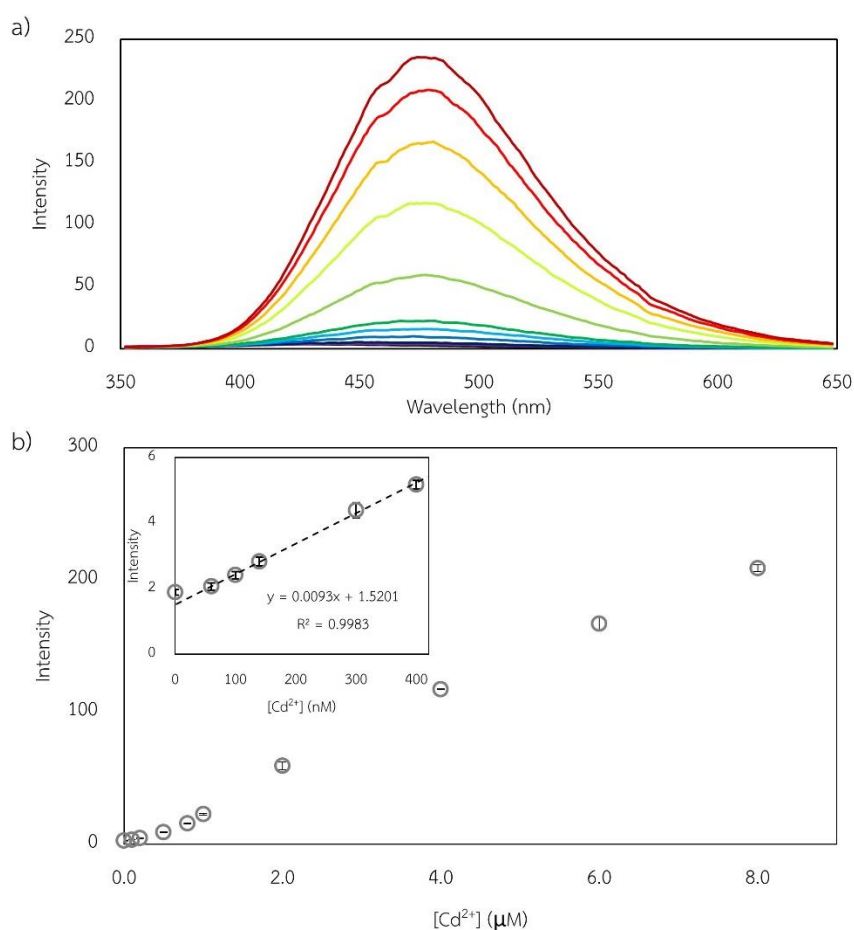


Figure 3.42. a) Fluorescence titration between 10 μM **L6** and Cd²⁺ in the presence of 20 equiv. TPA in Tris HCl buffered solution pH 7. b) Plot between emission intensity at 480 nm and concentration of Cd²⁺. (inset) Fluorescent titration calibration line at low concentration for determination of LOD.

3.5.5 Detection of Cd²⁺ in living cells

To demonstrate the application of **L6** in fluorescence cell imaging, HeLa cells were used as a model. The cell samples were incubated with 1 μM of **L6** followed by incubation of Cd²⁺ with the concentration varied from 0.01 to 10 μM. The fluorescence images were observed at 465 nm using the excitation wavelength of 350 nm. The images showed that **L6** could detect Cd²⁺ permeating into the cell cytoplasm. Furthermore, the fluorescence intensity increased with the concentration of Cd²⁺ added (Figure 3.43) that suggested possible applications of **L6** for localization and monitoring of Cd²⁺ in cells or tissues.

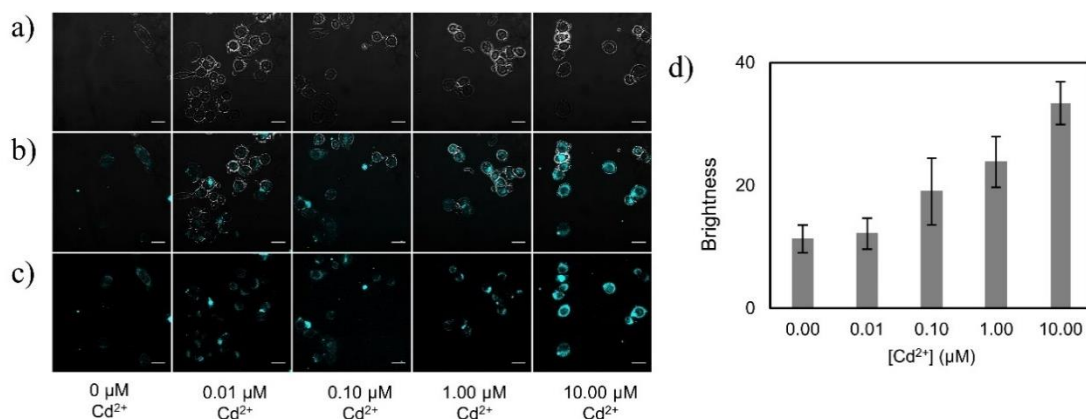


Figure 3.43. Fluorescence images of 1 μM **L6** and Cd^{2+} in HeLa cells. (a) bright-field transmission images (b) merged images (c) fluorescence image. (d) Average brightness $((R+G+B)/3)$ of cells corresponding to the fluorescent images. (scalebar = $25\mu\text{M}$ and image contrast and brightness were all adjusted equally).

3.6 Structures of Cd^{2+} Complexes

3.6.1 X-ray crystallography

X-ray crystallography was performed to determine the stoichiometry and the coordination mode of the ligand in the complexes. Single crystals of complexes **L1-Cd**, **L5-Cd**, and **L6-Cd** suitable for X-ray crystallographic analysis were obtained through slow evaporation of their solutions in acetonitrile, acetonitrile/methanol/diethyl ether, and diethyl ether/ethyl acetate, respectively. Structural determination shows that **L1**, **L5** and **L6** serve as chelating ligands in these complexes and coordinate to the central Cd^{2+} via N atoms in 1:1 Cd:L stoichiometry as shown in Figure 3.44. **L1-Cd** was crystallized in the orthorhombic crystal system in the chiral space group P212121 with the absolute structure parameters of 0.04(3). Cd^{2+} is heptacoordinated with the tridentate **L1**, two monodentate nitrate anions in the axial positions and one bidentate nitrate anion in the equatorial plane. The two axial monodentate nitrate bridges to the nearby Cd^{2+} ions leading to the formation of a 1D helical chain. The 21 screw axes of these helices are all parallel to the crystallographic b-axis, and the pitch is $11.911(4)$ Å (Figure 3.45). Complex **L5-Cd** was crystallized in the monoclinic space group P2/c and possesses a mononuclear discrete structure. The Cd^{2+} ion in this complex is also heptacoordinated with ligation

from four nitrogen atoms of the tetradentate **L5** and three oxygen atoms from a monodentate and a bidentate nitrate group. Whereas, complex **L6·Cd** was crystallized in the triclinic space group P-1, consisting of two monocationic $[\text{Cd}(\text{L6})(\text{NO}_3)]^+$ complexes and a dianionic $[\text{Cd}(\text{NO}_3)_4]^{2-}$ complex per asymmetric unit. In the cationic species, each Cd(II) ion is octacoordinated and surrounded by six nitrogen atoms from the hexadentate **L6** and two oxygen atoms from a bidentate nitrate group. While the Cd^{2+} in the anionic species is also octacoordinated by eight oxygen atoms from four different chelating nitrate groups. These results clearly support that the coordination number of the Cd^{2+} can go up to eight, which is consistent with the greater association constant and sensing selectivity of **L6** binding to Cd^{2+} ion in comparison to Zn^{2+} . Unfortunately, single crystals of Zn^{2+} complexes with these series of ligands could not be obtained after much effort. However, our previous results with a similar amidoquinoline ligand indicated that Zn^{2+} preferred to form a pentacoordinated complex.

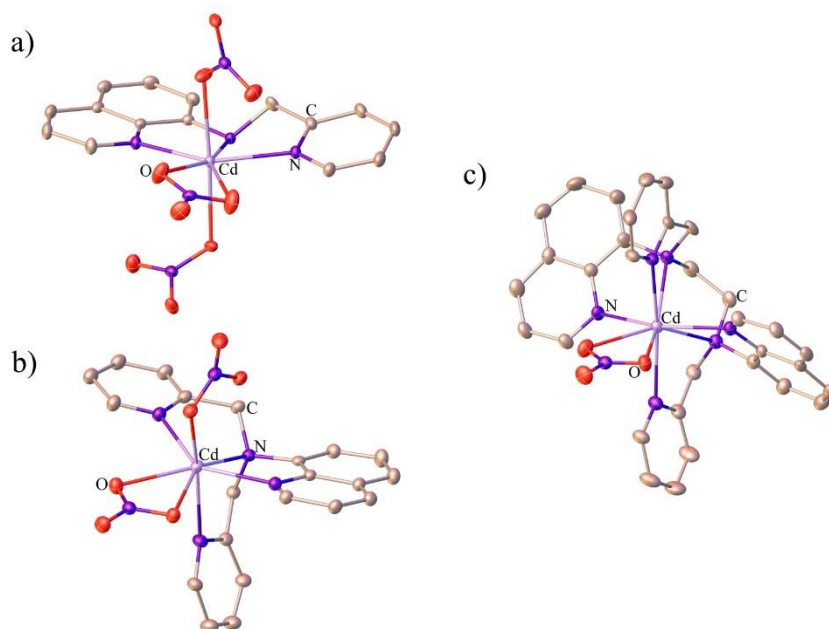


Figure 3.44 The coordination environment of Cd(II) ion and the ligand L in (a) **L1·Cd**, (b) **L5·Cd**, and (c) **L6·Cd**. The ellipsoids drawn at the 30% probability level and all hydrogen atoms are omitted for clarity.

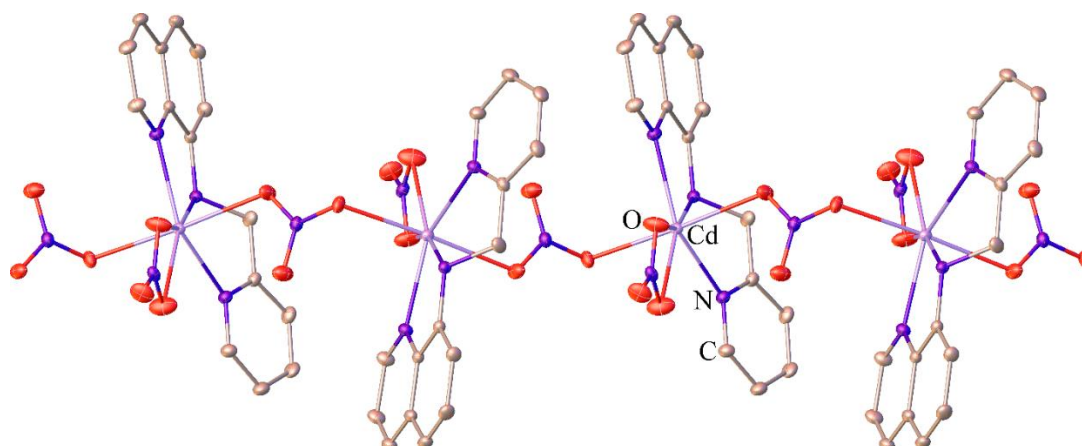


Figure 3.45. The coordination environment of Cd(II) ion and the ligand **L1**. The ellipsoids drawn at the 30% probability level and all hydrogen atoms are omitted for clarity.

3.6.2 ^1H NMR titration

^1H NMR titration spectra of **L6**·Cd or **L6**·Zn in $(\text{CD}_3)_2\text{SO}$ (Figure 3.46–3.47) showed new set of signals with the increasing amount of Cd^{2+} or Zn^{2+} up to 1.0 equivalence which also confirmed the formation of 1:1 complex with the Cd^{2+} or Zn^{2+} . The ^1H NMR spectrum of **L6** showed one signal of pyridine proton H_i at 8.46 ppm and two signals of quinoline protons H_a and H_c at 8.62 and 8.20 ppm. Upon addition of 0.50 equivalent of Zn^{2+} to the solution of **L6**, new three signals appeared at 9.15, 8.67 and 8.55 ppm assigned to H_a , H_c and H_i . The results suggested that Zn^{2+} was coordinated by all 3 N atoms of **L6** forming a symmetric hexacoordinated complex. While the ^1H NMR spectrum of **L6**·Cd complex displayed two new sets of signals at 9.03, 8.69, 8.50, 8.69, 8.61 and 8.38 ppm assigned to H_a , H_i , H_c , H_a' , H_i' and H_c' , respectively. The results indicated that **L6**·Cd complex have asymmetric structure which is consistent with the X-ray crystallography result. The difference in the chemical shifts is the result of the different anisotropic effects of the pyridine ring to the protons on the quinoline ring.

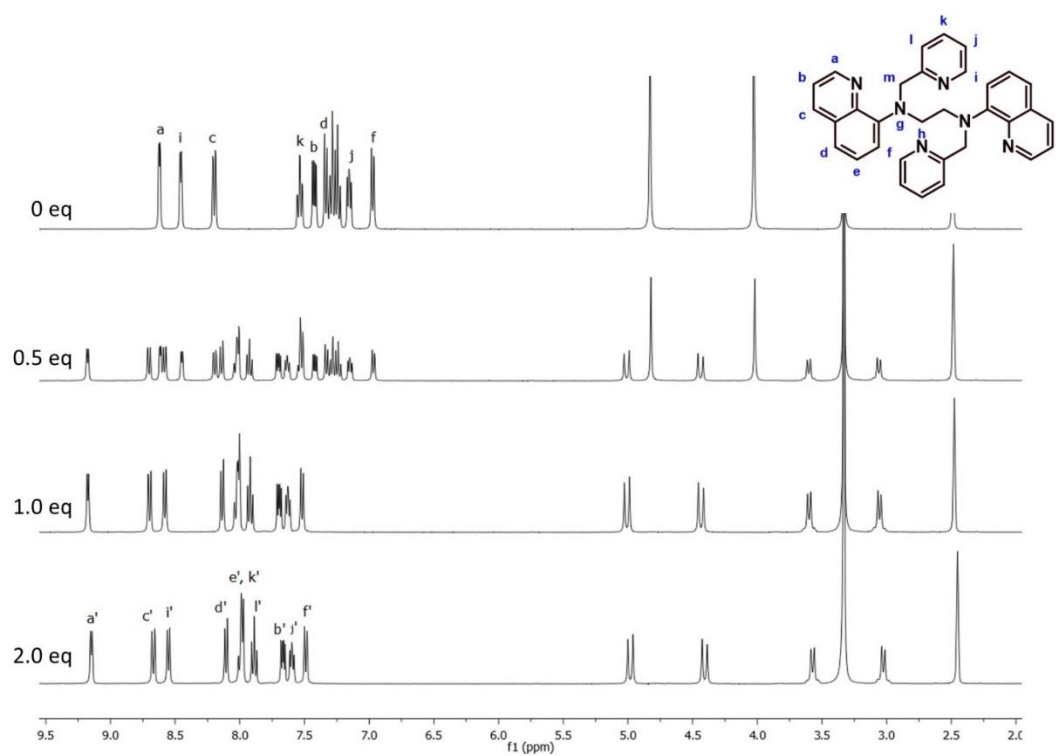


Figure 3.46. ^1H NMR titration spectrum of $\text{L6}\cdot\text{Zn}$ in $(\text{CD}_3)_2\text{SO}$.

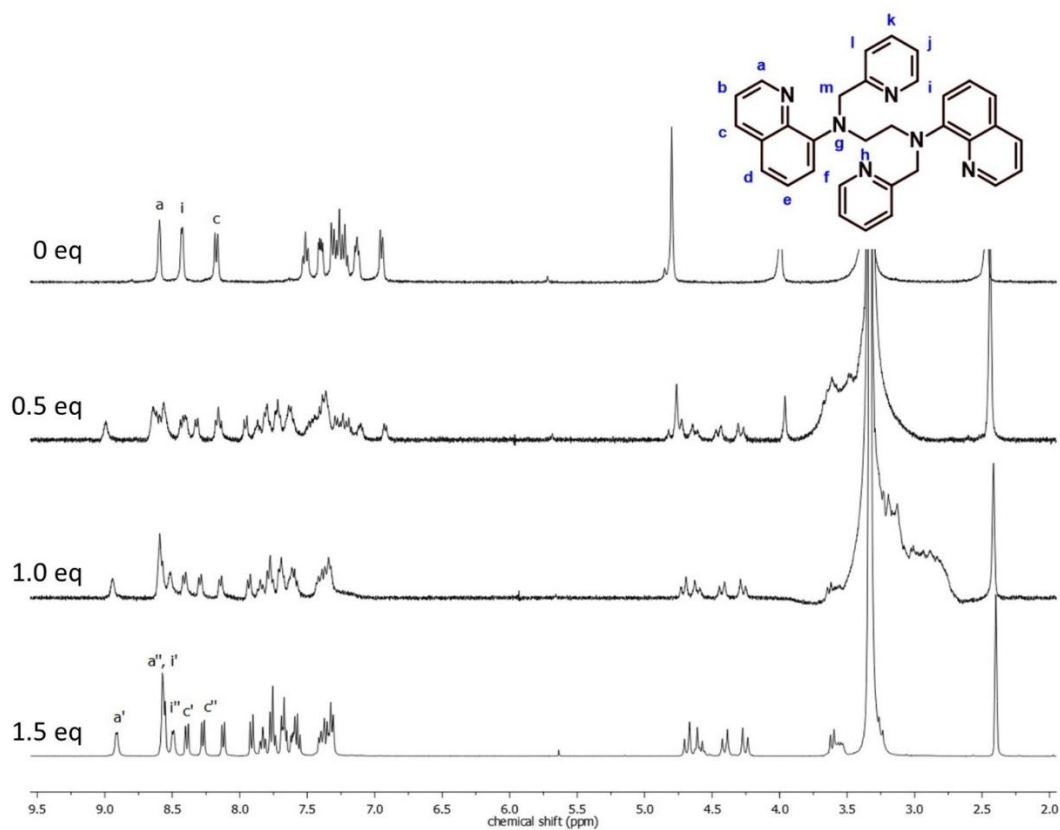


Figure 3.47 ^1H NMR titration spectrum of $\text{L6}\cdot\text{Cd}$ in $(\text{CD}_3)_2\text{SO}$.

CHAPTER 4

CONCLUSION

In conclusion, series of quinoline-based fluorescence ligands (**L1–L17**) were successfully synthesized and studied. The effects of amino protons and denticity of the ligands on Zn^{2+} and Cd^{2+} binding ability were demonstrated. The absence of amino proton and the increase of N binding atoms in the ligands increased the ligand binding constants to both Zn^{2+} and Cd^{2+} that the increase in Cd^{2+} binding was more pronounced. The maximum binding to Zn^{2+} was reached with the tetradentate ligand without amino proton (**L5**) while the maximum binding to Cd^{2+} was observed with the hexadentate ligand without amino proton (**L6**). The ligand showed strong fluorescence enhancement to both metal ion with concentration dependence. Modification of **L5** by varying the substituents at 5th position on quinoline showed that the presence of an electron withdrawing group such as nitrile (**L14**) gave higher fluorescence enhancement but lower the metal ion association constant. Moreover, replacing picolyl group with picolyl group (**L10–L13**) decreased not only the fluorescence enhancement but also the association constants. **L5** and **L6** were thus the optimum ligands as a “turn-on” fluorescent dye for monitoring Zn^{2+} and Cd^{2+} concentrations in aqueous media and cell or tissue samples. The selective binding of **L6** toward Cd^{2+} was dramatically improved by addition of TPA as a masking agent for interfering metal ions such as Zn^{2+} , Hg^{2+} , Cu^{2+} , Pb^{2+} and Co^{2+} . Application of **L6** for detection and determination of Cd^{2+} concentration was demonstrated in solution and in cells. The effects of amino protons and denticity should be useful for ligand design in metal ion fluorescence sensing applications.

For future research work, charge neutralization of metal-ligand complex should be carefully considered in ligand designing. For example, hepta- or octadentate ligand which can produce 2 negative charges when binding with Cd^{2+} may give higher association constant and selectivity.

APPENDIX

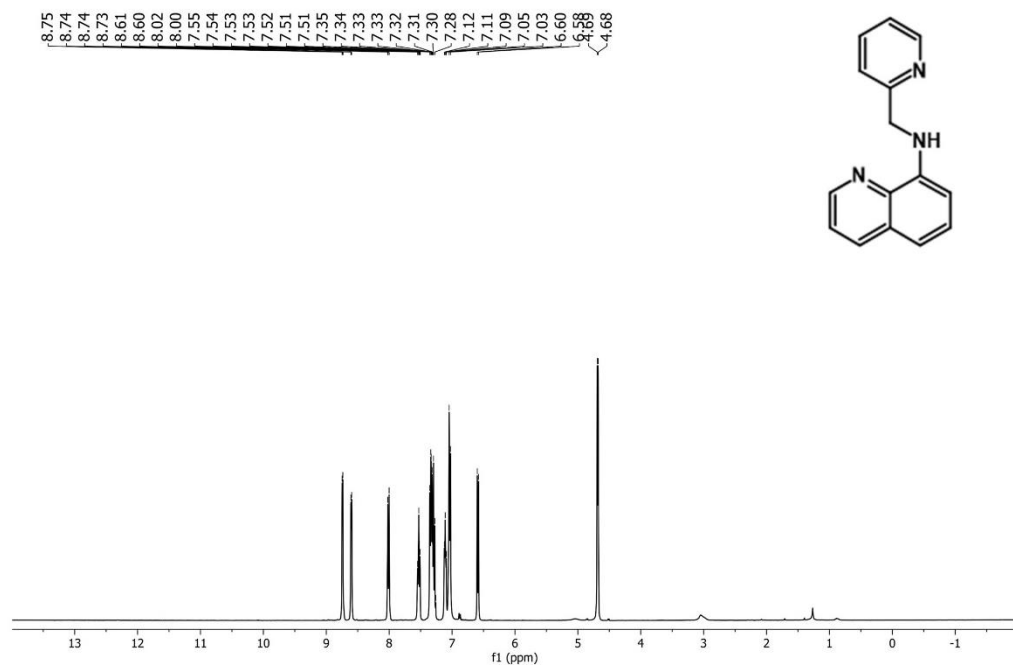


Figure A 1 ^1H NMR of **L1** in CDCl_3 .

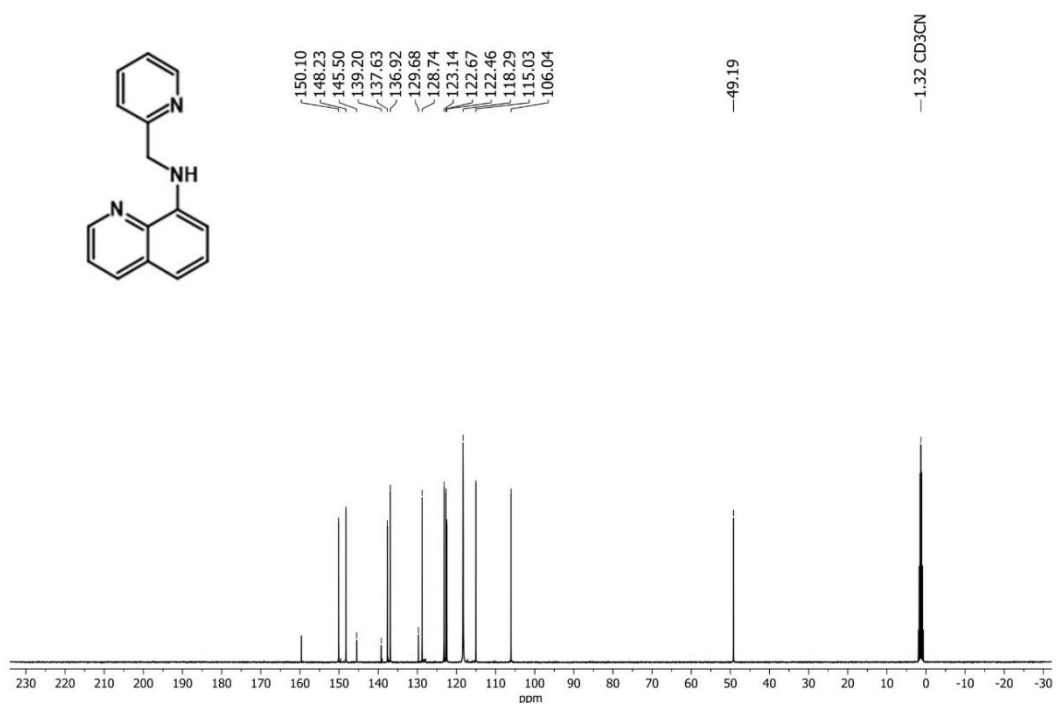
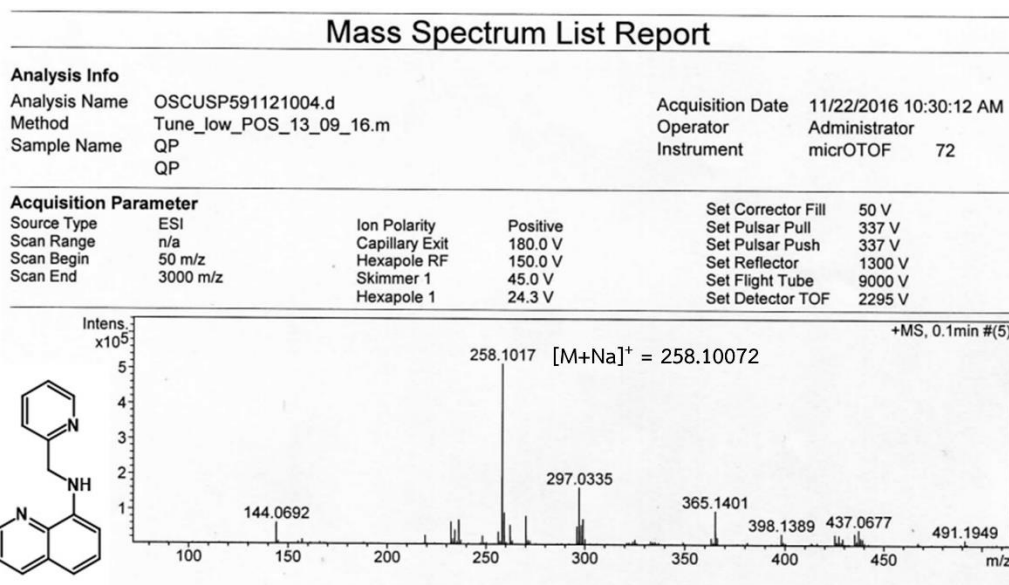
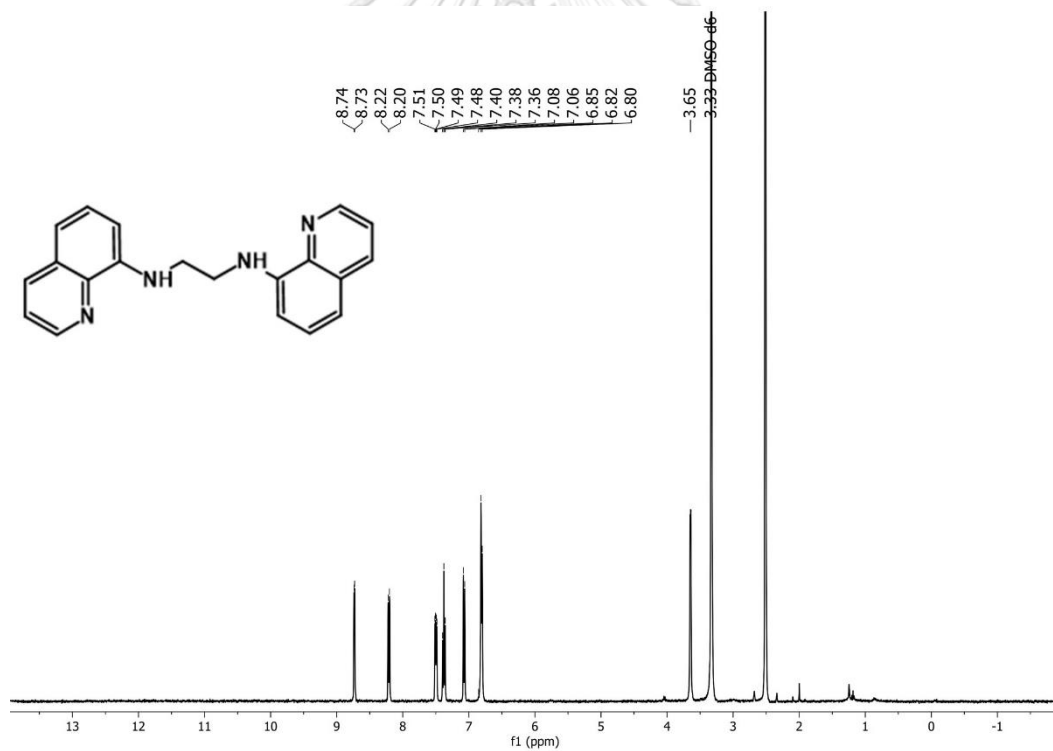


Figure A 2 ^{13}C NMR of **L1** in CD_3CN .

Figure A 3 HRMS of **L1**.Figure A 4 ^1H NMR of **L2** in $(\text{CD}_3)_2\text{SO}$.

Generic Display Report

Analysis Info

Analysis Name D:\Data\Data Service\190813\QQ_RB7_01_2895.d
Method nv_pos_6min_profile_wguardcol_190624.m
Sample Name QQ
Comment

Acquisition Date 8/13/2019 7:58:18 PM

Operator CU.
Instrument micrOTOF-Q II

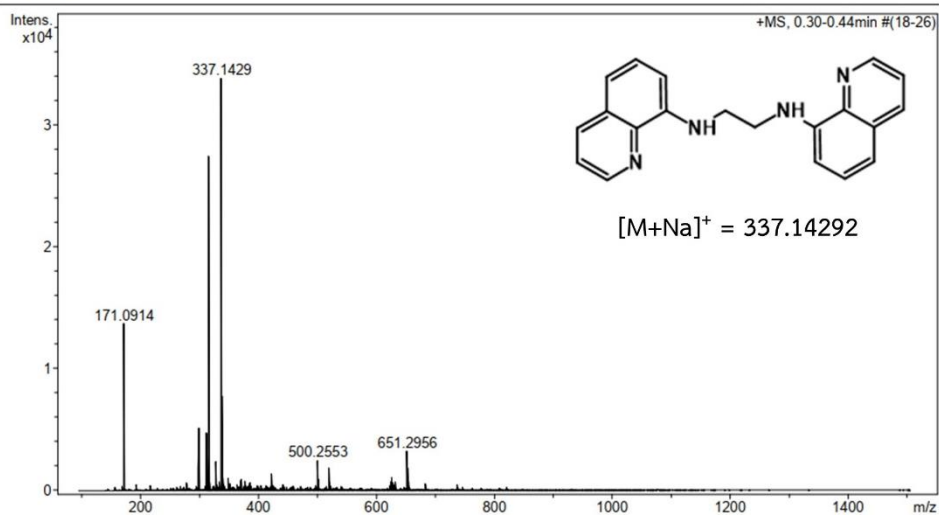
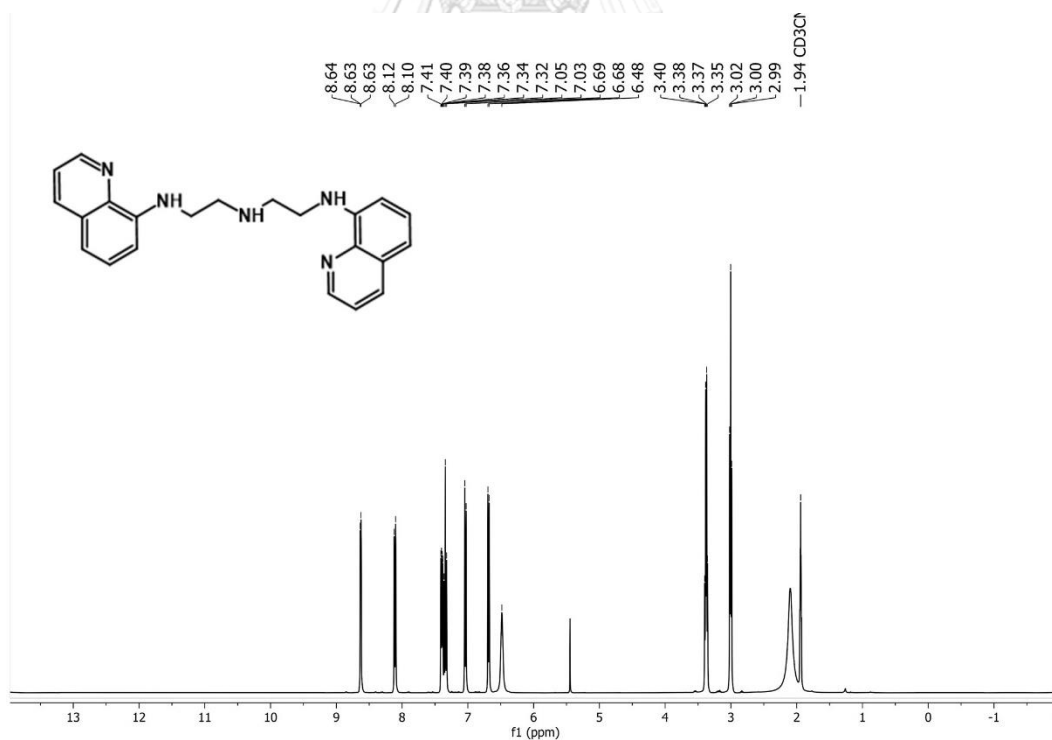
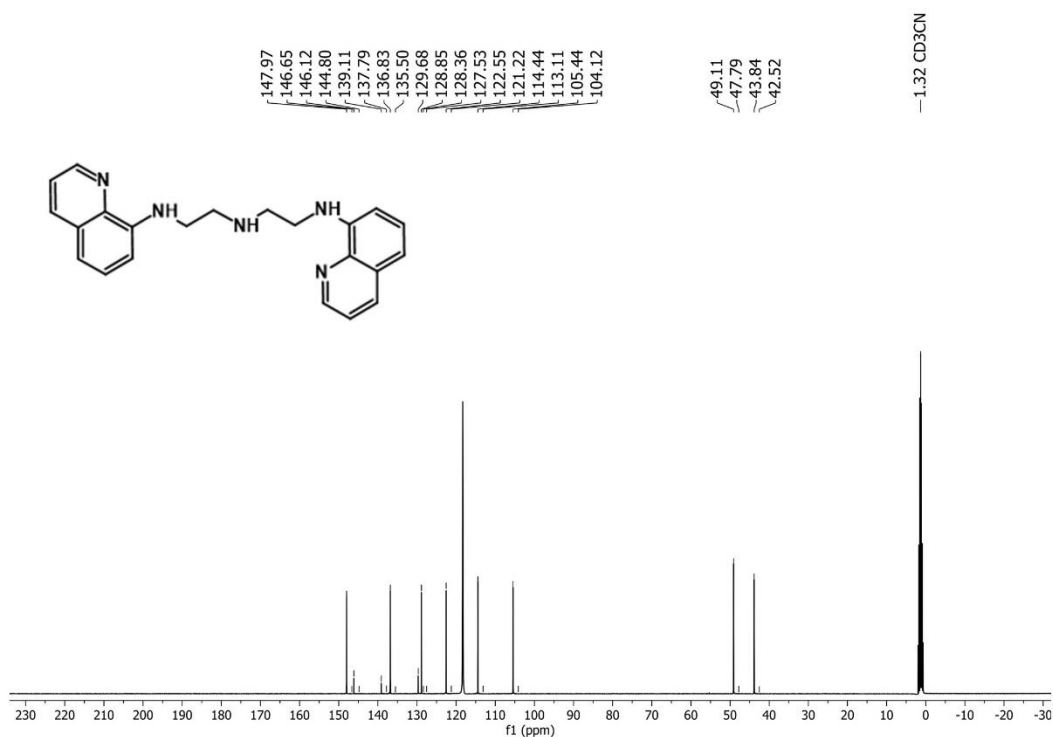


Figure A 5 HRMS of L2.

Figure A 6 ¹H NMR of L3 in CD₃CN.

Figure A 7 ^{13}C NMR of L3 in CD₃CN.

Generic Display Report

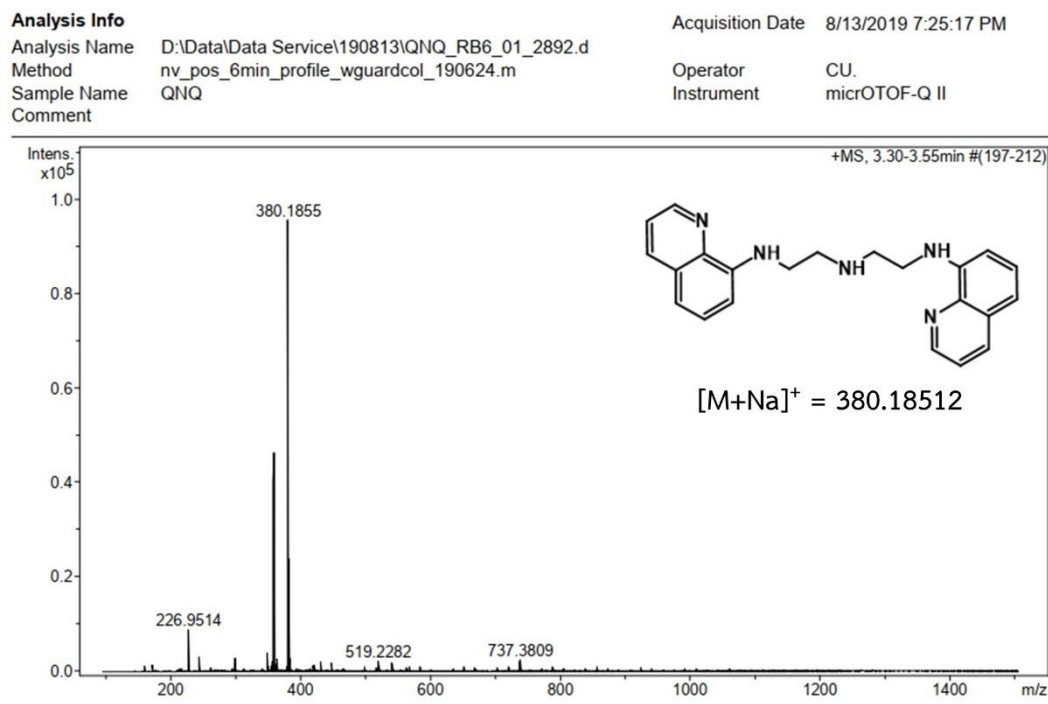
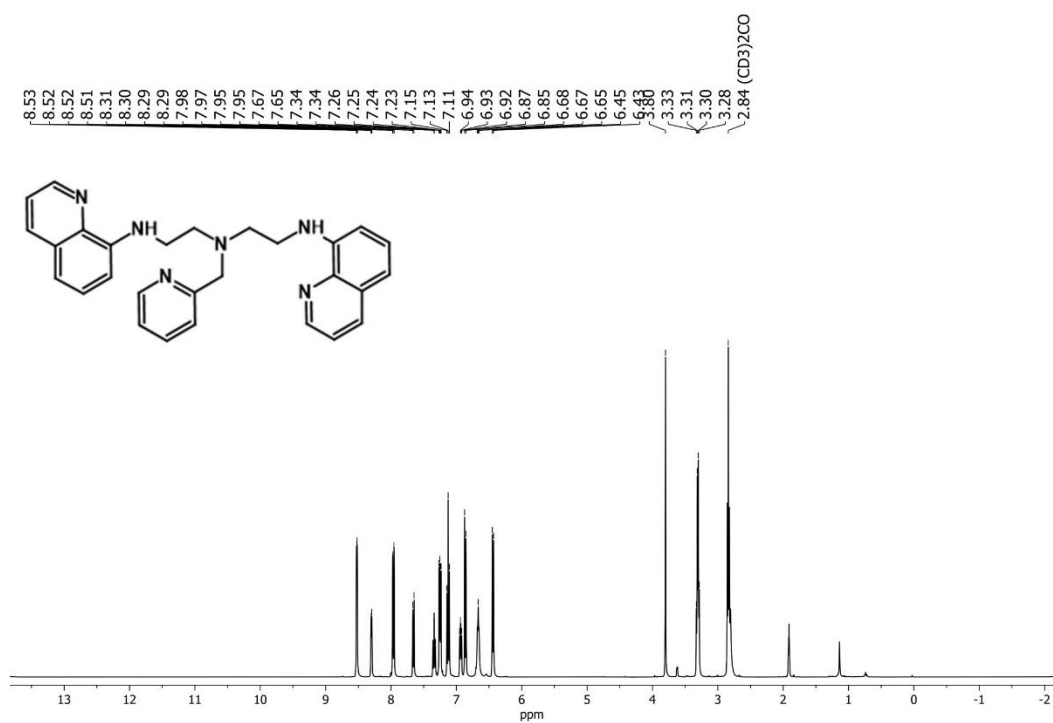
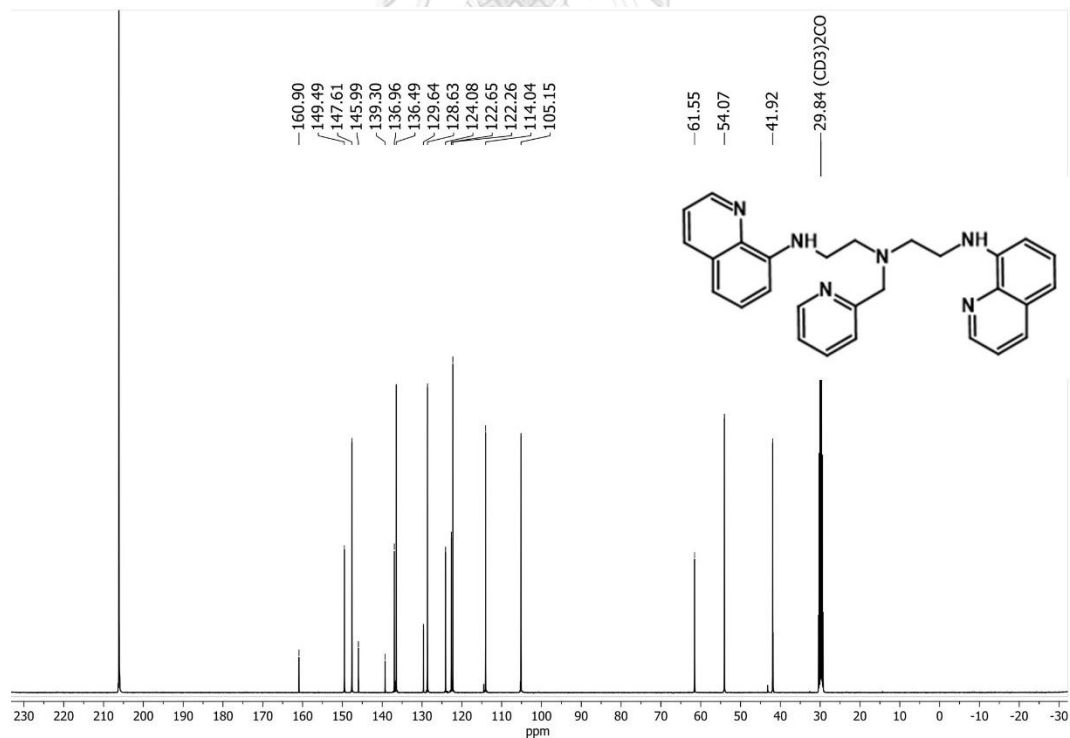


Figure A 8 HRMS of L3.

Figure A 9 $^1\text{H NMR}$ of **L4** in $(\text{CD}_3)_2\text{CO}$.Figure A 10 $^{13}\text{C NMR}$ of **L4** in $(\text{CD}_3)_2\text{CO}$.

Generic Display Report

Analysis Info

Analysis Name D:\Data\Data Service\190813\QPQ_RB8_01_2896.d
Method nv_pos_6min_profile_wguardcol_190624.m
Sample Name QPQ
Comment

Acquisition Date 8/13/2019 8:04:38 PM

Operator CU.
Instrument micrOTOF-Q II

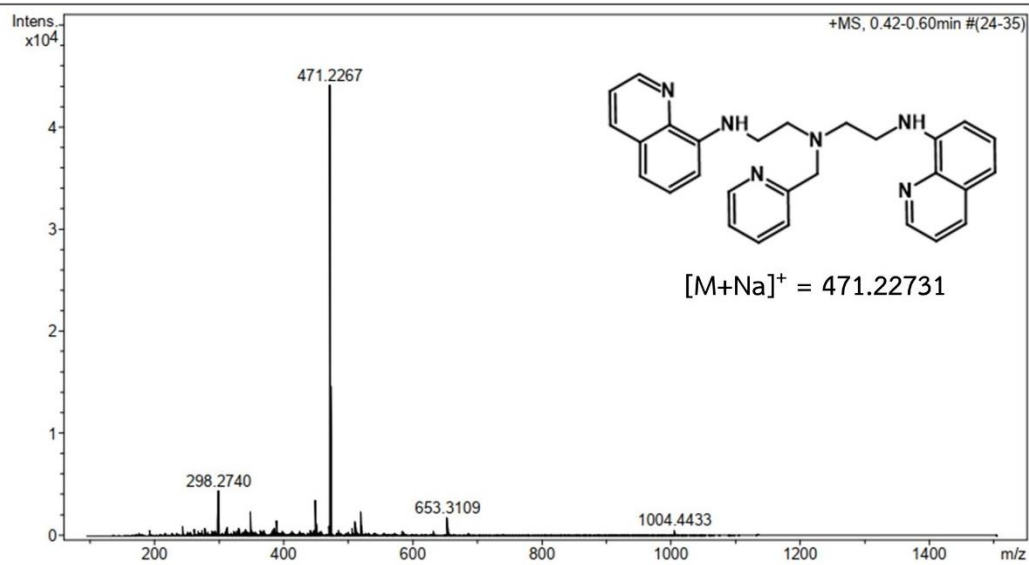
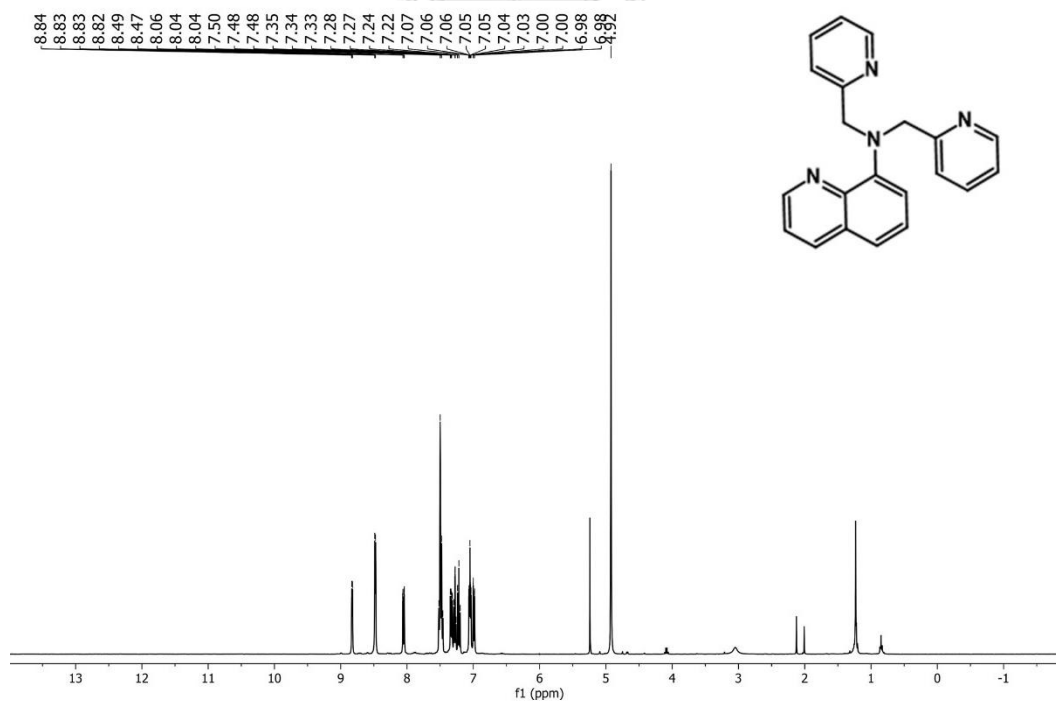
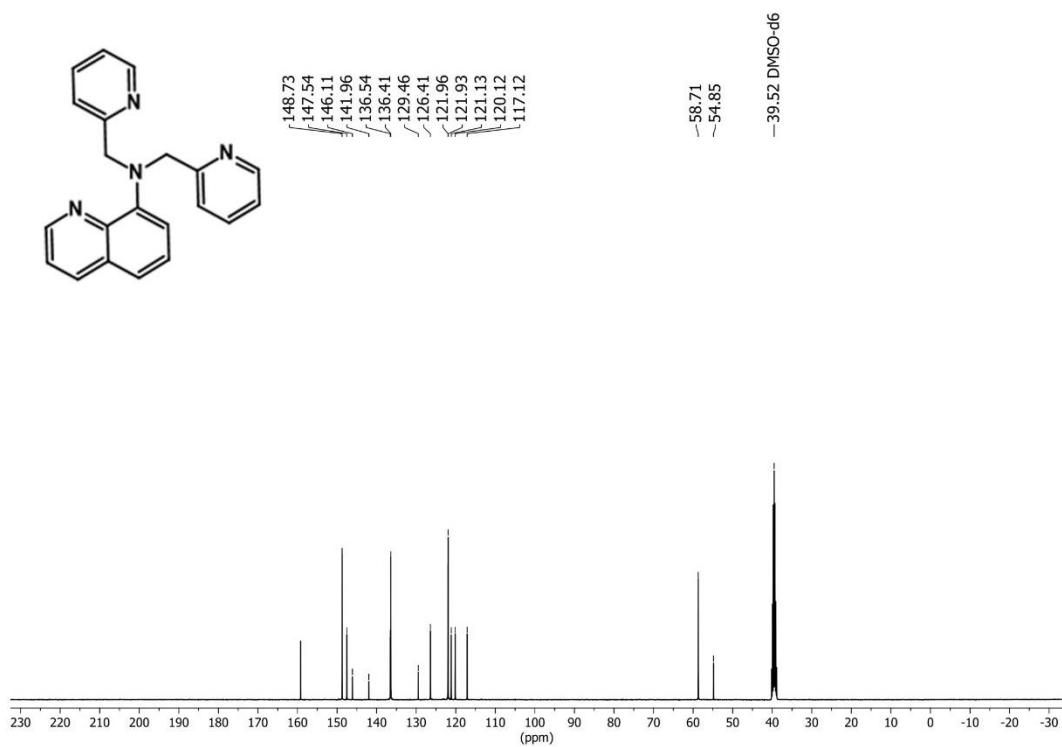


Figure A 11 HRMS of L4.

Figure A 12 ¹H NMR of L5 in CD₃Cl.

Figure A 13 ^{13}C NMR of L5 in $(\text{CD}_3)_2\text{SO}$.

Generic Display Report

Analysis Info

Analysis Name D:\Data\Data Service\190813\Q2P_RB3_01_2880.d
 Method nv_pos_6min_profile_wguardcol_190624.m
 Sample Name Q2P
 Comment

Acquisition Date 8/13/2019 4:56:41 PM

Operator CU.
 Instrument micrOTOF-Q II

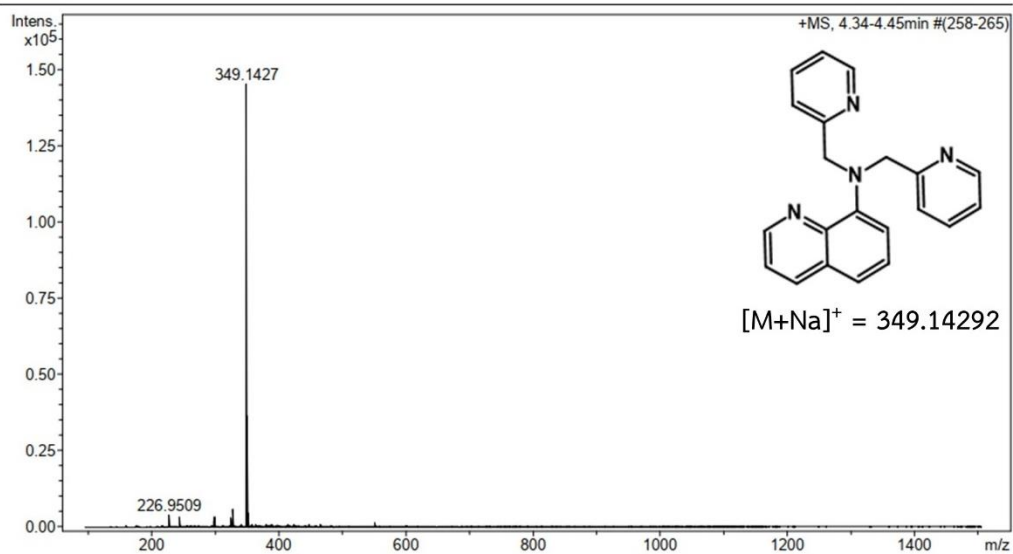
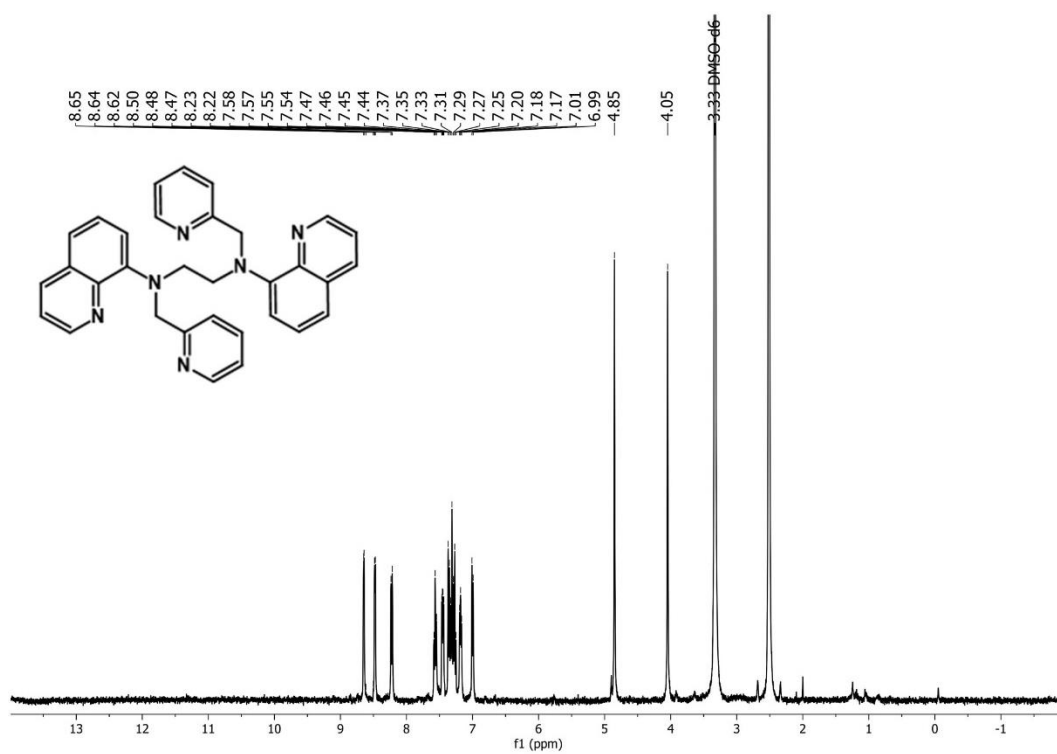
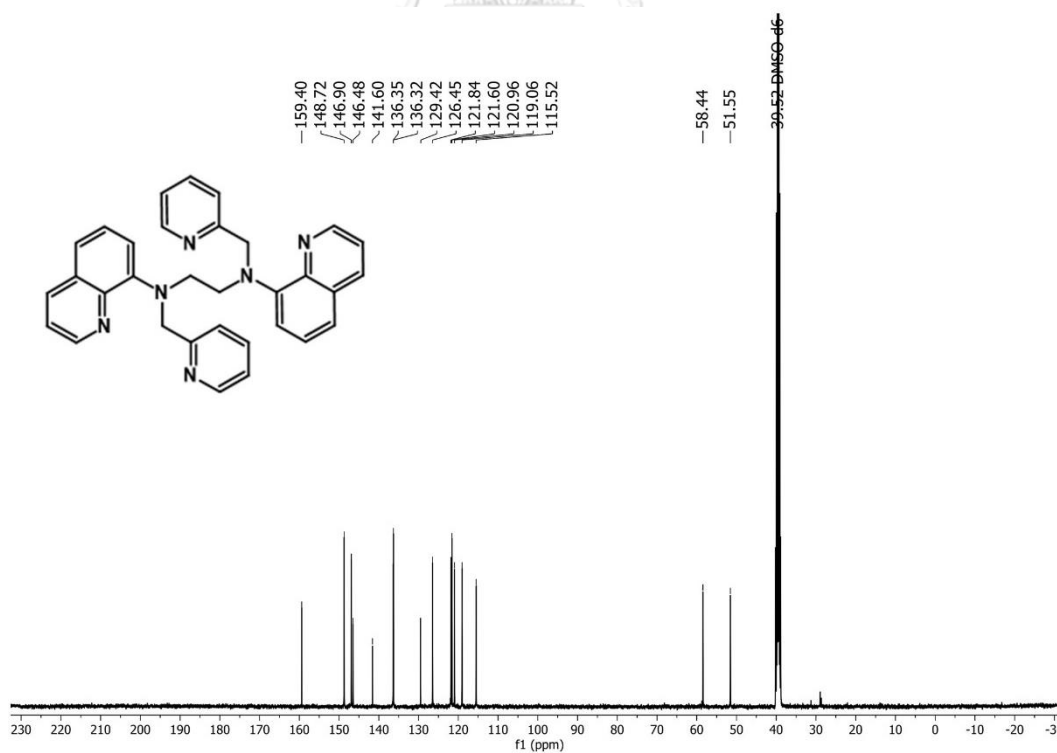


Figure A 14 HRMS of L5.

Figure A 15 ^1H NMR of L6 in $(\text{CD}_3)_2\text{SO}$.Figure A 16 ^{13}C NMR of L6 in $(\text{CD}_3)_2\text{SO}$.

Generic Display Report

Analysis Info	Acquisition Date 11/30/2020 4:31:28 PM	
Analysis Name D:\Data\Data Service\201130\QNNQ_RA6_01_4941.d	Operator CU.	
Method nv_pos_5min_profile_190214.m	Instrument microTOF-Q II	
Sample Name QNNQ		
Comment		

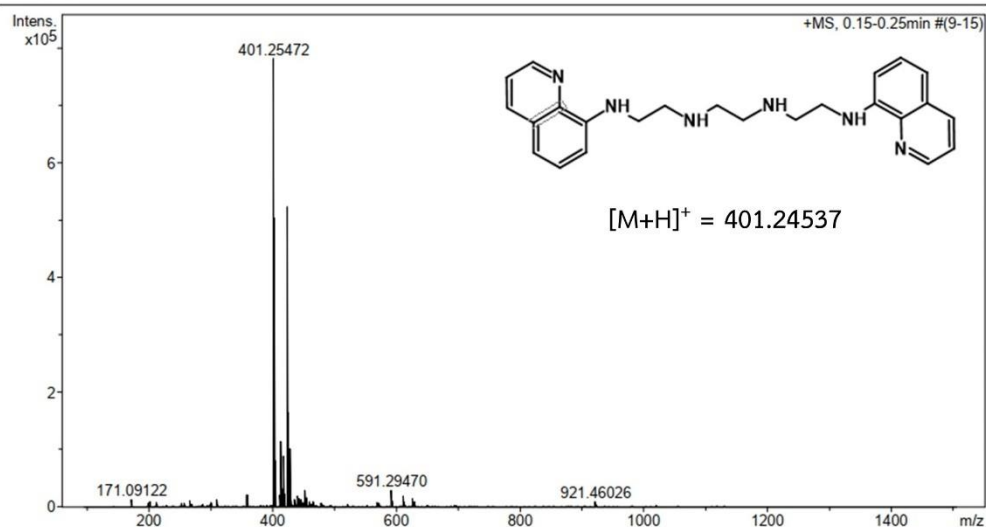


Figure A 23 HRMS of QNNQ.

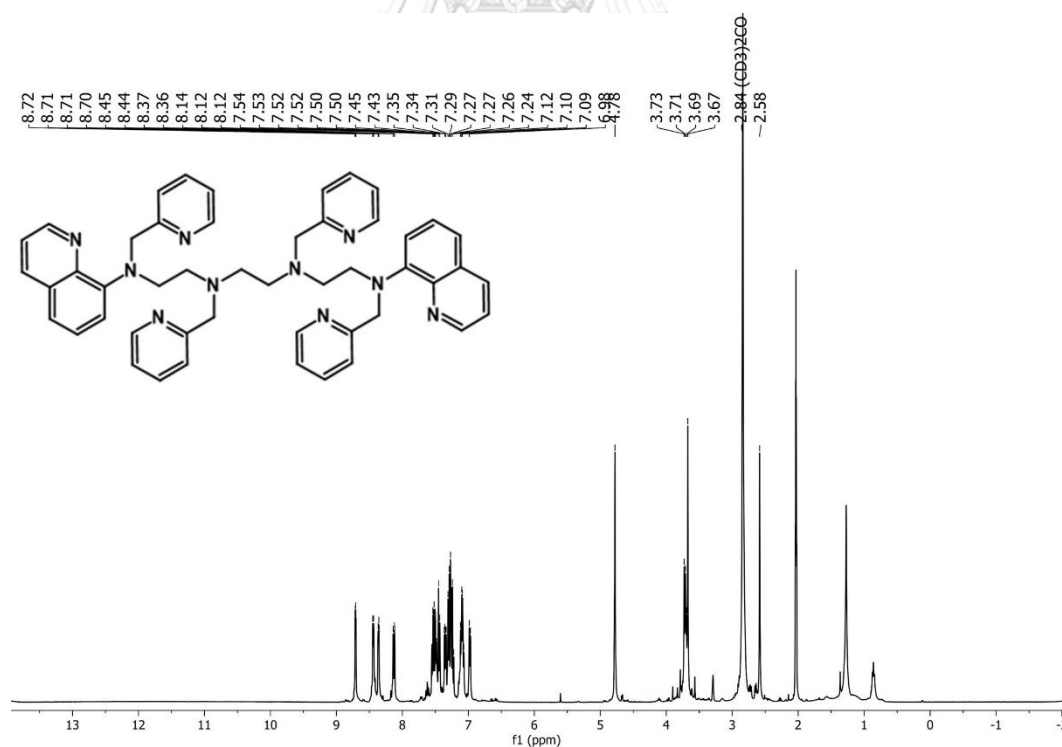
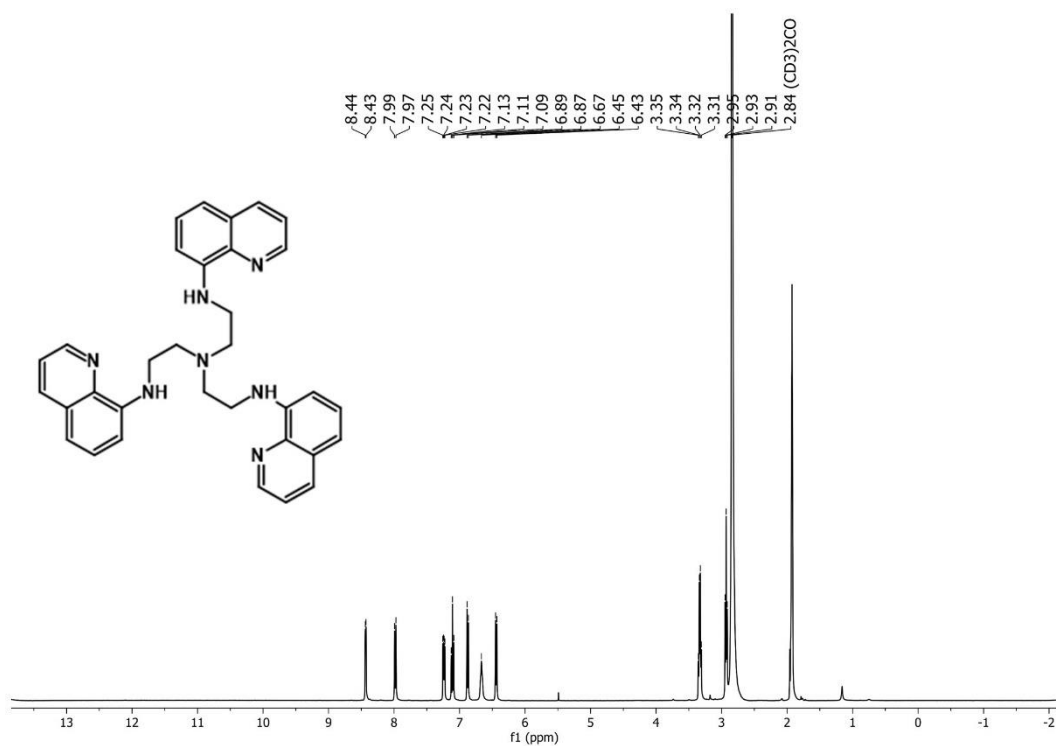
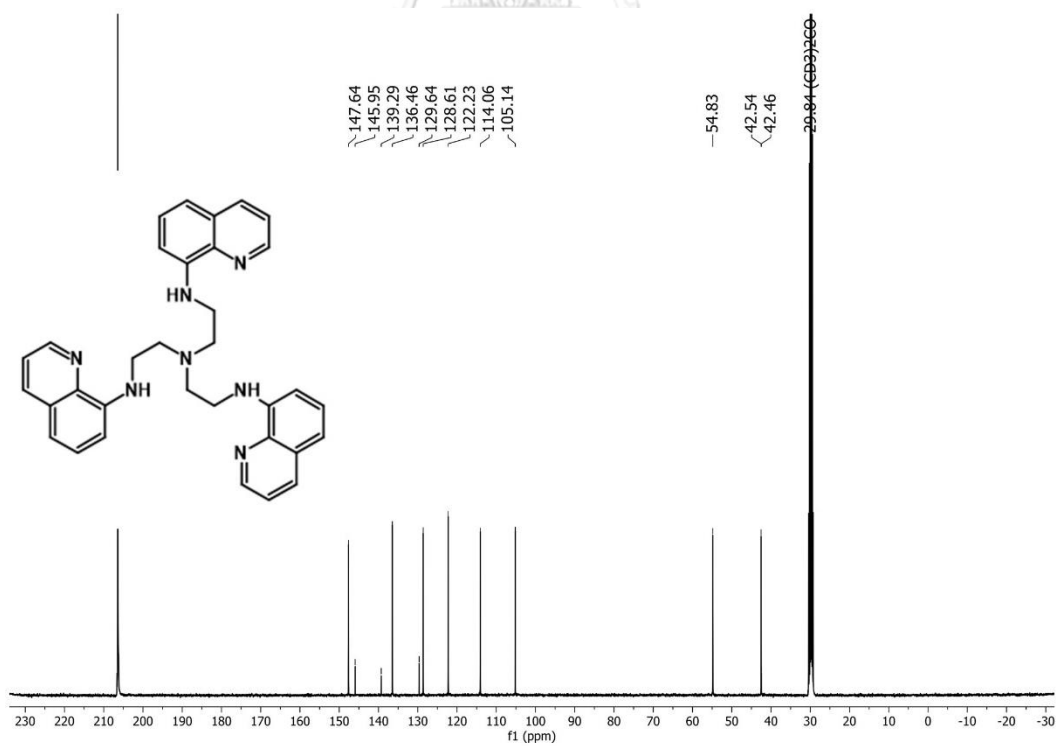


Figure A 24 ^1H NMR of L8 in $(\text{CD}_3)_2\text{CO}$.

Figure A 25 ^1H NMR of **3QN** in $(\text{CD}_3)_2\text{CO}$.Figure A 26 ^{13}C NMR of **3QN** in $(\text{CD}_3)_2\text{CO}$.

Generic Display Report

Analysis Info

Analysis Name D:\Data\Data Service\190813\3QN_RB2_01_2879.d
Method nv_pos_6min_profile_wguardcol_190624.m
Sample Name 3QN
Comment

Acquisition Date 8/13/2019 4:50:15 PM

Operator CU
Instrument micrOTOF-Q II

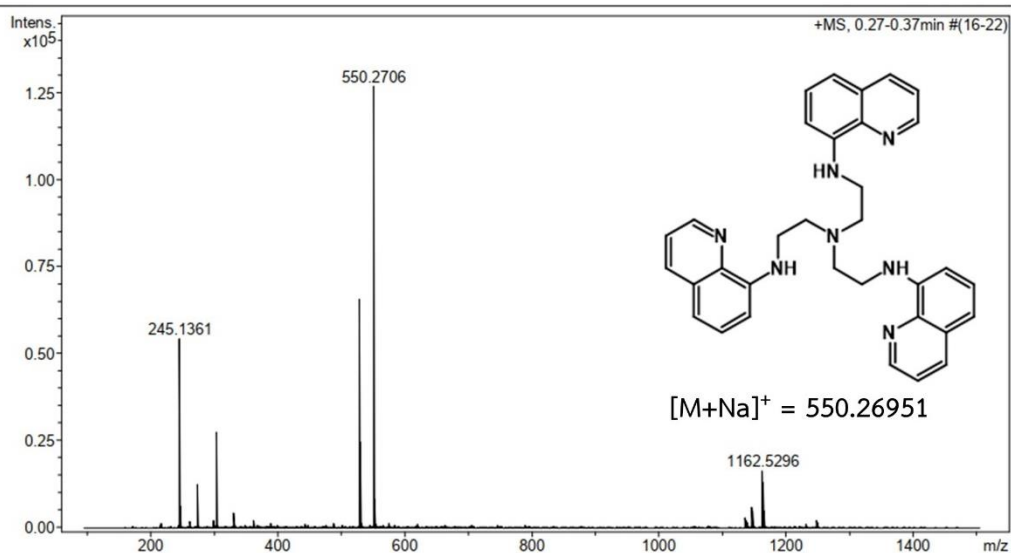
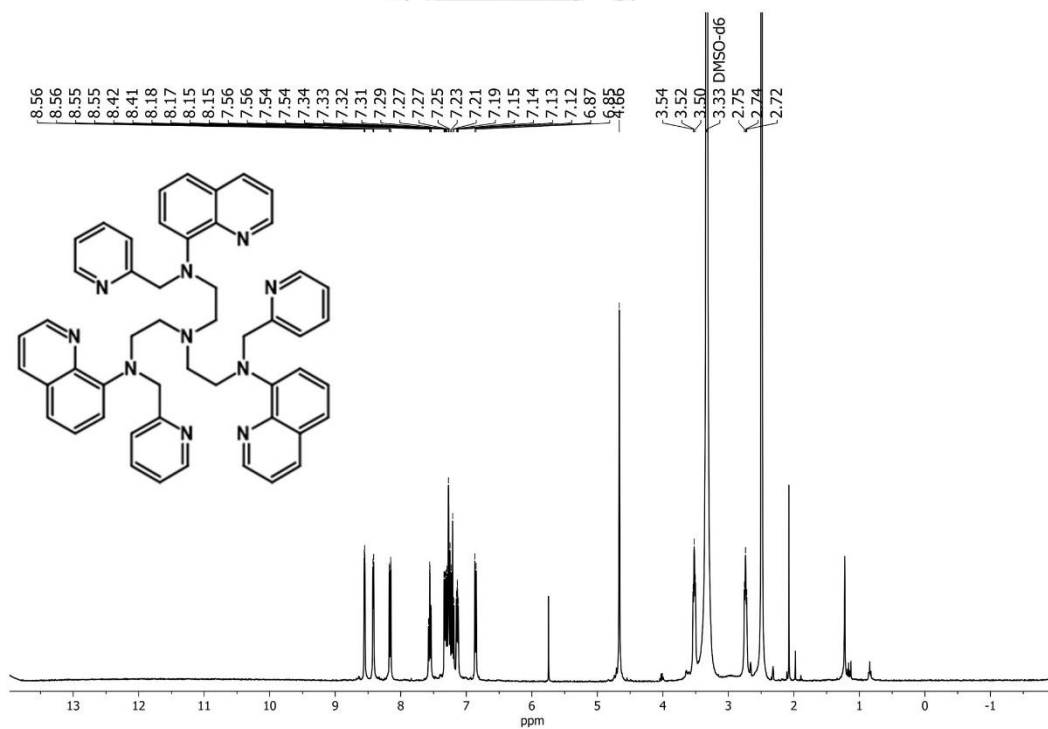
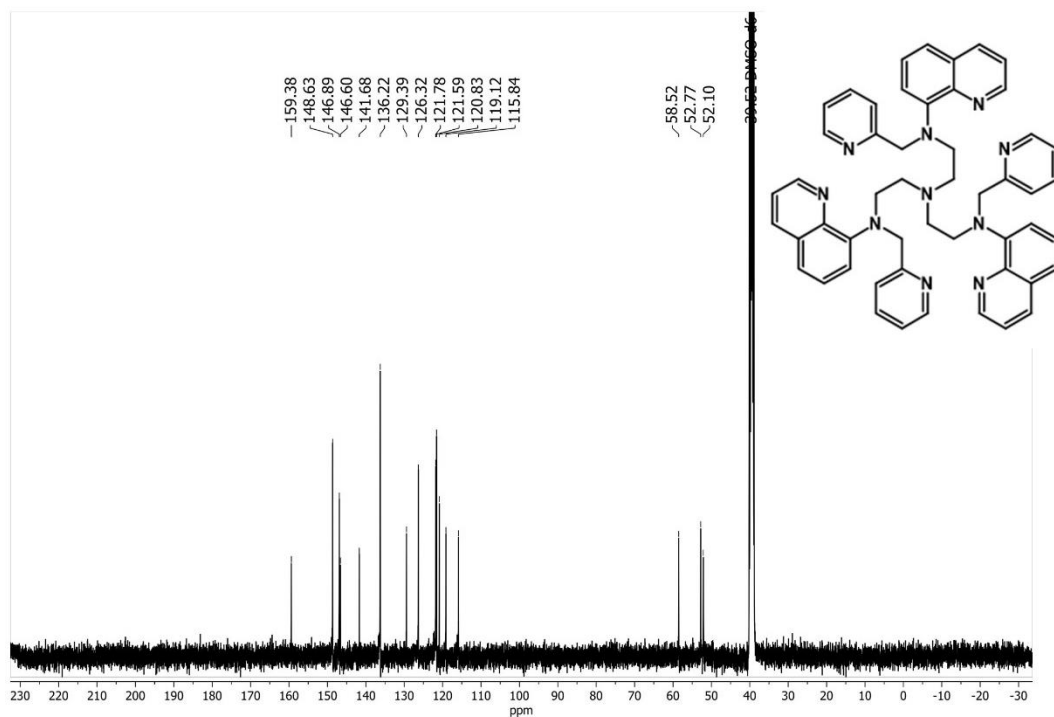


Figure A 27 HRMS of 3QN.

Figure A 28 ^1H NMR of L9 in $(\text{CD}_3)_2\text{SO}$.

Figure A 29 ^{13}C NMR of L9 in $(\text{CD}_3)_2\text{SO}$.

Generic Display Report

Analysis Info

Analysis Name D:\Data\Data Service\201130\3QPN_RA7_01_4943.d
 Method nv_pos_5min_profile_190214.m
 Sample Name 3QPN
 Comment

Acquisition Date 11/30/2020 4:44:17 PM

Operator CU.
 Instrument micrOTOF-Q II

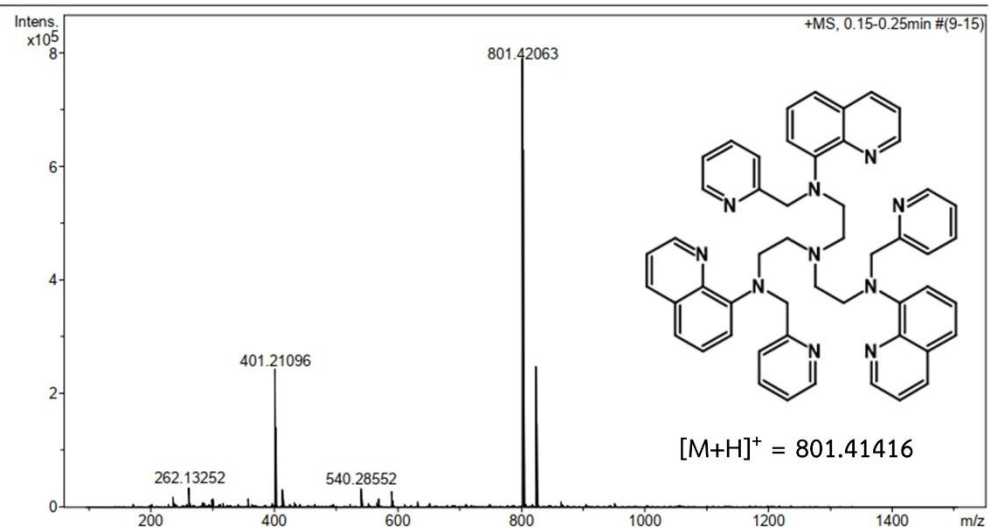
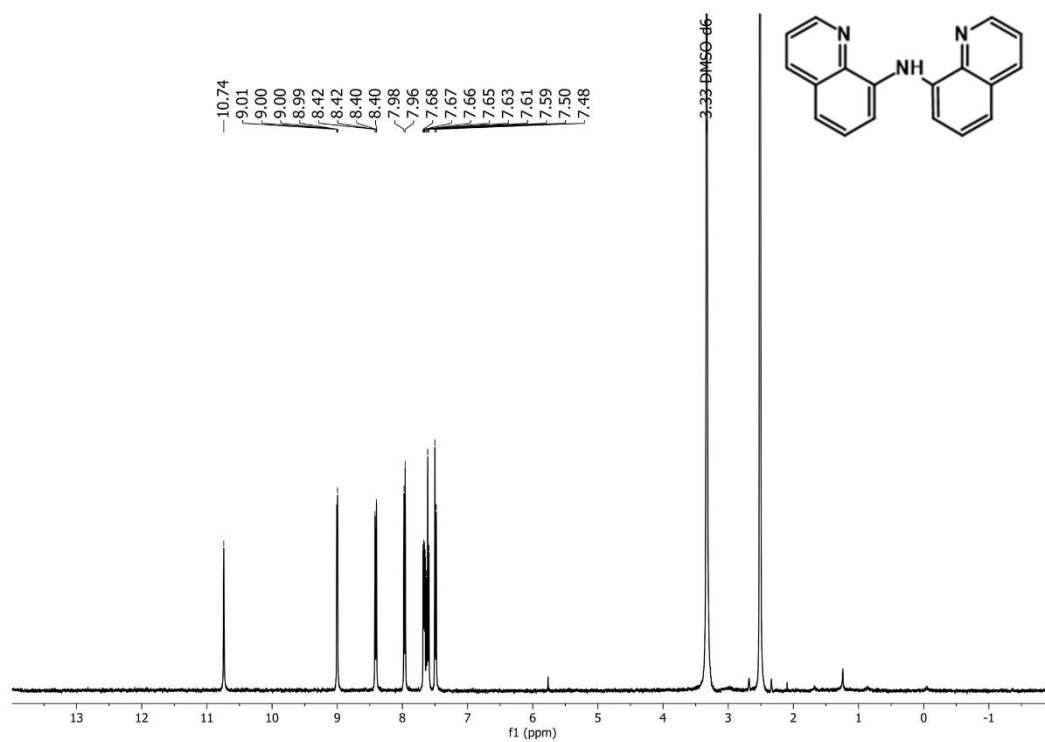
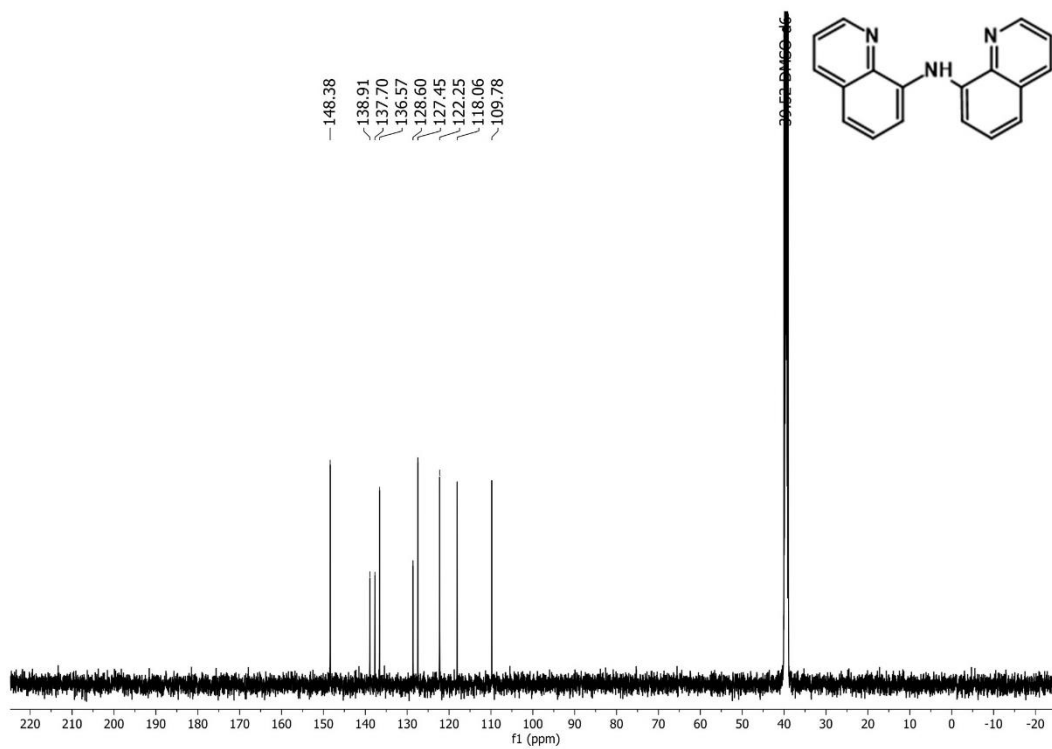


Figure A 30 HRMS of L9.

Figure A 31 ^1H NMR of **L10** in $(\text{CD}_3)_2\text{SO}$.Figure A 32 ^{13}C NMR of **L10** in $(\text{CD}_3)_2\text{SO}$.

Generic Display Report

Analysis Info

Analysis Name D:\Data\Data Service\201130\2Q_RA8_01_4944.d
Method nv_pos_5min_profile_190214.m
Sample Name 2Q
Comment

Acquisition Date 11/30/2020 4:50:41 PM

Operator CU.
Instrument micrOTOF-Q II

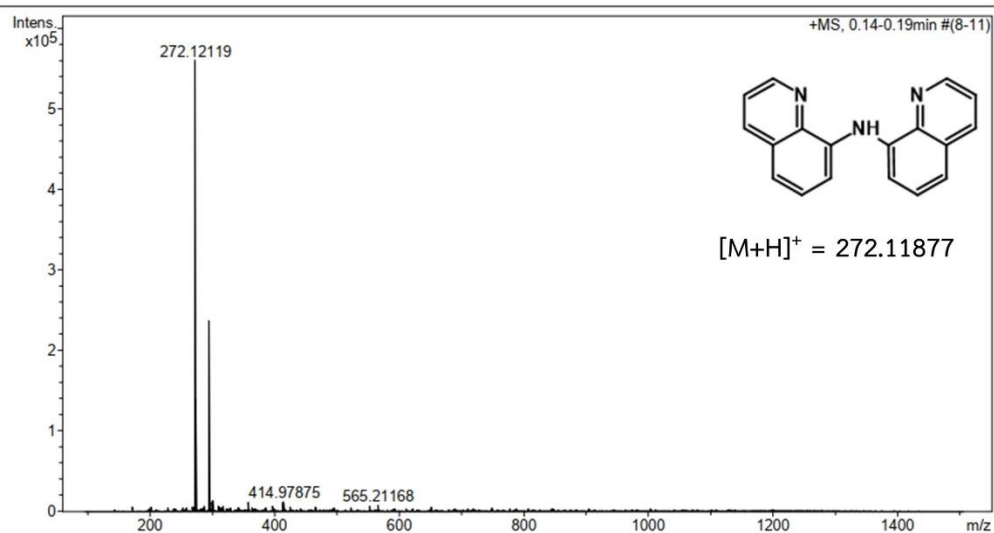
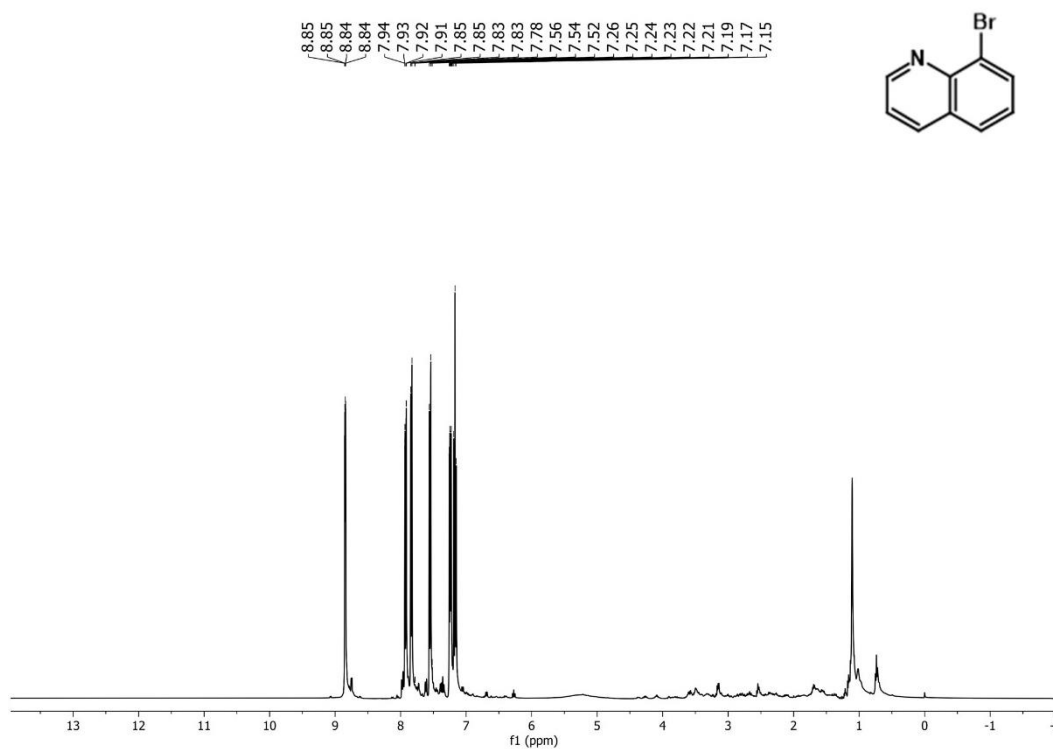
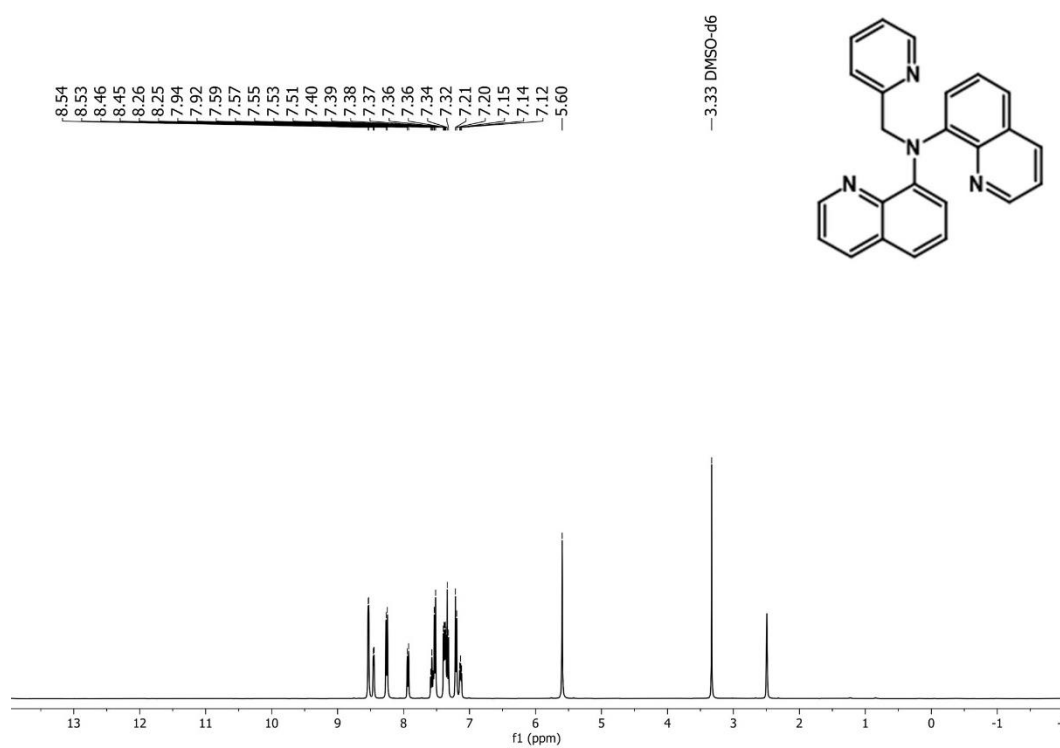
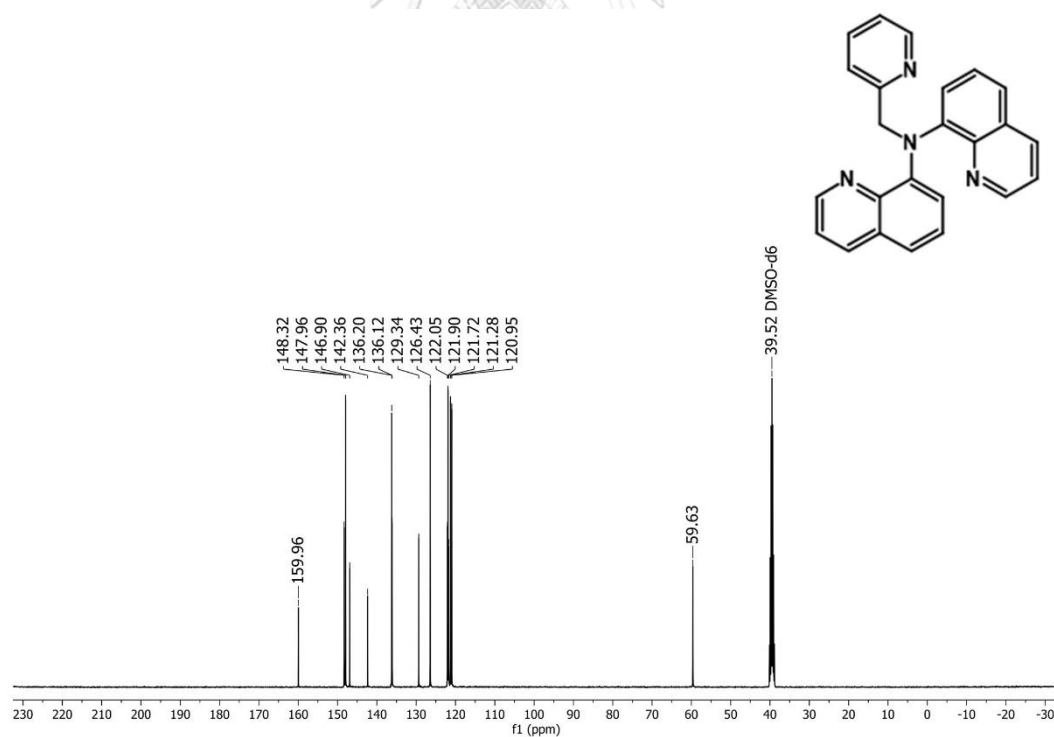


Figure A 33 HRMS of L10.

Figure A 34 ¹H NMR of 8-bromoquinoline in CD₃Cl.

Figure A 35 ^1H NMR of **L11** in $(\text{CD}_3)_2\text{SO}$.Figure A 36 ^{13}C NMR of **L11** in $(\text{CD}_3)_2\text{SO}$.

Generic Display Report

Analysis Info

Analysis Name D:\Data\Data Service\171006_pos_2QP.d
Method NV_pos_0.3min_profile_1segment_lowNubulizerDrygas.m
Sample Name 171006_pos_2QP-2
Comment

Acquisition Date 10/6/2017 10:45:11 AM

Operator CU.
Instrument microTOF-Q II

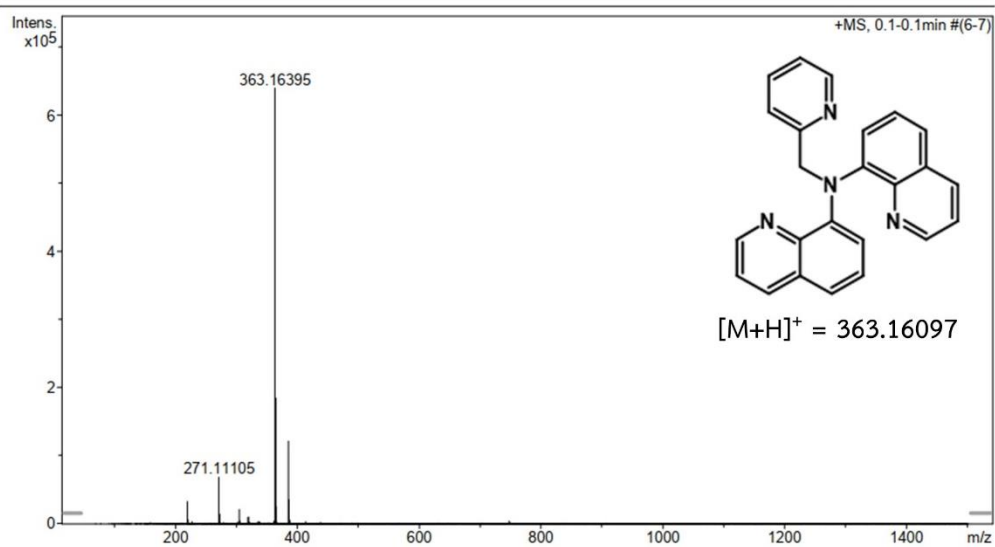
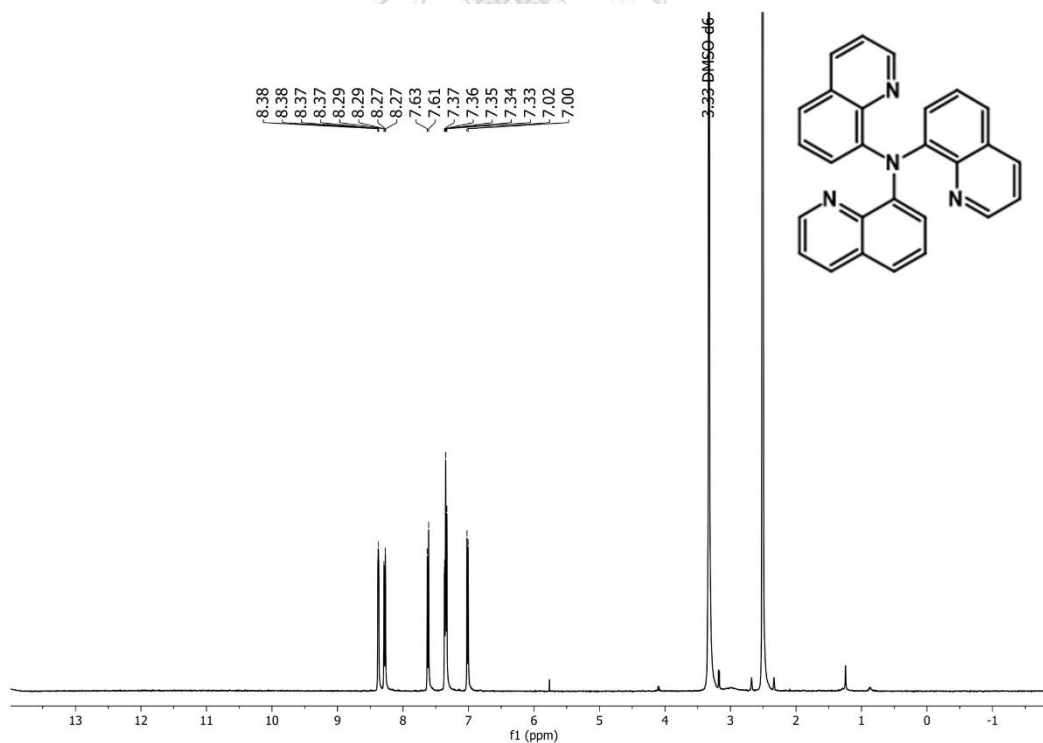
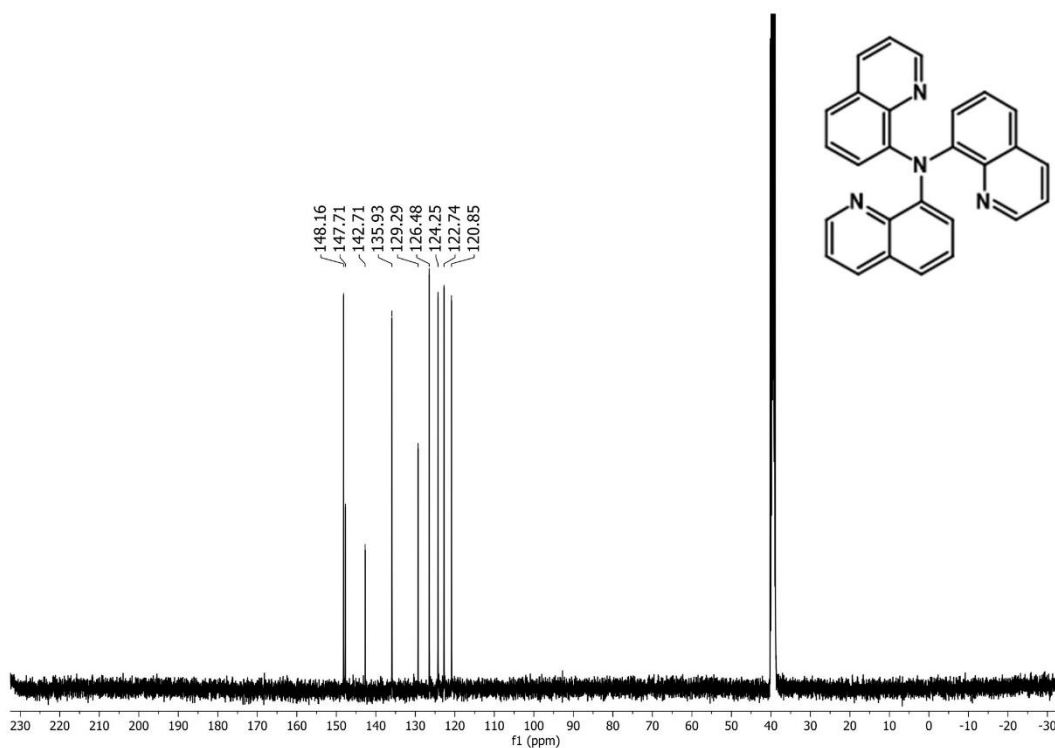


Figure A 37 HRMS of L11.

Figure A 38 ¹H NMR of L12 in (CD₃)₂SO.

Figure A 39 ^{13}C NMR of L12 in $(\text{CD}_3)_2\text{SO}$.

Generic Display Report

Analysis Info		Acquisition Date	
Analysis Name	D:\Data\Data Service\170908_pos_NC3_3Q.d	9/8/2017 10:42:40 AM	
Method	NV_pos_0.3min_profile_1segment_lowNubulizerDrygas.m	Operator	Chem CU.
Sample Name	170908_pos_NC3_3Q	Instrument	micrOTOF-Q II
Comment			

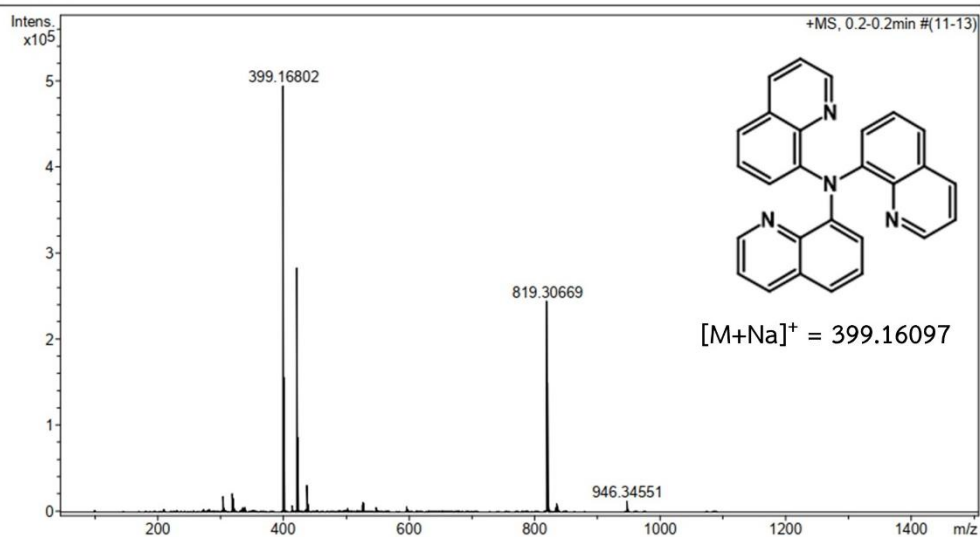
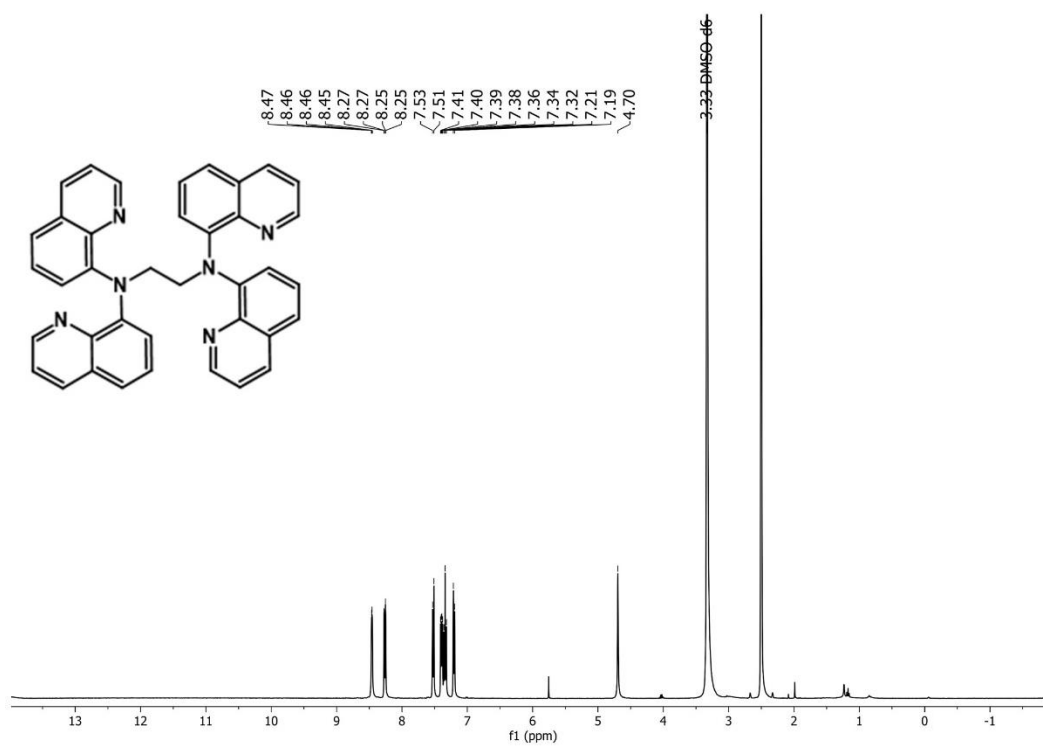
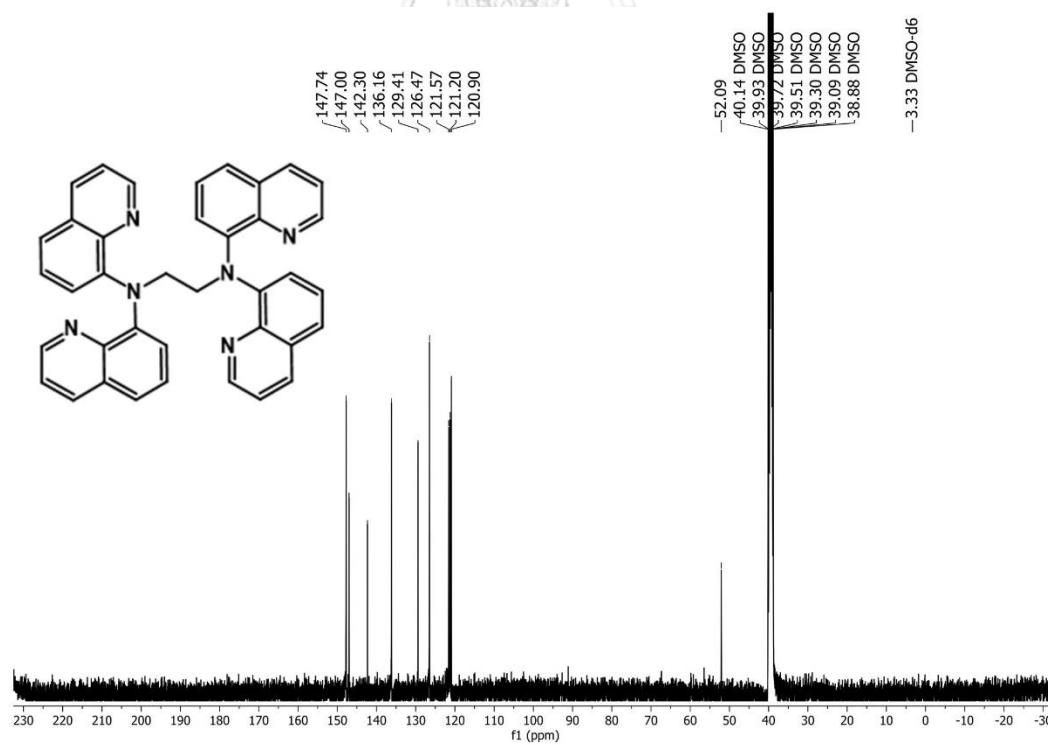


Figure A 40 HRMS of L12.

Figure A 41 ^1H NMR of **L13** in $(\text{CD}_3)_2\text{SO}$.Figure A 42 ^{13}C NMR of **L13** in $(\text{CD}_3)_2\text{SO}$.

Generic Display Report

Analysis Info

Analysis Name D:\Data\Data Service\210104\2Q2Q_RA8_01_5118.d
Method nv_pos_5min_profile_190214.m
Sample Name 2Q2Q
Comment

Acquisition Date 1/4/2021 4:36:17 PM

Operator CU.
Instrument micrOTOF-Q II

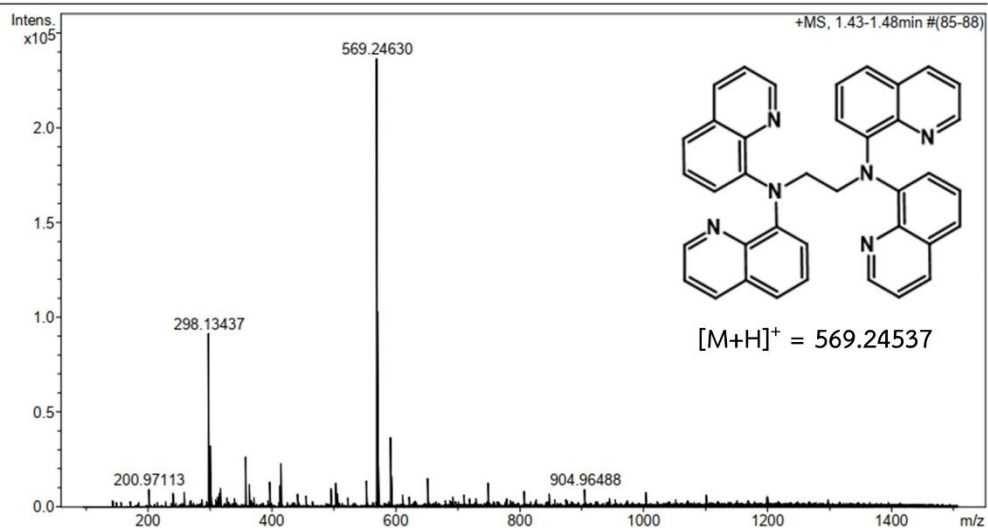
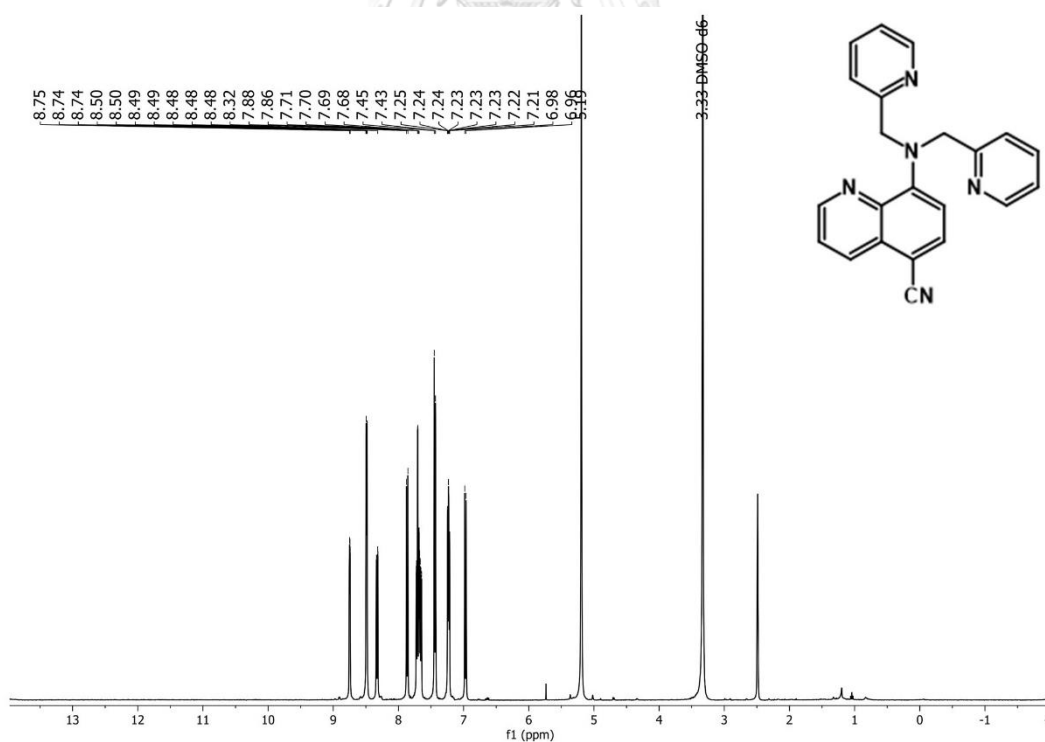
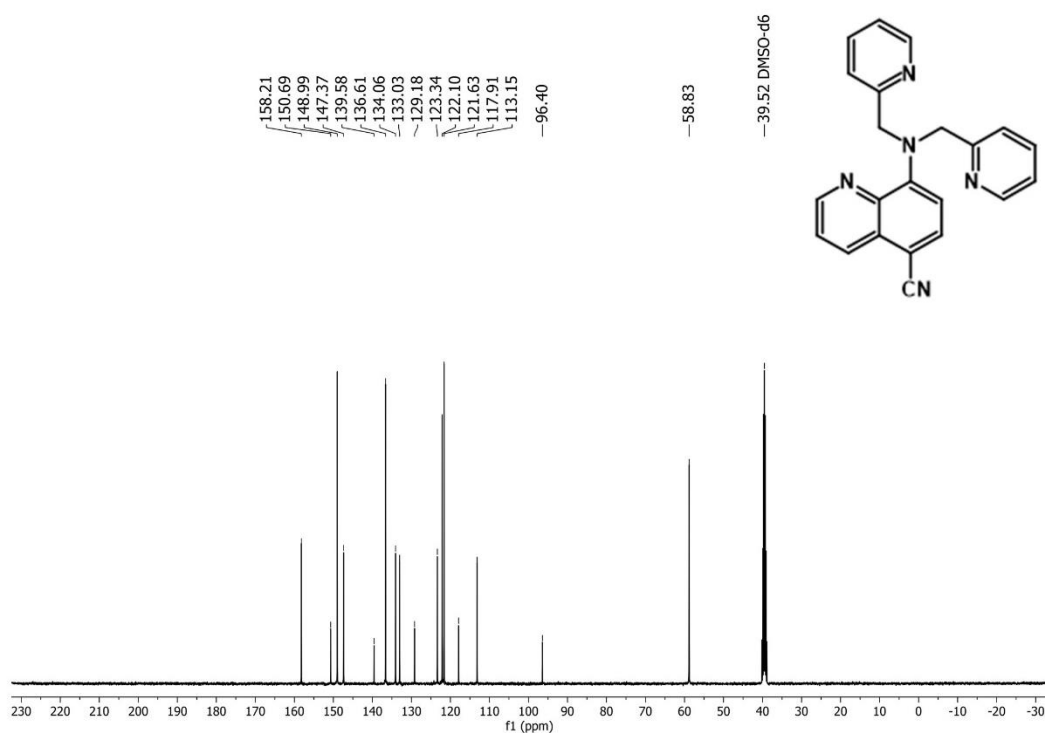
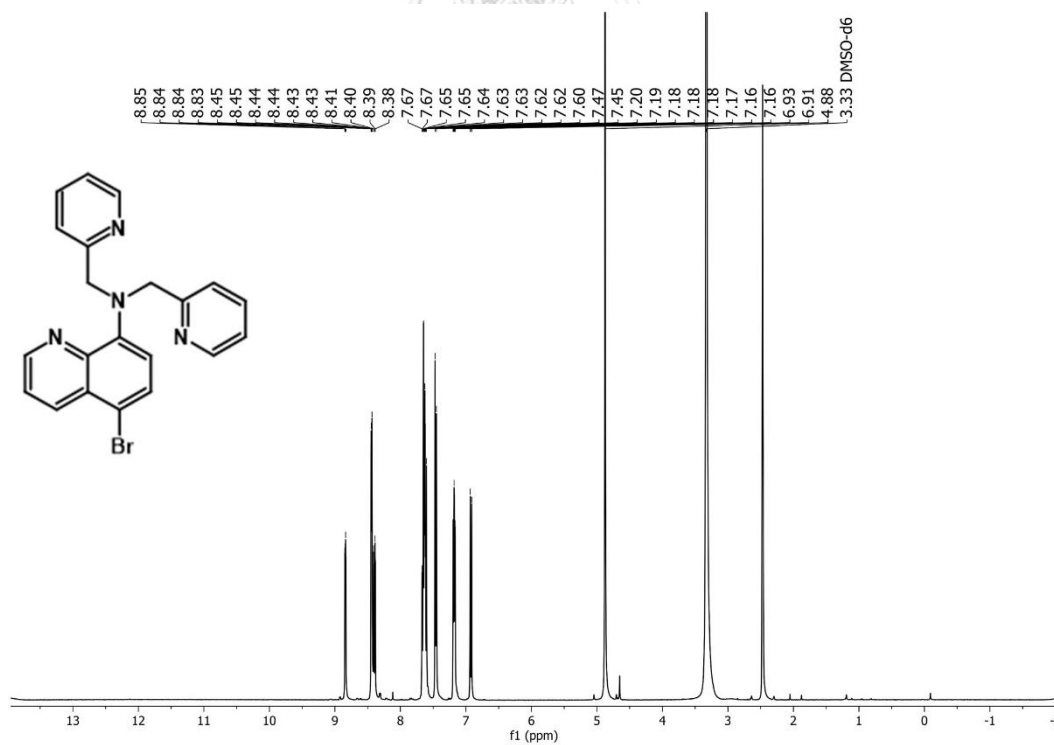
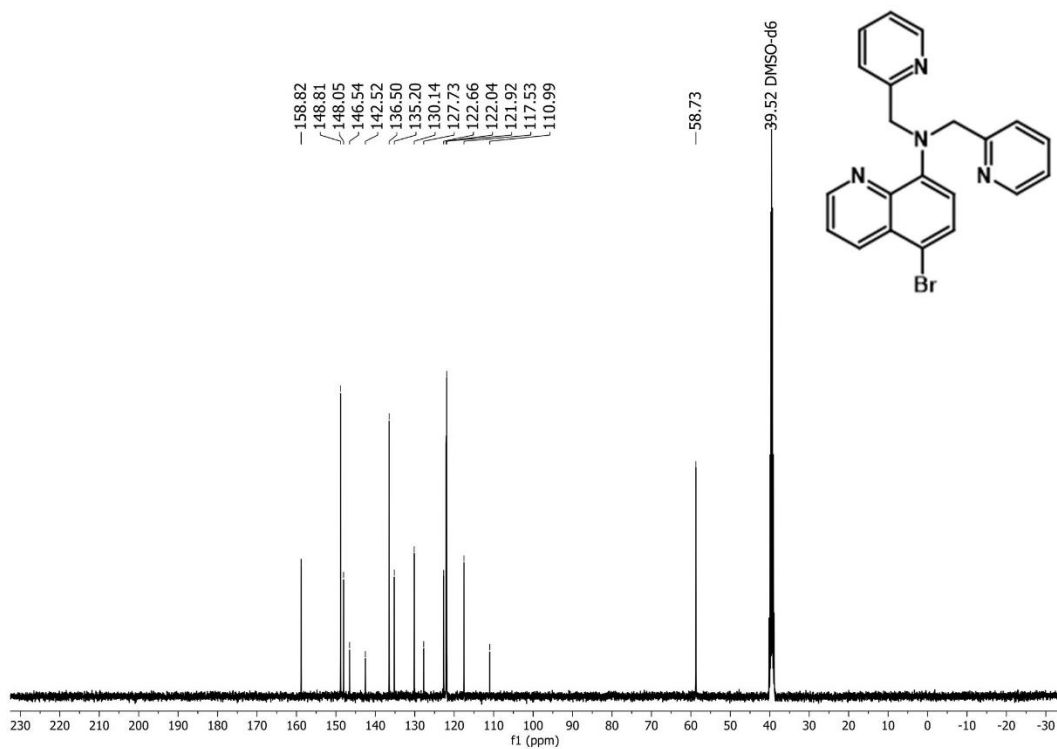
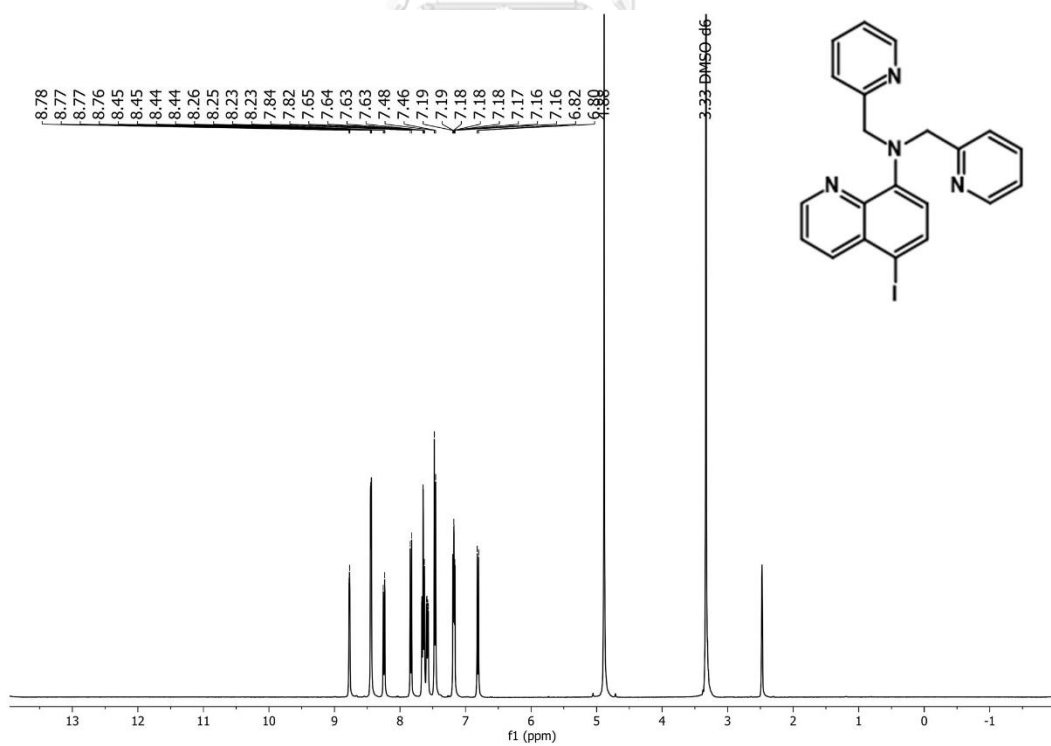
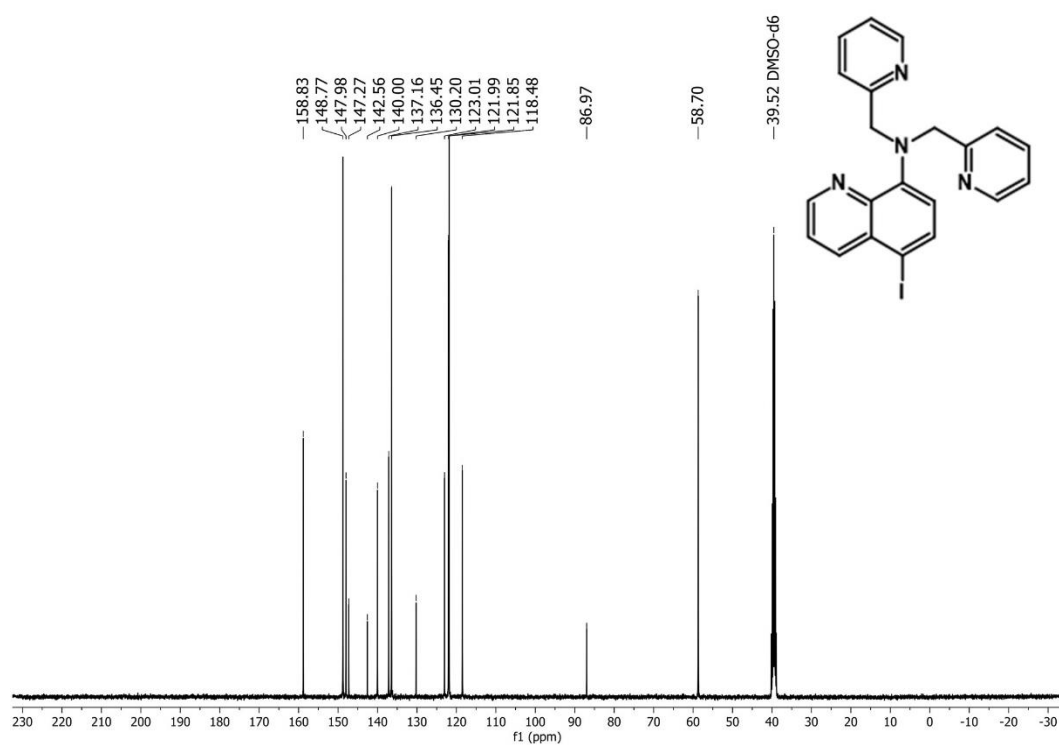
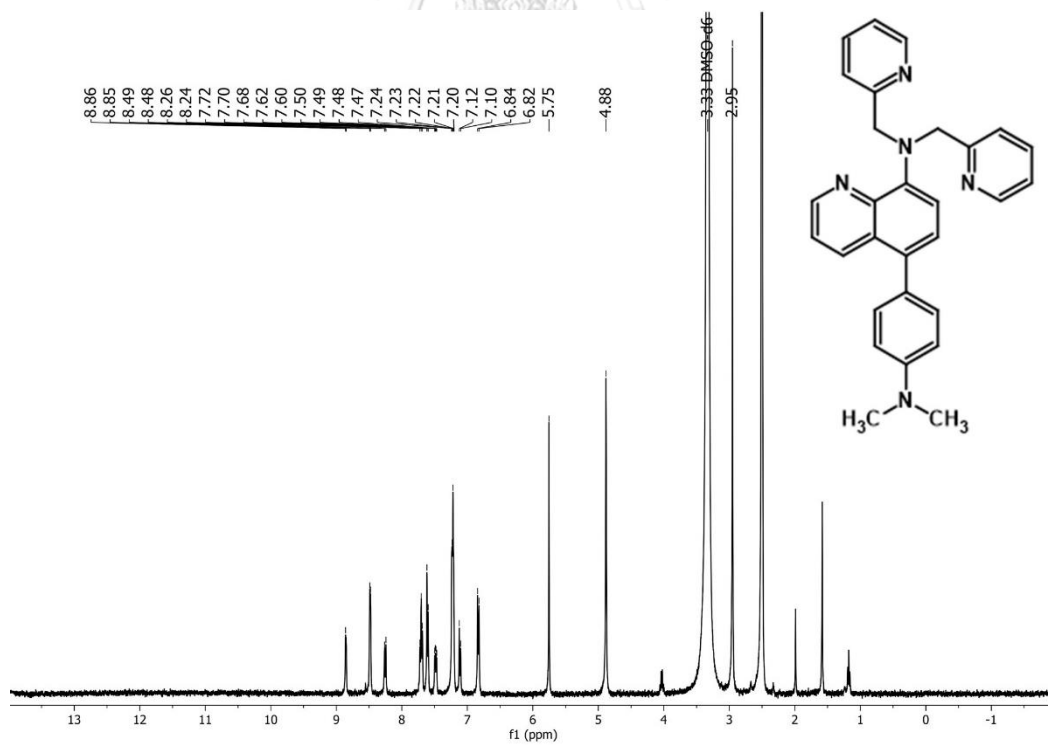


Figure A 43 HRMS of L13.

Figure A 44 ¹H NMR of L14 in (CD₃)₂SO.

Figure A 45 ^{13}C NMR of **L14** in $(\text{CD}_3)_2\text{SO}$.Figure A 46 ^1H NMR of **L15** in $(\text{CD}_3)_2\text{SO}$.

Figure A 47 ^{13}C NMR of **L15** in $(\text{CD}_3)_2\text{SO}$.Figure A 48 ^1H NMR of **L16** in $(\text{CD}_3)_2\text{SO}$.

Figure A 49 ^{13}C NMR of L16 in $(\text{CD}_3)_2\text{SO}$.Figure A 50 ^1H NMR of L17 in $(\text{CD}_3)_2\text{SO}$.

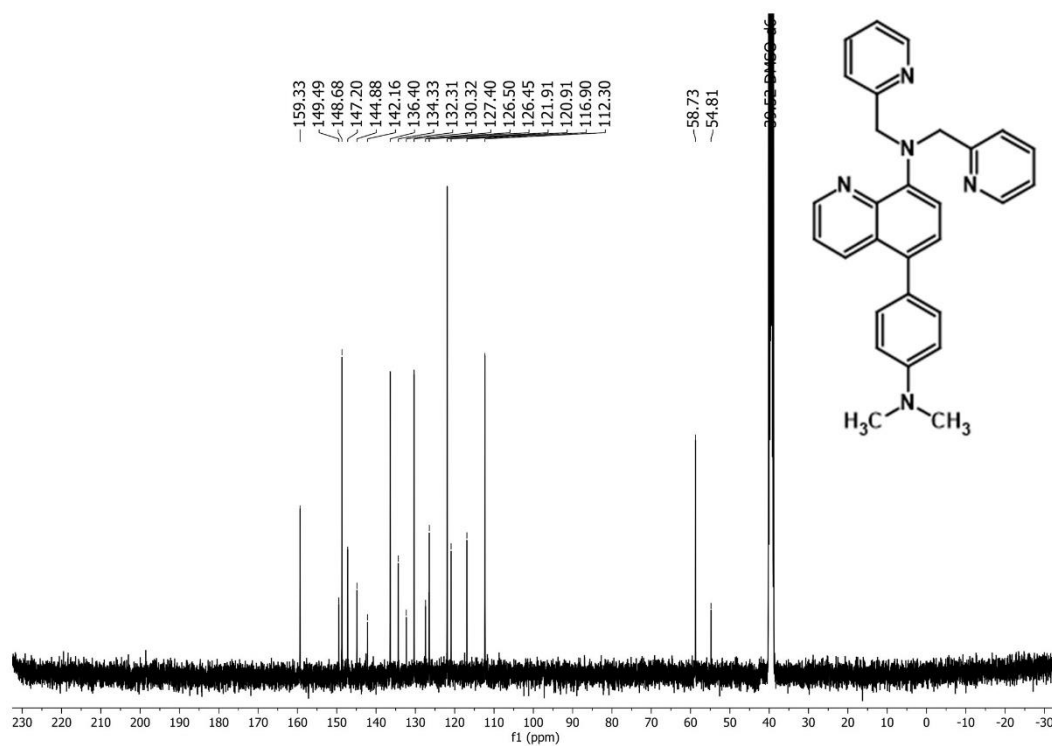


Figure A 51 ^{13}C NMR of L17 in $(\text{CD}_3)_2\text{SO}$.

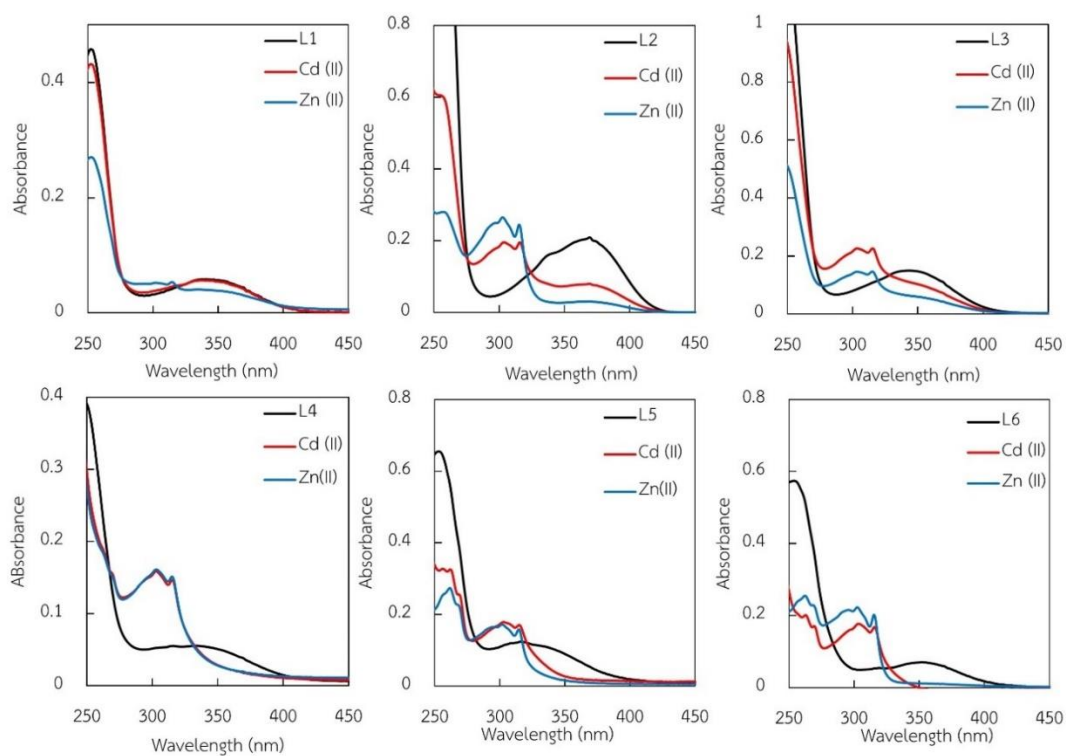


Figure A 52 absorbance of **L1–L6** (30 μM) in the presence of Cd^{2+} or Zn^{2+} (30 μM) in aqueous solution.

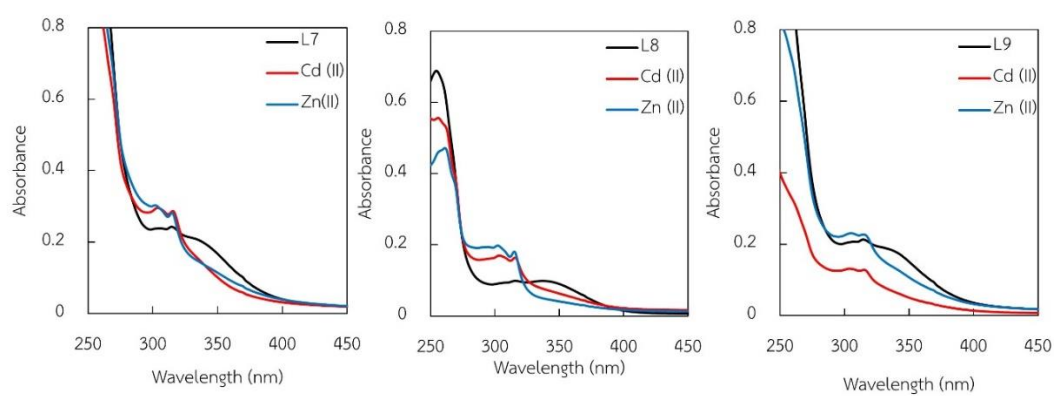


Figure A 53 absorbance of **L7–L9** (30 μM) in the presence of Cd^{2+} or Zn^{2+} (30 μM) in aqueous solution.

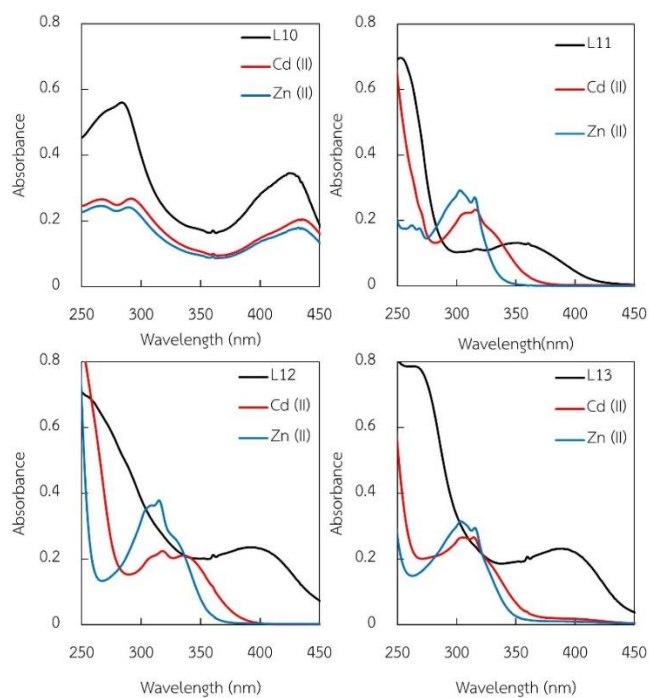


Figure A 54 absorbance of **L10–L13** (30 μM) in the presence of Cd^{2+} or Zn^{2+} (30 μM) in aqueous solution.

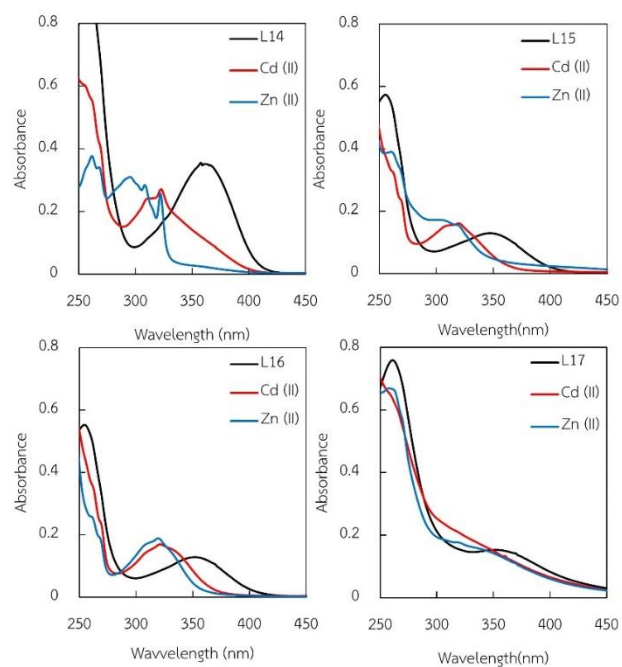
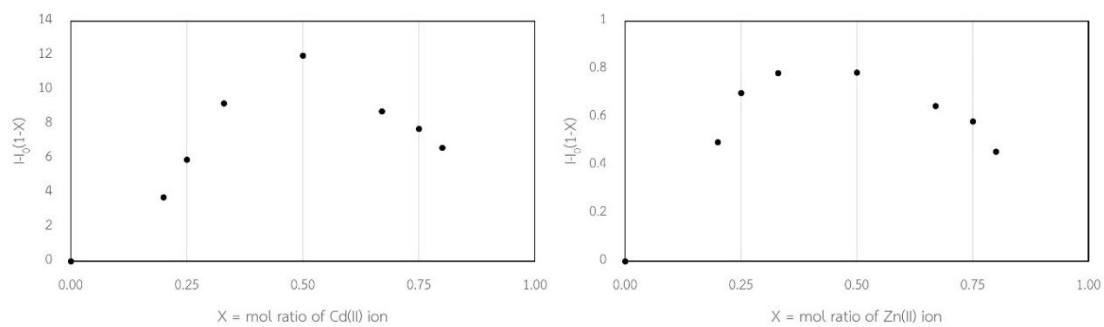
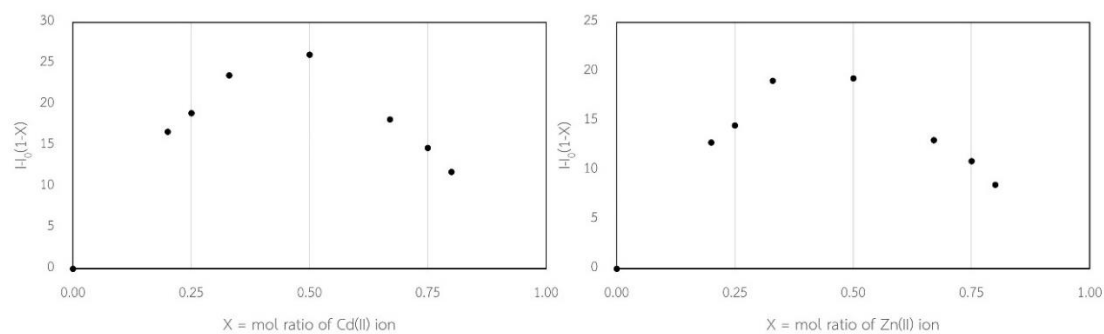
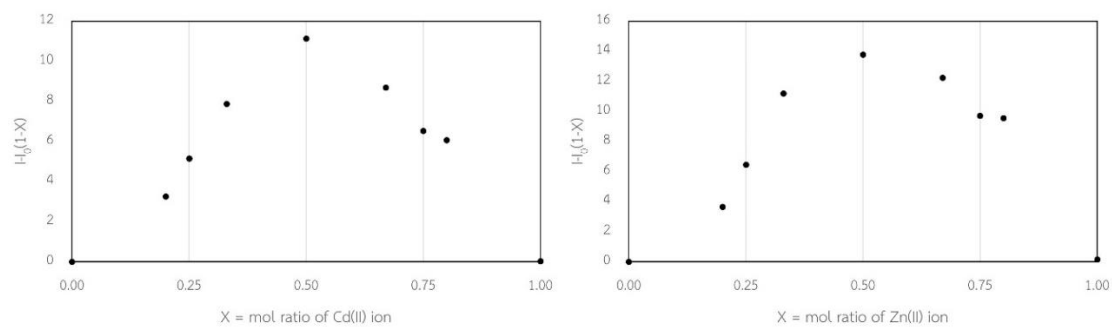


Figure A 55 absorbance of **L14–L17** (30 μM) in the presence of Cd^{2+} or Zn^{2+} (30 μM) in aqueous solution.

Figure A 56 Job's plots of L1 with Cd²⁺ (left) and Zn²⁺ (right)Figure A 57 Job's plots of L2 with Cd²⁺ (left) and Zn²⁺ (right)Figure A 58 Job's plots of L3 with Cd²⁺ (left) and Zn²⁺ (right)

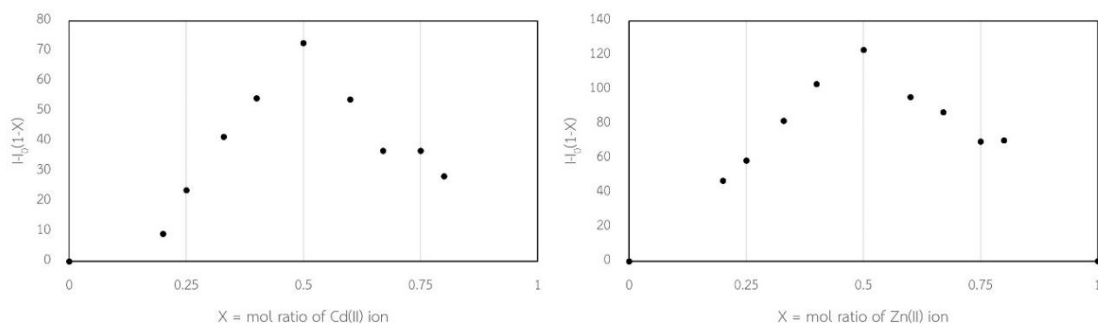


Figure A 59 Job's plots of L4 with Cd²⁺ (left) and Zn²⁺ (right)

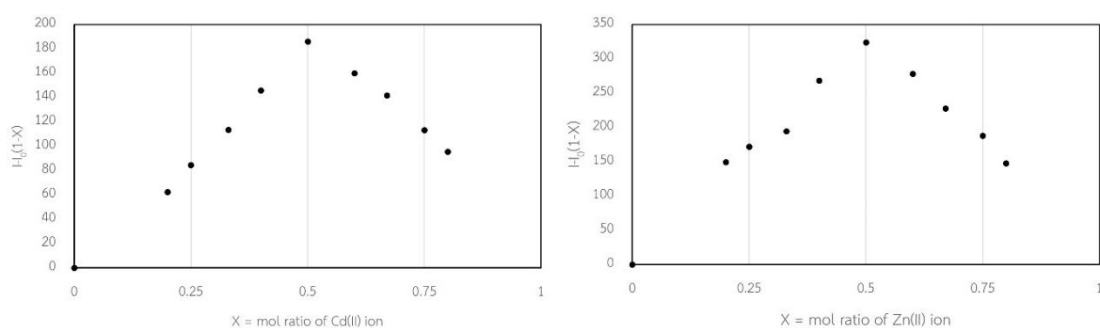


Figure A 60 Job's plots of L5 with Cd²⁺ (left) and Zn²⁺ (right)

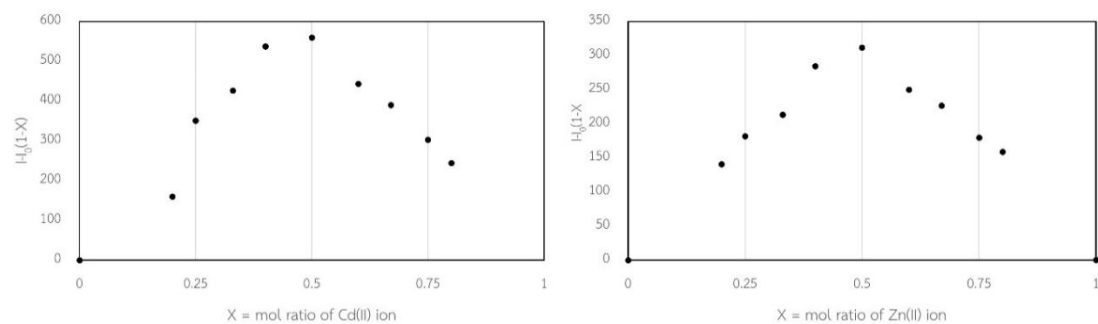


Figure A 61 Job's plots of L6 with Cd²⁺ (left) and Zn²⁺ (right)

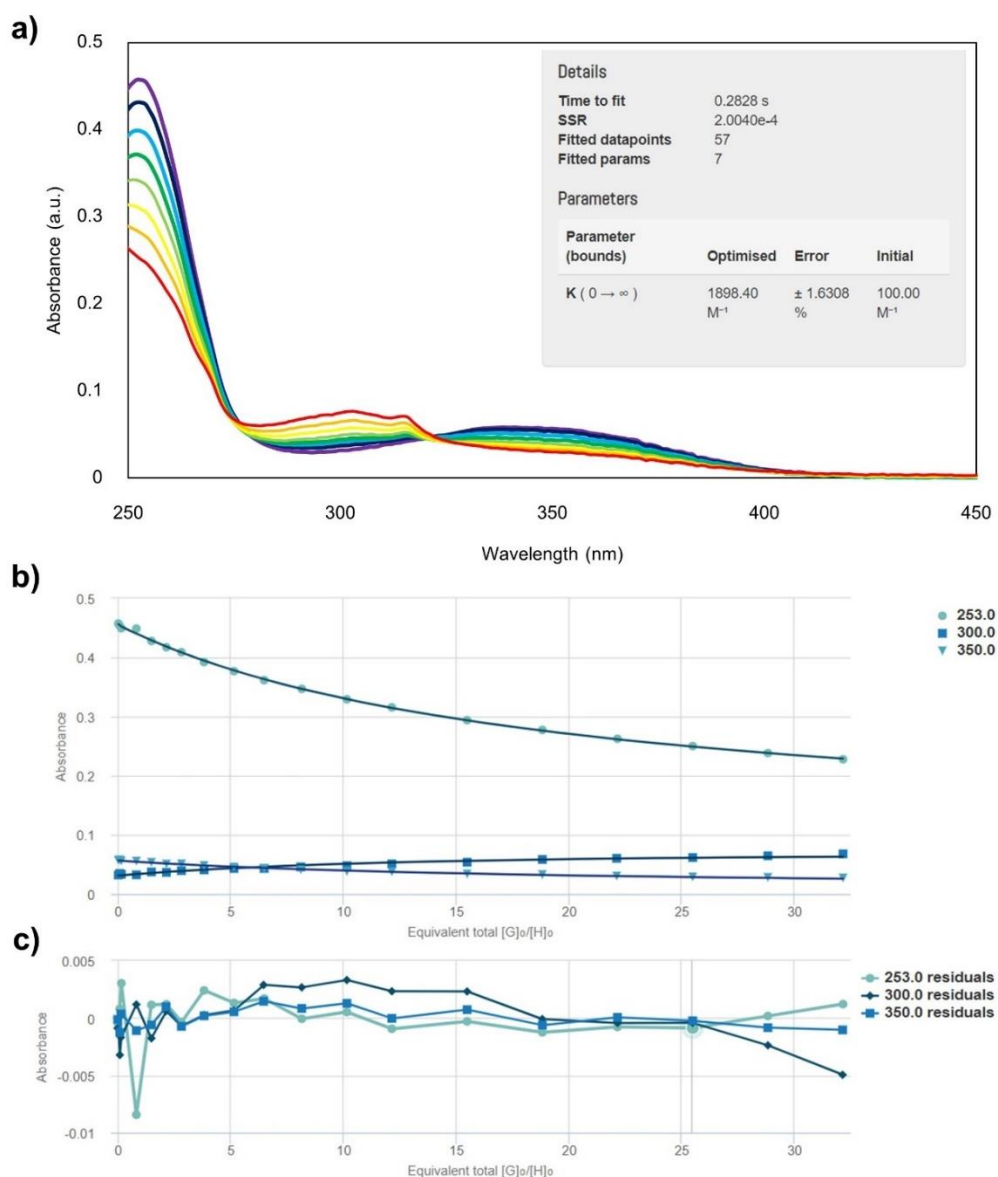


Figure A 62 a) UV titration between **L1** and Cd^{2+} (inset) summary table of the results of the curve fitting, b) scatter plots between absorbance and amount of Cd^{2+} at 253, 300 and 350 nm, the lines show non-linear curve fitting of the absorbance values at all three wavelengths used for determination of K_a value. c) the residual plots of the corresponding fitting.

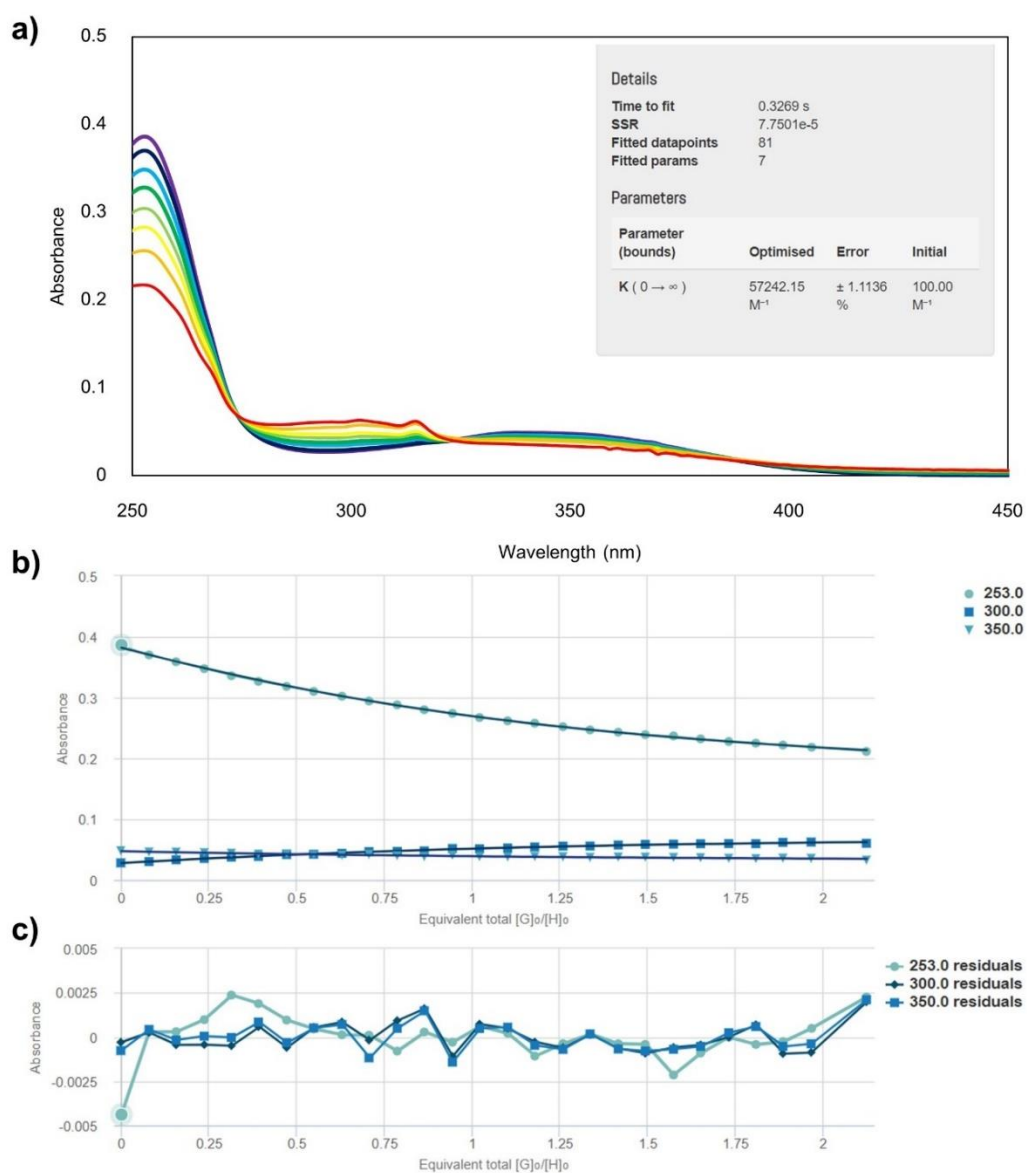


Figure A 63 a) UV titration between **L1** and Zn^{2+} (inset) summary table of the results of the curve fitting, b) scatter plots between absorbance and amount of Zn^{2+} at 253, 300 and 350 nm, the lines show non-linear curve fitting of the absorbance values at all three wavelengths used for determination of K_a value. c) residual plots of the corresponding fitting.

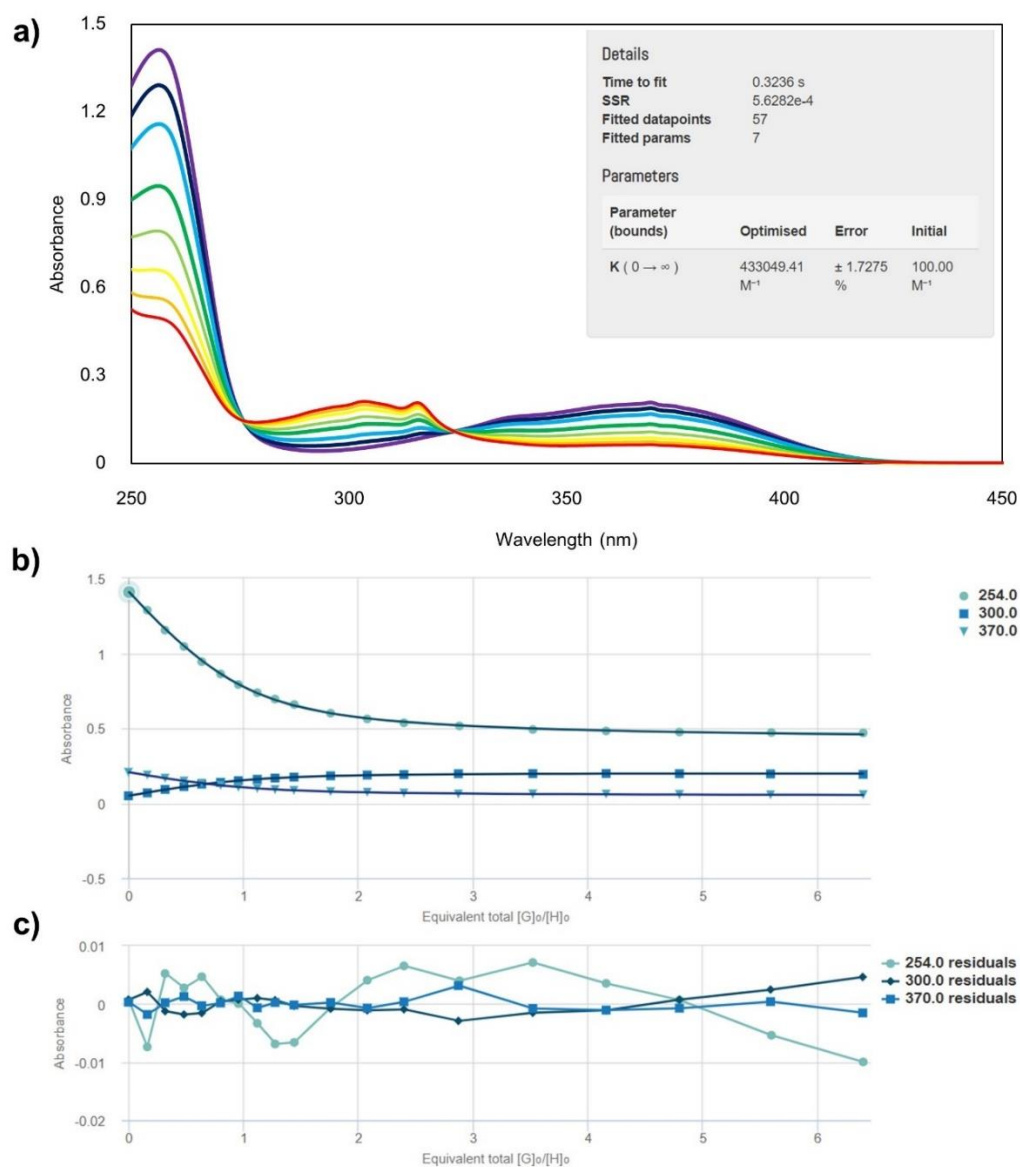


Figure A 64 a) UV titration between **L2** and Cd^{2+} (inset) summary table of the results of the curve fitting, b) scatter plots between absorbance and amount of Cd^{2+} at 254, 300 and 370 nm, the lines show non-linear curve fitting of the absorbance values at all three wavelengths used for determination of K_a value. c) the residual plots of the corresponding fitting.

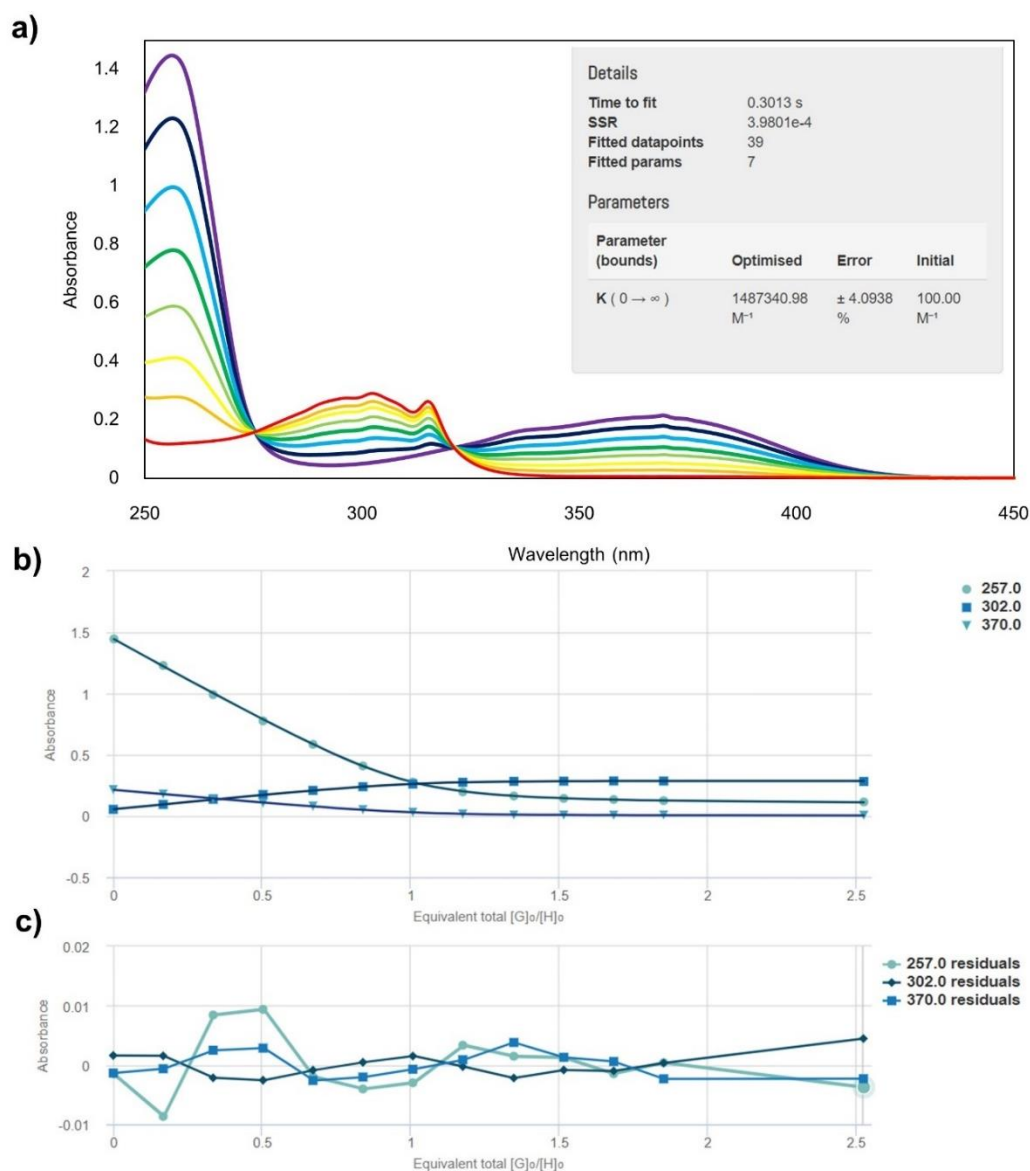


Figure A 65 UV titration between **L2** and Zn^{2+} (inset) summary table of the results of the curve fitting, b) scatter plots between absorbance and amount of Zn^{2+} at 254, 300 and 370 nm, the lines show non-linear curve fitting of the absorbance values at all three wavelengths used for determination of K_a value. c) residual plots of the corresponding fitting.

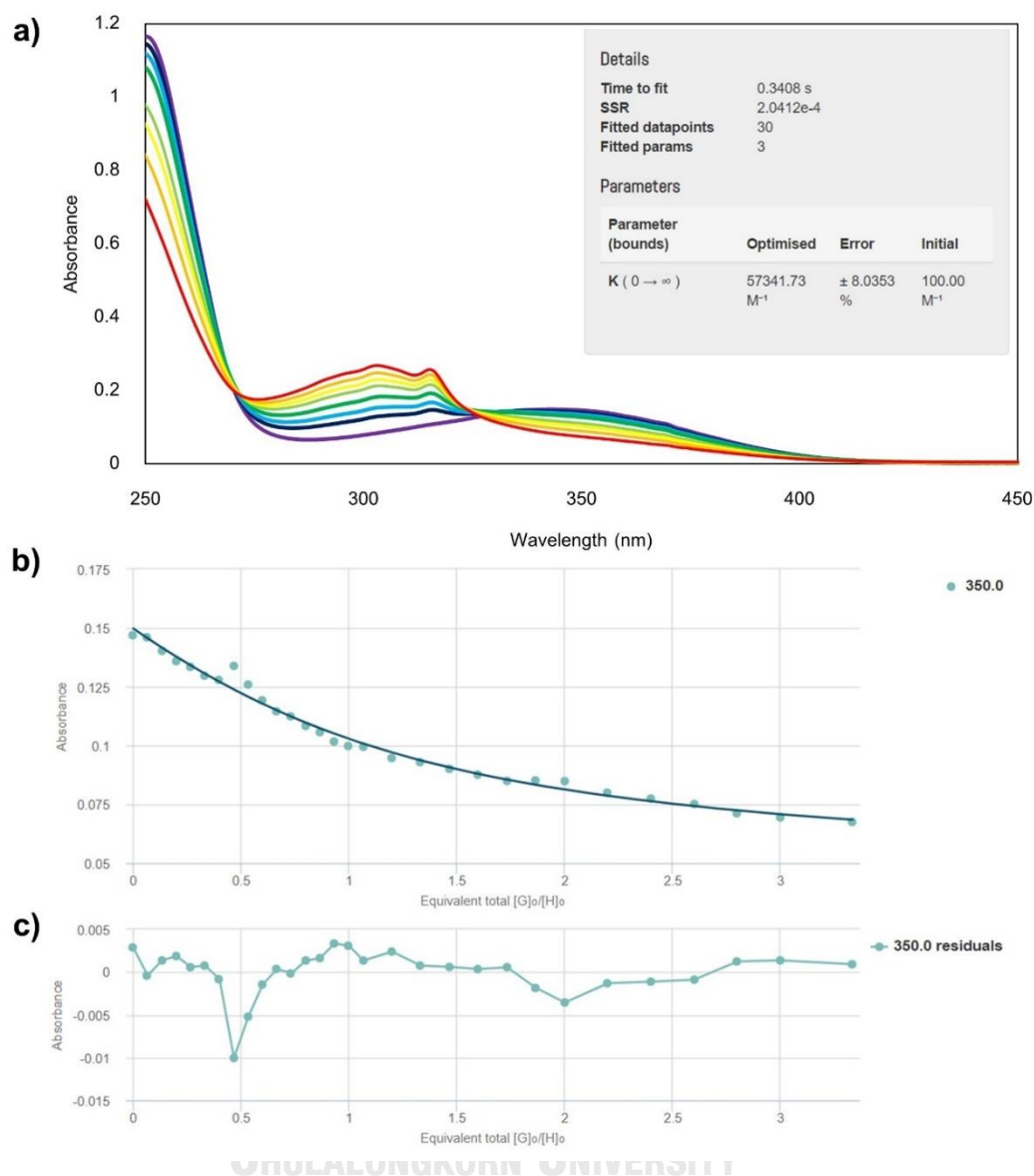


Figure A 66 a) UV titration between **L3** and Cd^{2+} (inset) summary table of the results of the curve fitting, b) scatter plots between absorbance and amount of Cd^{2+} at 350 nm, the line shows non-linear curve fitting of the absorbance values used for determination of K_a value. c) residual plots of the corresponding fitting.

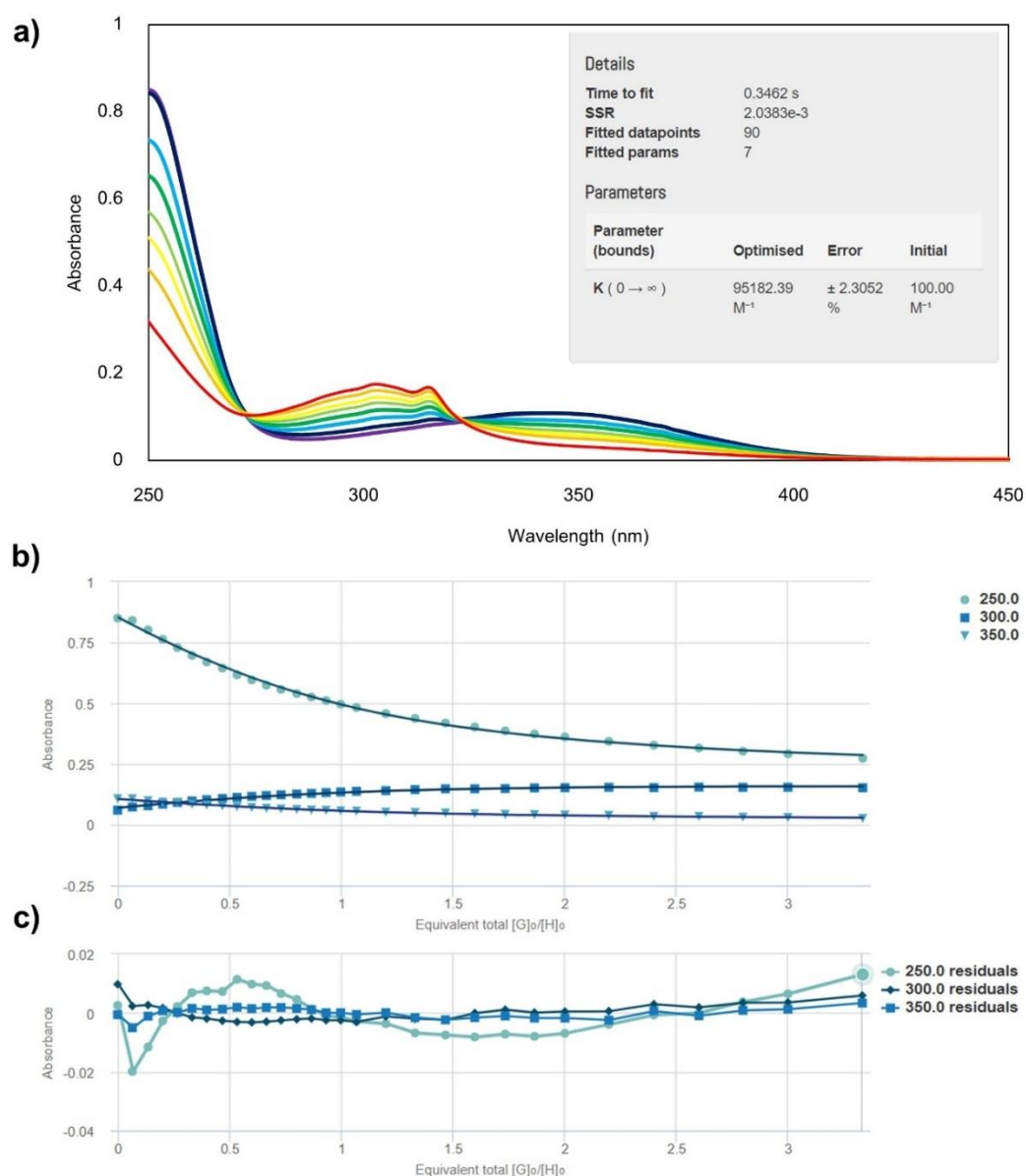


Figure A 67 a) UV titration between **L3** and Zn^{2+} (inset) summary table of the results of the curve fitting, b) scatter plots between absorbance and amount of Zn^{2+} at 250 300 and 300 nm, the lines show non-linear curve fitting of the absorbance values at all three wavelengths used for determination of K_a value. c) residual plots of the corresponding fitting.

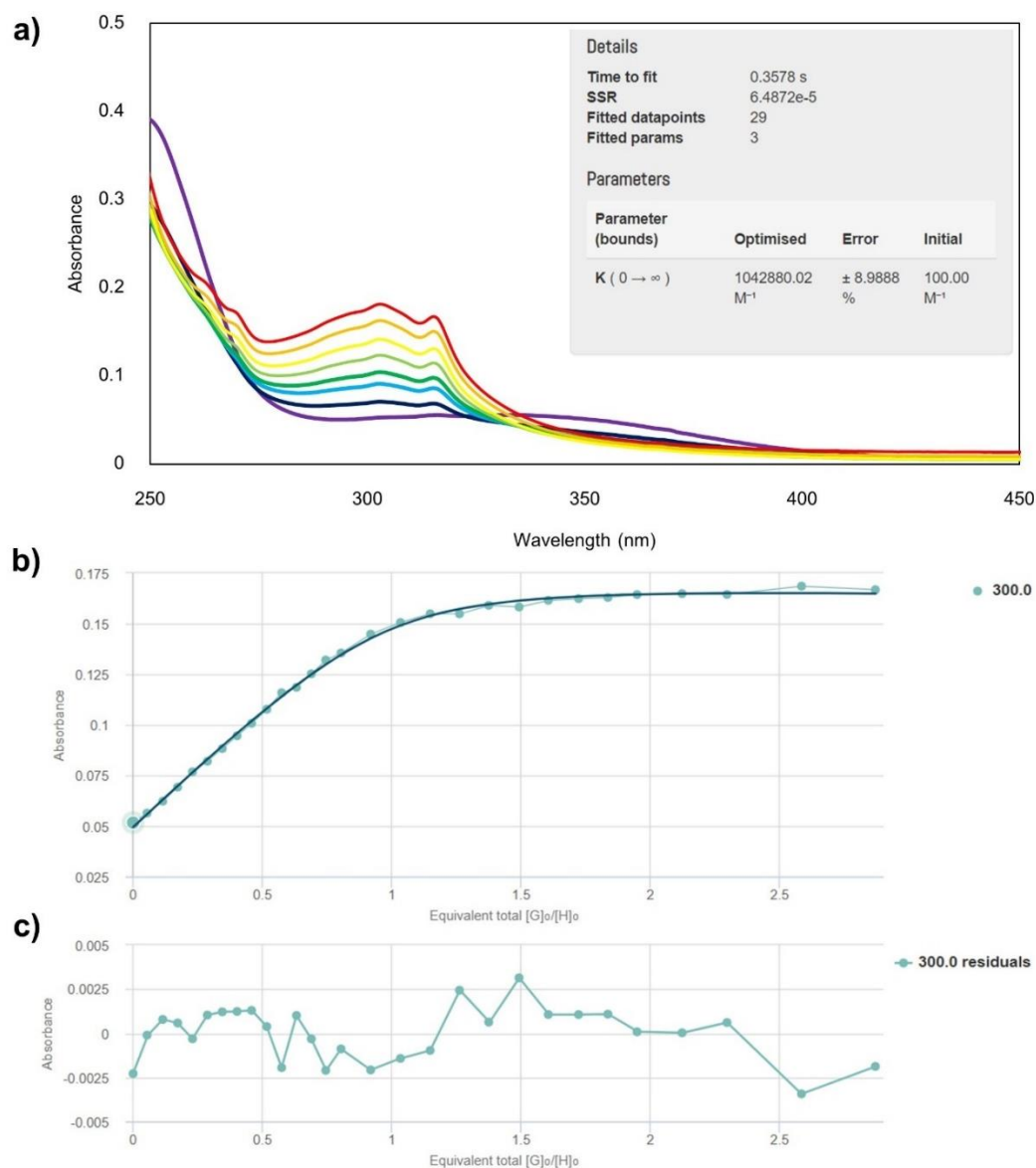


Figure A 68 UV titration between **L4** and Cd^{2+} (inset) summary table of the results of the curve fitting, b) scatter plots between absorbance and amount of Cd^{2+} at 300 nm, the line shows non-linear curve fitting of the absorbance values used for determination of K_a value. c) residual plots of the corresponding fitting.

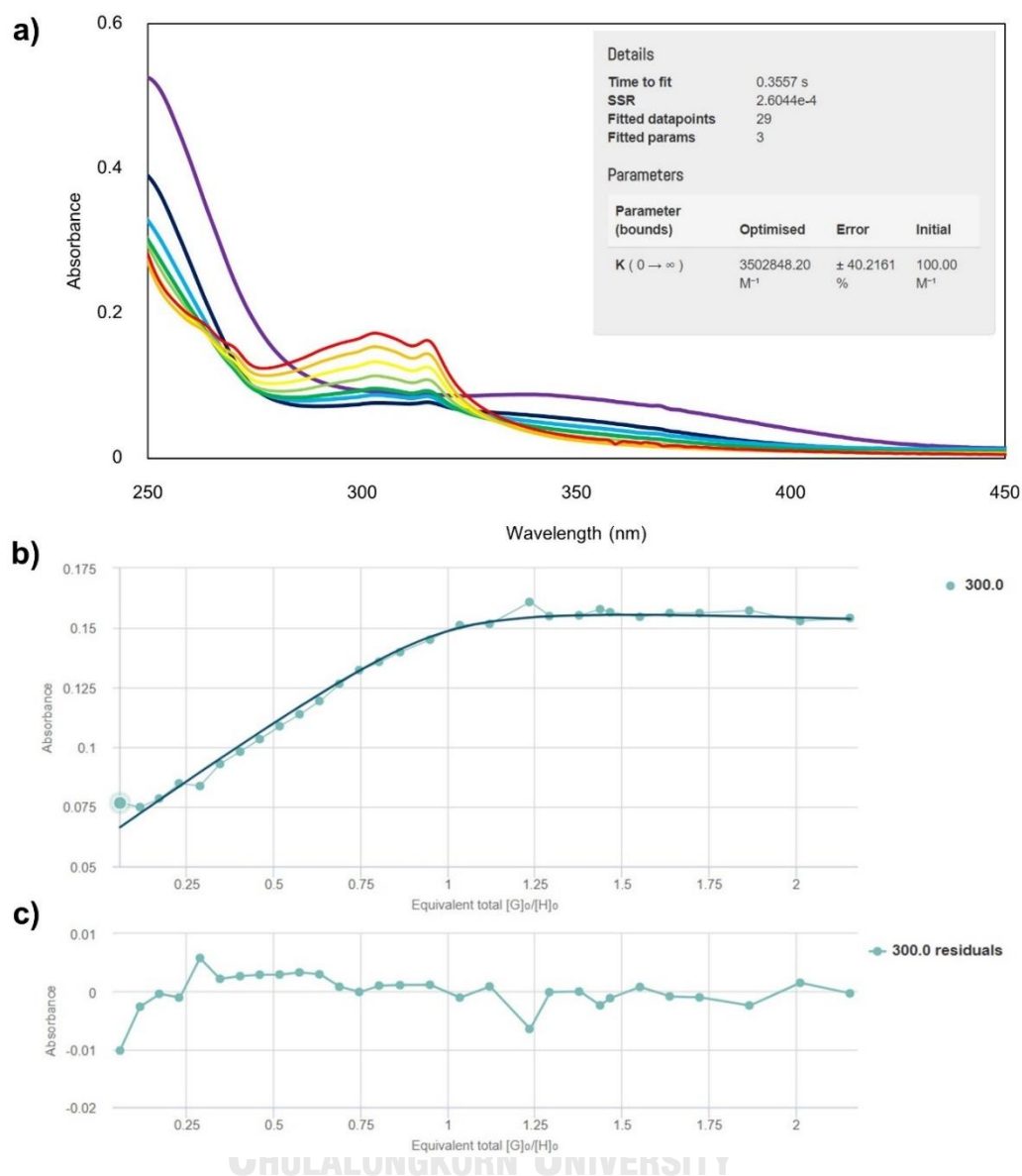


Figure A 69 UV titration between **L4** and Zn^{2+} (inset) summary table of the results of the curve fitting, b) scatter plots between absorbance and amount of Zn^{2+} at 350 nm, the line shows non-linear curve fitting of the absorbance values used for determination of K_a value. c) residual plots of the corresponding fitting.

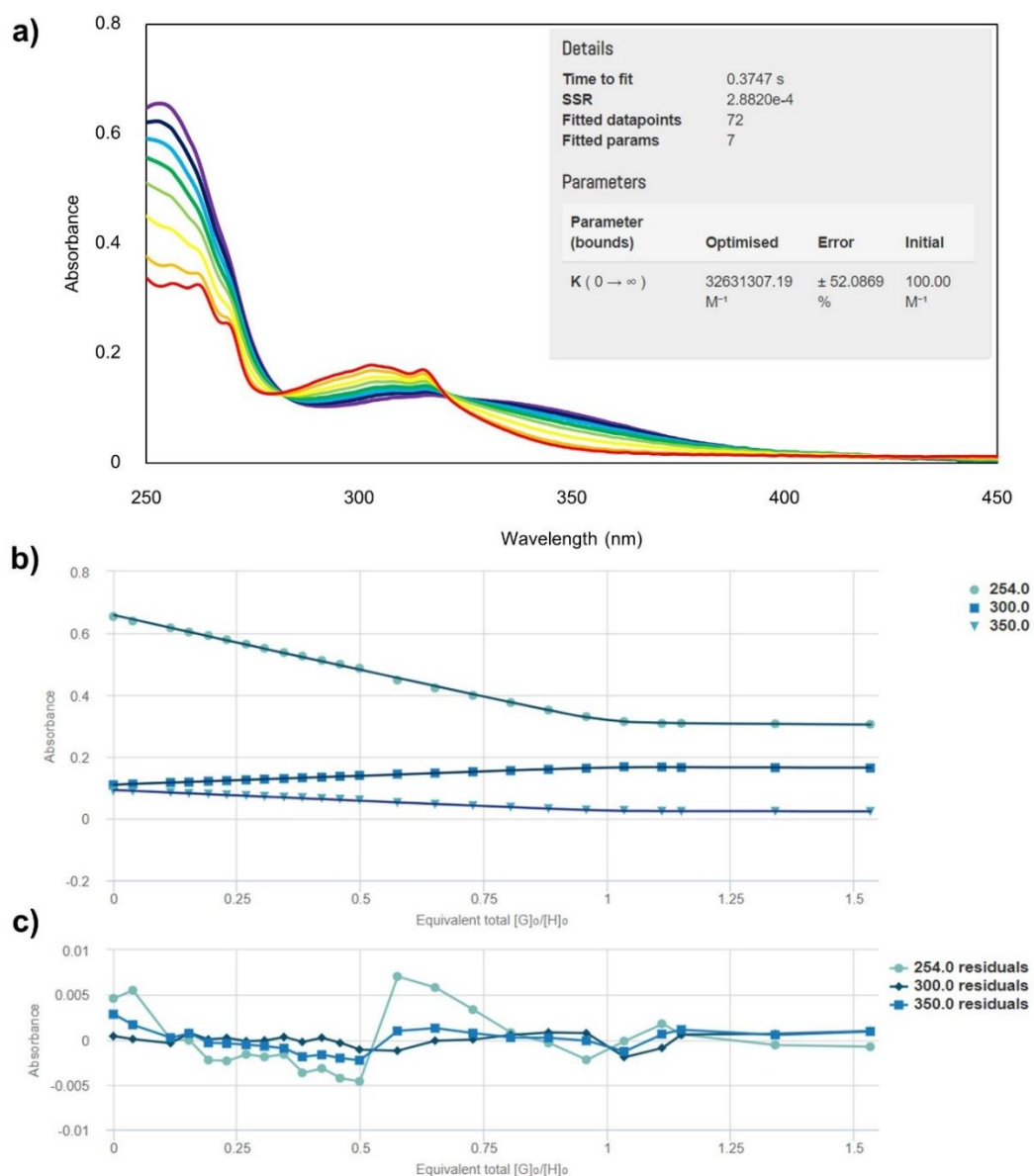


Figure A 70 a) UV titration between **L5** and Cd^{2+} (inset) summary table of the results of the curve fitting, b) scatter plots between absorbance and amount of Cd^{2+} at 254, 300 and 350 nm, the lines show non-linear curve fitting of the absorbance values at all three wavelengths used for determination of K_a value. c) residual plots of the corresponding fitting.

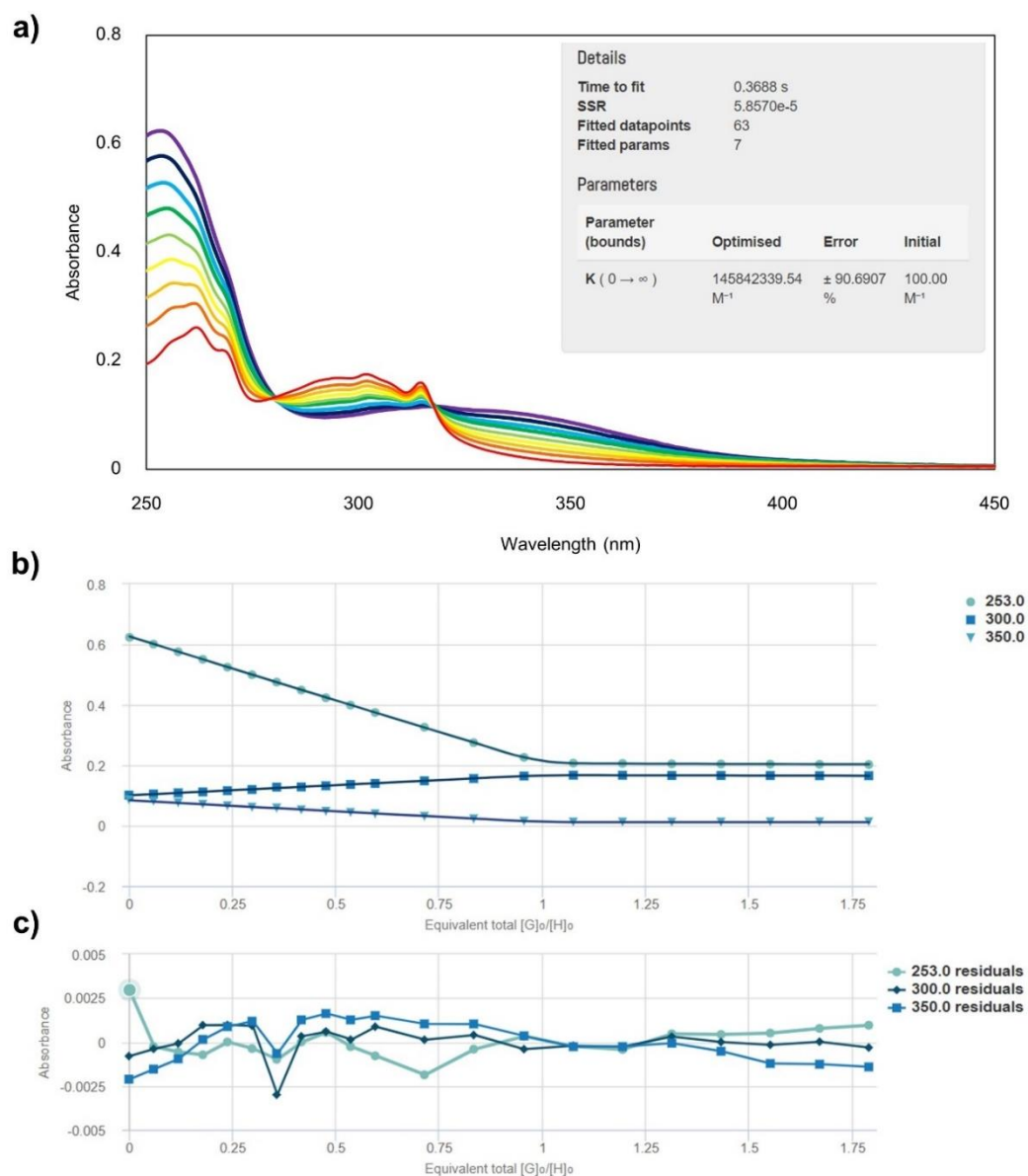


Figure A 71 a) UV titration between **L5** and Zn^{2+} (inset) summary table of the results of the curve fitting, b) scatter plots between absorbance and amount of Zn^{2+} at 253, 300 and 350 nm, the lines show non-linear curve fitting of the absorbance values at all three wavelengths used for determination of K_a value. c) residual plots of the corresponding fitting.

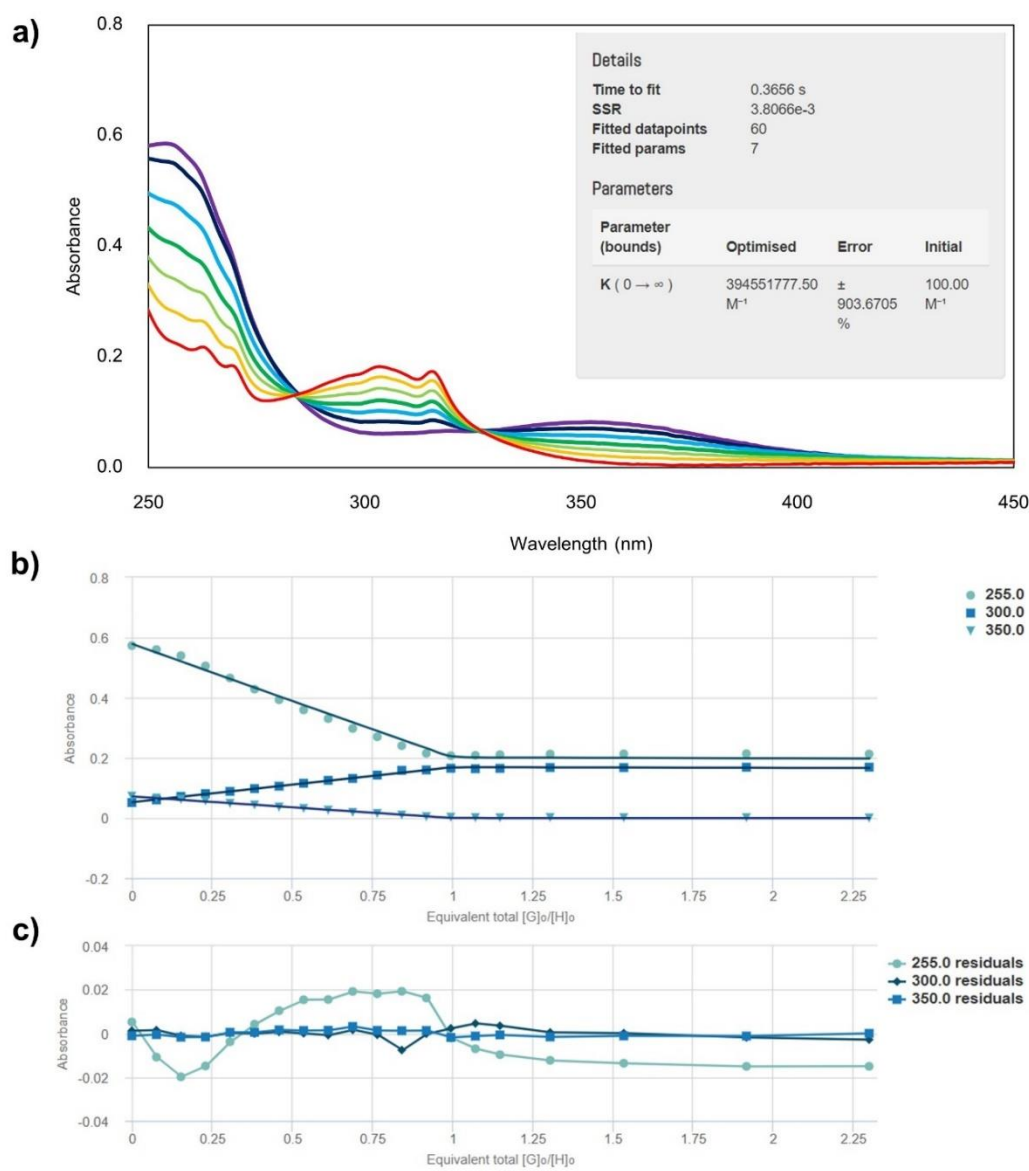


Figure A 72 a) UV titration between **L6** and Cd^{2+} (inset) summary table of the results of the curve fitting, b) scatter plots between absorbance and amount of Cd^{2+} at 255, 300 and 350 nm, the lines show non-linear curve fitting of the absorbance values at all three wavelengths used for determination of K_a value. c) residual plots of the corresponding fitting.

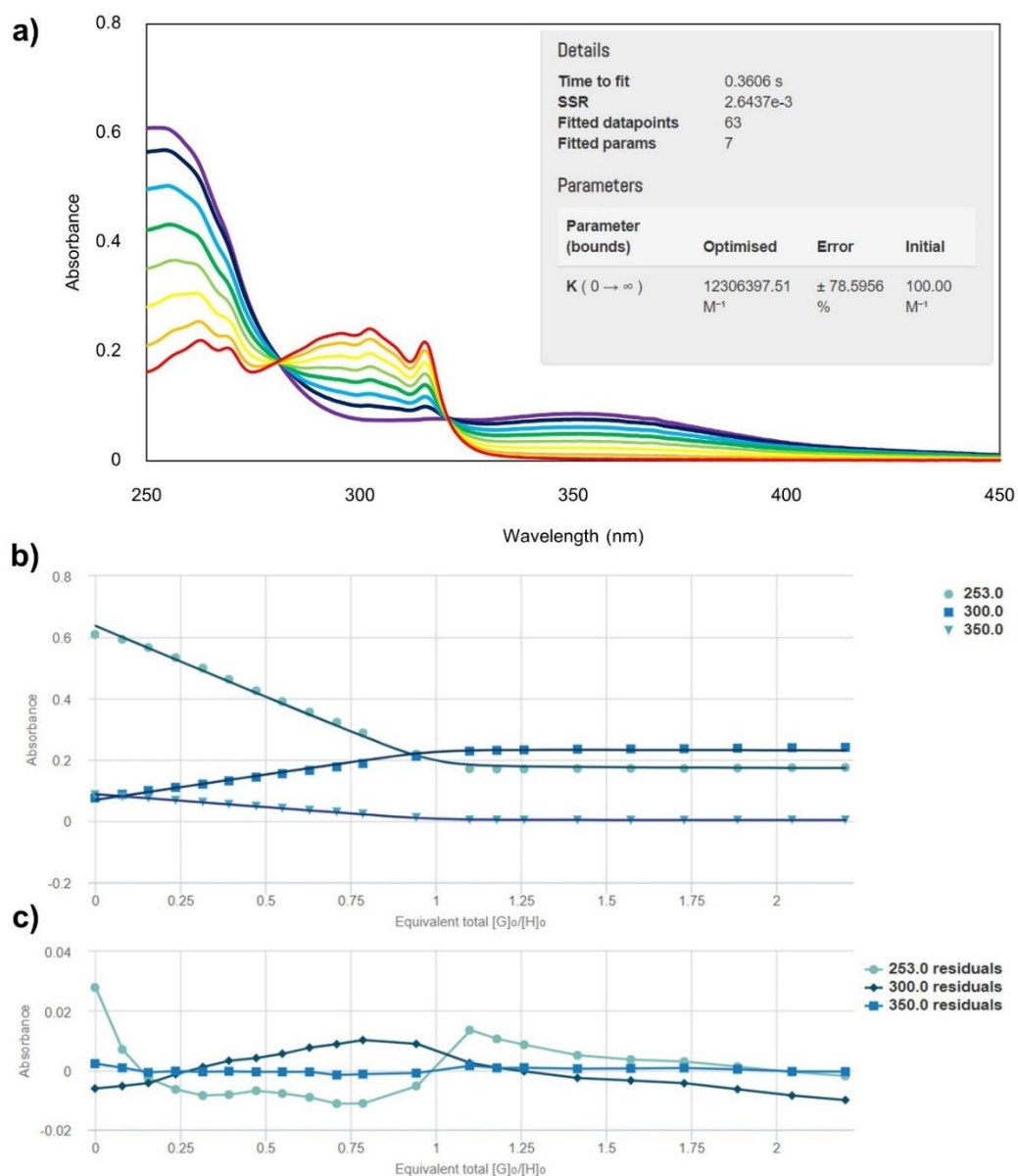


Figure A 73 a) UV titration between **L6** and Zn^{2+} (inset) summary table of the results of the curve fitting, b) scatter plots between absorbance and amount of Zn^{2+} at 253, 300 and 350 nm, the lines show non-linear curve fitting of the absorbance values at all three wavelengths used for determination of K_a value. c) residual plots of the corresponding fitting.

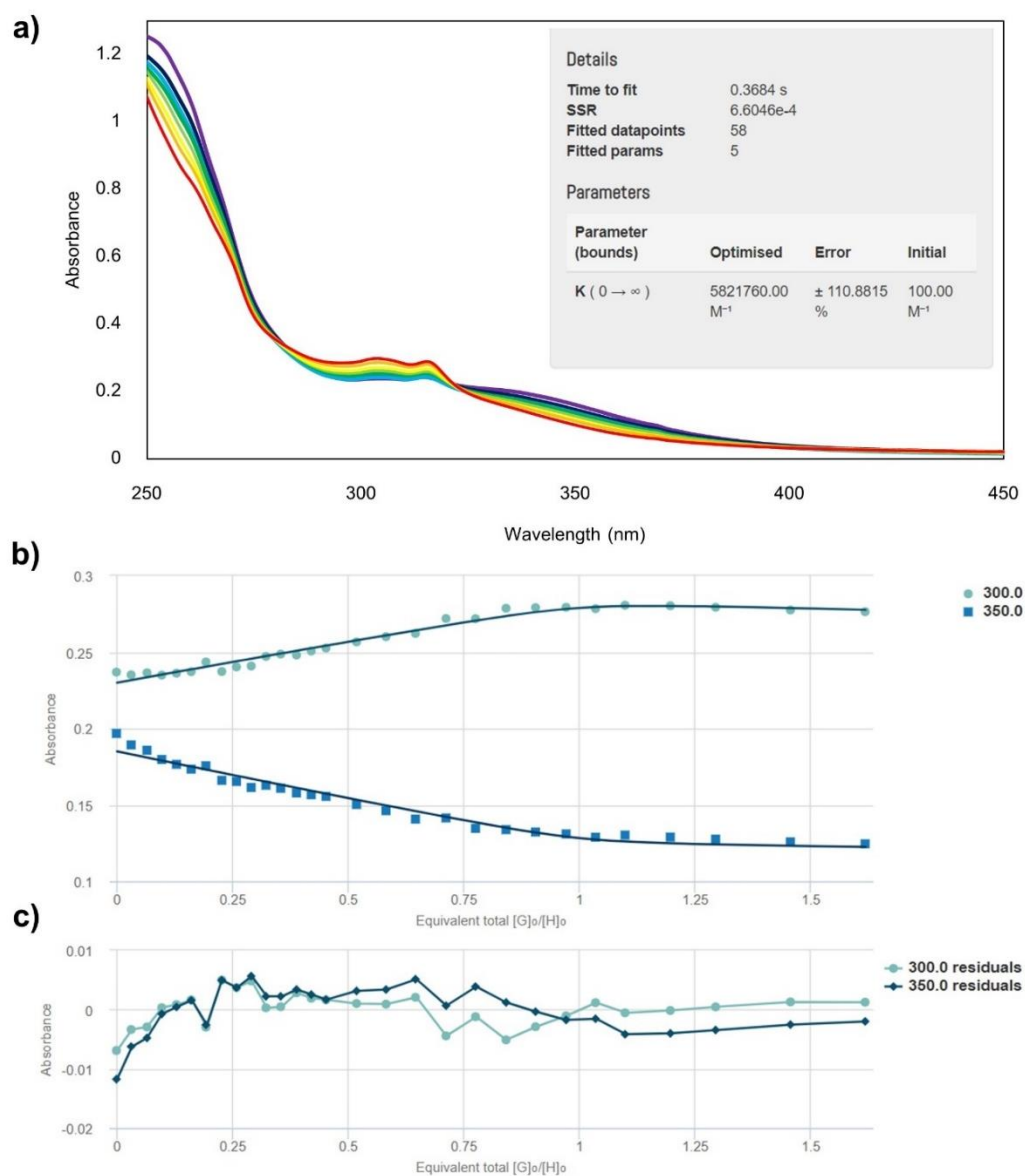


Figure A 74 a) UV titration between **L7** and Cd^{2+} (inset) summary table of the results of the curve fitting, b) scatter plots between absorbance and amount of Cd^{2+} at 300 and 350 nm, the lines show non-linear curve fitting of the absorbance values at both wavelengths used for determination of K_a value. c) residual plots of the corresponding fitting.

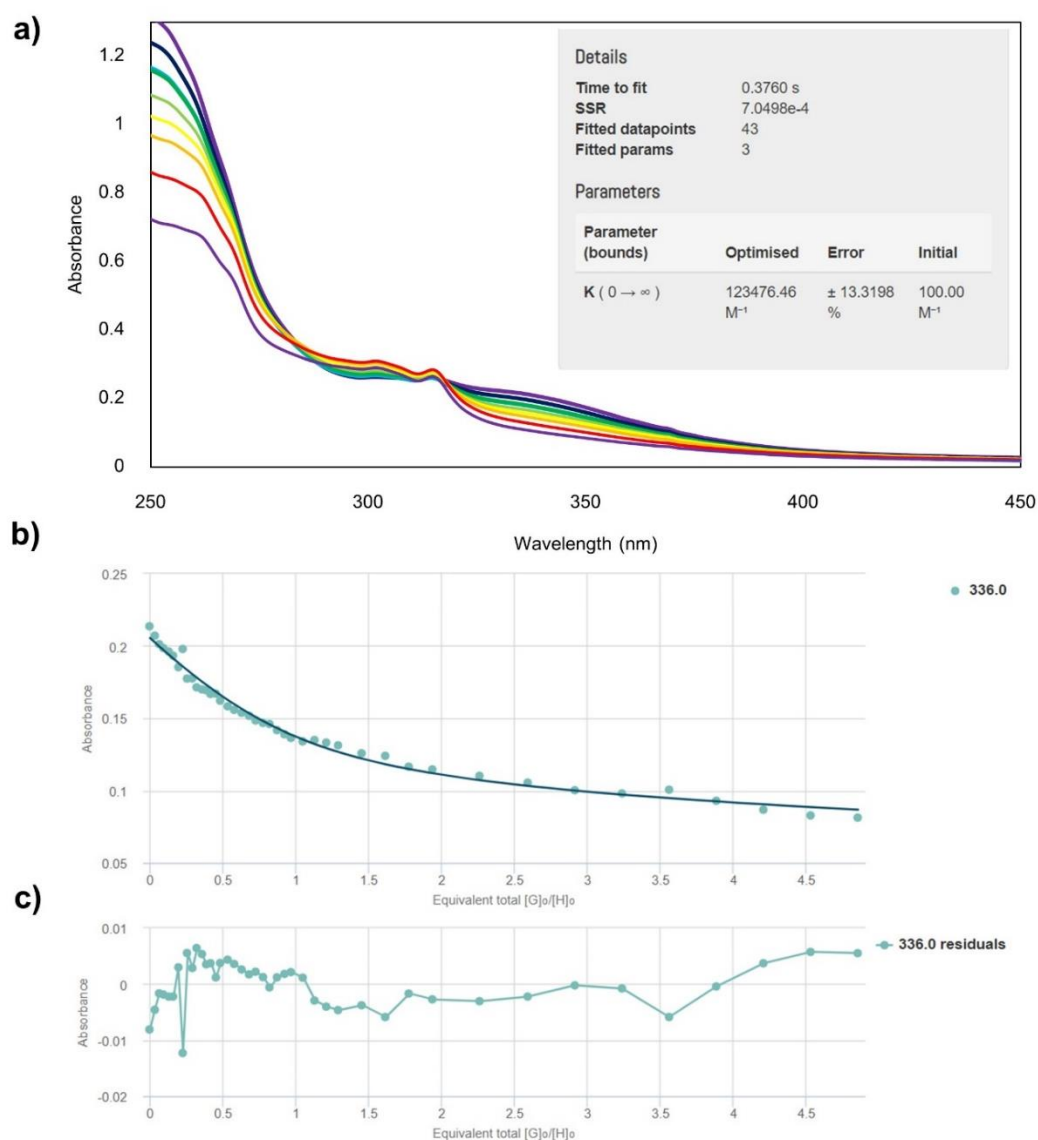


Figure A 75 a) UV titration between **L7** and Zn^{2+} (inset) summary table of the results of the curve fitting, b) scatter plots between absorbance and amount of Zn^{2+} at 336 nm, the line shows non-linear curve fitting of the absorbance values used for determination of K_a value. c) residual plots of the corresponding fitting.

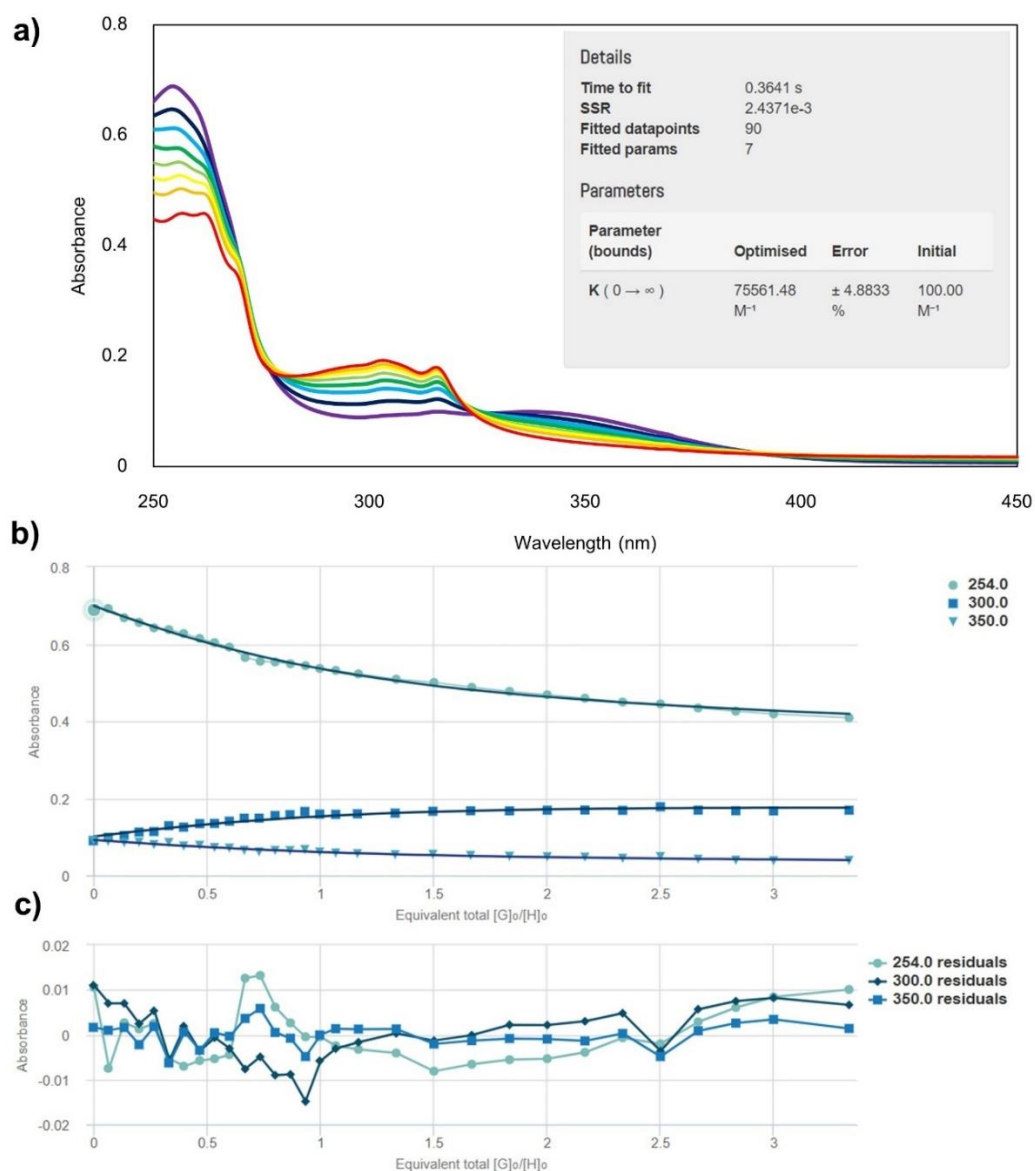


Figure A 76 a) UV titration between **L8** and Cd^{2+} (inset) summary table of the results of the curve fitting, b) scatter plots between absorbance and amount of Cd^{2+} at 254, 300 and 350 nm, the lines show non-linear curve fitting of the absorbance values at all three wavelengths used for determination of K_a value. c) residual plots of the corresponding fitting.

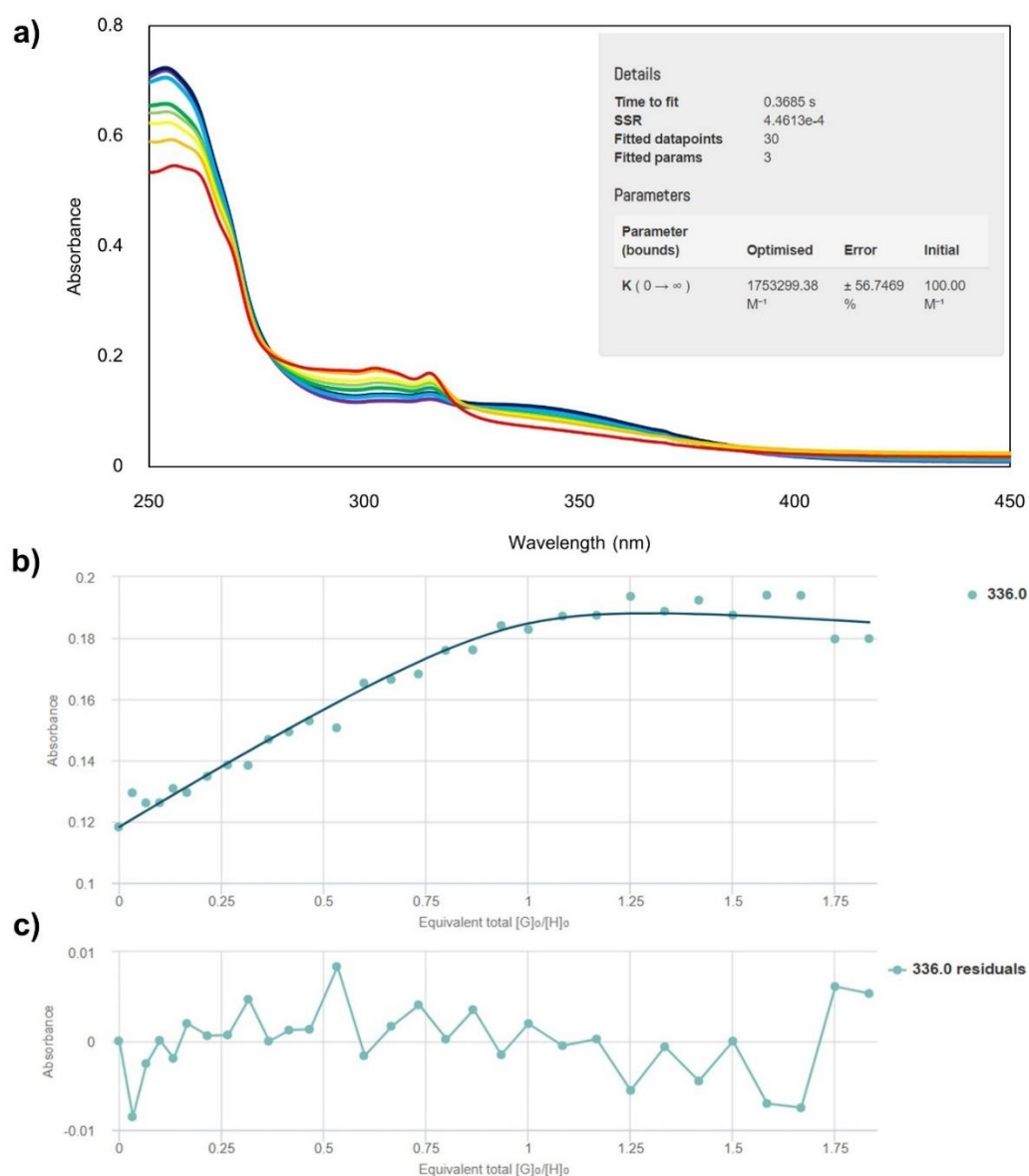


Figure A 77 a) UV titration between **L8** and Zn^{2+} (inset) summary table of the results of the curve fitting, b) scatter plots between absorbance and amount of Zn^{2+} at 336 nm, the line shows non-linear curve fitting of the absorbance values used for determination of K_a value. c) residual plots of the corresponding fitting.

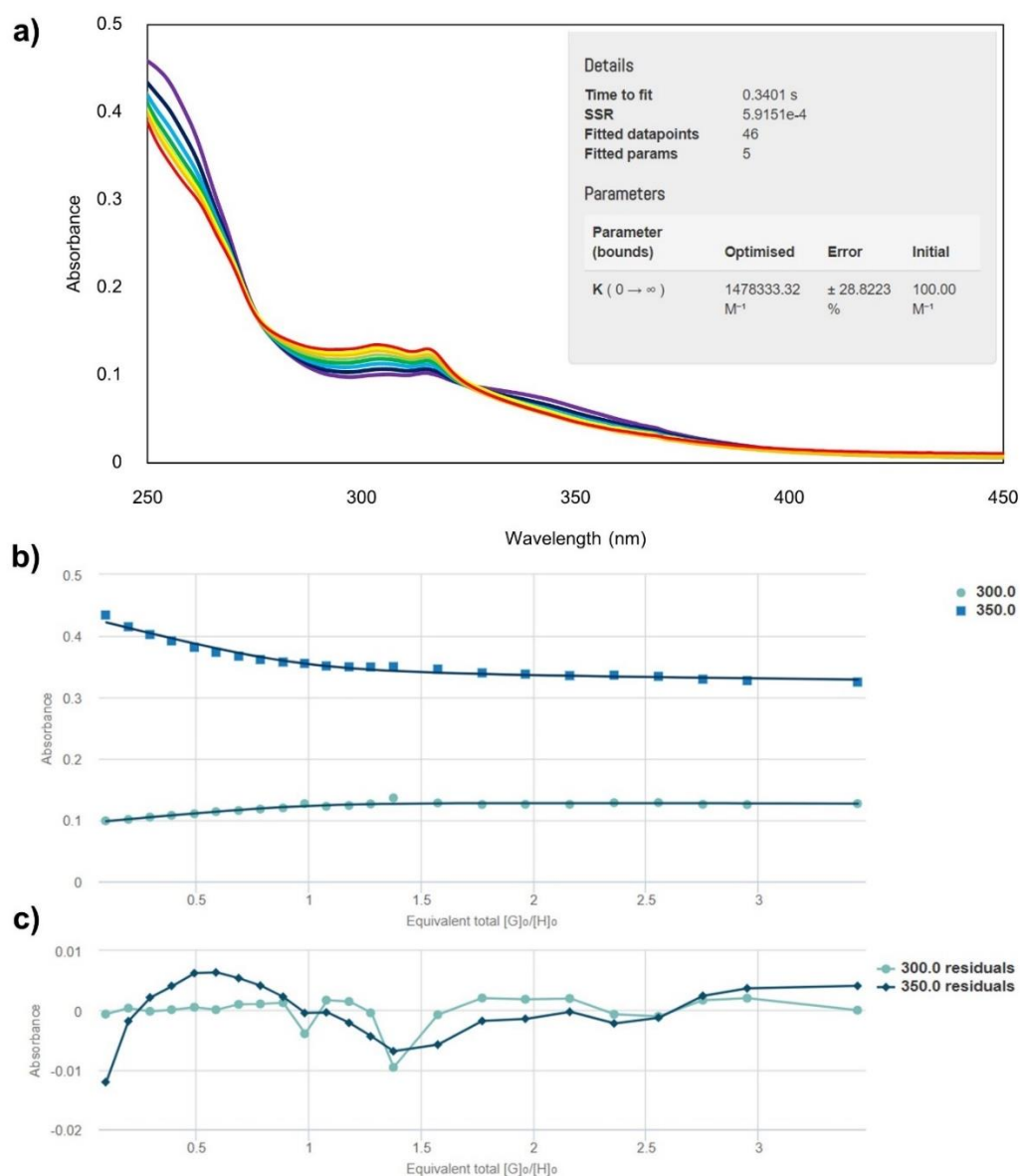


Figure A 78 a) UV titration between **L9** and Cd^{2+} (inset) summary table of the results of the curve fitting, b) scatter plots between absorbance and amount of Cd^{2+} at 300 and 350 nm, the lines show non-linear curve fitting of the absorbance values at both wavelengths used for determination of K_a value. c) residual plots of the corresponding fitting.

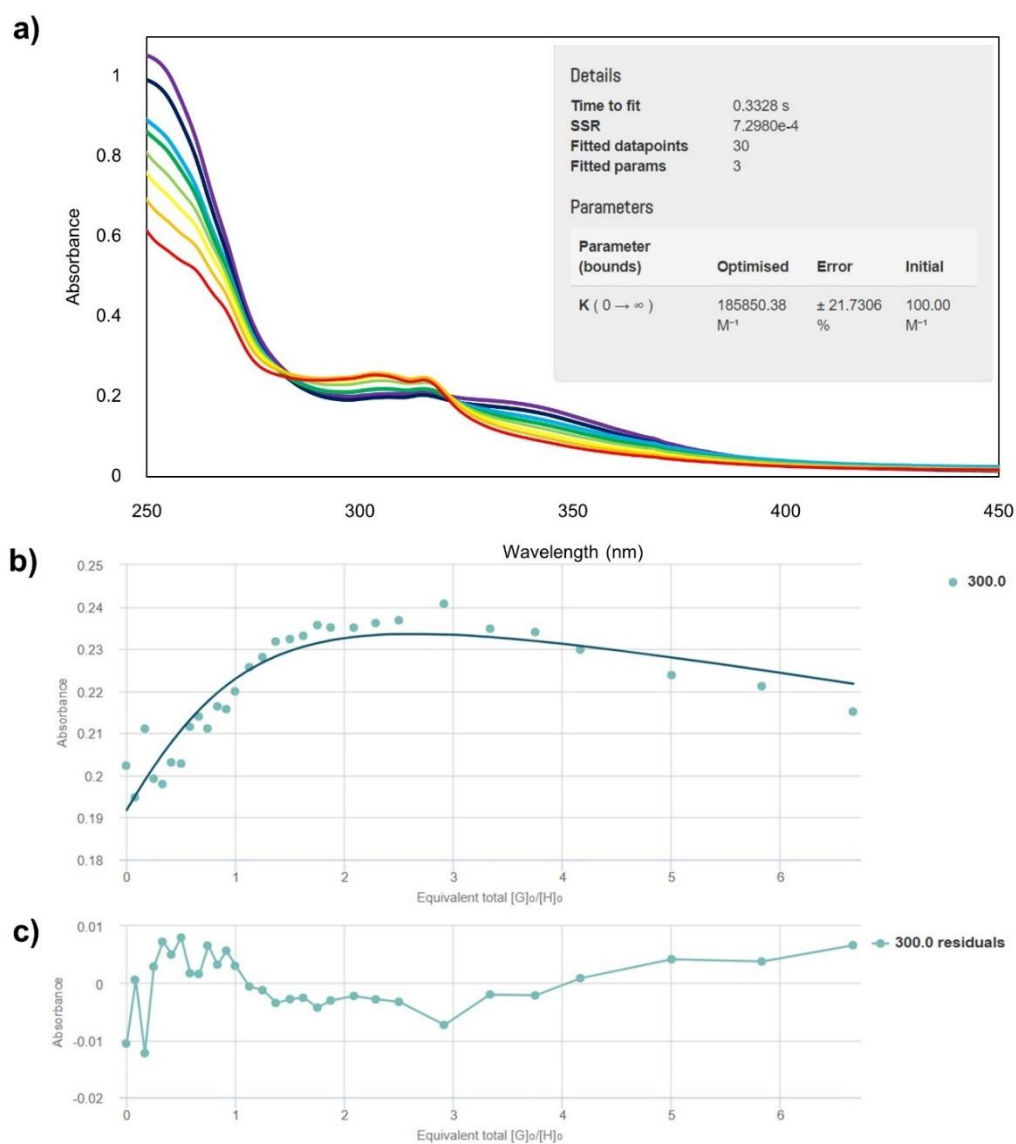


Figure A 79 a) UV titration between **L9** and Zn^{2+} (inset) summary table of the results of the curve fitting, b) scatter plots between absorbance and amount of Zn^{2+} at 300 nm, the line shows non-linear curve fitting of the absorbance values used for determination of K_a value. c) residual plots of the corresponding fitting.

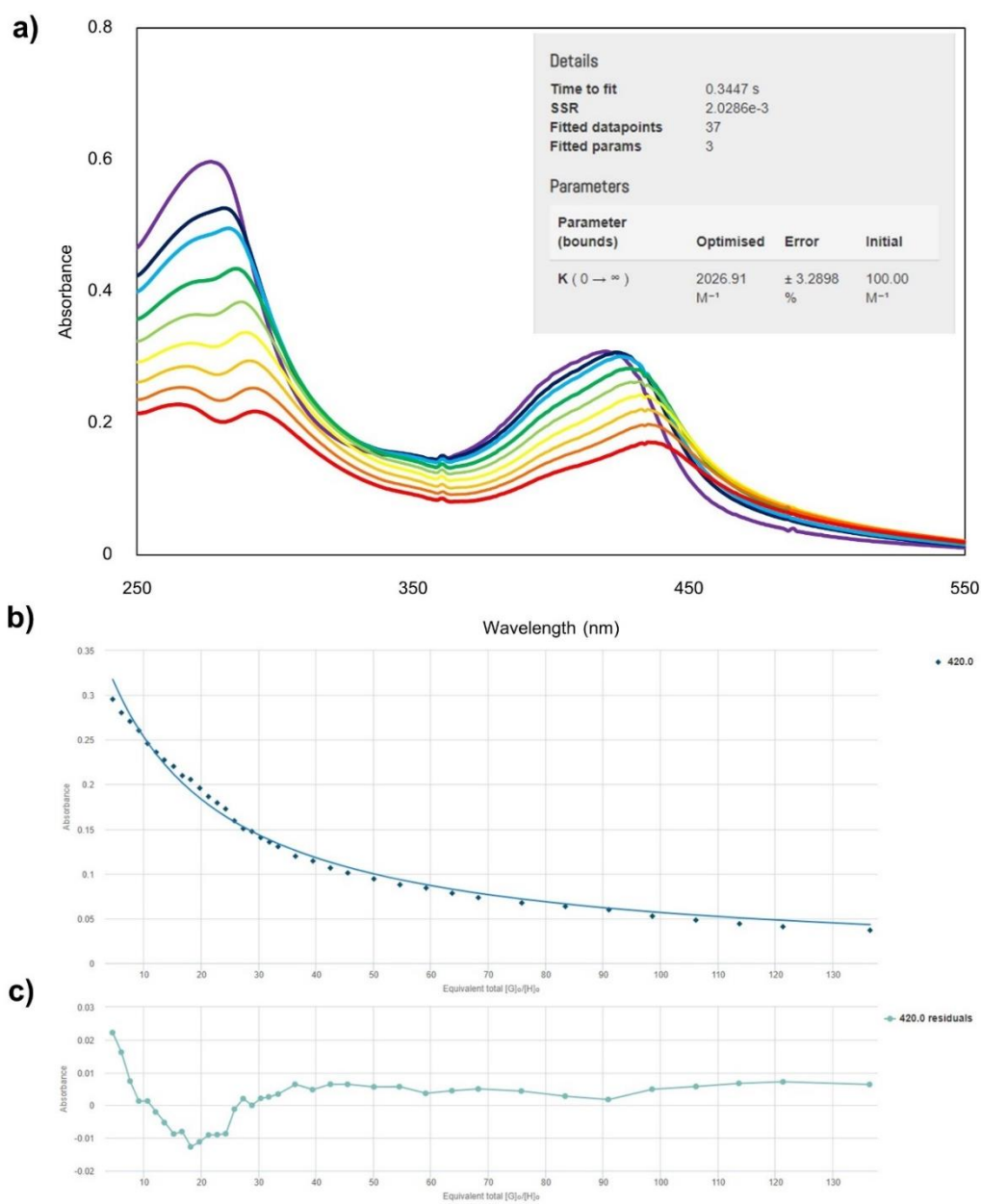


Figure A 80 a) UV titration between **L10** and Cd^{2+} (inset) summary table of the results of the curve fitting, b) scatter plots between absorbance and amount of Cd^{2+} at 420 nm, the lines show non-linear curve fitting of the absorbance values used for determination of K_a value. c) residual plots of the corresponding fitting.

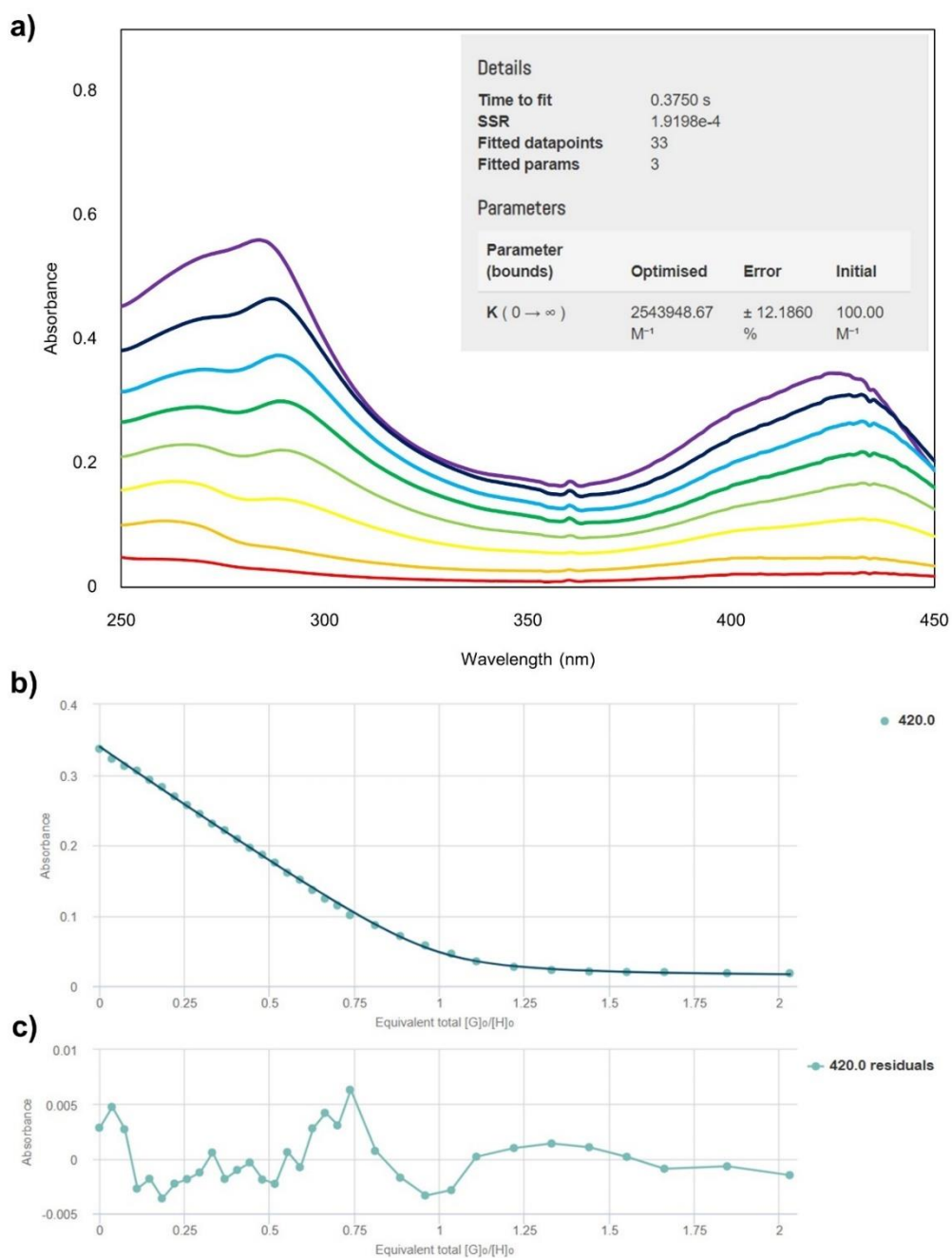


Figure A 81 a) UV titration between **L10** and Zn^{2+} (inset) summary table of the results of the curve fitting, b) scatter plots between absorbance and amount of Zn^{2+} at 420 nm, the line shows non-linear curve fitting of the absorbance values used for determination of K_a value. c) residual plots of the corresponding fitting.

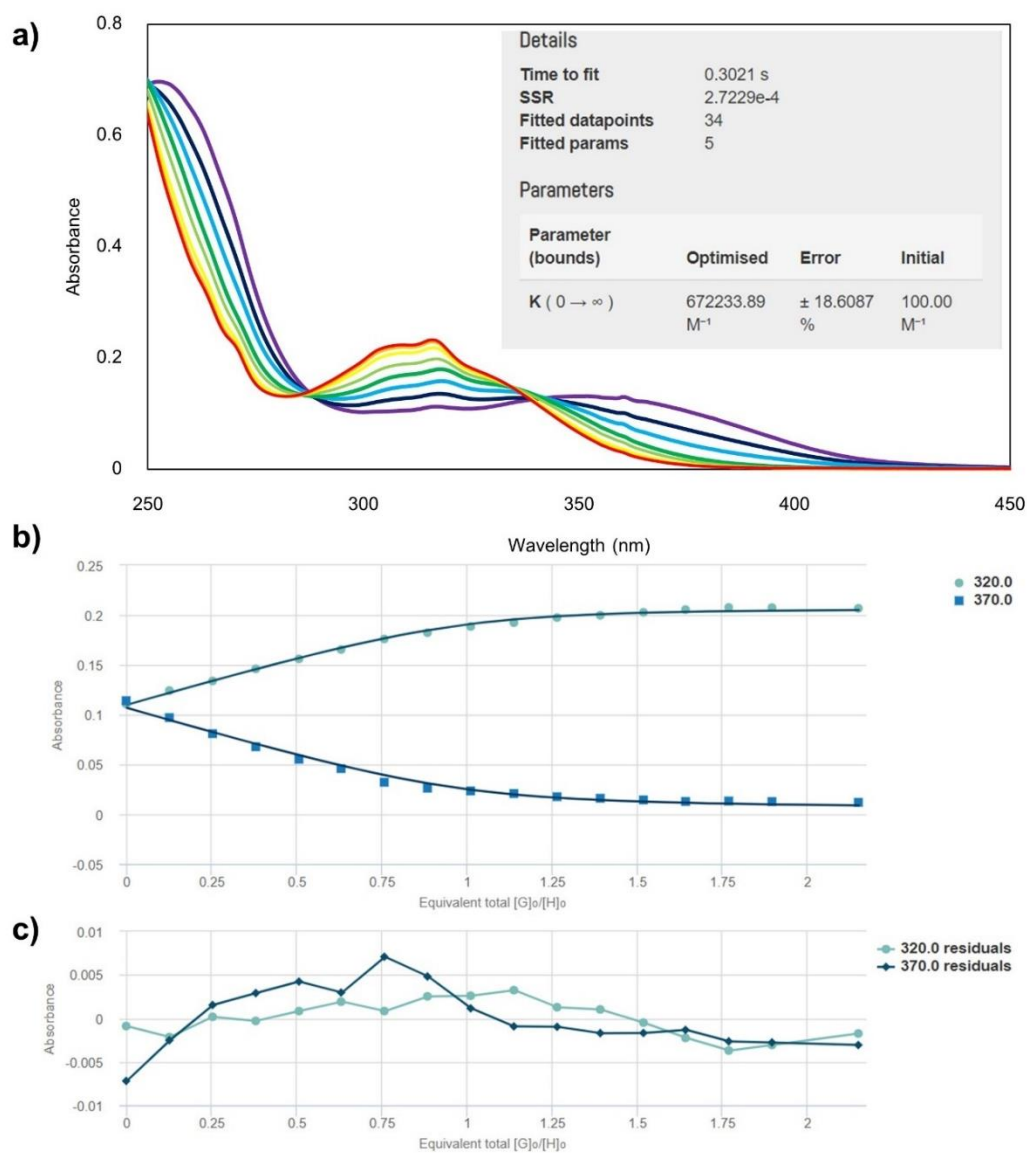


Figure A 82 a) UV titration between **L11** and Cd^{2+} (inset) summary table of the results of the curve fitting, b) scatter plots between absorbance and amount of Cd^{2+} at 300 and 370 nm, the lines show non-linear curve fitting of the absorbance values at both wavelengths used for determination of K_a value. c) residual plots of the corresponding fitting.

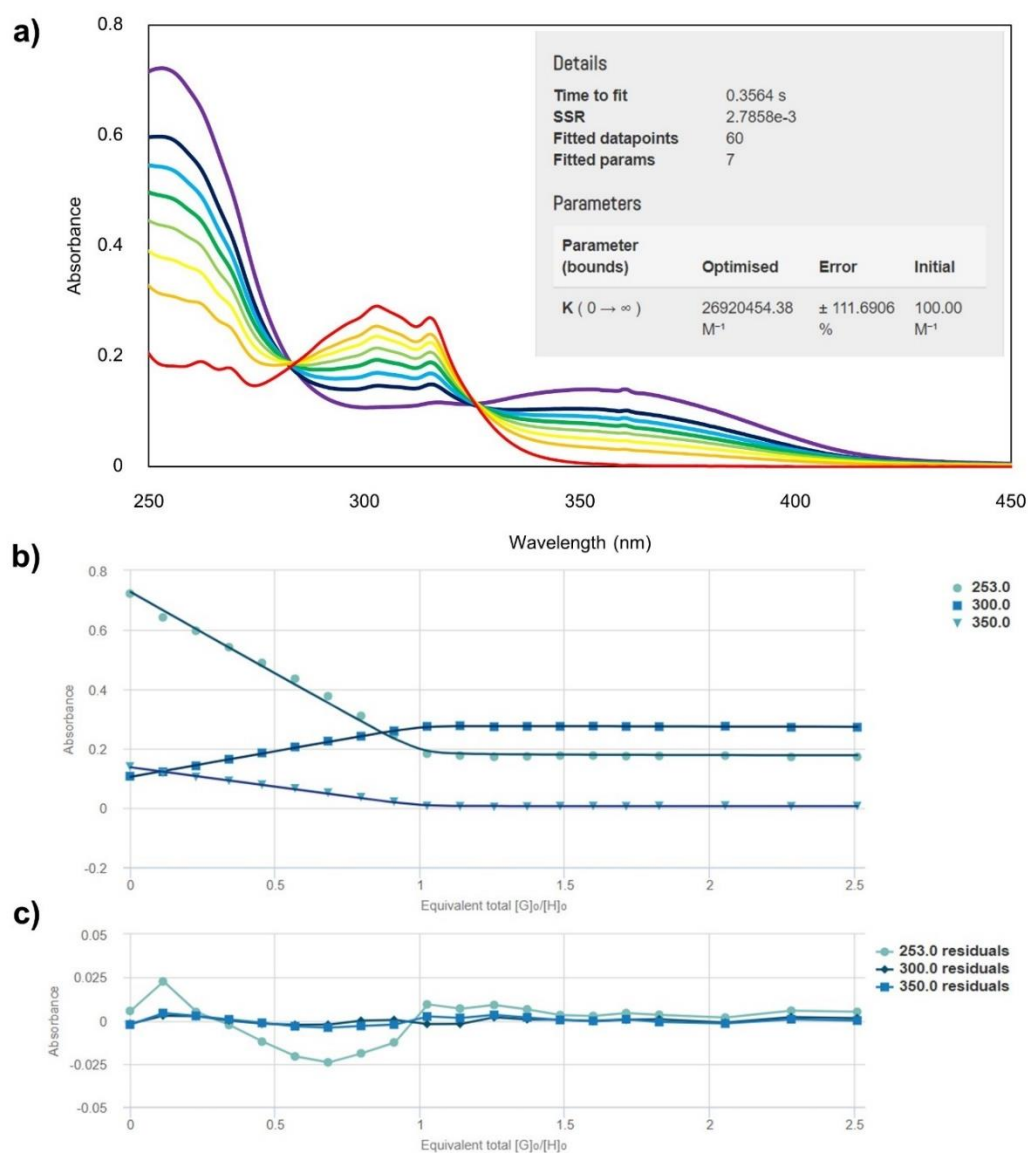


Figure A 83 a) UV titration between **L11** and Zn^{2+} (inset) summary table of the results of the curve fitting, b) scatter plots between absorbance and amount of Zn^{2+} at 253, 300 and 350 nm, the lines show non-linear curve fitting of the absorbance values at all three wavelengths used for determination of K_a value. c) residual plots of the corresponding fitting.

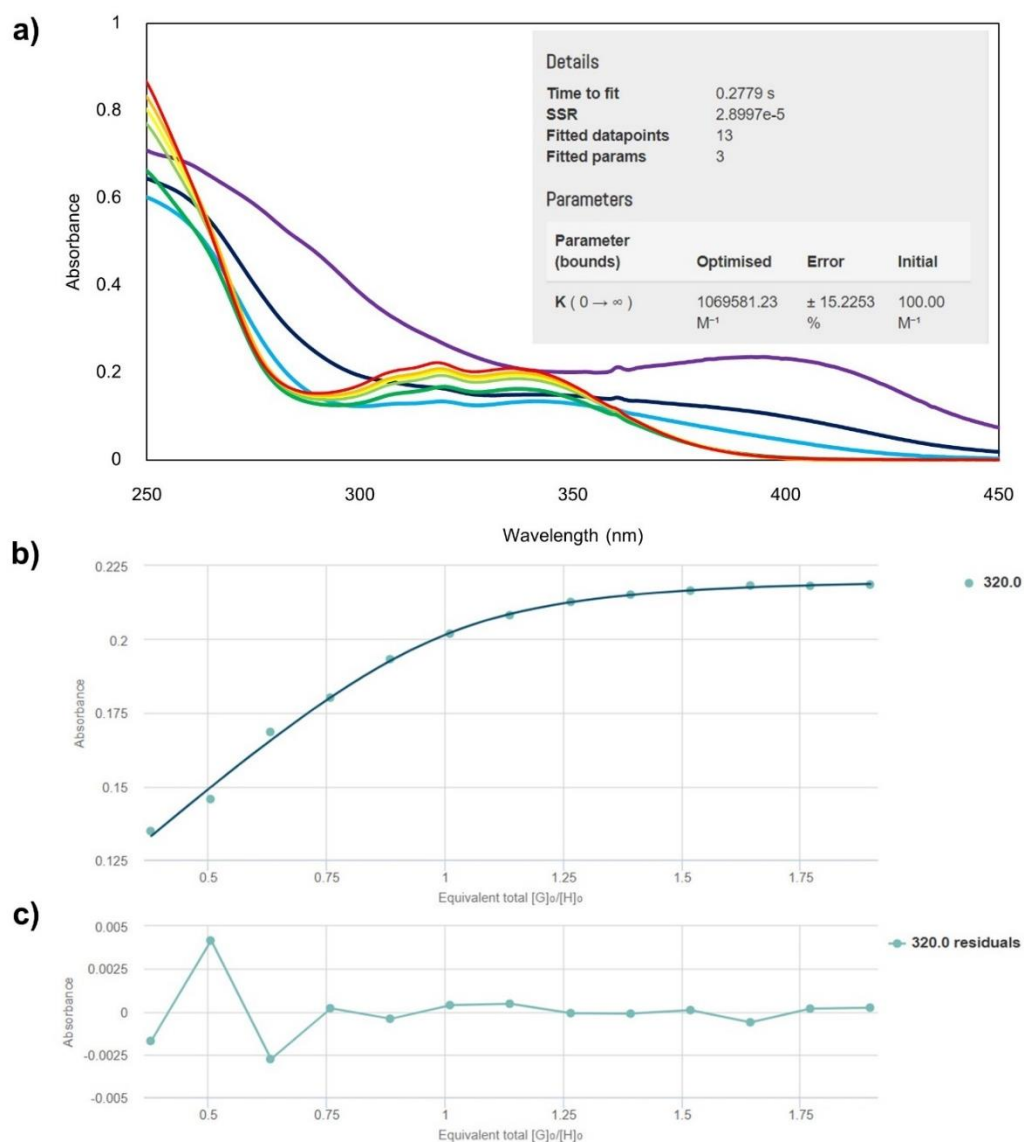


Figure A 84 a) UV titration between **L12** and Cd^{2+} (inset) summary table of the results of the curve fitting, b) scatter plots between absorbance and amount of Cd^{2+} at 320 nm, the line shows non-linear curve fitting of the absorbance values used for determination of K_a value. c) residual plots of the corresponding fitting.

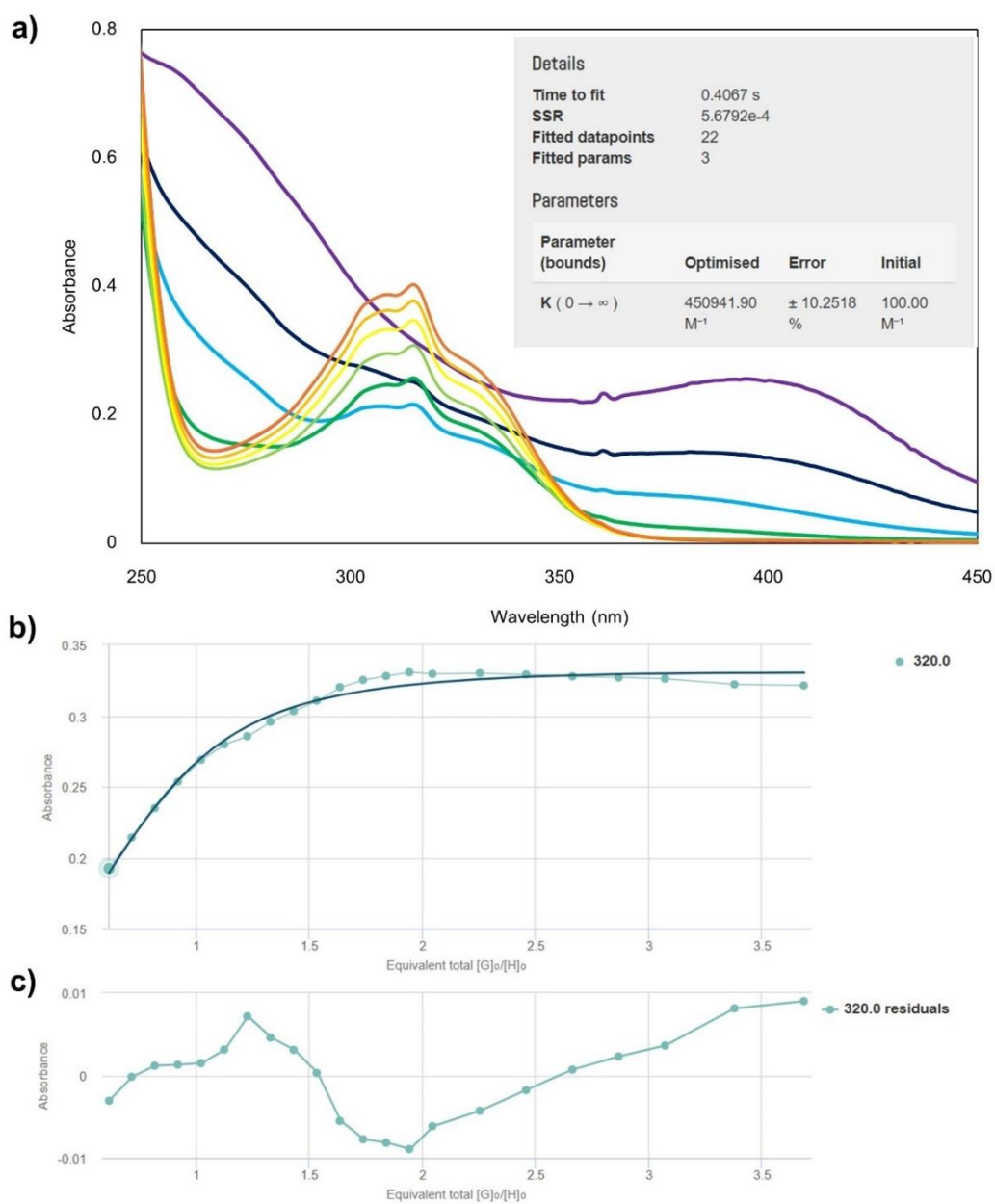


Figure A 85 a) UV titration between **L12** and Zn^{2+} (inset) summary table of the results of the curve fitting, b) scatter plots between absorbance and amount of Zn^{2+} at 320 nm, the line shows non-linear curve fitting of the absorbance values used for determination of K_a value. c) residual plots of the corresponding fitting.

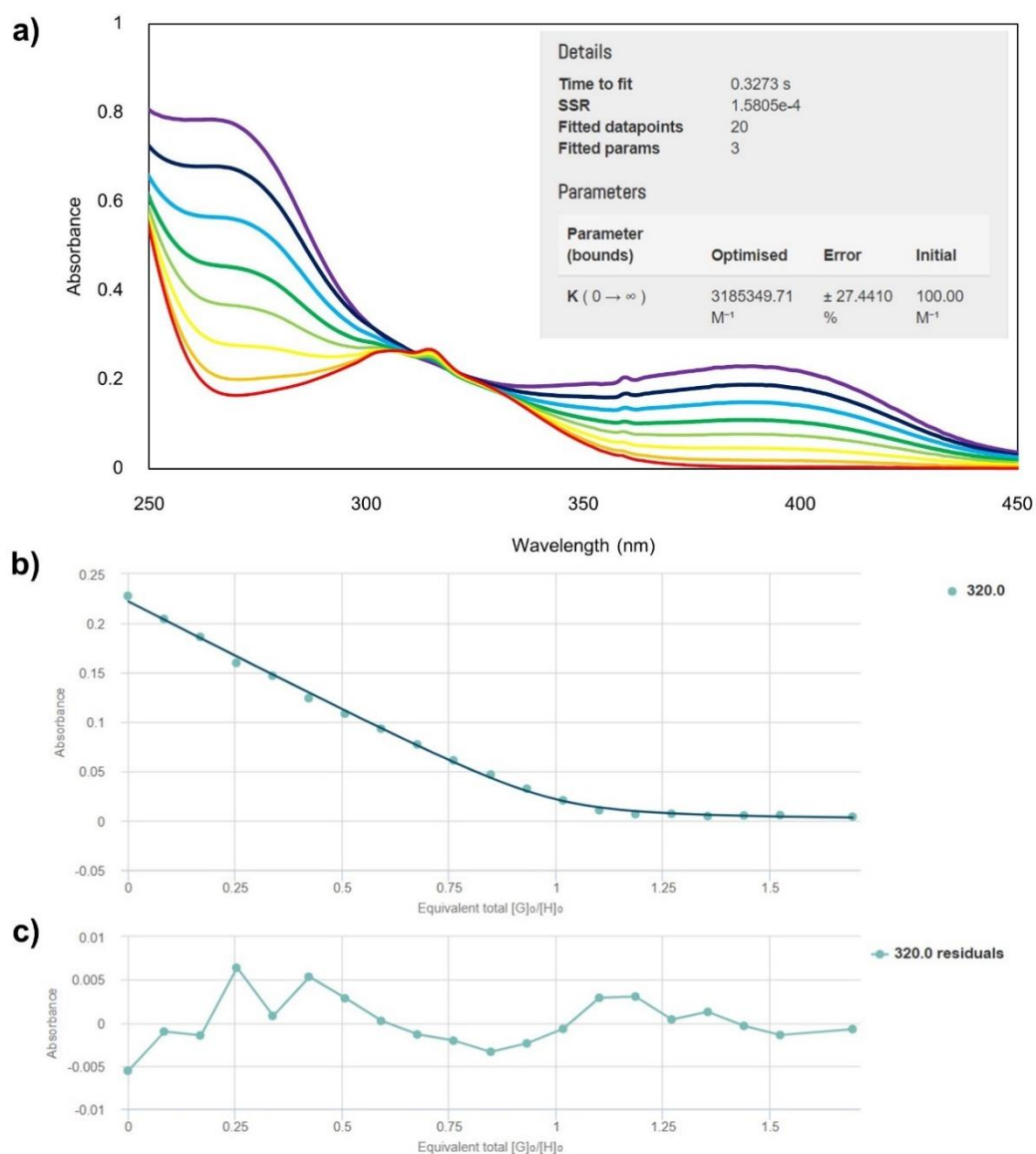


Figure A 86 a) UV titration between **L13** and Cd^{2+} (inset) summary table of the results of the curve fitting, b) scatter plots between absorbance and amount of Cd^{2+} at 320 nm, the line shows non-linear curve fitting of the absorbance values used for determination of K_a value. c) residual plots of the corresponding fitting.

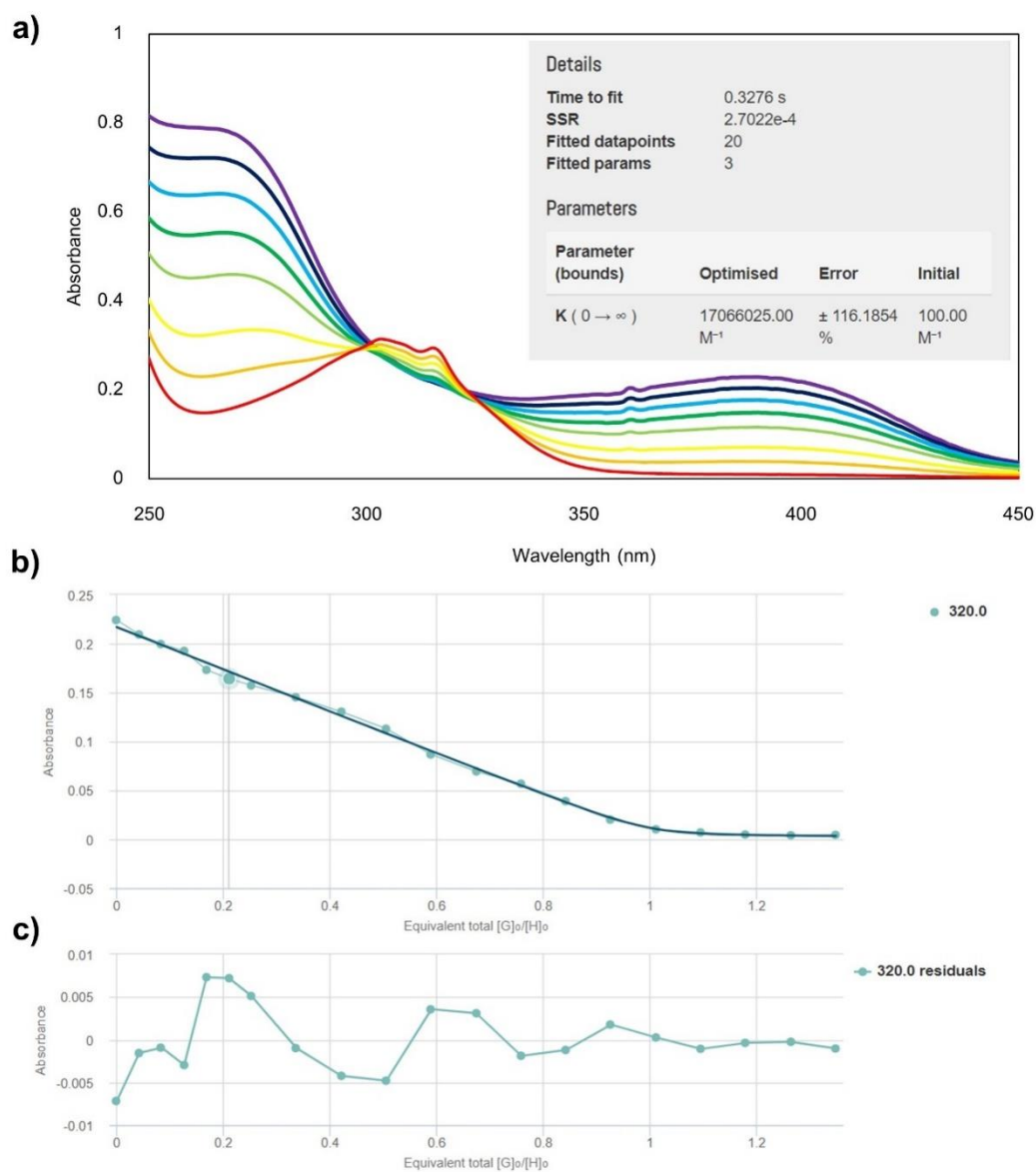


Figure A 87 a) UV titration between **L13** and Zn^{2+} (inset) summary table of the results of the curve fitting, b) scatter plots between absorbance and amount of Zn^{2+} at 320 nm, the line shows non-linear curve fitting of the absorbance values used for determination of K_a value. c) residual plots of the corresponding fitting.

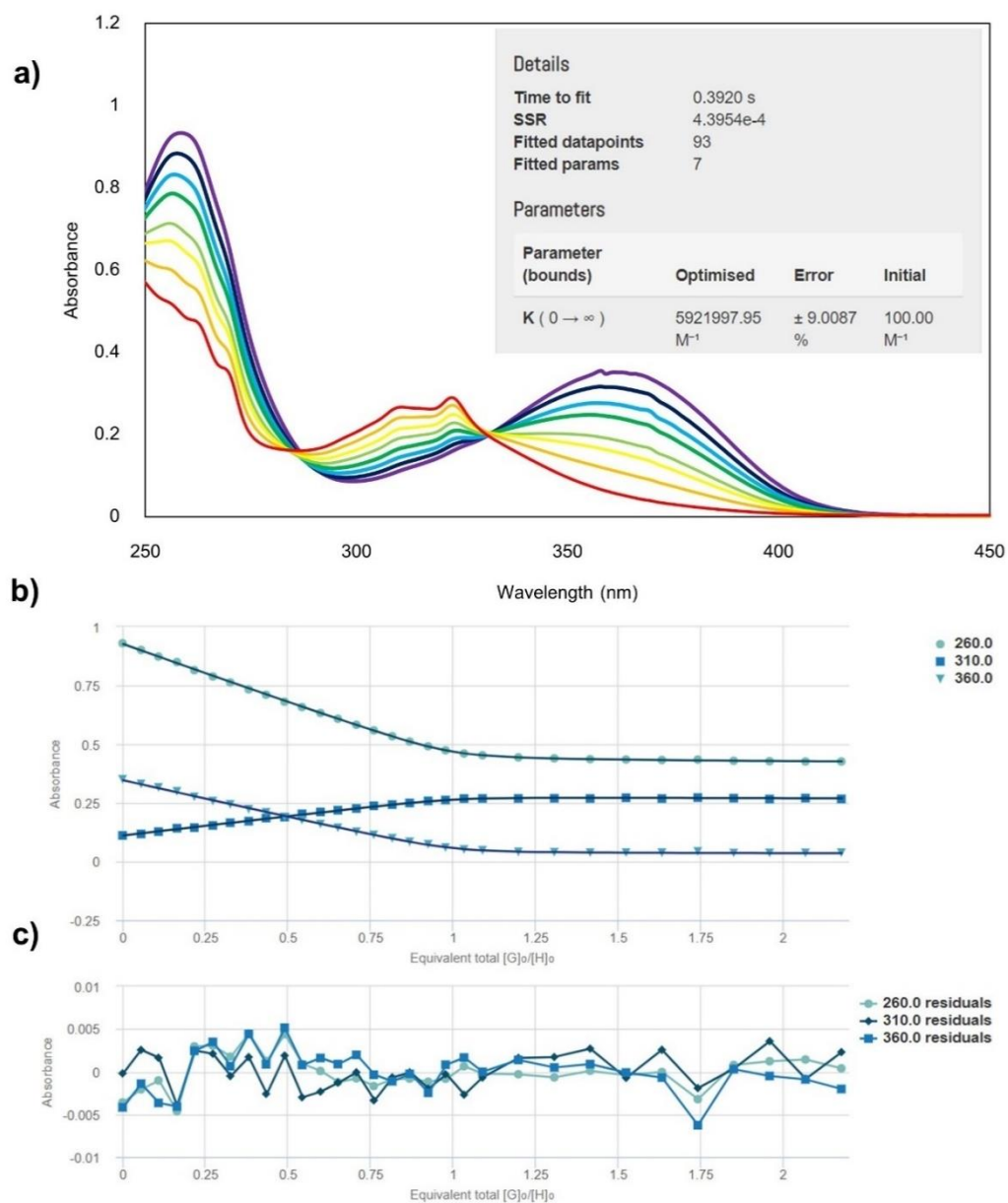


Figure A 88 a) UV titration between **L14** and Cd^{2+} (inset) summary table of the results of the curve fitting, b) scatter plots between absorbance and amount of Cd^{2+} at 260, 310 and 360 nm, the lines show non-linear curve fitting of the absorbance values at all three wavelengths used for determination of K_a value. c) residual plots of the corresponding fitting.

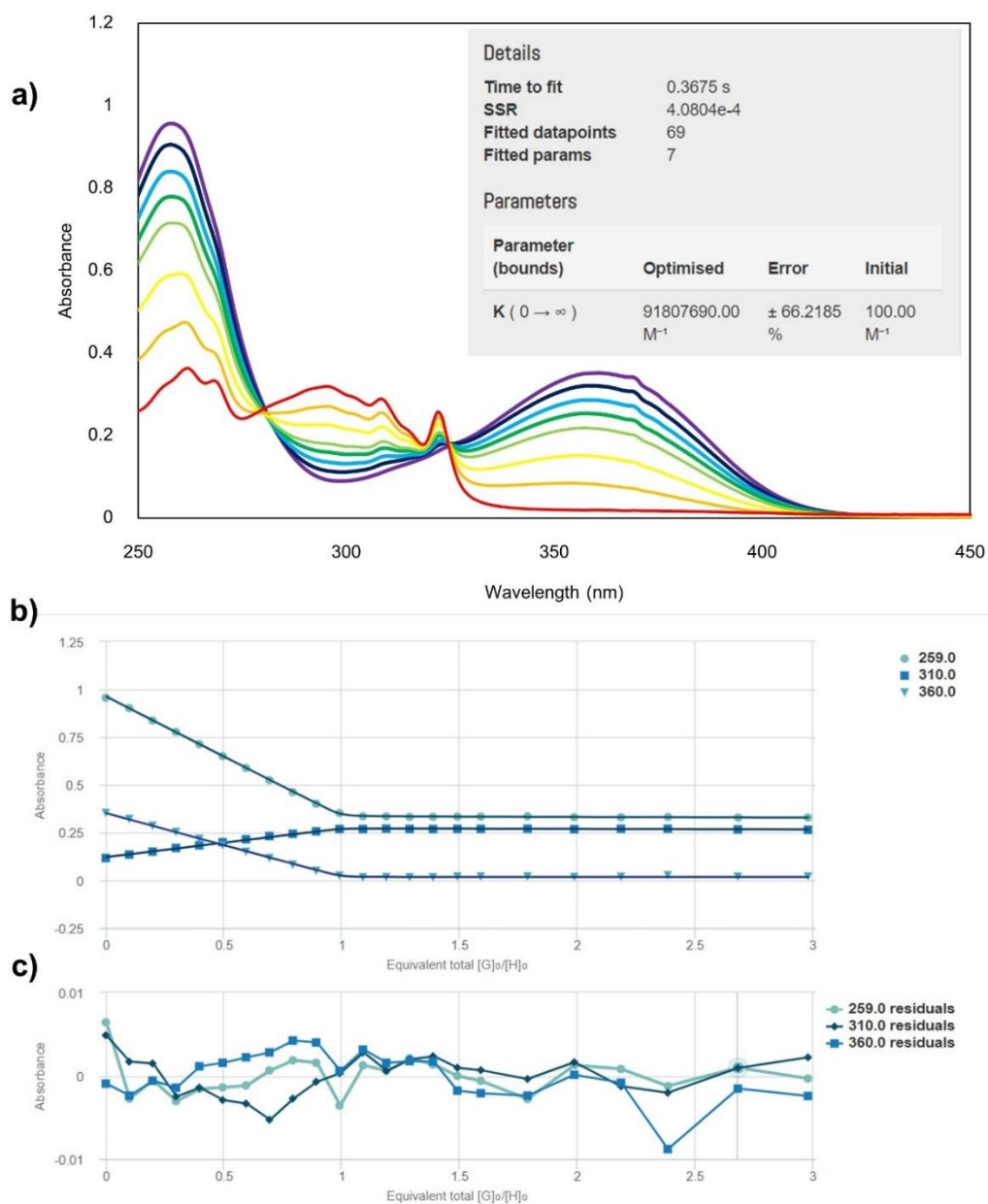


Figure A 89 a) UV titration between **L14** and Zn^{2+} (inset) summary table of the results of the curve fitting, b) scatter plots between absorbance and amount of Zn^{2+} at 259, 310 and 360 nm, the lines show non-linear curve fitting of the absorbance values at all three wavelengths used for determination of K_a value. c) residual plots of the corresponding fitting.

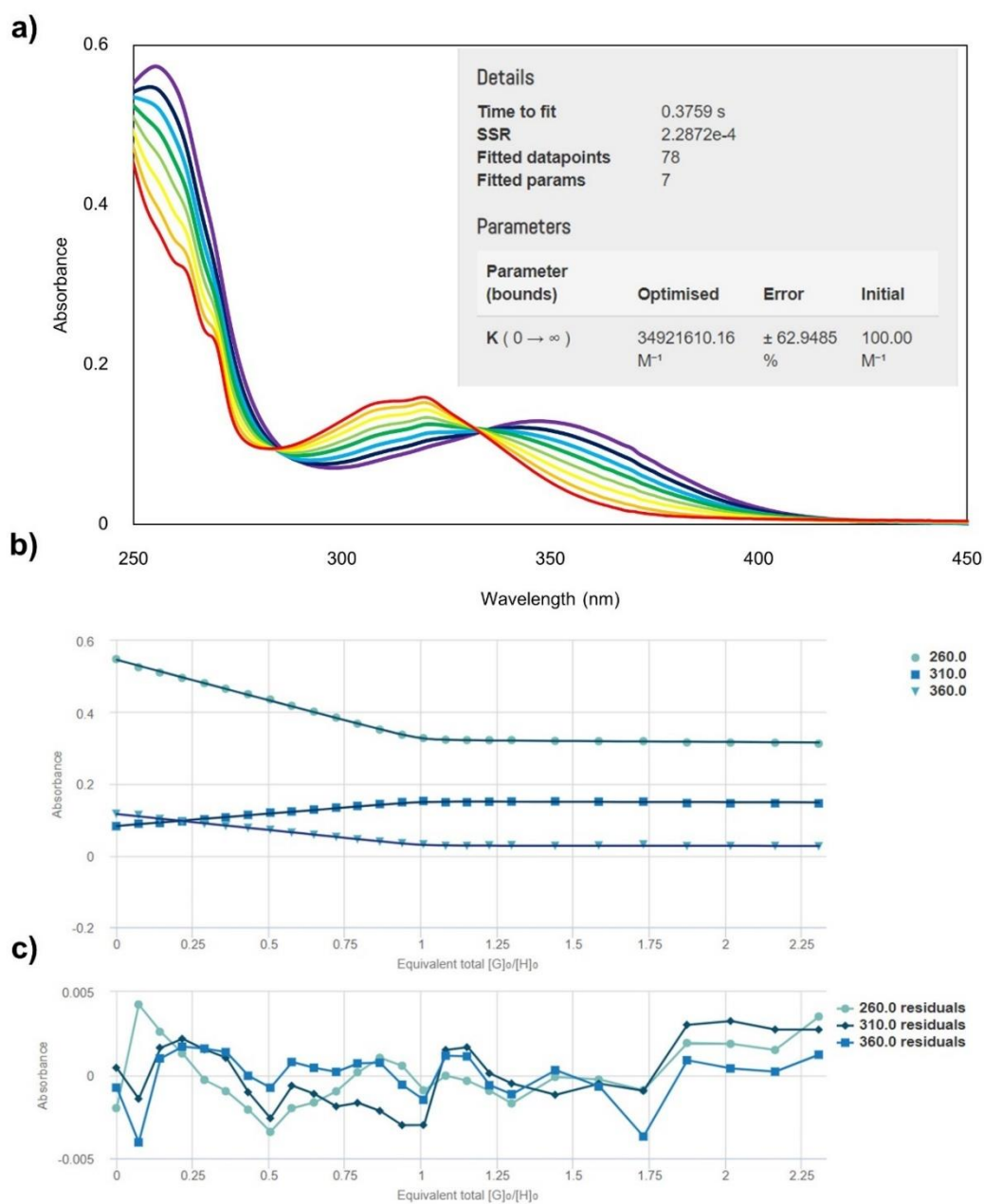


Figure A 90 a) UV titration between **L15** and Cd^{2+} (inset) summary table of the results of the curve fitting, b) scatter plots between absorbance and amount of Cd^{2+} at 260, 310 and 360 nm, the lines show non-linear curve fitting of the absorbance values at all three wavelengths used for determination of K_a value. c) residual plots of the corresponding fitting.

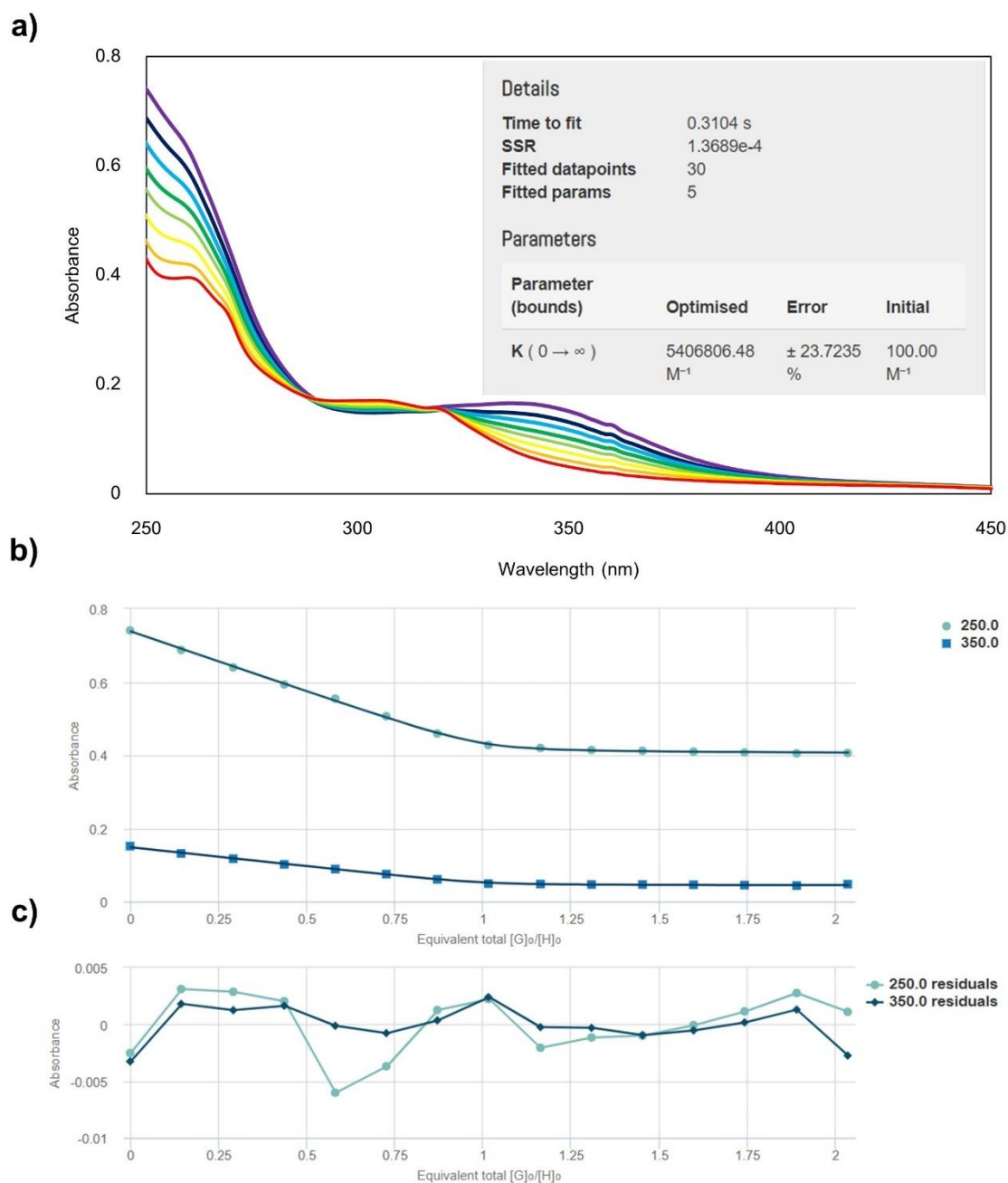


Figure A 91 a) UV titration between **L15** and Zn^{2+} (inset) summary table of the results of the curve fitting, b) scatter plots between absorbance and amount of Zn^{2+} at 250 and 350 nm, the lines show non-linear curve fitting of the absorbance values at both wavelengths used for determination of K_a value. c) residual plots of the corresponding fitting.

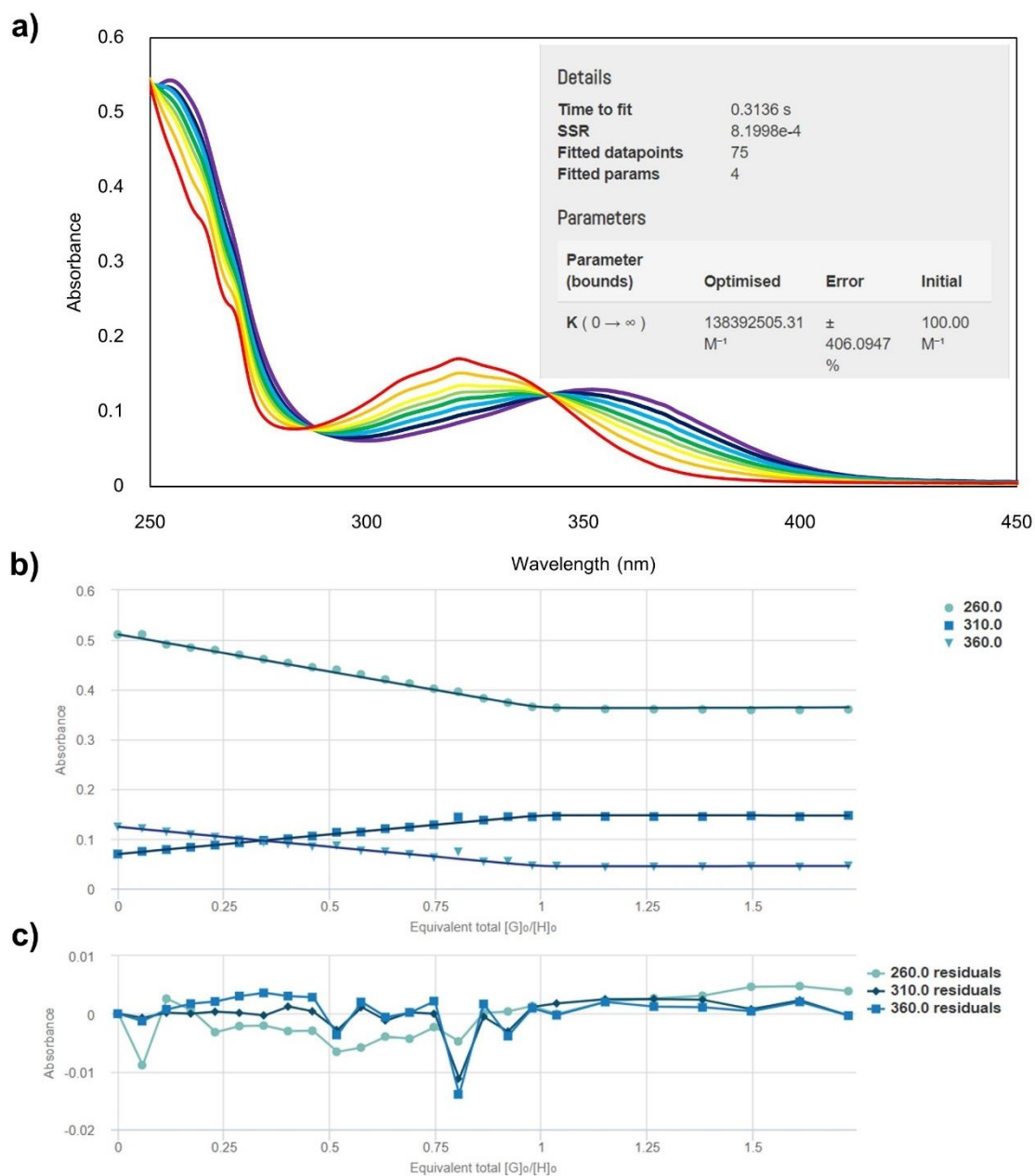


Figure A 92 a) UV titration between **L16** and Cd^{2+} (inset) summary table of the results of the curve fitting, b) scatter plots between absorbance and amount of Cd^{2+} at 260, 310 and 360 nm, the lines show non-linear curve fitting of the absorbance values at all three wavelengths used for determination of K_a value. c) residual plots of the corresponding fitting.

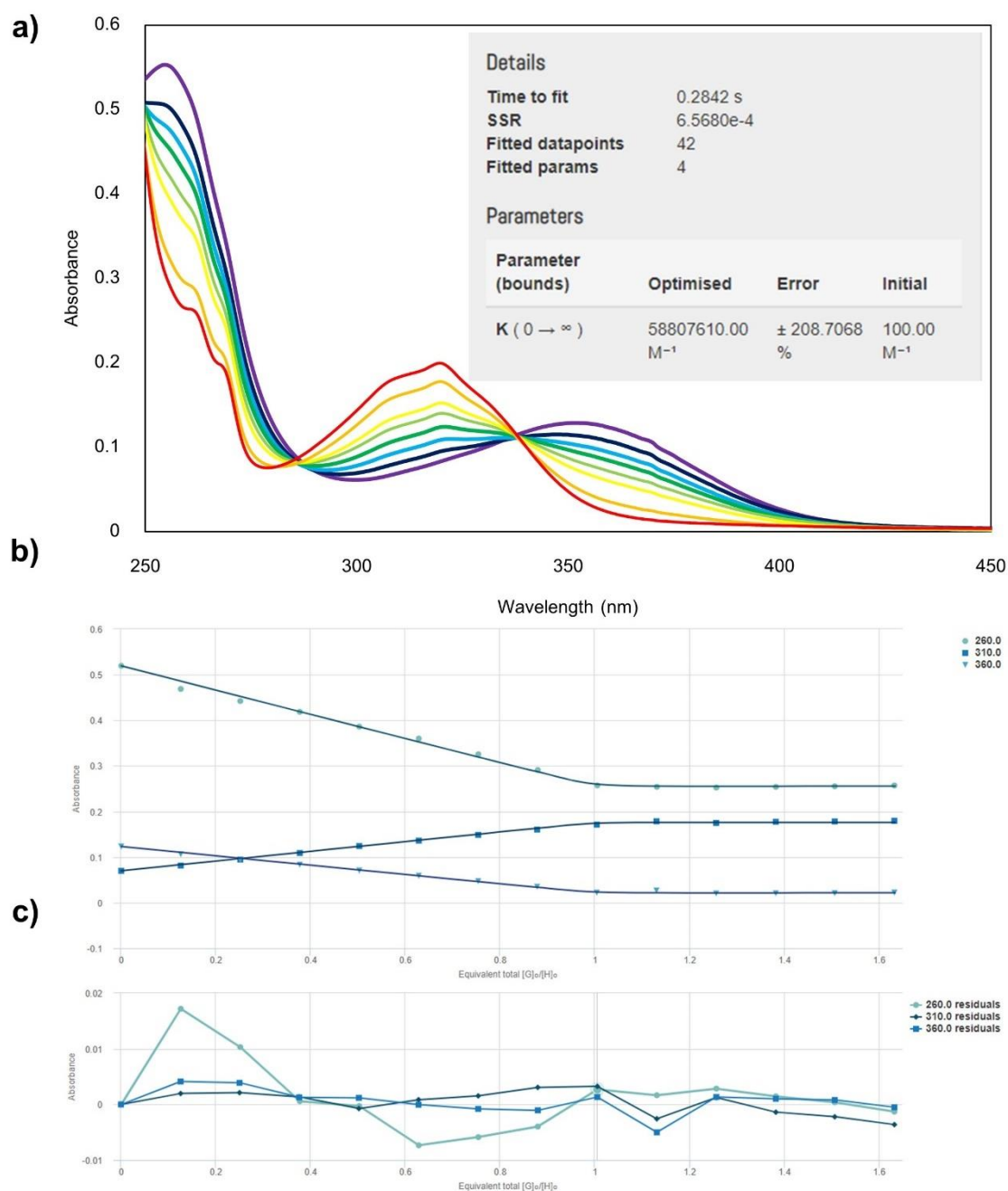
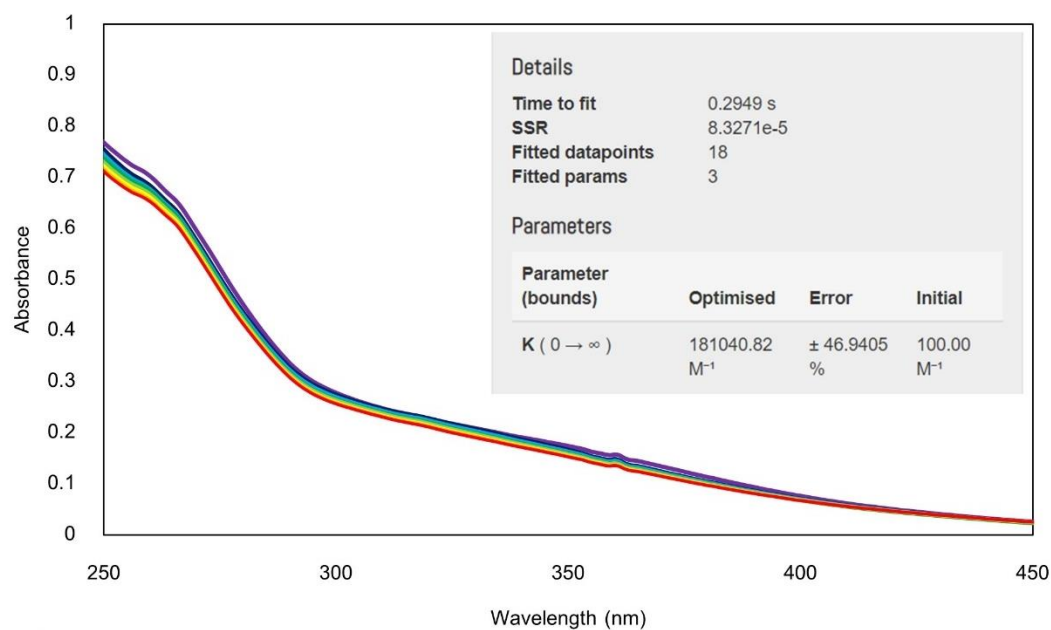
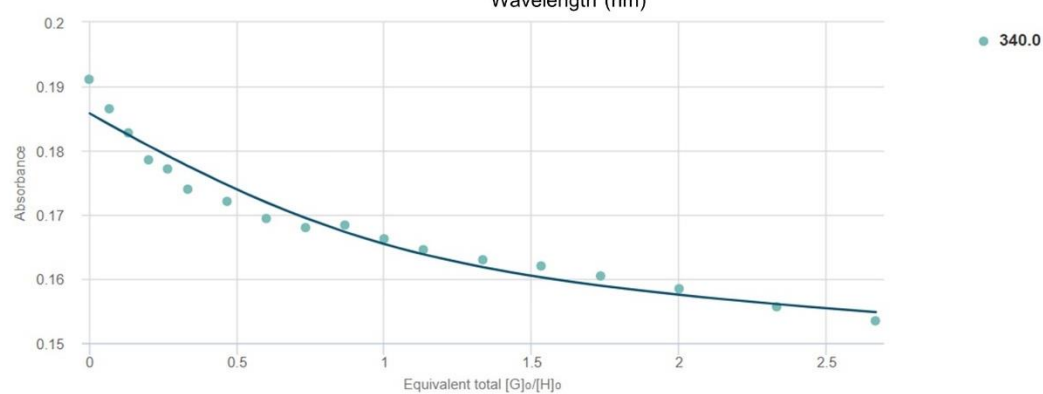


Figure A 93 a) UV titration between **L16** and Zn^{2+} (inset) summary table of the results of the curve fitting, b) scatter plots between absorbance and amount of Zn^{2+} at 260, 310 and 360 nm, the lines show non-linear curve fitting of the absorbance values at all three wavelengths used for determination of K_a value. c) residual plots of the corresponding fitting.

a)



b)



c)

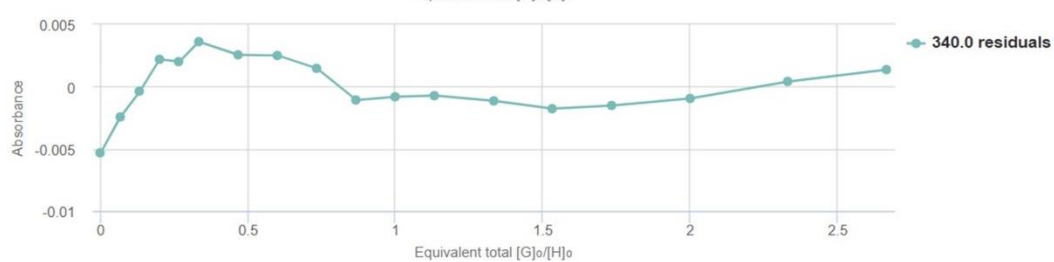


Figure A 94 a) UV titration between **L17** and Cd^{2+} (inset) summary table of the results of the curve fitting, b) scatter plots between absorbance and amount of Cd^{2+} at 340 nm, the line shows non-linear curve fitting of the absorbance values used for determination of K_a value. c) residual plots of the corresponding fitting.

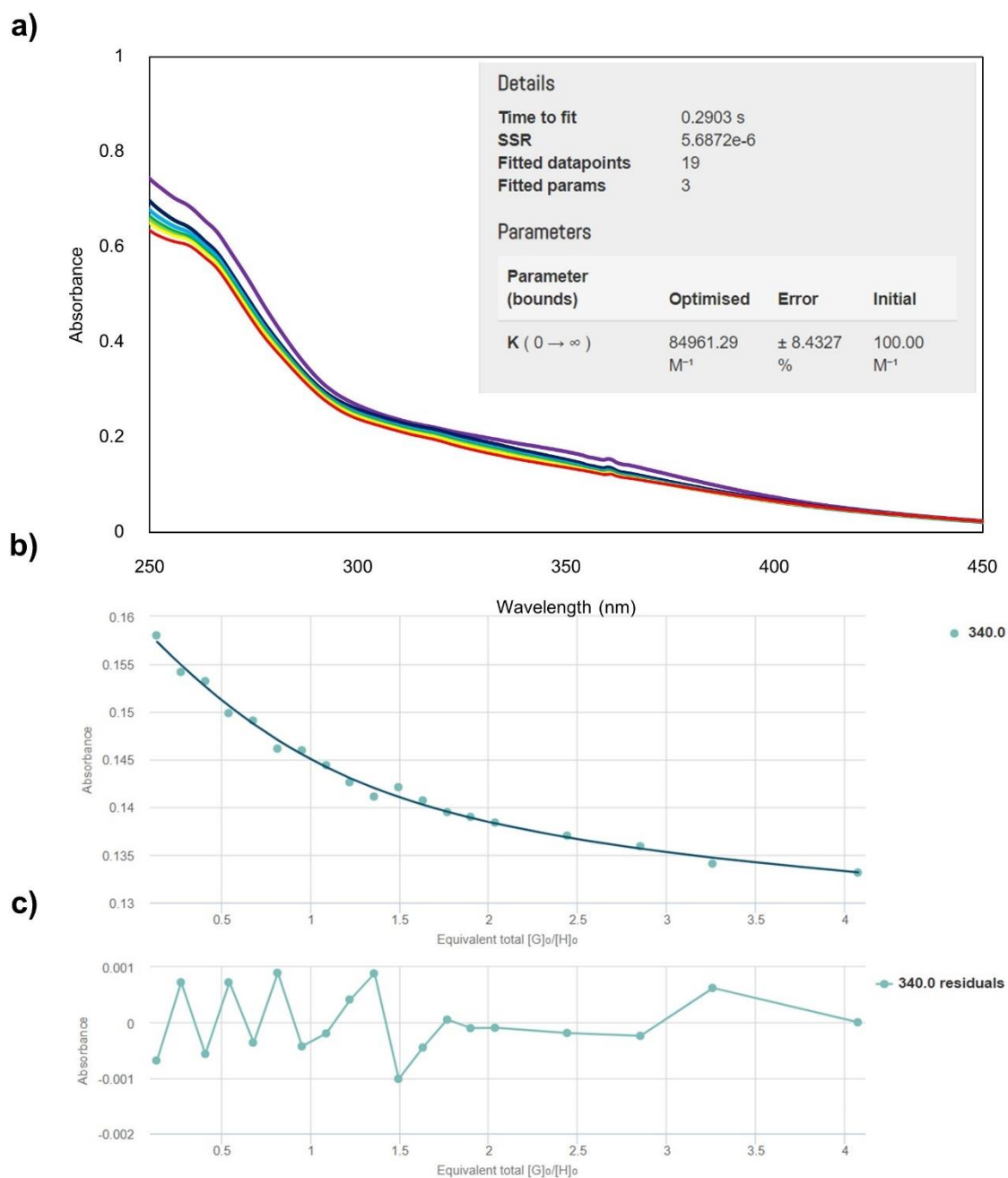


Figure A 95 a) UV titration between **L17** and Zn^{2+} (inset) summary table of the results of the curve fitting, b) scatter plots between absorbance and amount of Zn^{2+} at 340 nm, the line shows non-linear curve fitting of the absorbance values used for determination of K_a value. c) residual plots of the corresponding fitting.

REFERENCES

1. *Jablonski diagram*. 2020 2020/08/16; Available from: <https://chem.libretexts.org/@go/page/1769>.
2. Lakowicz, J.R., *Introduction to Fluorescence*, in *Principle of Fluorescence Spectroscopy*. 2006, Springer: US. p. 1-26.
3. Valeur, B. and M.N. Berberan-Santos, *Internal Heavy atom Effect*, in *Molecular Fluorescence*. 2012, WILEY-VCH Verlag GmbH & Co. KGaA: Germany. p. 77.
4. Valeur, B. and M.N. Berberan-Santos, *Chemical Sensing via Fluorescence*, in *Molecular Fluorescence*. 2012, WILEY-VCH Verlag GmbH & Co. KGaA: Germany. p. 409-478.
5. Xuan, W., et al., *Reaction-Based "Off-On" Fluorescent Probe Enabling Detection of Endogenous Labile Fe²⁺ and Imaging of Zn²⁺-induced Fe²⁺ Flux in Living Cells and Elevated Fe²⁺ in Ischemic Stroke*. *Bioconjugate Chemistry*, 2016. **27**(2): p. 302-308.
6. Zhang, N., et al., *The fertilization-induced zinc spark is a novel biomarker of mouse embryo quality and early development*. *Scientific Reports*, 2016. **6**(1): p. 22772.
7. Nakano, S., et al., *Simultaneous Detection of ATP and GTP by Covalently Linked Fluorescent Ribonucleopeptide Sensors*. *Journal of the American Chemical Society*, 2013. **135**(9): p. 3465-3473.
8. Dong, H., X. Cao, and C.M. Li, *Functionalized Polypyrrole Film: Synthesis, Characterization, and Potential Applications in Chemical and Biological Sensors*. *ACS Applied Materials & Interfaces*, 2009. **1**(7): p. 1599-1606.
9. Shiraishi, Y., et al., *Thermoresponsive Copolymer Containing a Coumarin-Spiropyran Conjugate: Reusable Fluorescent Sensor for Cyanide Anion Detection in Water*. *ACS Applied Materials & Interfaces*, 2011. **3**(12): p. 4649-4656.
10. Chen, L., et al., *Covalent Organic Framework Functionalized with 8-Hydroxyquinoline as a Dual-Mode Fluorescent and Colorimetric pH Sensor*. *ACS*

- Applied Materials & Interfaces, 2018. **10**(18): p. 15364-15368.
11. de Silva, A.P., et al., *Signaling Recognition Events with Fluorescent Sensors and Switches*. Chemical Reviews, 1997. **97**(5): p. 1515-1566.
 12. Callan, J., A. Silva, and D. Magri, *Luminescent Sensors and Switches in the Early 21st Century*. Tetrahedron, 2005. **61**: p. 8551-8588.
 13. Gunnlaugsson, T., et al., *Fluorescent Photoinduced Electron Transfer (PET) Sensors for Anions; From Design to Potential Application*. Journal of Fluorescence, 2005. **15**(3): p. 287-299.
 14. Ghosh, M., et al., *Exploring the Scope of Photo-Induced Electron Transfer-Chelation-Enhanced Fluorescence-Fluorescence Resonance Energy Transfer Processes for Recognition and Discrimination of Zn²⁺, Cd²⁺, Hg²⁺, and Al³⁺ in a Ratiometric Manner: Application to Sea Fish Analysis*. ACS Omega, 2018. **3**(4): p. 4262-4275.
 15. Valeur, B. and M.N. Berberan-Santos, *Photoinduced Electron Transfer*, in *Molecular Fluorescence*. 2012, WILEY-VCH Verlag GmbH & Co. KGaA: Germany. p. 159-161.
 16. Zhao, N., et al., *Identifying the Role of Intramolecular Charge Transfer and Excited-State Proton Transfer in Fluorescence Mechanism for an Azido-Based Chemosensor*. The Journal of Physical Chemistry C, 2018. **122**(46): p. 26576-26583.
 17. Qian, F., et al., *Visible Light Excitable Zn²⁺ Fluorescent Sensor Derived from an Intramolecular Charge Transfer Fluorophore and Its in Vitro and in Vivo Application*. Journal of the American Chemical Society, 2009. **131**(4): p. 1460-1468.
 18. Zhou, G., M. Baumgarten, and K. Müllen, *Mesitylboron-Substituted Ladder-Type Pentaphenylenes: Charge-Transfer, Electronic Communication, and Sensing Properties*. Journal of the American Chemical Society, 2008. **130**(37): p. 12477-12484.
 19. Panja, S.K., N. Dwivedi, and S. Saha, *Tuning the intramolecular charge transfer (ICT) process in push-pull systems: effect of nitro groups*. RSC Advances, 2016. **6**(107): p. 105786-105794.

20. Chen, W., et al., *An intramolecular charge transfer and excited state intramolecular proton transfer based fluorescent probe for highly selective detection and imaging of formaldehyde in living cells*. *Analyst*, 2019. **144**(23): p. 6922-6927.
21. Misra, R. and S. Bhattacharyya, *Intramolecular Charge Transfer: Theory and Applications*. 2018.
22. Zhao, J., et al., *Excited state intramolecular proton transfer (ESIPT): from principal photophysics to the development of new chromophores and applications in fluorescent molecular probes and luminescent materials*. *Physical Chemistry Chemical Physics*, 2012. **14**(25): p. 8803-8817.
23. Valeur, B. and M.N. Berberan-Santos, *Excitation Energy Transfer*, in *Molecular Fluorescence*. 2012, WILEY-VCH Verlag GmbH & Co. KGaA: Germany. p. 213-261.
24. Chen, H., et al., *FRET-based sensor for visualizing pH variation with colorimetric/ratiometric strategy and application for bioimaging in living cells, bacteria and zebrafish*. *Analyst*, 2020. **145**(12): p. 4283-4294.
25. Sapsford, K.E., L. Berti, and I.L. Medintz, *Materials for Fluorescence Resonance Energy Transfer Analysis: Beyond Traditional Donor-Acceptor Combinations*. *Angewandte Chemie International Edition*, 2006. **45**(28): p. 4562-4589.
26. Feng, X., et al., *Aggregation-Induced Emission Enhancement of Aryl-Substituted Pyrrole Derivatives*. *The Journal of Physical Chemistry B*, 2010. **114**(50): p. 16731-16736.
27. Liu, D., et al., *Giant Truncated Metallo-Tetrahedron with Unexpected Supramolecular Aggregation Induced Emission Enhancement*. *Journal of the American Chemical Society*, 2020. **142**(17): p. 7987-7994.
28. Zhu, H., et al., *Twisted Donor- π -Acceptor Carbazole Luminophores with Substituent-Dependent Properties of Aggregated Behavior (Aggregation-Caused Quenching to Aggregation-Enhanced Emission) and Mechanoresponsive Luminescence*. *The Journal of Physical Chemistry C*, 2018. **122**(34): p. 19793-19800.
29. Zuo, Y., X. Wang, and D. Wu, *Uniting aggregation-induced emission and stimuli-*

- responsive aggregation-caused quenching, single molecule achieved multicolour luminescence*. *Journal of Materials Chemistry C*, 2019. **7**(46): p. 14555-14562.
30. Valeur, B. and M.N. Berberan-Santos, *Formation of Excimers and Exciplexes*, in *Molecular Fluorescence*. 2012, WILEY-VCH Verlag GmbH & Co. KGaA: Germany. p. 162-167.
 31. Lodeiro, C. and F. Pina, *Luminescent and chromogenic molecular probes based on polyamines and related compounds*. *Coordination Chemistry Reviews*, 2009. **253**(9): p. 1353-1383.
 32. Jang, H.-S., et al., *Unique Effects of the Chain Lengths and Anions of Tetra-alkylammonium Salts on Quenching Pyrene Excimer*. *ACS Applied Materials & Interfaces*, 2014. **6**(17): p. 14801-14811.
 33. Wu, J.-S., et al., *Fluorescence Turn On of Coumarin Derivatives by Metal Cations: A New Signaling Mechanism Based on C=N Isomerization*. *Organic Letters*, 2007. **9**(1): p. 33-36.
 34. Garside, M. *Refinery production of cadmium worldwide from 2010 to 2020*. 2021 2021/02/21; Available from: <https://www.statista.com/statistics/598261/global-refinery-production-of-cadmium/>.
 35. Satarug, S., et al., *A global perspective on cadmium pollution and toxicity in non-occupationally exposed population*. *Toxicology Letters*, 2003. **137**(1): p. 65-83.
 36. Johri, N., G. Jacquillet, and R. Unwin, *Heavy metal poisoning: the effects of cadmium on the kidney*. *Biometals*, 2010. **23**(5): p. 783-92.
 37. Picaud, T. and A. Desbois, *Interaction of Glutathione Reductase with Heavy Metal: The Binding of Hg(II) or Cd(II) to the Reduced Enzyme Affects Both the Redox Dithiol Pair and the Flavin*. *Biochemistry*, 2006. **45**(51): p. 15829-15837.
 38. Tchounwou, P.B., et al., *Heavy metal toxicity and the environment*. *Experientia supplementum* (2012), 2012. **101**: p. 133-164.
 39. Flick, D.F., H.F. Kraybill, and J.M. Dlmittroff, *Toxic effects of cadmium: A review*. *Environmental Research*, 1971. **4**(2): p. 71-85.

40. Cadmium 2015; Available from:
https://www.wqa.org/portals/0/technical/technical%20fact%20sheets/2015_cadmium.pdf.
41. Kim, H.N., et al., *Fluorescent and colorimetric sensors for detection of lead, cadmium, and mercury ions*. Chemical Society Reviews, 2012. **41**(8): p. 3210-3244.
42. Liu, X., et al., *A turn-on fluorescent sensor for zinc and cadmium ions based on perylene tetracarboxylic diimide*. Analyst, 2013. **138**(3): p. 901-906.
43. Song, E.J., et al., *A single molecule that acts as a fluorescence sensor for zinc and cadmium and a colorimetric sensor for cobalt*. Dalton Transactions, 2013. **42**(43): p. 15514-15520.
44. Bronson, R.T., et al., *Efficient Immobilization of a Cadmium Chemosensor in a Thin Film: Generation of a Cadmium Sensor Prototype*. Organic Letters, 2005. **7**(6): p. 1105-1108.
45. Lu, C., et al., *Ratiometric and Highly Selective Fluorescent Sensor for Cadmium under Physiological pH Range: A New Strategy to Discriminate Cadmium from Zinc*. The Journal of Organic Chemistry, 2007. **72**(9): p. 3554-3557.
46. Xue, L., Q. Liu, and H. Jiang, *Ratiometric Zn²⁺ Fluorescent Sensor and New Approach for Sensing Cd²⁺ by Ratiometric Displacement*. Organic Letters, 2009. **11**(15): p. 3454-3457.
47. Tang, X.-L., et al., *Design of a Semirigid Molecule as a Selective Fluorescent Chemosensor for Recognition of Cd(II)*. Organic Letters, 2008. **10**(17): p. 3653-3656.
48. Xue, L., et al., *Modulating Affinities of Di-2-picolyamine (DPA)-Substituted Quinoline Sensors for Zinc Ions by Varying Pendant Ligands*. Inorganic Chemistry, 2008. **47**(10): p. 4310-4318.
49. Xue, L., C. Liu, and H. Jiang, *Highly Sensitive and Selective Fluorescent Sensor for Distinguishing Cadmium from Zinc Ions in Aqueous Media*. Organic Letters, 2009. **11**(7): p. 1655-1658.
50. Zhao, Q., et al., *A Highly Selective On/Off Fluorescence Sensor for Cadmium(II)*.

- Inorganic Chemistry, 2011. **50**(20): p. 10041-10046.
51. Zhou, X., et al., *A Highly Selective Fluorescent Sensor for Distinguishing Cadmium from Zinc Ions Based on a Quinoline Platform*. Inorganic Chemistry, 2012. **51**(17): p. 9226-9231.
 52. Liu, Y., et al., *Cd²⁺-triggered amide tautomerization produces a highly Cd²⁺-selective fluorescent sensor across a wide pH range*. Dyes and Pigments, 2016. **133**: p. 339-344.
 53. Mikata, Y., et al., *TQOPEN (N,N,N',N'-Tetrakis(2-quinolylmethyl)-3-oxa-1,5-pentanediamine) Family as Heptadentate Fluorescent Cd²⁺ Sensors*. Inorganic Chemistry, 2017. **56**(13): p. 7404-7415.
 54. Song, H. and Z. Zhang, *A quinoline-based ratiometric fluorescent probe for discriminative detection of Zn²⁺ and Cd²⁺ with different binding modes, and its Zn²⁺ complex for relay sensing of pyrophosphate and adenosine triphosphate*. Dyes and Pigments, 2019. **165**: p. 172-181.
 55. Tomar, M., et al., *Facile synthesis of 5,8-linked quinoline-based copolymers*. Polymer International, 2012. **61**(8): p. 1318-1325.
 56. Melhuish, W.H., *QUANTUM EFFICIENCIES OF FLUORESCENCE OF ORGANIC SUBSTANCES: EFFECT OF SOLVENT AND CONCENTRATION OF THE FLUORESCENT SOLUTE1*. The Journal of Physical Chemistry, 1961. **65**(2): p. 229-235.
 57. *APEX3, SADABS and SAINT*. 2016: Bruker AXS Inc., Madison, Wisconsin, USA.
 58. Sheldrick, G., *SHELXT - Integrated space-group and crystal-structure determination*. Acta Crystallographica Section A, 2015. **71**(1): p. 3-8.
 59. Sheldrick, G., *Crystal structure refinement with SHELXL*. Acta Crystallographica Section C, 2015. **71**(1): p. 3-8.
 60. Spek, A., *Single-crystal structure validation with the program PLATON*. Journal of Applied Crystallography, 2003. **36**(1): p. 7-13.



จุฬาลงกรณ์มหาวิทยาลัย
CHULALONGKORN UNIVERSITY

VITA

NAME Jutawat Hojitsiriyant
DATE OF BIRTH 7 June 1991
PLACE OF BIRTH Bangkok, Thailand
INSTITUTIONS ATTENDED Chulalongkorn University
HOME ADDRESS 646 Petchkasem 92/2 Bangkhae,
Bangkok, Thailand

